

A thesis submitted for Doctorate of Philosophy

Carrier recovery for coherent optical communication systems

By

Jignesh Jokhakar

jignesh.jokhakar@monash.edu

Supervisors

Prof. Arthur J. Lowery

arthur.lowery@monash.edu

and

Dr. Bill Corcoran

bill.corcoran@monash.edu

ELECTRO-PHOTONICS LAB

Department of Electrical and Computer Systems Engineering,



MONASH
University

Monash University, Australia.

March, 2018

Acknowledgement

This work is an outcome of my efforts and support of many people very dear to me. First and foremost, I thank my main supervisor, Prof. Arthur Lowery for accepting me as one of his PhD. students. Apart from the technical discussions, Arthur's strong support has allowed me to get through the many ups and downs throughout this journey. Next, I thank my co-supervisor, Dr. Bill Corcoran for his ongoing help with experimental verification of my ideas. His ideas led me to successfully verify many concepts described in this thesis. I sincerely thank both Arthur and Bill for all their valuable contributions towards my research and publication work.

Further, I would like to thank my dear parents, Mr. Dhruvakumar and Mrs. Bindu Jokhakar. They have always been a pillar of strength and supported me including my decision to pursue Ph.D. I also thank my brother and sister-in-law, Mr Ritesh and Mrs Ranjana Jokhakar for their encouragement and support. I also thank my dear friend, Harish Vangala for helping me in documentation of this thesis using Latex. Finally, I thank my partner, Sonia for her emotional support and my friends; Vikram, Harsh, Janhavi and Khyati for being there for me throughout these testing years.

Declaration

Jignesh Jokhakar (2018)

I certify that I have not, knowingly, added any copyright content to my work without the owner's permission.

I declare that this thesis contains no material, to the best of my knowledge and belief, which has been accepted for the award of any other degree or diploma at any university or equivalent institution and that this thesis contains no material previously published or written by another person, except where due reference is made in the text of the thesis.

Signature:

JIGNESH JOKHAKAR

Date:

Abstract

Carrier recovery and synchronization are the base foundation for data extraction in any coherent communication system. Although explored for decades now, the most appropriate carrier recovery technique changes with application and requirements. While some implementation scenarios require less complex hardware, some may require lower latency and less computation. Some scenarios intend to use low-precision components to reduce the cost, while some relax the cost-constraints to boost the throughput. Considering these different requirements, this thesis explores different approaches to carrier recovery namely: digital signal processing, optoelectronic processing and all-optical processing. The improvements in performance or implementation constraints demonstrated by the proposed techniques over the conventional methods suggest their beneficial usage in future.

Contents

Contents	v
List of Figures	vii
List of Tables	ix
1 Introduction	1
1.1 Optical communications systems	1
1.2 Perturbing parameters	3
1.2.1 Carrier frequency offset	3
1.2.2 Phase noise	4
1.3 Thesis summary	5
1.3.1 Digital signal processing (DSP) approach (Chapter 3)	6
1.3.2 Optoelectronic approach (Chapter 4) [Publications 1.3.4(4-5)]	7
1.3.3 All-optical approach (Chapter 5)	7
1.3.4 Publications	10
2 The journey so far..	12
2.1 Early communication systems (1816-1930 A.D.).	12
2.2 Preliminary research in carrier recovery for wireless communications (1930-1980 A.D.).	13
2.2.1 Phase-locked loops	13
2.2.2 Techniques proposed in parallel with the PLLs.	15
2.3 Research in carrier recovery for optical communication (1980-2005 A.D.)	17
2.3.1 Optical phase-locked loop (OPLL)	17
2.3.2 All optical approaches	18
2.4 DSP techniques for carrier recovery in optical communication (post-2005 A.D.)	20
2.4.1 M^{th} power estimator	20
2.4.2 Blind phase search (BPS)	21
2.4.3 Viterbi-Viterbi monomial phase estimator (VVMPE)	23
2.4.4 Adaptive filters	24
2.4.5 Kalman filters	25
3 Digital signal processing for carrier-recovery	26
3.1 Introduction to Kalman filters	27
3.2 When should Kalman filters be used?	28
3.3 Kalman filter algorithms	28
3.3.1 Linear Kalman filter	28
3.3.2 Extended Kalman filter	30
3.3.3 Unscented Kalman filters	31
3.4 Why are unscented Kalman filters superior?	33
3.5 Parallel-processing Kalman filters for carrier recovery	36
3.5.1 State-space model equations and proposed nonlinear model	37
3.5.2 Experimental setup and results	38

3.6	Joint phase-noise and polarization state tracking	46
3.6.1	Nonlinear observation model	47
3.6.2	Modified Kalman filters for reduced complexity	48
3.6.3	Experimental setup	49
3.6.4	Simulations to investigate the range of tolerable linewidth and CFO.	52
3.6.5	Conclusions	56
4	Optoelectronic processing approach for carrier recovery	57
4.1	Introduction and problem statement	57
4.2	Coherent-optical orthogonal frequency division multiplexing	59
4.3	Concept of optoelectronic frequency offset estimator	61
4.4	System design and simulations	63
4.4.1	OEFOE Version 1	63
4.4.2	OEFOE Version 2	67
4.4.3	Effect of the phase mismatch between signals at outputs of 3-dB coupler	67
4.4.4	Effects of the delay variations in the optical delay line (τ_1)	68
4.4.5	Effect of the polarization misalignment in the polarization controllers	69
4.5	Variation of performance against cyclic prefix length	71
4.6	Simulated system performance	73
4.6.1	Laser Linewidth	73
4.6.2	AWGN loading	74
4.7	Chromatic dispersion and nonlinear effects of the fiber	75
4.7.1	Simulated transmission system: QPSK	75
4.7.2	Simulated transmission system: 16-QAM	76
4.7.3	Conclusions	79
5	All-optical processing approach for carrier recovery	80
5.1	Polarization-independence for optical injection locking.	81
5.1.1	Introduction	81
5.1.2	Injection locking and Optical injection locking	81
5.1.3	Problem statement and proposed solution	84
5.1.4	Proposed module design	85
5.1.5	Experimental proof of concept	87
5.1.6	Back-to-back test with injection locked self-homodyne receiver	88
5.1.7	Broad-linewidth laser experiments	91
5.1.8	Field test over a fiber link from Monash Clayton to Caulfield campus	93
5.2	Nonlinear interference noise cancellation using optical injection locking	95
5.2.1	Inter-channel nonlinear interference cancellation	95
5.2.2	Digital backpropagation for SPM compensation cascaded with the OIL-based NLIN cancellation.	107
5.2.3	XPM compensation	107
5.2.4	Experimental results	110
5.2.5	Conclusions	114
6	Conclusions	115
7	Appendix	120
7.1	Appendix A: Parallelized unscented Kalman filter architecture and algorithm	120
7.2	Appendix B: Choosing co-ordinate system for joint phase-noise and polarization-state observation model	123
7.3	Appendix C: Unscented Kalman filter algorithm for joint phase noise and polarization-state tracking	125
7.4	MATLAB codes	126
7.4.1	UKF for joint polarization-state and phase-noise tracking code.	126
7.4.2	R-UKF for joint polarization-state and phase-noise tracking code.	128
	Bibliography	193

List of Figures

1.1	Direct-detection optical communication system.	2
1.2	Coherent optical communication system.	3
1.3	10-Gbaud, QPSK constellation with: a) CFO=0 MHz and b) CFO=100 MHz.	4
1.4	10-Gbaud, 16-QAM constellation under the influence of: a) Laser phase noise and b) Nonlinear phase noise.	4
1.5	Thesis summary tree chart.	5
1.6	Contributions of the proposed techniques in signal processing for data recovery.	6
1.7	Time journey of carrier recovery in optical communication with important milestones.	11
2.1	Wadley loop working principle.	15
2.2	OPLL designs.	17
2.3	M^{th} power phase estimator's working principle.	20
2.4	Blind phase search working principle.	22
3.1	Linear Kalman filtering process.	29
3.2	Extended Kalman filtering process.	31
3.3	Unscented Kalman filtering process.	32
3.4	Intuitive working of Linear/Extended Kalman filters for: a) linear channel, b) nonlinear channel	34
3.5	Intuitive working of unscented Kalman filters for a) linear channel, b) nonlinear channel	34
3.6	Working of parallel-processing Kalman filters	36
3.7	correction method of LKF <i>vs.</i> UKF.	38
3.8	Experimental setup in: (a) back-to-back configuration (b) 800-km transmission link configuration. BPF: Band pass filter, VOA: Variable optical attenuator, CMZM: Complex Mach-Zehnder modulator, AWG: Arbitrary waveform generator, ECL: External cavity laser.	39
3.9	Experimental Q <i>vs.</i> OSNR, block lengths of: (a) 44 (b) 142 and (c) 198 samples.	40
3.10	Experimental Q <i>vs.</i> block length, OSNR = 10 dB.	41
3.11	Experimental Q <i>vs.</i> OSNR for 16-QAM, block length = 44.	42
3.12	Computation time in reference to that of LKF at block length = 44	43
3.13	Experimental Q <i>vs.</i> launch power over an 800-km optical fiber link, using optimal block length.	44
3.14	45
3.16	Experimental setup for a) back-to-back configuration and b) 800-km transmission link configuration; CMZM: complex Mach-Zehnder modulator, BPF: band pass filter, VOA: variable optical attenuator, ECL: external cavity laser, EDFA: erbium doped fiber amplifier.	49
3.17	Digital signal processing flow for a) CMA+VVPE/MMA+ML b) Kalman filters under test.	50
3.18	Experimental Q <i>vs.</i> OSNR (dB) in back-to-back configuration for 20 Gbaud QPSK and 20 Gbaud 16-QAM respectively.	51
3.19	Experimental Q <i>vs.</i> launch power (dBm) in 800 km link configuration for 20 Gbaud QPSK and 16-QAM respectively.	52
3.20	Simulated Q (dB) <i>vs.</i> linewidth (kHz) (simulations).	53
4.1	Receiver implementing the proposed estimator. ADC: Analog-to-Digital converter; LO: Local oscillator.	59
4.2	Cyclic prefix addition onto OFDM symbols.	60

4.3	Signal flow diagram of an OFDM system. FFT: fast fourier transform, IFFT: inverse fast fourier transform, LO: local oscillator.	61
4.4	Proposed optoelectronic CFO estimator (OEFOE) design. Inset: OFDM symbol frame structure.	64
4.5	Simulated system output <i>vs.</i> photodiode integration time for CFO = 410 MHz.	64
4.6	Scatterplots of Estimated CFO <i>vs.</i> Actual CFO (MHz).	65
4.7	OEFOE version 2 setup. PC: polarization controller; PBS: polarization beam splitter.	67
4.8	Simulated Q (dB) and estimate % error <i>vs.</i> coupler output phase mismatch (degrees).	68
4.9	Simulated Q (dB) and estimate % error <i>vs.</i> delay variations (ps) in optical delay line.	68
4.10	DSP estimated absolute CFO <i>vs.</i> proposed OEFOE Version 2 estimated absolute CFO.	70
4.11	Effect of the polarization misalignment.	70
4.12	Simulated CFO estimate (MHz) <i>vs.</i> time (μ s)	72
4.13	Estimate error (%) <i>vs.</i> Cyclic prefix (%).	72
4.14	OEFOE simulation schematic in VPItransmissionMaker software.	73
4.15	CFO estimate <i>vs.</i> laser linewidth (MHz) for CFO = 300 MHz.	74
4.16	Effect of the AWGN noise for 28-Gbaud QPSK, FFT length=156, number of subcarriers = 100, 15% cyclic prefix and carrier frequency offset (CFO) = 300 MHz.	74
4.17	Simulated CFO estimates <i>vs.</i> launch power (dBm) for QPSK and carrier frequency offset (CFO) = 300 MHz.	75
4.18	Simulated Q (dB) <i>vs.</i> Launch power (dBm) for 28-Gbaud QPSK signal with FFT length = 156, number of subcarriers = 100 and 15% cyclic prefix for link distances 200 km, 300 km, 500 km and 700 km.	76
4.19	Effect of the AWGN noise for 28-Gbaud 16-QAM with FFT length = 156, number of subcarriers = 100, 15 % Cyclic prefix and carrier frequency offset (CFO) = 300 MHz.	77
4.20	Simulated Q (dB) <i>vs.</i> Launch power (dBm) for 28-Gbaud 16-QAM signal with FFT length = 156, number of subcarriers = 100 and 15% cyclic prefix for link distances 200 km, 300 km, 500 km and 700 km.	77
5.1	Syncing of pendulums on a common beam.	82
5.2	Conventional OIL setup. VOA: variable optical attenuator; PC: polarization controller; PBS: polarization beam splitter; ADC: analog-to-digital converter.	82
5.3	Phase model for optical injection locking based on laser rate equations.	83
5.4	OIL setup with proposed modifications. OIL setup with the proposed modifications. SG: signal generator; PM: phase modulator.	84
5.5	Proposed polarization-locking module design with working concept.	85
5.6	Experimental setup for proof of concept. ECL: external cavity laser; PS: polarization scrambler; IL: Injection laser; LO: local oscillator laser; Rx: Receiver.	87
5.7	Peak-to-peak phase swing of the recovered signal and % modulation transfer through OIL setup. SOP: state of polarization.	87
5.8	Phase transfer (radians) <i>vs.</i> frequency deviation (MHz).	88
5.9	Experimental setup with proposed module and injection locking setup. CMZM: complex Mach-Zehnder modulator; EDFA: erbium doped fiber amplifier; BPF: bandpass filter; OSA: optical spectrum analyzer; DSP: digital signal processing.	89
5.10	Spectrum of the generated signal with guard band.	89
5.11	Q performance <i>vs.</i> OSNR (dB). Insets: Constellations of recovered signals at 22-dB OSNR with and without amplitude distortions.	90
5.12	Q (dB) <i>vs.</i> OSNR (dB) using low performance laser (LW=40 MHz) compared with a standard laser (LW=100 kHz). Insets: Recovered constellations at 22-dB OSNR for QPSK, 16-QAM with laser LW = 40 MHz.	92
5.13	Map showing the test link node locations.	93
5.14	Q performance <i>vs.</i> OSNR (dB) for field link (20 km) using low performance laser (output power: 0.5 dBm).	94
5.15	Scaled XPM efficiency (dB) <i>vs.</i> frequency (GHz).	97
5.16	OIL-based XPM compensation concept.	97
5.17	Spectral effects of OIL's phase-transfer bandwidth.	98
5.18	Phase transfer-function of the optical injection locking setup; P_{inj} : Injected power (dBm). Inset: 10-Gbaud modulated signal spectrum.	99

5.19	Experimental setup: AWG- arbitrary waveform generator; DCM- dispersion compensation module; EDFA- erbium doped fiber amplifier; AOM- acousto-optic modulator; WSS- wavelength selective switch (WaveShaper).	100
5.20	Q vs. injected power for various launch-powers and link lengths.	101
5.21	Q vs. launch-power with QPSK modulation.	104
5.22	Q vs. launch-power with 16-QAM modulation.	105
5.23	System compensating for XPM using optical injection locking and SPM using DBP (digital back-propagation).	107
5.24	Frequency response of the high-pass filter used in filtered-DBP. HPF: high pass filter.	109
5.25	Q (dB) vs. launch power (dBm) of system with (squares) and without filtering (triangles) in DBP.	111
5.26	Q vs. launch power comparison for QPSK.	112
5.27	Q vs. launch power comparison for 16-QAM.	113
6.1	Q -performance report of the proposed carrier-recovery methods.	118
7.1	(a) Architecture of parallelized unscented Kalman filter. (b) Internal structure of Block A.	120

List of Tables

1.1	Proposed techniques with their compensation capabilities.	8
1.2	Performance of the proposed techniques with respect to the requirement aspects.	9
1.3	Other comparable implementation parameters.	9
3.1	Simulated maximum tolerable limits of CFO and linewidth before experiencing cycle slips for QPSK and 16-QAM signals. The values in the brackets show the tolerable limits while keeping the Q penalty less than 1 dB.	45
3.2	Number of complex multiplications per symbol detection required by the algorithms.	49
3.3	Performance gain observed with the unscented Kalman filter (UKF) against conventional algorithms and the extended Kalman filter (EKF).	54
3.4	Performance gain observed with the reduced-unscented Kalman filter (R-UKF) against conventional algorithms and the extended Kalman filter (EKF). Negative values indicate penalties.	54
4.1	Parameter values taken for simulations.	65
5.1	Number of complex multiplications per symbol detection required by the algorithms.	105
6.1	Proposed techniques with their compensation capabilities.	115
6.2	Performance of the proposed techniques with respect to the requirement aspects.	119

Introduction

Optical communication has enabled extraordinary data-carrying capacity in communication systems. Data rates in the tens of terabits per second per fibre have become possible owing to the large bandwidth provided by optical fibres [1] [2]. Researchers across the globe are working towards developing technologies to satisfy the increasing and never-ending market requirements such as higher data rates, low cost system deployment, lower latency in data extraction *etc.* To meet these requirements, efficient techniques to detect the transmitted symbols without errors are needed. Depending on the application, an efficient technique can be the one that gives low errors for a particular signal to noise ratio or can also be the one that gives a satisfactory and detectable output with least complexity in terms of computation and hardware. It can also be a system that recovers the data with a lower latency. In this thesis, techniques to achieve or assist carrier recovery in optical communication systems are proposed, with each of the techniques observed to be "efficient" in one or more aspects mentioned above.

1.1 Optical communications systems

Transmission of data as optical signals over optical fibers became of interest to communications engineers due to relatively large usable bandwidth in the range of multiple terahertz frequencies that promoted higher data rate transmissions compared with the radio frequencies [3]. In addition to a large available bandwidth, the low attenuation of the optical fiber allowed for long distance transmission of these high bandwidth signals. The first commercial optical communication systems used intensity modulation/direct detection (IM/DD) technique in 1975. As shown in Fig. 1.1, a continuous wave laser signal's intensity is modulated according to the binary data to be transmitted. On the receiver side, a photodetector converts this intensity fluctuation to electrical signal, to be processed for data extraction.

Although simple to design, the IM/DD systems could not support the modulation schemes that carried data in the phase of the carrier such as quadrature phase-shift keying (QPSK) and quadrature-amplitude modulation (QAM). This inability of IM/DD systems plays against them as the intensity modulation schemes are more susceptible to noise [3]. As a result, around 1981, coherent optical

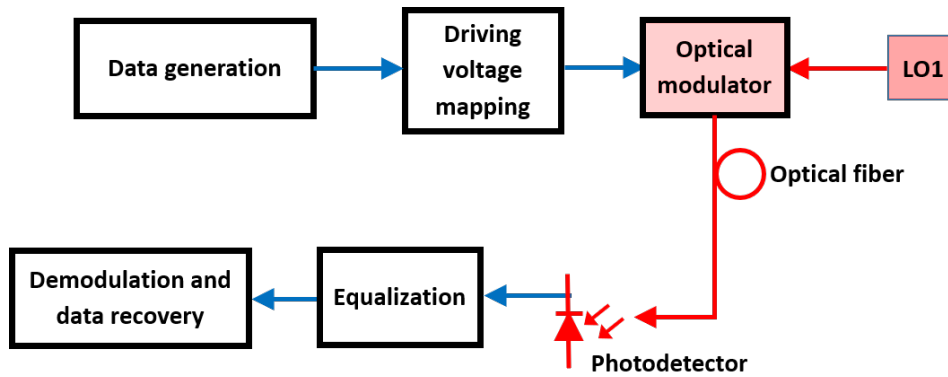


Figure 1.1: Direct-detection optical communication system.

communication schemes were explored owing to their increased receiver sensitivity and access to the complex field of the received signal [4]. The phase information along with the amplitude information allows mitigation of chromatic dispersion (CD) and polarization mode dispersion (PMD) by digitally processing the signal [5] [6]. Additionally, bandwidth-efficient and noise-tolerant phase modulation schemes can be used with coherent reception. Unfortunately, the hardware complexity, slow analog-to-digital convertors (ADCs) and crude analogue phase recovery methods before 2000 restricted the usage of coherent receivers for high data rates. The advent of high-speed ADCs, increased usage of phase modulation, requirements for long-distance transmission and high data-rates caused coherent optical communication systems to be favoured over IM/DD systems after 2005 [7].

A general coherent optical communication system is shown in Fig. 1.2. The data to be transmitted is mapped onto in-phase (I) and quadrature signals (Q) based on the type of modulation used. These I and Q signals then drive the optical modulator that modulates a CW laser signal (LO1) in amplitude and phase. The output modulated optical signal is transmitted over an optical fiber and received by a coherent optical receiver. The coherent receiver takes the received signal and a CW laser signal (LO2) as inputs. The outputs of the receiver are two electrical signals representing the I and Q signals. The optical to electrical conversion is performed by balanced photodiodes internal to the coherent receivers. Under ideal conditions, these electrical signals at the output of coherent receivers will be exactly the same as the I and Q signals at the transmitter. Unfortunately, the coherent optical communications system brings additional problems with its benefits. Essentially, anything that distorts the phase of the received signal causes issues as the coherent receivers are sensitive to the phase. This causes errors in data extraction. These include, the laser's finite linewidth, the frequency offsets between LO1 and LO2 [8] and the nonlinear phase distortions induced by the fiber [9]. Carrier recovery needs to be performed in this case along with channel equalization to recover the transmitted symbol. Following this, the symbol can be demodulated and the data can be recovered.

The scope of this thesis is restricted to carrier recovery in coherent optical communication systems.

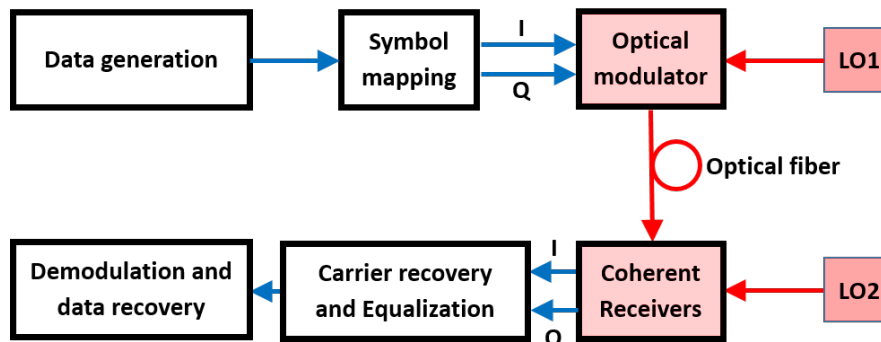


Figure 1.2: Coherent optical communication system.

Just like in radio frequency (RF) wireless communication, the data in optical communications is modulated onto a high frequency carrier. However, in optics, the carrier is an extremely high frequency (in hundreds of THz range), continuous wave, optical signal. In addition to the benefits of modulation in RF communications, modulating the signal on an optical signal allows transmissions over hundreds of kilometers due to low attenuation in optical fibers in the C-band (1530 nm-1565 nm) and large usable bandwidth allowing high data throughputs. Regardless, both of these systems require the carrier to be recovered at the receiver for proper data extraction in the case when the data is modulated on the phase of the carrier, *i.e.* when QPSK or QAM techniques are implemented.

The main problems that carrier recovery targets to solve are as follows:

1. Carrier frequency offset (CFO)
2. Phase noise (PN)
 - laser phase noise.
 - fiber-induced nonlinear interference noise.

1.2 Perturbing parameters

1.2.1 Carrier frequency offset

As shown in Fig. 1.2, a coherent optical communication system consists of a local oscillator laser (LO1) at the transmitter and a local oscillator laser (LO2) at the receiver. The optical beam from LO1 is modulated by the modulator according to the data carrying electrical drive signals. At the receiver, the received optical signal is down-converted to electrical domain by beating it with the optical signal from LO2. In order to bring the received signal to baseband, the frequency of LO1 and LO2 should be the same. This is seldom the case due to continuous drifts in the laser's frequencies. This difference in frequencies between LO1 and LO2 is called carrier frequency offset (CFO) and causes errors in detection of the received signal [3] [8]. This distorting effect can be observed in Fig. 1.3.

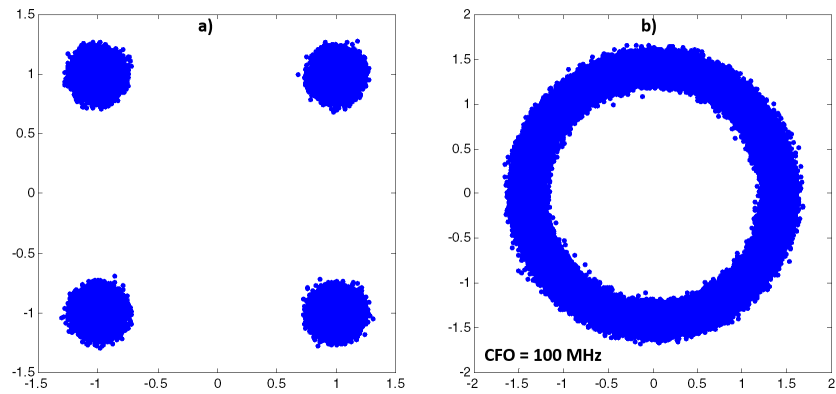


Figure 1.3: 10-Gbaud, QPSK constellation with: a) CFO=0 MHz and b) CFO=100 MHz.

1.2.2 Phase noise

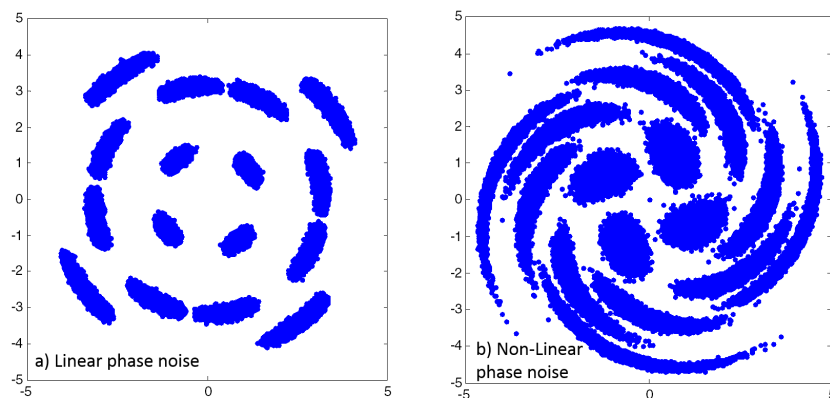


Figure 1.4: 10-Gbaud, 16-QAM constellation under the influence of: a) Laser phase noise and b) Nonlinear phase noise.

Laser linear phase noise

The output of a laser is not monochromatic, i.e. a laser does not radiate at one particular frequency but rather shows a finite linewidth. This finite linewidth is the direct result of the phase noise caused majorly by spontaneous emissions in the gain medium. This further causes many frequency components showing up over time in the CW signal. The phase noise gets its random nature due to these random spontaneous emissions. Statistical analysis shows that laser phase noise follows a Wiener random process model [3] [8].

Nonlinear interference phase noise (NLIN)

The phase noise can also be introduced due to the nonlinear interaction of a signal's intensity fluctuations with the phase of the signal. This interaction could be from the same signal as self-phase modulation (SPM), or another signal transmitted along with, known as the cross-phase modulation (XPM) [10]. The

random intensity fluctuations in the signal due to the amplified spontaneous emission (ASE) added from an EDFA also results in random phase fluctuations (Gordon-Mollenauer effect) [11]. All these factors *i.e.* the SPM, XPM and the ASE-induced phase noise contribute to the nonlinear phase noise.

Fig. 1.4 shows the effect of the linear and nonlinear phase noise on a 16-QAM signal constellation. The distinctive effects that can be observed are due to the fact that the nonlinear phase noise depends on the intensity of the signal. Thus, it is deterministic and not random noise. Due to the Kerr effect, the refractive index of the fiber depends on the intensity of the signal causing intensity-dependent phase fluctuations. As a result of the interaction between the phase and intensity, the signal constellation appears as shown in Fig. 1.4b. On the other hand, the laser phase noise is not intensity-dependent and causes pure phase-shifts (Fig. 1.4a).

The distorted constellations in Fig. 1.3 and Fig. 1.4 clearly show that these distortions will cause errors in data extraction unless carrier recovery is performed to correct them.

1.3 Thesis summary

The complete work in this thesis can be summarized as shown in the tree chart in Fig. 1.5. The goal of achieving carrier recovery for coherent optical communication systems is explored using different approaches, namely, the digital signal processing (DSP), the optoelectronic approach and all optical approach.

Fig. 1.6 gives the data-processing sequence in conventional receiver systems to recover the transmitted data. The contributions of each project in the chapters of this thesis are linked accordingly. The contributions will be briefly discussed below.

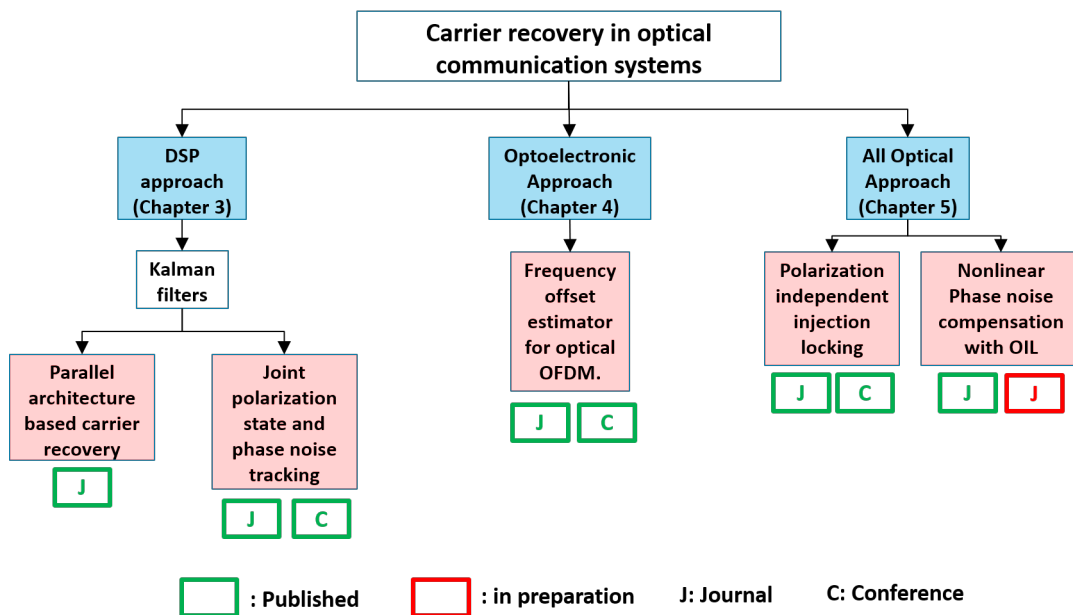


Figure 1.5: Thesis summary tree chart.

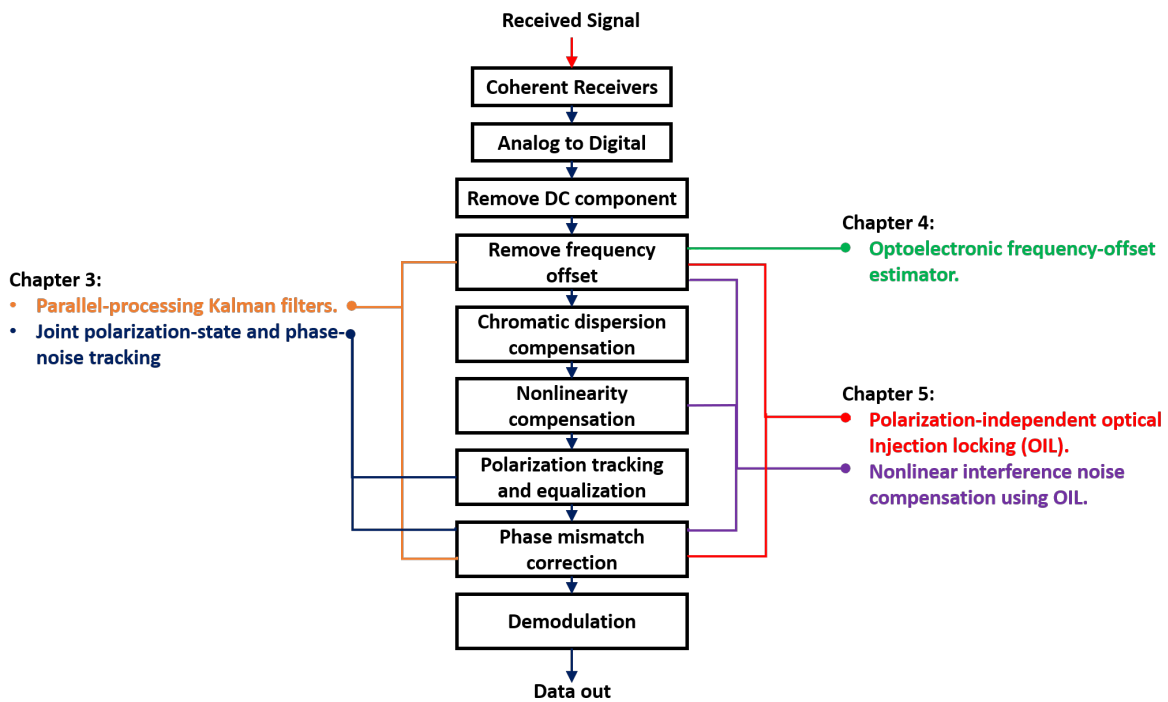


Figure 1.6: Contributions of the proposed techniques in signal processing for data recovery.

1.3.1 Digital signal processing (DSP) approach (Chapter 3)

For the DSP approach, the thesis focuses on using the Kalman filters for two different applications-

Parallel architecture based carrier recovery [Publication 1.3.4(1)]

This work was inspired from the work by Inoue and Namiki [12] where a parallel-processing architecture for linear Kalman filters (LKF) is proposed to achieve carrier recovery by tracking the CFO and PN simultaneously. Chapter 3 of this thesis proposes an extension to this concept and describes a parallel-processing architecture for unscented Kalman filters (UKF). The signal quality and computation latency are compared with the LKF and other phase recovery algorithms. Due to the inherent benefits of UKF over LKF in the case of a nonlinear channel, performance benefits are observed in the proposed system. In addition to that, the UKF structure allows for more parallelization than the LKF, resulting in lower latency compared with the LKF. This benefit, however, comes at the cost of more parallel computations and associated hardware requirements.

Joint polarization-state and phase noise tracking [Publications 1.3.4(2-3)]

The randomly drifting state of polarization (SOP) of the received signal needs to be tracked for error-free data recovery. Conventionally, the SOP tracking is performed with digital tap-delay filters updated using some adaptive tracking algorithm. The phase noise is compensated using one of the phase estimation techniques to recover the symbols for demodulation. A single algorithm using the extended Kalman

filter (EKF) was proposed by [13] that simultaneously tracks the SOP and PN. Using the unscented Kalman filter (UKF) instead, better performance than EKF is verified for simultaneous tracking of SOP and PN.

A technique to reduce the computation complexity of the UKF and the EKF is also proposed and implemented on the UKF (named R-UKF) and the EKF (named R-EKF). The results show that the R-EKF, although least complex, gives worse performance than the conventional methods. The R-UKF gives better performance than conventional methods with reduced complexity. Moreover, the R-UKF maintains almost steady (< 1 -dB variation) Q performance up to 600-kHz laser linewidths and 6.8-Mrad/s SOP angular rotations.

1.3.2 Optoelectronic approach (Chapter 4) [Publications 1.3.4(4-5)]

After detecting the optical signal, the electrical signal needs to be sampled and processed using digital signal processing (DSP) to extract the data. Depending on the type and number of algorithms used, the DSP will consume time and energy accordingly. Optoelectronic processing can be considered as an alternative to DSP for particular operations. Chapter 4 focuses on using analog components to perform carrier recovery. An optoelectronic frequency offset estimator (OEFOE) using off-the-shelf passive optical components and slow photodiodes is proposed to estimate the carrier frequency offset of OFDM optical systems. The proposed OEFOE works with slow ADCs (in the range of MHz) and almost-negligible computations that can be easily performed by a simple micro-controller. Thus, the CFO can be estimated in real time without the use of power-consuming DSPs and thus potentially may result in energy savings at the receiver. Additionally, as the CFO estimation algorithms can be completely removed from the DSP block, the OEFOE also results in lowering the latency of the system in recovering the data. The OEFOE showed to estimate the CFO within the range $[-1250 +1250]$ MHz with $< 4\%$ estimation error.

1.3.3 All-optical approach (Chapter 5)

For all-optical processing, the optical injection locking (OIL) for carrier recovery is investigated. A considerable work has already been done in this area [14] [15] and the techniques proposed in this thesis aids the existing OIL-based carrier recovery.

Polarization-independent optical injection locking [Publications 1.3.4(6-7)]

The OIL setup is highly sensitive to the SOP of injected signal. In order to maintain the lock, the SOP of the injected signal needs to be aligned with the polarization of the slave laser cavity. Unfortunately, the signal transmitted over the deployed networks change the polarization state frequently due to environmental events around the fiber. So when deployed in field networks, the setup keeps losing lock every time the SOP of the signal drifts. To resolve this issue, a pluggable module is designed that

takes a signal on any random SOP and aligns it to a fixed, known SOP. This fixed, known SOP, is then manually aligned to the slave laser cavity's polarization. The module is made using off-the-shelf passive components and does not perform any polarization tracking; it simply realigns any SOP to a known SOP state. Thus, by plugging the proposed module before the OIL setup, the injection lock can be continuously maintained. The proof of concept is given by testing the proposed module over a field fiber link between Monash University's Clayton and Caulfield campuses.

Nonlinear interference noise (NLIN) compensation [Publications 1.3.4(8-9)]

In this part, optical injection locking is explored for nonlinear NLIN compensation. In the case when the fiber spans, *i.e.* the distance between consecutive regenerators/ optical amplifiers in the link, are shorter than 100 km and the link consists of many such short spans, the XPM dominates the inter-channel NLIN in a multi-channel WDM signal. Additionally, in dispersion-uncompensated links, this XPM effect is limited in bandwidth due to walk-off. Using this property and a residual carrier as pilot tone, the phase distortions can be extracted from the signal using OIL, to be cancelled by conjugate coherent receivers. The technique also results in partial compensation of the laser and ASE-induced phase noise. A peak-*Q* improvement of 1 dB is observed in experimental verifications. The performance can be further improved by SPM compensation achieved using digital-back propagation. This gives an additional 0.9-1 dB improvement in peak-*Q* and a total 640-km extension in transmission reach.

Tables 1.1 and 1.2 summarize the capabilities and performance analysis of the proposed techniques.

Proposed techniques and compensation capabilities. ✓: compensated, ✗: not compensated			
Technique	Carrier frequency offset	Phase noise	Additional utility
Parallelized Kalman filters for single carrier system	✓	✓	✗
Joint polarization-state and phase noise tracking	✗	✓	Polarization state tracking
Optoelectronic frequency offset estimator	✓	✗	✗
Polarization-independent optical injection locking	✓	✓(Partial)	Maintained injection lock with drifting polarization
Optical injection locking based nonlinearity compensation	✓	✓(Partial)	Nonlinear phase noise compensation

Table 1.1: Proposed techniques with their compensation capabilities.

Performance report  : Gain,  : Penalty			
Technique	Q performance	Latency	Complexity
Parallelized Kalman filters for single carrier system			
Joint polarization-state and phase noise tracking	  (low OSNRs in R-UKF)	 (for UKF)  (for R-UKF)	 (for UKF)  (for R-UKF)
Optoelectronic frequency offset estimator	Unchanged		 (Computational)  (Hardware)
Polarization-independent optical injection locking	Unchanged		 (Computational)  (Hardware)
Optical injection locking based nonlinearity compensation			 (Computational)  (Hardware)

Table 1.2: Performance of the proposed techniques with respect to the requirement aspects.

Other relevant comparable parameters are described in Table 1.3

Technique	Receiver footprint	Ease of integration	Implementation Cost
DSP techniques	Coherent receiver followed by ADC and DSP	Easy	Low
OEFOE	Optoelectronic device in parallel with Coherent receiver	Moderate	Moderate
OIL	Homodyne receiver setup with injection capabilities to local oscillator	slightly tough due to hardware complexity	Moderate

Table 1.3: Other comparable implementation parameters.

1.3.4 Publications

1. J. Jokhakar, B. Corcoran and A. J. Lowery, "Parallelized unscented Kalman filters for carrier recovery in coherent optical communication," *Opt. Lett.* 41, 3253-3256 (2016).
2. J. Jignesh, B. Corcoran, C. Zhu, and A. J. Lowery, "Unscented Kalman filters for polarization state tracking and phase noise mitigation," in *Optical Fiber Communication Conference'16*, Anaheim, USA (2016) paper Tu2A.4.
3. J. Jokhakar, B. Corcoran, C. Zhu, and A. J. Lowery, "Unscented Kalman filters for polarization state tracking and phase noise mitigation," *Opt. Express* 24, 22282-22295 (2016).
4. J. Jokhakar, B. Corcoran, C. Zhu and A. J. Lowery, "Electro-Optic frequency offset estimator for optical OFDM," in *European Conference and Exhibition on Optical communication (ECOC'16)*, Dusseldorf, Germany (2016), paper W.4.SC3.12.
5. J. Jokhakar, B. Corcoran, C. Zhu and A. J. Lowery, "Simple optoelectronic frequency offset estimator for optical OFDM," *Opt. Express* 25, 32161-32177 (2017).
6. J. Jokhakar, B. Corcoran and A. J. Lowery, "Polarization-independent optical injection locking," in *Optical Fiber Communication Conference'17*, Los Angeles, USA (2017), paper Th4I.4.
7. J. Jokhakar, B. Corcoran and A. J. Lowery, "Polarization independent optical injection locking for carrier recovery in optical communication systems," *Opt. Express* 25, 21216-21228 (2017).
8. J. Jokhakar, A. J. Lowery and B. Corcoran, "Inter-channel nonlinear phase noise compensation using optical injection locking," *Opt. Express* 26, 5733-5746 (2018).
9. J. Jokhakar, B. Corcoran and A. J. Lowery, "Nonlinearity compensation using optical injection locking aided by digital back-propagation," in *European Conference and Exhibition on Optical communication (ECOC'18)*, Rome, Italy (2018), paper Tu4H.4.

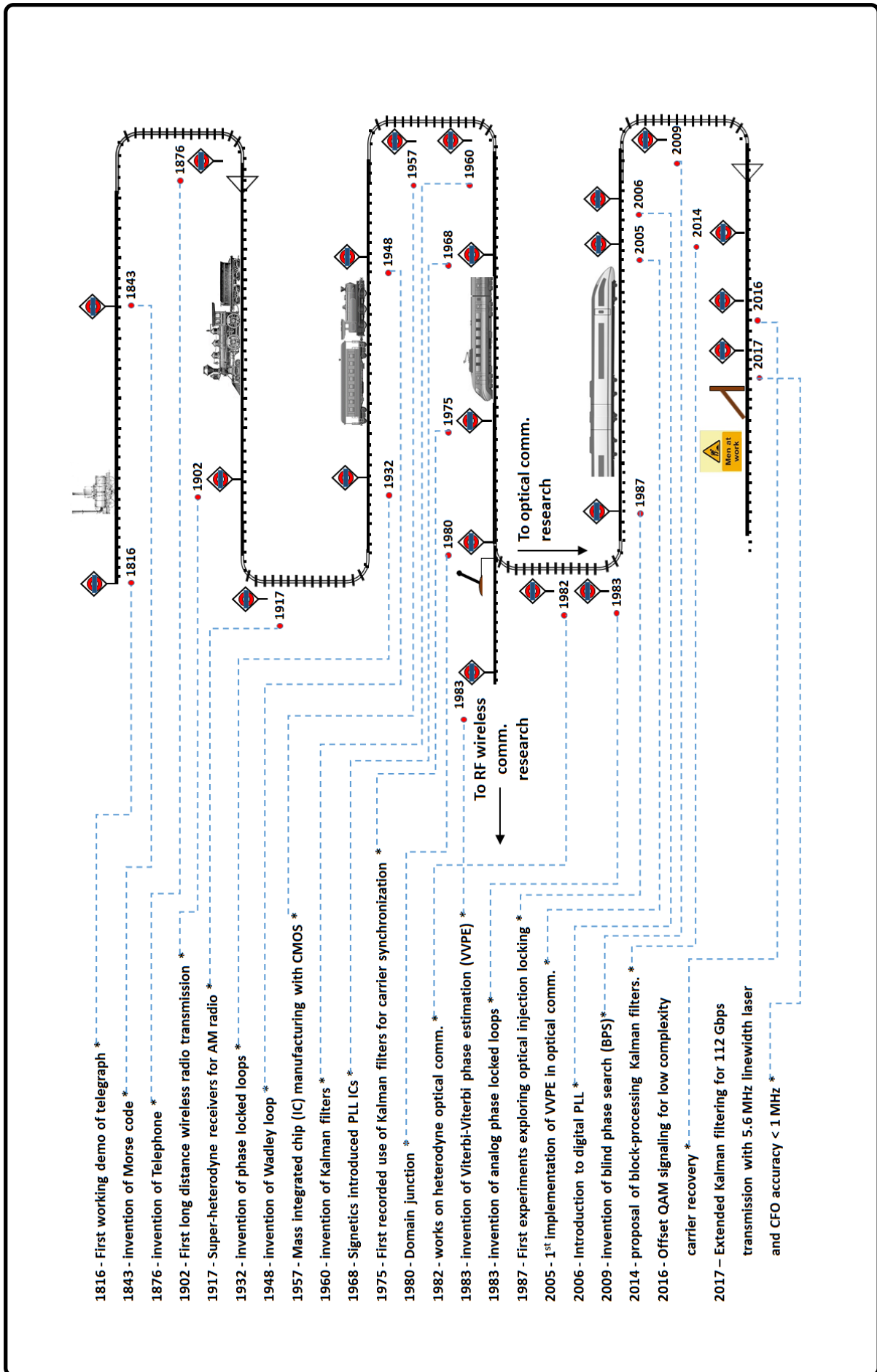


Figure 1.7: Time journey of carrier recovery in optical communication with important milestones.

The journey so far...

In this chapter we go on a brief journey of past contributions in carrier recovery by numerous inventors and researchers. The journey map is visualized in the figure to your left. Considering the fact that the majority of the carrier recovery techniques proposed for optical communications was inspired by wireless radio frequency (RF) communication systems, it becomes necessary to explore the previous work.

2.1 Early communication systems (1816-1930 A.D.).

The history of electrical, machined communication technology can be traced back to 1816 AD with the invention of electric telegraph by Francis Ronalds in London [16]. Although Francis demonstrated the first working telegraph line communication over long distances, it was an amalgamation of works by many previous inventors stretching all the way back to 1774 when an anonymous writer suggested electrostatic telegraph in *Scots* magazine [16].

The following years saw many advancements in communication technology such as the invention of Morse code by Samuel Morse and its transmission over telegraph in 1843 [17], the first demonstration of telephone by Alexander Graham Bell and Thomas Watson in 1876 and the first long distance wireless radio transmission by Guglielmo Marconi in 1902 [18]. Many sources credit Oliver Lodge, John Stone and Nikola Tesla for similar works which usually is a matter of dispute; but we digress here.



Around the same time, in 1901-02, Reginald Fessenden proposed a heterodyne technique that allowed for frequency tuning [19]. In this technique, the received signal at one frequency would beat with a locally generated continuous wave signal at slightly different frequency in a mixer to give sum and difference products. By carefully choosing the frequency difference between these two signals, the products would lie in audible range. By using the heterodyne technique, the Morse codes transmitted over wireless

telegraph could now be heard and noted precisely. This technology would later on inspire the coherent communication technology.

We now reach the year 1917-18 when Edwin Armstrong used Fessenden's heterodyne concept in his super-heterodyne receivers [20]. These super-heterodyne receivers were now used in detecting amplitude-modulated (AM) signals instead of Morse codes. By 1930, all the radio receivers used Armstrong's super-heterodyne technique for detecting broadcast radio channels. These receiver, nonetheless, suffered from weak image rejection problems at high frequencies. Double-conversion or triple-conversion super-heterodyne receivers were invented that down-converted the signal multiple times, first to bring down the frequencies low enough to give good image rejection and the rest to bring the signal to fixed intermediate



frequency before detection. By 1930 the double-conversion super-heterodyne receiver was extensively used for military communications owing to its good sensitivity and accurate frequency selectivity. But these receivers suffered from a major drawback *i.e.* the local oscillators had to be extremely stable in frequency. The drifts in the LO frequencies would cause the reception to snap or deteriorate in quality. This, essentially, laid the pillars of research in carrier recovery and synchronization.

2.2 Preliminary research in carrier recovery for wireless communications (1930-1980 A.D.).

During this period in our journey, most of the processing was performed by analog circuits. Digital processing was minimal due to the primitive computers lacking processing capabilities and slow analog to digital converters (ADC). As a result, most of the research was focused on system designing rather than algorithm development.

2.2.1 Phase-locked loops

The first potential research done towards carrier synchronization or carrier recovery was the invention of the *phase locked loop* (PLL) in 1932 [21]. These PLLs enabled homodyne receiver setups as an alternative to the super-heterodyne receivers. With this homodyne setup, the local oscillator's phase was locked on to that of the incoming signal, negating low frequency offsets and phase jitters. As a result, the PLLs solved the frequency drift issues in the receivers. The usage of PLLs in communication devices increased from 1932 onwards, mainly for analog television receivers. By the year 1957, the concept of integrated circuits (IC) was introduced by Jack Kilby for which he was later awarded the Nobel prize. Fabricating the analog devices on a small integrated circuit using CMOS technology made large-scale, low cost electronic device manufacturing possible that revolutionized the communication technology. In 1968, Signetics

introduced the monolithic integrated PLL circuits on chip that again boosted their use in communication devices [22].

John Costas, in 1956, modified the PLL design such that the loop acts on the in-phase and quadrature component of the signal separately to increase the sensitivity of detecting the phase error. His design was named after him as the *Costas loop* [23]. The Costas loop increased the sensitivity of the receiver by a factor of two, because of which, it was adopted by majority of communication systems using phase modulation. Regardless, the issue of limited tracking speed due to finite loop bandwidth still persisted.

The years to come after the introduction of PLL ICs saw the research on carrier recovery taking up a great pace. The PLL became more important with the usage of phase-modulation techniques like phase-shift keying (PSK) and quadrature-amplitude modulation (QAM). These modulation schemes required removal of phase offsets between the local CW signal and the received signal at the receiver for correct data extraction, performed by the PLLs. The PLL design consists of a feedback loop that is filtered to limit the speed of tracking to few kHz. Researchers started improving upon the existing PLL designs to combat their speed limitations.

Enhancement of PLL performance was also proposed using decision-directed phase error correction by Taylor *et al.* [24] and Chang *et al.* [25]. These techniques were proposed for PSK modulated signal where the carrier tone is absent due to the quadrature modulation. The data-aided [24] or decision directed PLLs [25] use training data or decisions to remove the data component. As a result, the carrier tone is recovered that can be tracked by the PLL. The decision-directed PLL requires high signal to noise ratio. If this condition is not met, there may be incorrect decisions causing the PLL to have incorrect tracking feedback. We will see that this concept was later on adopted in the decision-directed digital phase recovery and equalizers in decades to come.

Speaking of decision-directed equalizers, two designs for simultaneous equalization and carrier recovery were proposed by Chang *et al.* : a baseband equalizer and a passband equalizer. The baseband equalizer performed the demodulation before the channel equalization [25]. The decision taken from the output of the equalizer would be used by the PLL to tune the local oscillator. As the equalizer is within the loop, the LO update is delayed and thus limits the tracking range of the system. The passband approach, on the other hand performs equalization in passband before demodulation, thus removing the tapped equalizers from the loop for fast tracking of phase offsets. Although these techniques may sound good for joint carrier recovery and equalization, no simulation or experimental verification was performed. In addition to that, these techniques cannot be adopted in optical communication as passband equalization needs optical filters whose channel response is difficult to update at a fast rate. The baseband equalization approach can be done, but the system will require signal processing module and a laser module to interact with each other frequently, making the system too complex.

In 1979, Messerschmitt proposed frequency detector designs to aid the PLL in initial acquisition [26]. Two designs were proposed in this work: one extracting the frequency offset using correlation technique in analog domain and other finding the frequency offset using the direction and magnitude of data constellation rotation in digital domain. In Chapter 4 of this thesis, I have proposed an optoelectronic frequency offset estimator whose working concept can be related to the correlator technique proposed by Messerschmitt.

2.2.2 Techniques proposed in parallel with the PLLs.

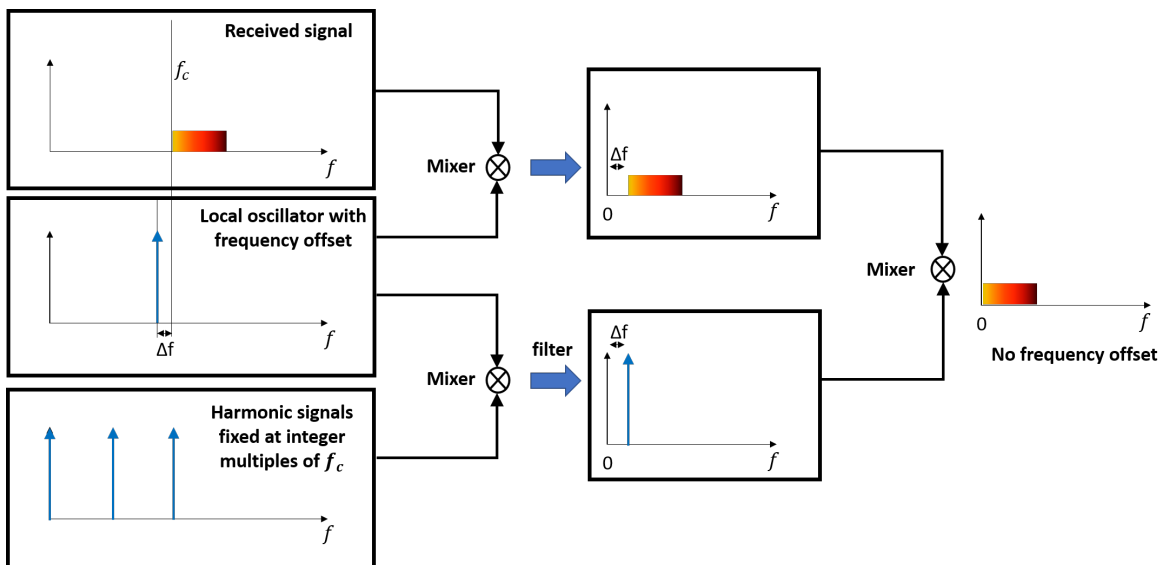
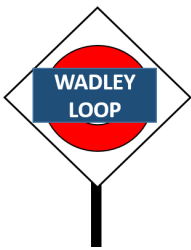


Figure 2.1: Wadley loop working principle.



Around 1948, research on solving the frequency drift issues of super-heterodyne receivers was explored by Trevor Wadley in England. In his work, a harmonic generator generates harmonics on integer multiples of the carrier frequencies. These harmonics beat with the local oscillator as well as the received signal giving two more signals that are aligned in frequency, negating the frequency drifts as shown in Fig. 2.1. This technique was called the *Wadley loop* [27].

Although this technology was commercialized into a product by *Racal* as RA17 receiver in 1954, the technology could not compete with the integrated PLL circuits, introduced in 1957, due to its requirement for stable coherent harmonic signals and large multi-stage analogue filters.

The early 1970's saw research focused on enhancing vestigial side-band systems for their application in television signals. Additional pilot-tones were added to the signal along with the vestigial sideband for correcting frequency offsets and phase jitter. In 1971, Yang *et al.* proposed carefully placing pilot tones at specific frequencies (f_1 and f_2) such that they make a relationship with the carrier frequency ($2f_2 = f_1 + f_c$) [28]. With a frequency offset, δ , the required carrier frequency can be extracted from the

offset pilot tones as $f_c + \delta = 2(f_2 + \delta) - (f_1 + \delta)$. The system is aided with a PLL that extracts the phase jitter information from the pilot tones and uses it for cancellation from the original perturbed signal.

In 1974, Even *et al.* proposed using a single pilot tone (f_1) along with a suppressed carrier (f_c) to achieve carrier recovery in VSB systems. Here, the carrier is embedded in the signal and difficult to extract using filtering [29]. Thus, a second pilot tone was locally generated with the relation $f_2 = f_1 + f_c$. Using remodulation, the carrier frequency is shifted to a known frequency f_2 . The signal at f_2 can then be locked on to the generated tone at f_2 using a PLL. The generated tone at f_2 has the phase jitter information that is used to cancel them out from the original signal. In Chapter 5, nonlinear phase noise cancellation in optical communication systems will be proposed using optical injection locking (OIL). This work loosely resembles Yang's and Even's concept of phase noise extraction from pilot tones and using it to cancel out distortions from the received signal.

Alexander proposed a technique that uses a reference-based detection method in 1975 [30]. In this method, the constellation plane is divided by reference phasors and the phase difference between the signal and the reference phasors is used as an error signal to control the VCO. However, this technique only provides a rough estimate of whether the frequency should be increased or decreased. Similar reference-based technique was proposed by Hogge [31], with logic circuitry that determines the phase difference with respect to all the reference and informs the VCO the exact frequency rotation needed to be performed for carrier recovery. This technique can be related to the blind phase search algorithm [32] in digital signal processing, used oftenly in phase estimation for optical communication systems.

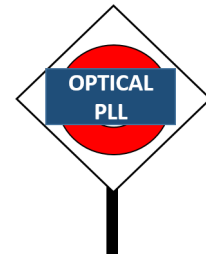


Some methods have been proposed that perform carrier recovery and equalization simultaneously using digital processing. In 1971, Kobayashi proposed a delay-line filter-based sequence estimation [33] and Ungerboeck proposed a maximum likelihood sequence estimation method using his modified Viterbi decoding algorithm for data sequence estimation [34]. In 1975, Luvison *et al.* proposed a sequence estimation with data-aided loops performing channel equalization and carrier recovery using Kalman filters [35]. As we shall see, a large portion of this thesis is dedicated to Kalman filters for carrier recovery and synchronization in

optical communication system. But for now, let us just understand that Luvison's paper was one of the earliest works on Kalman filters used for synchronization in communications after its formulation in 1959 [36]. In 1971, Lawrence *et al.* had proposed Kalman filters for channel equalization [37]. For optical communications, Kalman filters were implemented much later for carrier recovery, after 2012. These contributions will be discussed later in this chapter.

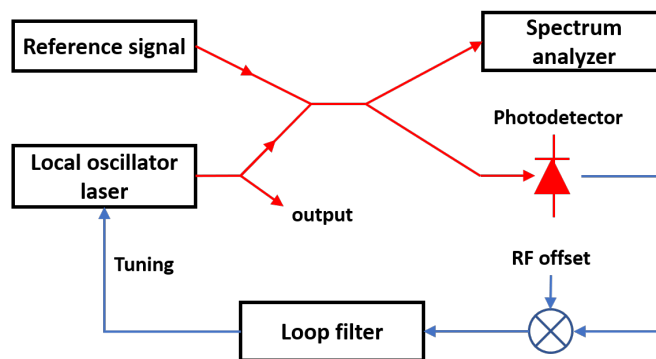
2.3 Research in carrier recovery for optical communication (1980-2005 A.D.)

Up until 1980, the research on carrier-recovery focused mainly on RF communications and continued in the years to come after. But simultaneously, experiments on coherent optical communications had started surfacing [4] [38]. Thus, we will now focus on the research carried out specifically for optical communications. Wherever applicable, we shall go back to RF domain to relate the techniques used in optical communications inspired from RF communications.

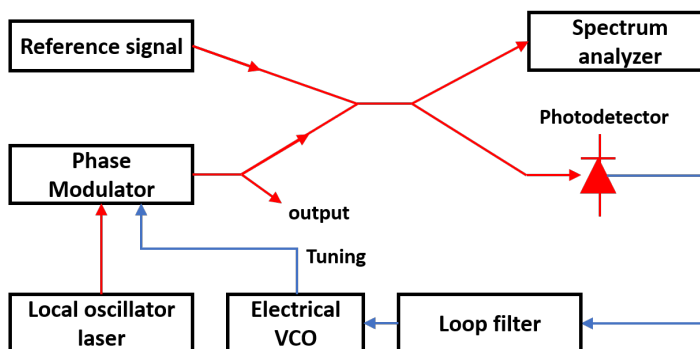


2.3.1 Optical phase-locked loop (OPLL)

The speed of analog-to-digital converters in this period was enough to sample the low data-rate RF signals (few Mbps) at the Nyquist sampling frequency, but not sufficient for the high-data rate optical signals. Thus, most of the research in optical communication in the era, 1980 to 2005, used analog-processing techniques. Fig. 2.2a shows the basic design of an OPLL where a photodetector is used as a phase discriminator and the error signal is used to tune the local oscillator laser. Initially, analog *optical phase-locked loops* were investigated for PSK modulated signals in linear and Costas loop configurations [39]. In 1985, Kazavsky demonstrated a decision-driven optical phase-locked loop restricted to BPSK modulated



(a) OPLL with laser tuning.



(b) OPLL with electrical control.

Figure 2.2: OPLL designs.

signals. This work can be related to Chang's work [40] on decision directed-PLLs for RF communications. The decision is used to remove the data component from signal that recovers the carrier tone, to be used by the OPLL for locking the phase. The work was later explored and extended in 2004 by Camatel *et al.* who proposed a sub-carrier OPLL controlling an electrical VCO instead of the laser directly [41]. In this, an electrical VCO drives the laser CW signal to generate tones controlled by electrical VCO input. Thus, by controlling the electrical VCO with the loop's error signal, the phase of the CW signal was locked on to the reference signal. Essentially, fast tracking was achieved with less complex systems as shown in Fig. 2.2b. He further extended this work in 2006 by using a 90° -hybrid and using both I and Q signal outputs to make the system usable even for suppressed-carrier signals.

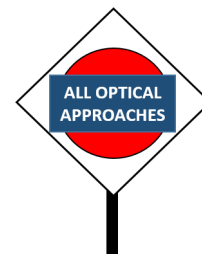
A separate group of researchers were also exploring the sensitivity benefits of coherent receivers over direct-detection in early 80's. Many experiments were carried out between 1982-83 by Malyon, Wyatt, Hodgekinson and Smith at British Telecom research labs, Kikuchi and Okoshi at Univ. of Tokyo and Shikada *et al.* at Nippon Electric Co. These experiments focused on BER measurements for heterodyne optical communication systems and sensitivity comparisons with direct-detection (DD) systems. The highest sensitivity gain of 16.9 dB was recorded in heterodyne systems over DD for PSK modulated signals [4]. This benefit was, however, restricted by laser linewidth because the data rates were low. Kazovsky explored the multi-channel transmission over optical fiber intending to reach 1 Gbps at that time, using FSK and coherent receivers [42]. He explored the sensitivity gains achieved from coherent reception and the required channel spacing for different modulation formats. His description on reduction in sensitivity for signals with close-by channels could have been the first observation of four-wave mixing effects in multi-channel system. Iwashita *et al.* in 1988 demonstrated an unamplified, long distance transmission over a 202-km link at 2-Gbps using coherent reception for FSK modulated signal [43]. A narrow linewidth distributed feedback (DFB) laser was used for this experiment to resolve the phase noise issue with FSK modulation. Until 2017, the highest transmission reach achieved without errors is 300 km using FSK for 300 Mbps and the highest data rate achieved was 10 Gbps using FSK for 40 km transmission link.

2.3.2 All optical approaches

To solve the phase noise issue due to broad linewidths for PSK signals, Tamura *et al.* proposed sending a pilot tone along with the phase-modulated signal on orthogonal polarization [44]. As the signals on both polarizations have identical phase drifts, they were detected separately and mixed in electrical domain, thus canceling the phase noise. The technique, however, would fail for polarization-multiplexed systems. A similar technique was proposed by Nakamura *et al.* in 2010 using a dual-polarization coherent receiver, where a pilot tone, with its phase synchronous with the signal carrier, is transmitted on a polarization that is orthogonal to the signal. Using a polarization-multiplexed coherent receiver, the pilot tone was made

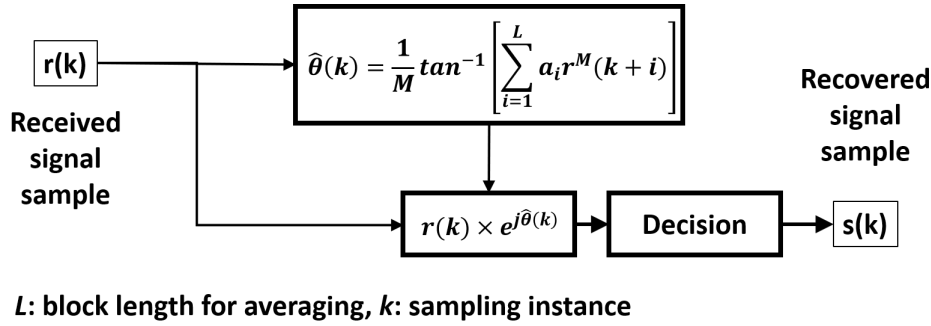
to beat with the signal to create an homodyne configuration [45]. Cheng *et al.* proposed a time-division multiplexing the pilot tone or transmitting it along a separate fiber [46]. These techniques suffer from temperature-based delay variations in time-multiplexed pilot system or require a separate dedicated fiber. Consequently, these techniques are feasible for data extraction within short distances or in labs but not for practical implementation over long distances in the field.

Other methods to remove or avoid the effects of laser phase noise were also proposed. These include conversion of phase modulation to intensity modulation using a correlating optical delay and using a single photodetector to detect the pulses [47]. Although an interesting concept, one can simply use an intensity modulator to achieve the same results. Additionally, the system cannot take the advantage of high sensitivity coherent receivers. Another method explored for all-optical carrier recovery was *optical injection-locking* [48]. In this thesis, optical injection locking is investigated and will be discussed in detail in Chapter 5. Croussore *et al.* suggested the use of DPSK that differentially encodes the phase between consecutive symbols [49]. With this, the receiver can be a simple delay interferometer followed by a balanced diode configuration (no local oscillator, no frequency offset). The phase offsets were reduced by phase regeneration using phase-sensitive amplifiers (PSA).



Another all-optical processing approach was proposed by Kim *et al.*, where an optical carrier with polarization and phase the same as a pump signal (received signal) is generated in a phase-sensitive oscillator when pumped by the received signal [50]. Slavik *et al.* proposed a technique where the modulation of the signal is stripped using nonlinearity, i.e. the data signal and a pump, when passed through a highly nonlinear fiber (HNLF), creates an idler without modulation on it. Simultaneously, the pump, when passed through another HNLF with the local oscillator, creates the LO idler. The frequency difference between the two idlers gives the CFO and the phase difference gives the phase offset. Both of these can be extracted by mixing the two idlers using a simple photodetector. Thus, DSP-free carrier recovery is achieved, conserving DSP latency and processing power [51].

Mendinueta *et al.* proposed sending a pilot tone along with the signal that is generated using the same laser. Both the signal and the pilot tone were sent over a multimode fiber, to be separated at the receiver and mixed in a coherent receiver in a self-homodyne manner. Again, a DSP-free carrier recovery was achieved [52].

Figure 2.3: M^{th} power phase estimator's working principle.

2.4 DSP techniques for carrier recovery in optical communication (post-2005 A.D.)

Till 2005, carrier recovery still relied mostly on pilot-based homodyne techniques and optical PLLs for carrier recovery. With the introduction of high-speed analog-to-digital converters and digital processing capabilities, coherent techniques became interesting again. Many digital techniques and algorithms for carrier recovery were proposed after 2005.



2.4.1 M^{th} power estimator

M^{th} power phase estimation is the most investigated technique for M-PSK modulation. It is also called the *Viterbi-Viterbi phase estimation* algorithm when used for QPSK signals (when $M=4$) [53]. Although, initially proposed for RF wireless communications, the VVPE has been adopted in optical communications. In this, the sampled M-PSK signal is raised to the M^{th} power to remove the modulation and extract the phase offset, to be used for phase correction in the original signal. Its working is illustrated in Fig. 2.3. Before the period when high-speed ADCs were commercially available, this technique was proposed as an analog-processing technique for QPSK-modulated optical signals by Noe *et al.* [54]. The raising to a power was achieved using two consecutive frequency multipliers and finding the fourth-root of the signal was performed by regenerative frequency dividers. The work also showed delay-based frequency discriminator for frequency offset estimation. As such, a complete carrier recovery was achieved while keeping the BER better than 10^{-3} for up to a 1.8-MHz linewidth for 10-Gbaud QPSK signals. However, VVPE suffers from weak tolerance to higher linewidths that result in cycle slips. The first demonstration of M^{th} power phase estimation as digital signal processing was proposed by Noe [55] where he proposed that, given sufficiently high-speed ADCs, the digital processing technique can achieve phase offset estimation for laser linewidths >1.8 MHz ($BER < 10^{-3}$). The VVPE technique also suffers from cyclic slips when the phase noise shifts the signal sample into a different constellation quadrant. Differential phase encoding was employed to prevent the cycle slips by considering the phase difference between consecutive samples, rather than the phase of the sample

itself. To improve upon this, Nazarathy *et al.* proposed Doubly-Differential Encoding (DDE), where the present symbol is dependent on the previous two symbols, leading to automatic cancellation of frequency offsets [56].

Alternatives to M^{th} -power estimator: Many other techniques have been proposed over the years to overcome the shortcomings of the VVPE/ M^{th} -power estimator. Qi and Hauske proposed a multiplier-free technique that achieves carrier recovery with less complexity compared with the VVPE, without a performance penalty. This technique used the sign and magnitude of the in-phase and quadrature components of the received signal to estimate the CFO from FFT and the phase noise by dynamic tracking [57]. Kalogerakis *et al.* proposed a *digital delay lock loop* (DLL) or *digital phase locked loops* (DPLL) against the M^{th} -power estimator and kept the BER better than 10^{-3} for up to a 4-MHz linewidth for 10-Gbaud QPSK signals [58]. The DPLL controls the phase of the constellation and provides appropriate rotation instead of controlling the laser drive signals, as in PLLs. Thus, the signal is delayed until the loop calculates the required phase shift, increasing the latency of the system. Qiu *et al.* also implemented the DPLLs for carrier recovery in a parallelized structure [59]. The received signal samples are broken down into blocks that are processed in parallel by separate DPLLs to estimate the CFO and the carrier phase offsets. To reduce the complexity, they proposed estimating the phase offsets using one stream and using its results to update the offsets in the other streams [59]. A pilot-aided parallelized carrier recovery was proposed by Zhuge *et al.* that breaks the incoming signal into blocks such that the pilot symbols are at the beginning of each block. Using these pilot symbols and DPLLs for each parallel stream, carrier recovery was achieved with a 12% increase in transmission reach if aided by ML [60]. This concept was extended by the same group by modifying the parallel pipelining structure such that the pilot symbols come one after another to reduce the phase drifts between consecutive pilot symbols. As a result, accurate phase estimation is achieved with a shorter buffer length [61]. The block-processing approach was again used by Inoue and Namiki who implemented the block-processing approach for carrier recovery using the Kalman filters. Because of the Kalman filters' enhanced estimation performance over other methods, their technique achieved accurate carrier recovery with a lower latency [12]. The parallel block-processing method was also used to lower the high-speed ADC requirements for high baud rate optical signals; Hoffmann *et al.* proposed a parallel-processing M^{th} -power estimator with lowered clock rates in each parallel block.

2.4.2 Blind phase search (BPS)

So far, the methods proposed have focused on carrier recovery for QPSK or M-PSK. With an increase in data requirements and transmission speeds over the years, the research community started exploring M -QAM ($M > 4$) modulation schemes to increase the throughput. Unfortunately, the VVPE and M^{th} -power estimator algorithms fail to perform satisfactorily for M -QAM signals. The *blind phase*

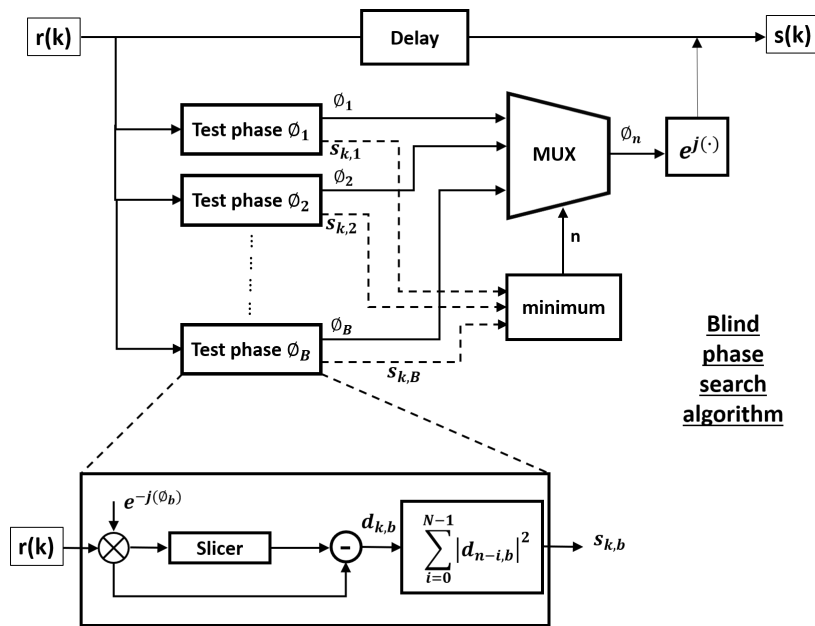


Figure 2.4: Blind phase search working principle.

search (BPS) approach proposed by Pfau *et al.* is the conventional technique used for carrier recovery in M -QAM modulated signals [32]. In this, the current signal sample, along with fixed number of previous samples are rotated by several test phases. The distances of these rotated samples from the nearest constellation point are calculated. These distances are then summed up for each test phase. The test phase that gives the minimum summed distance also gives the correct decision for the current sample. The working of the algorithm is shown in Fig. 2.4. The BPS algorithm proved to be hardware efficient along with being capable of performing carrier recovery for 16-QAM signals. A linewidth tolerance of up to 4.1 MHz and 1.4 MHz was achieved by the BPS for 10 Gbaud QPSK and 16-QAM signals, respectively, at $BER=10^{-3}$.



The BPS method, although capable of achieving carrier recovery for 16-QAM modulated signals, was highly complex in terms of computation. Alternatively, QPSK partitioning was proposed by Fatadin *et al.* The symbols in a 16-QAM constellation on the inner and outer ring can be seen to form two QPSK constellations with different amplitudes [62]. The middle ring can again be divided in two sets, each forming a QPSK constellation with a phase offset. By fragmenting the constellation in several QPSK constellations, VVPE can be used to estimate the correct phase of the symbols with some added logic to map to the correct symbol on the 16-QAM constellation. It was shown that the *QPSK partitioning* performed similar to the BPS algorithm with less complexity.

2.4.3 Viterbi-Viterbi monomial phase estimator (VVMPE)

A generalized version of the VVPE, the VVMPE was proposed by Wang *et al.*, in which the signal sample is considered in polar form. The phase part is raised to the fourth power as in VVPE and the magnitude part is operated by some nonlinear function [63]. In case of M -QAM modulation, this nonlinear function is a simple raising of power to some value l . If l is set as 4, the VVMPE becomes a simple VVPE algorithm. The value of l is usually taken as $l > 4$ for 16-QAM.

This way, more weight is given to the outer ring symbols in the constellation who suffer less phase-error due to noise than the inner ring symbols. However, for optical communication, the VVMPE alone does not perform well. Sparthakis *et al.*, proposed to use the VVMPE in conjunction with a maximum-likelihood estimator for CFO estimation and carrier phase recovery [64]. Their work shows that a VVMPE+ML system performs similarly to the BPS algorithm, but with reduced complexity for 16-QAM. A slightly different nonlinear function for the magnitude part of the signal sample is proposed by Argyris *et al.* which shows better performance than the BPS algorithm [65]. A combination of BPS and ML was also explored by Zhou [66]. He showed that a two-stage ML followed by a BPS algorithm reduces the BER considerably for lower number of test phases compared with a single-stage BPS. A 64-Tbps link was successfully tested over 320 km using this BPS+ML methods aided with pre-processing to match the frequency response of the components for polarization-division multiplexed 36-QAM signals [67]. A modified and simplified version of BPS was proposed by Li *et al.* that achieves carrier phase recovery in two stages [68]. In the first stage, a regular BPS with half the required number of test phases is implemented to get a coarse estimation. Following this, the second stage performs the fine adjustments by searching through the surrounding test phases for accurate phase estimation. Thus, the total number of test phases used reduces, leading to reduction in latency.

Pilot-tone aided techniques have also been suggested for 16-QAM signals. The concept was very similar to pilot-assisted analog carrier recovery techniques, except for being performed digitally. A pilot tone is inserted on to the signal whose squared magnitude is more than that of the signal spectrum envelope. The pilot tone drifts from its actual frequency of insertion with the frequency offset. Thus, the relative drift of the pilot tone in received signal spectrum gives the CFO estimate. Moreover, the pilot tone after coherent reception contains phase noise added to the signal due to finite laser linewidths. Thus, if the pilot tone is added in a guard band of the signal spectrum, so it is spectrally distinct from the data spectrum, it can be extracted out and used to remove the phase noise from the signal. Such a technique was used in [69] and showed that pilot-aided techniques with ML perform better than any other carrier recovery technique for 16-QAM. Because the pilot tone can cancel nonlinear phase noise along with the laser phase noise, this technique was also proposed for joint carrier recovery and



nonlinearity compensation [70]. This technique was, in turn, extended to coherent optical OFDM systems where the guard band was provided by null sub-carriers around the frequency chosen to insert the pilot tone [71] [72]. Instead of adding a pilot tone, pilot symbols can also be added in the time domain such that the pilot symbols are repeated sequence of a symbol. Such a pilot sequence causes an impulse train in the frequency domain, converted to a single impulse due to limited bandwidth of the receiver. This impulse then gives the CFO estimate from the spectrum. This technique avoids insertion of a pilot and allows for more power being pushed to the data-carrying payload. However, this technique can only perform CFO estimation and requires long sequence of pilot symbols, which increases the system overhead.

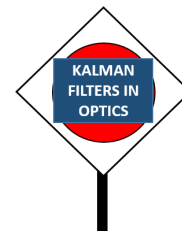
2.4.4 Adaptive filters

Adaptive filter based techniques, where the filter-weights are dynamically updated to track the phase offsets in the signal, have been proposed for 16-QAM modulation. Meiyappan *et al.* proposed a decision-aided technique where a complex-weighted filter, which is updated decision-directed ML approach, to track the changing phase offset [73]. Sigron *et al.* proposed a *multi-symbol delay detection* (MSDD) scheme that uses a differential precoding on the transmitter side and multiple weighted decisions on the receiver side to achieve accurate differential phase estimate. A decision feedback filter structure was designed where the taps of the feedforward filter are updated using Wiener update or LMS update. This approach was specific to QPSK but was later on upgraded for 16-QAM by modifying the normalization factor according to the QAM constellation. The technique is proved to achieve carrier recovery with its performance independent of the CFO. It is claimed to have unlimited CFO capture range with improved performance over VVPE and BPS+2ML (BPS cascaded with two stages of ML detection) [74] [75]. Khalil *et al.* proposed processing the real and imaginary parts of the received signal separately using a radial-directed constant/multi modulus algorithm to find the error between the magnitudes of the received signal and the nearest constellation ring. Using the errors from the real and imaginary parts, the filter taps are updated. This technique achieved carrier recovery with less complexity compared with the BPS algorithm [76]. This technique was upgraded by using LMS update instead of CMA/MMA with exact training-based error rather than absolute value error. This resulted in increased linewidth tolerance (600 kHz to 1.2 MHz) and BER performance improvement.



2.4.5 Kalman filters

Finally, a brief discussion on the *Kalman filters* for carrier recovery in optical communications is given here. Because of their capabilities to give optimum estimates in the mean-squared error sense, Kalman filters hold great potential to achieve optimum performance in the carrier recovery. They will be discussed in detail in Chapter 3. Barletta *et al.* proposed a new lower bound of the information transferred in channels perturbed by laser phase noise. Before this, the lower bound was calculated by Monte-Carlo approach using Wiener filtering [77]. The new bound was calculated using a Monte-Carlo approach with Kalman-filtering based carrier recovery [77]. Kalman filters were also proposed to compensate for the phase noise in semiconductor lasers, which often has a non-Lorentzian lineshape. In this work, the laser's rate equations were used to model the Kalman state equations. This method gave an 8-dB improvement in sensitivity over a decision-directed PLL for 28-GBaud 16-QAM signal [78]. Jain *et al.* proposed the extended Kalman filters for simultaneous tracking of linear and nonlinear phase noise for a 100G QPSK-modulated system [79]. Recently, extended Kalman filters (EKF) were explored for carrier phase recovery in optical filter bank multicarrier systems with offset QAM signals. This system gave performance comparable to the BPS with very low complexity [80]. The EKF was again investigated by Li *et al.* for carrier recovery in a 112-Gbps QPSK system and compared with the VVPE and BPS. Their results showed that the EKF achieved a linewidth tolerance up to 5.6 MHz and CFO estimation error less than 1 MHz, while keeping the BER better than 10^{-3} [81]. Although Kalman filters have been shown to achieve performance gains against conventional methods in simple carrier recovery, their capabilities are often not fully utilized, especially for nonlinear models. This thesis attempts to use their full capabilities in the form of unscented Kalman filters (UKF) and gives performance comparisons.



We are at the end of this 200-year journey that we covered in this chapter. We have discussed the major inventions and contributions that have led us to the technology we have today at our disposal for carrier recovery. A few contributions that are specific to the applications were not mentioned, but will be discussed in appropriate chapters of this thesis. The thesis explores various approaches for carrier recovery and proposes novel techniques, considering implementation parameters in practical systems.

Digital signal processing for carrier-recovery

In this chapter, the digital-processing Kalman filters are explored with simulations and experimentally for two different applications related to carrier-recovery in optical communication systems.

The two applications addressed are-

1. Parallel-processing Kalman filters for carrier recovery.
2. Joint polarization-state and phase noise tracking.

Various types of Kalman filters, namely linear (LKF), extended (EKF) and unscented Kalman filters (UKF), are investigated. The outcomes of the experiments and simulations suggest the superiority of UKF in terms of the signal quality-factor Q for both applications. Techniques to reduce the latency or the computational efforts of the UKF without drastically sacrificing the Q -performance are also proposed.

Publications based on this chapter:

1. J. Jokhakar, B. Corcoran and A. J. Lowery, "Parallelized unscented Kalman filters for carrier recovery in coherent optical communication," *Opt. Lett.* 41, 3253-3256 (2016).
2. J. Jignesh, B. Corcoran, C. Zhu, and A. J. Lowery, "Unscented Kalman Filters for Polarization State Tracking and Phase Noise Mitigation," in *Optical Fiber Communication Conference'16*, Anaheim, USA (2016), paper Tu2A.4.
3. J. Jokhakar, B. Corcoran, C. Zhu, and A. J. Lowery, "Unscented Kalman filters for polarization state tracking and phase noise mitigation," *Opt. Express* 24, 22282-22295 (2016).

3.1 Introduction to Kalman filters

A Kalman filter is essentially a algorithm that implements a predictor-corrector type estimator, which is optimal in the sense that it minimizes the estimated error covariance—when some presumed conditions are met. It can also be thought of as an estimator that removes the noise from a series of observations based on decisions of previous observations and a dynamically updated process model. The process model is an approximation to the channel that generates the observations.

Since the time of its introduction in 1959-60, the Kalman filter has been the subject of extensive research and application, particularly in the area of communications, autonomous or assisted navigation and tracking. This is not only because of the advances in digital computing which made the use of the filter practical, but also for the relative simplicity and robust nature of the filter itself.

The Kalman filter estimates an unknown parameter x_k at time instance k from the observed signal sample y_k . The observations y_k consist of the unknown parameters corrupted by some channel H and observation noise, n_k , giving the observation model as-

$$y_k = Hx_k + n_k \quad (3.1)$$

The Kalman filter gives the minimum-mean squared error in estimates if following conditions are met -

1. **The unknown parameter should follow the Wiener process model; i.e. it should show autoregressive qualities.**

The value of the unknown parameter at time instance k , x_k , should depend on its value at previous time instance $k - 1$. This gives us the first state-space equation of the process model-

$$x_k = Ax_{k-1} + Bu_k + w_k \quad (3.2)$$

where A is a fixed time-update function that relates two consecutive values of x . The second term, Bu_k , in Eq. (3.2) describes a calibration function that is sometimes added to the system. For simplicity of explanation, let us assume $B = 0$ and ignore the second term without losing generality. w_k is the process noise added during the parameter update. From Eq. (3.2) if w_k is AWGN noise, the unknown parameter will follow the Wiener process (a random walk).

2. **The process noise and observation noise should be Gaussian in nature.**

If n_k and w_k are independent, white, and with normal probability distributions $p(n_k) \sim \mathcal{N}(0, Q)$ and $p(w_k) \sim \mathcal{N}(0, R)$, by the Rao-Blackwell Theorem [82], the MMSE estimate gives the best estimate of all the estimators, linear or nonlinear. Here, R and Q are the process noise variance and observation noise variance respectively.

As Kalman filters are designed with an intention to achieve the minimum mean-squared error, Kalman filters prove to be the best estimators if the above two conditions are met.

3.2 When should Kalman filters be used?

The choice of estimators depends on the type of unknowns to be estimated. There are many other estimators proposed in literature, but the ones that are commonly used are mentioned here.

Algorithm 1 Alg.1: When to use Kalman filters

```

if the unknown is deterministic and quantized then
  Use-
  1. Maximum Likelihood Estimator (MLE) [83] OR
  2. Least-Squared Estimator (LSE) [83]
end
else
  if the unknown is stochastic and continuous then
    if the unknown is stationary i.e. its variance remains constant over time then
      Use-
      1. Minimum-mean square error estimator (MMSE) [83]
      2. Least mean square estimator (LMS) [83]
      3. Maximum a Posteriori estimator (MAP) [83]
      4. Wiener filter [83]
    end
    if the unknown is non-stationary i.e. its variance changes over time then
      Use-
      1. Kalman filter
    end
  end
end

```

3.3 Kalman filter algorithms

The types of Kalman filters explored in this thesis are:

1. Linear Kalman filter
2. Extended Kalman filter
3. Unscented Kalman filter

3.3.1 Linear Kalman filter

The equations for the Kalman filter fall into two groups: time update equations and measurement update equations. The time update equations basically pass the previous state and error covariance estimates through the time update operator, A , to obtain the *a priori* estimates, \hat{x}_k^- and P_k^- as in A.2.1 and A.2.2. The measurement update equations are responsible for incorporating a new measurement into the *a priori* estimate to obtain an improved *a posteriori* estimate. The time update equations can also be thought of as predictor equations, while the measurement update equations can be thought of as corrector equations.

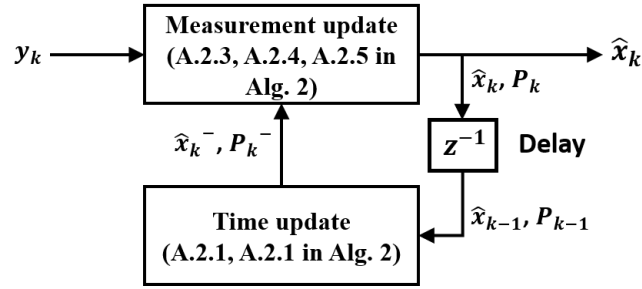


Figure 3.1: Linear Kalman filtering process.

The first task during the measurement update is to compute the Kalman gain, K_k , as in A.2.3. The next step is to actually measure the process to obtain y_k , and then to generate an *a posteriori* state estimate by incorporating the measurement, as in A.2.4. The final step is to obtain an *a posteriori* error covariance estimate via equation A.2.5. After each time and measurement update pair, the process is repeated with the previous *a posteriori* estimates used to project or predict the new *a priori* estimates.

Algorithm 2 Alg.2: Linear Kalman filter**Variables:** x_k : unknown variable to be estimated for sample ' k '. \hat{x}_k : estimated output of x_k . y_k : received signal sample for sample ' k '. K_k : Kalman gain.**for** $k = 1 : N$ **do**▷ For N signal samples**Time update equations:**

A.2.1: $\hat{x}_k^- = A\hat{x}_{k-1}$

A.2.2: $P_k^- = AP_{k-1}A^T + Q$

Measurement update equations:

A.2.3: $K_k = P_k^- H^T (HP_k^- H^T + R)^{-1}$

A.2.4: $\hat{x}_k = \hat{x}_k^- + K_k(y_k - H\hat{x}_k^-)$

A.2.5: $P_k = (I - K_k H)P_k^-$

end

A few points need to be noted here. From A.2.4, we can understand the effect of the Kalman gain on the state estimate.

Case: $K_k = 0$

If $K_k = 0$, the estimate becomes-

$$\hat{x}_k = \hat{x}_k^- \quad (3.3)$$

which means that the current observation has no effect on the current estimate. Also the current estimate is determined by the *a priori* estimate. In other words, if the Kalman gain, K_k , is 0, the filter has successfully estimated the state parameter and tracking is achieved. This can also be inferred from A.2.3. If $P_k^- = 0$, it means that the variance in the estimate is 0 and that the filter estimate is correct. By substituting this condition in A.2.3, we get $K_k = 0$. Thus, A.2.3 and A.2.4 support each other.

Case: $K_k = H^{-1}$

Further, if $K_k = H^{-1}$,

$$\hat{x}_k = H^{-1}y_k \quad (3.4)$$

which means the previous estimate has no effect on the current estimate, and so the current estimate depends only on the current observation. From A.2.3, if we put $P_k^- = 1$, which means the previous estimate is completely uncertain, and if $R=0$, we again get $K_k = H^{-1}$. Essentially, the Kalman gain, K_k should become H^{-1} when the system loses track, but this is possible only when $R=0$. However, this is not the case usually. As a result, the Kalman filter has to start from scratch until it achieves tracking and P_k^- becomes 0 again.

3.3.2 Extended Kalman filter

As mentioned before, the linear Kalman filters is an optimum estimator. However, this is true only when the process and observation models (Eqs. (3.1) and (3.2)) are linear. Unfortunately, the linear Kalman filter loses accuracy for nonlinear channels *i.e.* when

$$x_k = g(x_{k-1}) + w_k \quad (3.5)$$

and

$$y_k = f(x_k) + n_k \quad (3.6)$$

Here, $f(\cdot)$ and $g(\cdot)$ are nonlinear functions. With most natural phenomena being nonlinear, the LKF has found very few applications. As a solution, the extended Kalman filter (EKF) was suggested by Kalman himself in early works [36]. The EKF was applied in 1966 by NASA for estimating the position and velocity of a lunar orbiter [84] and then investigated for navigation and course-correction for a space probe flying-by Mars and Venus [85].

The extended Kalman filter works by linearization of the nonlinear process and then uses a regular LKF over the linearized models. In something akin to a Taylor series, the estimation process can be linearized around the current estimate by using the partial derivatives of the process and measurement functions ($g(\cdot)$ and $f(\cdot)$) to compute estimates even in the face of nonlinear relationships. The basic operation of the EKF is the same as the LKF.

Here, G and F are the partial derivatives of the nonlinear functions $f(\cdot)$ and $g(\cdot)$ with respect to x which allows linear operations to be used. In the case where multiple parameters have to be estimated, *i.e.* when x is a vector of unknowns, G and F become Jacobian matrices [36].

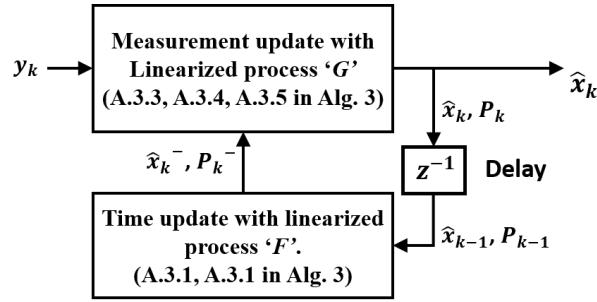


Figure 3.2: Extended Kalman filtering process.

Algorithm 3 Alg.3: Extended Kalman filter

Variables:
 x_k : unknown variable to be estimated for sample ' k '.
 \hat{x}_k : estimated output of x_k .
 y_k : received signal sample for sample ' k '.
 K_k : Kalman gain.

for $k = 1 : N$ **do** ▷ For N signal samples

Time update equations:

A.3.1: $\hat{x}_k^- = g(\hat{x}_{k-1}^-)$

A.3.2: $P_k^- = G_k P_{k-1}^- G_k^T + Q$

Measurement update equations:

A.3.3: $K_k = P_k^- F_k^T (F_k P_k^- F_k^T + R)^{-1}$

A.3.4: $\hat{x}_k = \hat{x}_k^- + K_k (y_k - f(\hat{x}_k^-))$

A.3.5: $P_k = (I - K_k F_k) P_k^-$

end

Although many works claim that EKFs give satisfactory results in nonlinear channels/ process, EKF is still not optimum; just like the LKF, the linearization process degrades the accuracy of the Kalman filter. For certain applications in this thesis, the EKF performed similarly to conventional methods, specific to those applications, with no additional performance-gain. To get an optimal performance of Kalman filters in nonlinear channels, the use of unscented Kalman filters (UKF) is proposed in this thesis.

3.3.3 Unscented Kalman filters

The UKF is founded on the intuition that it is easier to approximate a probability distribution than it is to approximate an arbitrary nonlinear function or transformation. With this intuition, an estimate from previous time instance, \hat{x}_{k-1} is extrapolated to a cloud of points spread according to the previous time instance's covariance P_{k-1} . These points are called as Sigma points. Each sigma point is then propagated through the nonlinearity yielding, in the end, a cloud of transformed points. The new approximated mean (\hat{x}_k^-) and covariance (P_k^-) are then computed from the cloud of transformed sigma points. This process is called unscented transformation. The unscented transformation is a method for calculating the statistics of a random variable which has undergone a nonlinear transformation [86]. The unscented Kalman filter, further, uses the observations at current time instance (y_k) and updates these approximated

mean(\hat{x}_k^-) and covariance (P_k^-) to final estimated (\hat{x}_k) and covariance (P_k) through the updated Kalman gain K_k . This concept is believed to be named 'unscented' by the inventor, Jeffrey Uhlmann, as this idea struck him on seeing an unscented aerosol spray dispersing in the air guided by the air flow. Although, he himself claimed that he named it 'unscented' to avoid it being called the 'Uhlmann' filter.

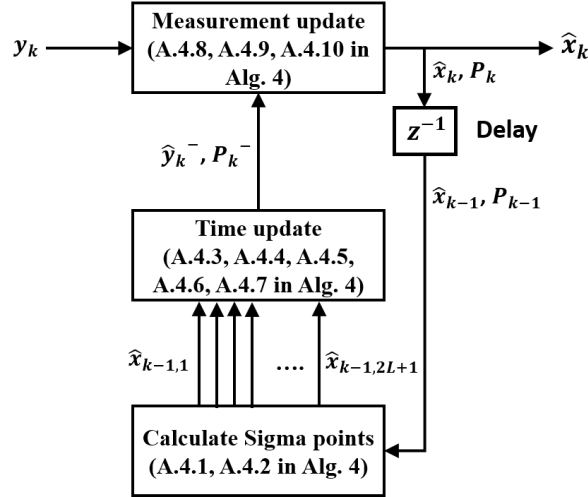


Figure 3.3: Unscented Kalman filtering process.

Algorithm 4 Alg.4: Unscented Kalman filter

Given:

L : Number of unknown parameters to be estimated

$$\lambda = L(10^{-3} - 1)$$

$$\alpha^2 = 10^{-3}$$

$$\beta = 2$$

$$w_1 = \lambda / (L + \lambda)$$

$$w_1^c = \lambda / (L + \lambda) + 1 - \alpha^2 + \beta$$

$$w_{2 \dots (2L+1)} = w_{2 \dots (2L+1)}^c = 1/2(L + \lambda)$$

for $k = 1 : N$ do

▷ For N signal samples

Calculate sigma points:

A.4.1: $\hat{x}_{k-1,i} = \hat{x}_{k-1} + \sqrt{(L + \lambda)(P_{k-1})_i}$; for $i=1 \dots L$

▷ $(P_{k-1})_i$ is the i^{th} column of the matrix P_{k-1}

A.4.1: $\hat{x}_{k-1,i} = \hat{x}_{k-1} - \sqrt{(L + \lambda)(P_{k-1})_i}$; for $i=L+1 \dots 2L$

Time update equations:

A.4.3: $\hat{x}_{k,i}^- = g(\hat{x}_{k-1,i})$; $i = 1 \dots (2L + 1)$.

A.4.4: $\hat{x}_k^- = \sum_{i=1}^{2L+1} w_i \hat{x}_{k,i}^-$

A.4.5: $y_{k,i}^- = f(\hat{x}_{k,i}^-)$; $i = 1 \dots (2L + 1)$.

A.4.6: $\hat{y}_k^- = \sum_{i=1}^{2L+1} w_i y_{k,i}^-$

A.4.7: $P_k^- = \sum_{i=1}^{2L+1} w_i^c (y_{k,i}^- - \hat{y}_k^-)(y_{k,i}^- - \hat{y}_k^-)^* + Q$

Measurement update equations:

A.4.8: $K_k = P_k^- (P_k^- + R)^{-1}$

A.4.9: $\hat{x}_k = \hat{x}_k^- + K_k (y_k - \hat{y}_k^-)$

A.4.10: $P_k = (I - K_k) P_k^-$

end

3.4 Why are unscented Kalman filters superior?

Kalman filters are prediction-update estimators. Iteratively, the state-parameters and the estimation variance ("the uncertainty") are predicted based on previous decisions and are updated based on current observations. Just like any other adaptive filter based on the MMSE criterion, a Kalman filter achieves the minimum mean-squared error by finding the mean of the *a posteriori* probability *i.e.* finding $E(X/\mathbf{Y})$ or probability of transmitting 'X' symbol given 'Y' observation. In other words if we find the pdf of the received signal 'Y' for a particular transmitted symbol 'X', the MMSE estimate can be found by its mean and the transmitted symbol's *a priori* probability (Baye's rule) [83].

Consider a symbol X transmitted over a linear channel H . During transmission, the symbol X accumulates random AWGN noise, giving a Gaussian shaped pdf to the signal \mathbf{X} .

$$\mathbf{X} = X + \mathbf{N} \quad (3.7)$$

When this Gaussian spread signal \mathbf{X} is transmitted over a linear channel, A , the received signal is given as

$$\mathbf{Y} = A\mathbf{X} + \mathbf{N} \quad (3.8)$$

For a linear channel A , the pdf of the received signal \mathbf{Y} will maintain the shape of pdf of \mathbf{X} ; in this case, Gaussian pdf. Thus, for a given transmitted signal \mathbf{X} , we get the *a posteriori* pdf of \mathbf{Y} , $P(\mathbf{Y}/\mathbf{X})$. By Baye's rule and using the *a priori* pdf of transmitted signal, we can find the *a posteriori* pdf.

$$P(X/\mathbf{Y}) = \frac{P(\mathbf{Y}/\mathbf{X}) \cdot P(X)}{P(\mathbf{Y})} \quad (3.9)$$

By taking the mean, we get the MMSE estimate of X as

$$\hat{X} = E(X/\mathbf{Y}) \quad (3.10)$$

The improved estimation accuracy of the unscented Kalman filters can be explained using an analogy. Let's say there is an empty well somewhere in an imaginary land. "Curious Bob" stays nearby and passes the well everyday. The well is so deep that Curious Bob cannot see the base of the well from the top. The top rim of the well is circular with a particular diameter, but he wants to know the features of the base of the well such as the diameter and spread.

Now Bob has an extendable rod with rollers on both ends. The rod automatically extends itself in length until both ends hit the well sides. Also, the rod glows in dark and transmits its current length to Curious Bob. Carefully placing the rod along the diameter of the top rim, Curious Bob slides the rod down the well such that it passes along the diameter and reaches the base of the well as shown in Fig. 3.4.

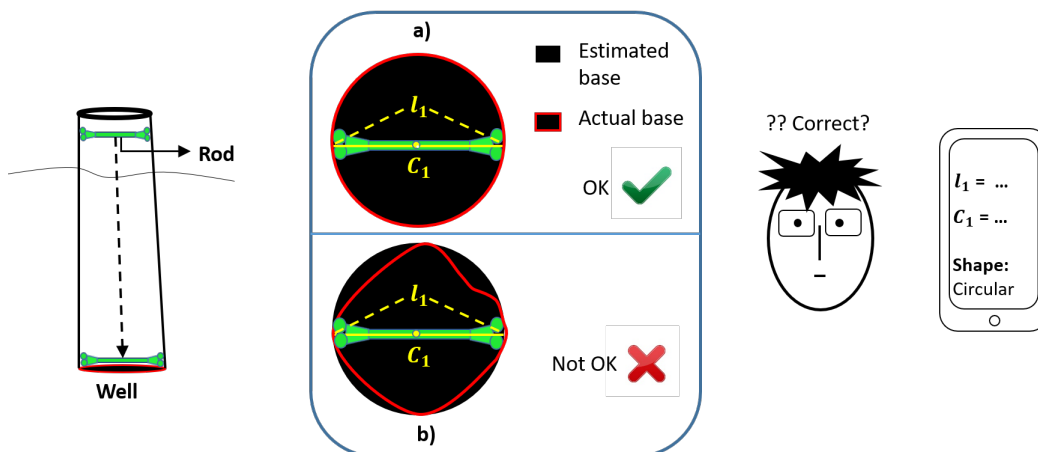


Figure 3.4: Intuitive working of Linear/Extended Kalman filters for: a) linear channel, b) nonlinear channel

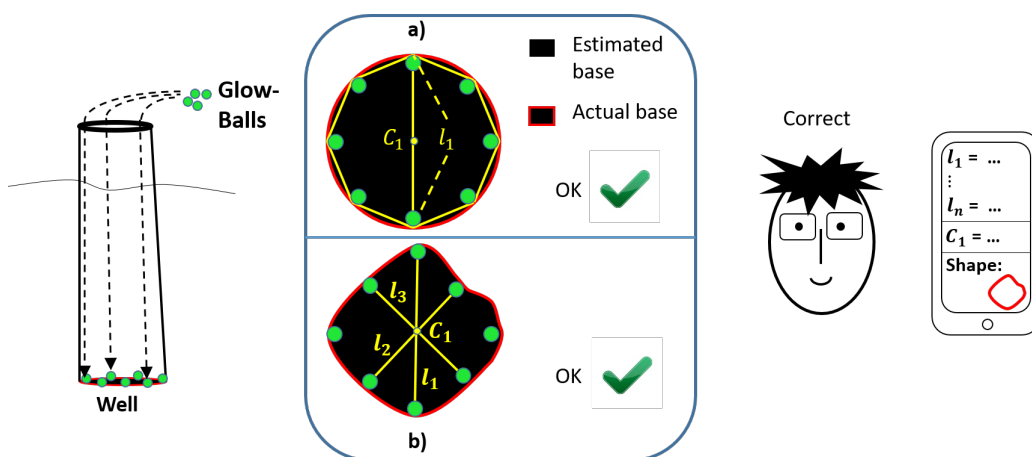


Figure 3.5: Intuitive working of unscented Kalman filters for a) linear channel, b) nonlinear channel

The length of the rod (l_1) gives the diameter of the well and the position of the glowing stick in the well gives the centre position (C_1). From this, Curious Bob infers that the base of the well is circular with diameter l_1 and the centre at point C_1 .

However, there is a big assumption that Curious Bob made in this hypothesis. He assumed that, because the top rim of the well is circular, the base will also be circular. But what if it's not? In that case, Bob will not get complete information of the base, leaving him misinformed.

To get more information, Bob has thought of an alternative technique. He designed a set of glowing balls such that each of them transmits its distance from every other ball (l_1, l_2, \dots, l_n). He then carefully rolls each ball such that they fall along the edge of the base as shown in Fig. 3.5. Now, Bob can find the diameter of the base from the data transmitted by the balls. This time, he can even find the shape of the base by looking at the positions of the glowing balls as shown in Fig. 3.5. Thus, Bob can now know if the shape of the base is circular and get more information such as the centre position (C_1), the spread of the base in different direction (l_1, l_2, \dots, l_n) etc.

This logic can be extended to explain the differences between the Linear/Extended Kalman filters

and the unscented Kalman filters. The top rim of the well relates to the pdf of transmitted signal \mathbf{X} and the lower base of the well relates to the *a posteriori* pdf $P(\mathbf{X}/\mathbf{Y})$. The well itself acts as a channel mapping \mathbf{X} to \mathbf{Y} with A and N . The length of the rod suggests the variance and its midpoint suggests the mean.

In the case of a linear channel described in Eq. (3.8), the shape of the *a posteriori* pdf $P(\mathbf{X}/\mathbf{Y})$ remains the same as that of \mathbf{X} , *i.e.* the shape of the base of the well is same as that of the top rim as shown in Figs. 3.4(a) and 3.5(a). Consider a Gaussian distributed transmitted signal $\mathbf{X} \sim \mathcal{N}(\mu_x, \sigma_x^2)$ transmitted over a linear channel A . The signal $\mathbf{Y} \sim \mathcal{N}(\mu_y, \sigma_y^2)$ at the output of the linear channel also has a Gaussian-distribution. Then, \hat{X} and the estimation uncertainty can be found using the mean and variance of the signal \mathbf{Y} , (μ_y, σ_y^2) respectively for a given X . These mean and variance are just the scaled versions of the mean and variance of \mathbf{X} , *i.e.*

$$\mu_y = A\mu_x \text{ and } \sigma_y^2 = A\sigma_x^2 A^T \quad (3.11)$$

Thus, for linear channels, the mean and variance of the signal \mathbf{X} are sufficient parameters to estimate the *a posteriori* pdf $P(\mathbf{X}/\mathbf{Y})$ whose mean gives the MMSE estimate. In other words, Bob's rod technique works for linear channels. Unfortunately, the estimation fails when the channel is nonlinear *i.e.*

$$\mathbf{Y} = f(\mathbf{X}) + \mathbf{N} \quad (3.12)$$

Here, $f(\cdot)$ is a nonlinear function. In this case, the base of the well no longer holds the same shape as the top rim *i.e.* the *a posteriori* pdf $P(\mathbf{X}/\mathbf{Y})$ is different than that of \mathbf{X} as shown in Figs. 3.4 and 3.5. Thus, the length of the rod will vary with the alignment of the rod, suggesting higher order moments affecting the estimation process. But, the LKF and EKF assume the shape of the *a posteriori* pdf to be same as that of the \mathbf{X} like in linear channels. Thus, an EKF or LKF would assume the shape of the base of the well to be circular just like the top rim. This mismatch in the estimated base and the actual base as shown in Fig. 3.4(b) causes Bob to make errors in judging the base. Similarly, the mismatch in the estimated and actual *a posteriori* pdfs in nonlinear channels causes errors in estimating the transmitted symbol X .

The extended Kalman filter (EKF) attempts to solve the nonlinearity issue by linearizing the nonlinear channel. Due to linearization, the EKF considers only mean and variance, ignoring the higher moments of the pdf. Curious Bob's assumption that the base of the well is circular follows this notion. Although many researchers have adopted the EKF for their simplicity and satisfactory results for nonlinear channels [13,37,79,81,87], they are not optimum. This is reflected in the results that will be shown later in this chapter.

A better solution for estimation in nonlinear channels is the unscented Kalman filter (UKF). The concept of an UKF is analogous to Bob's glowing-ball method as shown in Fig. 3.5. The glow-balls represent the sigma points in the UKF that are transferred through the nonlinear channel. Just like the glow-balls that are carefully rolled, such that they roll to the edges of the base, the sigma points are

carefully chosen such that they accurately acquire the non-Gaussian *a posteriori* pdf after being transferred through the nonlinear model. The estimated base for a nonlinear channel matches with the actual base as shown in Fig. 3.5(b), giving Bob a better judgment of the actual base. Similarly, the UKF gives better estimate of the *a posteriori* pdf from the sigma points transferred through the nonlinear channel. Intuitively it follows that the UKF works well for both linear and nonlinear channels as shown in Fig. 3.5, except that it would not give major benefits in linear channels over LKF.

It is clear from the explanation that rolling multiple glow-balls in the well, with careful alignment, takes more effort compared with rolling a rod down the well. Using the same logic, calculating sigma points and transferring them through the nonlinear channel takes more computational effort compared with transferring just the mean and variance in the case of LKF/EKF. Thus, UKF gives the benefits in estimation accuracy at the cost of high computational complexity.

3.5 Parallel-processing Kalman filters for carrier recovery

This section describes the proposed parallel-processing unscented Kalman filter and compares its quality-factor (Q) and latency performance with the parallel-processing linear Kalman filter previously proposed by Inoue *et al.* [12].

The work described in this section is a comparative study with the work done by Inoue *et al.* using LKF. Moreover, as explained in Section 3.4, the UKF are inherently stronger than the extended Kalman

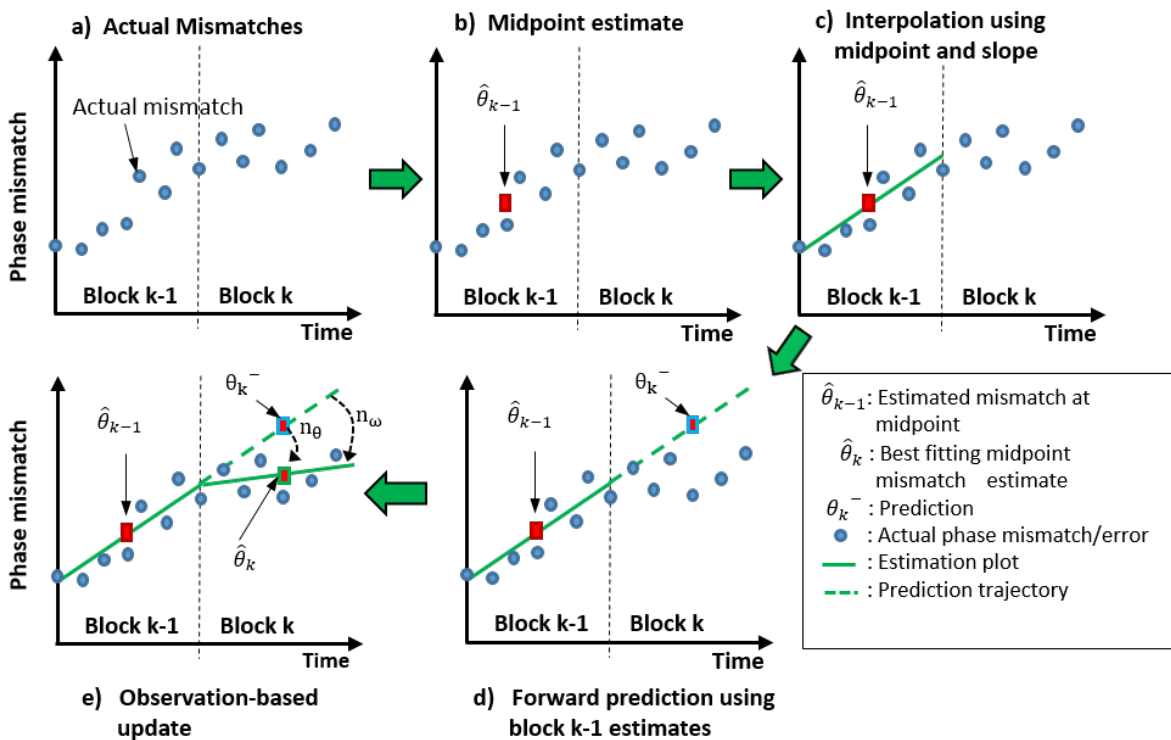


Figure 3.6: Working of parallel-processing Kalman filters

filters (EKF) for the nonlinear channels. For these reasons, we omit the investigation of EKF in this section and compare the performances of UKF with the previously proposed LKF. In this application, the CFO and PN cause phase drifts in the received signal. As a result there is a phase mismatch between the actual phase that carries the data according to the modulation used and the phase of received signal. Parallelized Kalman filters estimate and compensate for this phase mismatch induced by PN and CFO. Thus, the phase mismatch becomes the unknown to be estimated.

For the parallelized architecture, the received sampled signal is divided into fixed-length blocks (Fig. 3.6(a)). Although the phase mismatch is the unknown to be estimated, the parallel processing architecture, instead, estimates: 1) the slope of the phase mismatch in k^{th} block, ω_k and 2) the value of phase mismatch at the midpoint of k^{th} block, θ_k (Fig. 3.6(b)). Hence, the Kalman filter estimates a vector $\hat{x}_k = [\hat{\theta}_k \ \hat{\omega}_k]$ instead of directly estimating the phase mismatch $\phi_{n,k}$. This is essential to enable parallelization.

In this application, k is used for the block index and ' n ' is used as the sample index. This is because the Kalman filter runs once per block and thus the estimates of the Kalman filter at block k is affected by its estimates in block $k - 1$. Thus, the state parameter vector to be estimated by the Kalman filters is $x_k = [\theta_k \ \omega_k]$. The estimate of the phase mismatch at each sample in the block is then interpolated (Fig. 3.6(c)) using [12]

$$\phi_{n,k} = \theta_k + \left(n - \frac{N_B + 1}{2} \right) \omega_k \quad (3.13)$$

where $\phi_{n,k}$ is the instantaneous phase mismatch/error at n^{th} sample of k^{th} block, with each block having a length N_B samples. This procedure is demonstrated graphically in Fig. 3.6.

Parallelized Kalman filters first predict the state parameters for k^{th} block, $\hat{x}_k^- = [\hat{\theta}_k^- \ \hat{\omega}_k^-]$ from $(k - 1)^{\text{th}}$ block's estimates $\hat{x}_{k-1} = [\hat{\theta}_{k-1} \ \hat{\omega}_{k-1}]$ (Fig. 3.6(d)). After receiving the observations from the sampled signal in k^{th} block, the estimates are updated/corrected to calculate $\hat{x}_k = [\hat{\theta}_k \ \hat{\omega}_k]$ and the interpolation is again performed using Eq. (3.13) (Fig. 3.6(e)).

3.5.1 State-space model equations and proposed nonlinear model

In the case of parallelized linear Kalman filter (LKF) proposed in [12], the state update equations are

$$\theta_{k+1} = N_B \times \omega_k + \theta_k \text{ and } \omega_{k+1} = \omega_k + n_f \quad (3.14)$$

where: N_B is the block length, ω_k and θ_k are the slope of the phase mismatch and the phase mismatch at the midpoint of the k^{th} block respectively. The quantity n_f denotes the 'process noise' (*i.e.* change in the mismatch slope) between consecutive blocks. The LKF observation model considered in [12] is

$$\tilde{\theta}_k = \theta_k + n_\theta \text{ and } \tilde{\omega}_k = \omega_k + n_\omega \quad (3.15)$$

where: $\tilde{\theta}_k$ and $\tilde{\omega}_k = \omega_k$ are the observations for phase mismatch midpoint and slope, and n_θ and n_ω are

the observation error associated with these state parameters. These state equations do not consider the amplitude noise. Thus, more accurate estimates can be calculated if both the phase mismatch and the amplitude noise are accounted for in the state model.

A modified observation model is proposed as shown in Eq. (3.16) which incorporates both phase, n_θ , and amplitude noise, n_a , in the observation noise, (n_y) .

$$\tilde{y}_k = e^{j\theta_k} + n_y \quad \text{and} \quad \tilde{\omega}_k = \omega_k + n_\omega \quad (3.16)$$

The LKF cannot be used here since the observation model is now nonlinear (*i.e.* the model observation \tilde{y}_k is nonlinearly dependent on the parameter θ_k as the effect of the phase is $e^{j\theta_k}$). Instead, an unscented Kalman filter in parallel-processing architecture is developed in this thesis.

To summarize, the parallelized Kalman filter takes N_B samples in one k^{th} block as inputs and gives N_B phase-mismatch estimates $\phi_{n,k}$ as outputs, where $n=1, \dots, N_B$. From these phase-mismatch estimates, it updates the state parameters from \hat{x}_{k-1} to \hat{x}_k for the next block. The algorithm and the architecture of the parallel-processing unscented Kalman filter are discussed in Appendix A.

Figs. 3.7(a-b) show a graphical representation of the corrections that the linear and unscented Kalman filters apply. If the received signal is stripped of its modulation, the residual component is of the form $y_k = e^{j\tilde{\theta}_k} + n_a$. Moreover, the LKF attempts to minimize the arc n_θ , and so instead of trying to approach y_k , it tries to approach $e^{j\tilde{\theta}_k}$ by minimizing the phase difference n_θ . The UKF attempts to minimize the vector n_y to approach y_k in Fig. 3.6(b), which gives a more accurate estimate of the mismatch. Unlike the LKF, the observation noise in UKF, n_y , includes the phase as well as amplitude noise. As a result, the Kalman gain of UKF is a complex value for the UKF, giving a phase shift as well as scaling. The performances of the UKF and the LKF are compared in the next section.

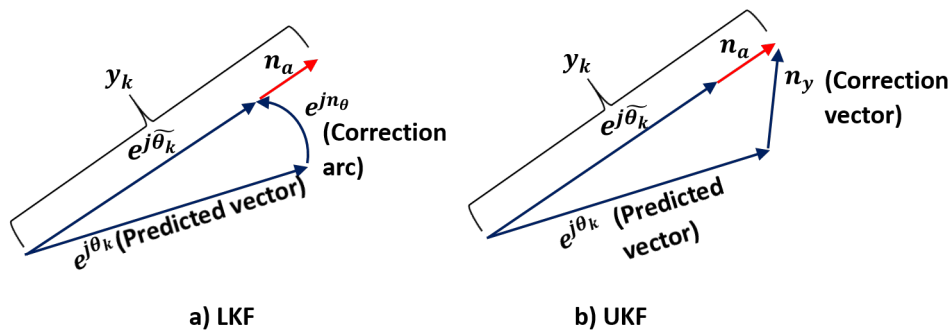


Figure 3.7: correction method of LKF vs. UKF.

3.5.2 Experimental setup and results

The proposed system was verified experimentally in back-to-back configuration and over an 800-km optical fiber transmission link as shown in Fig. 3.8. A 10-GBaud single-carrier signal is fed from a

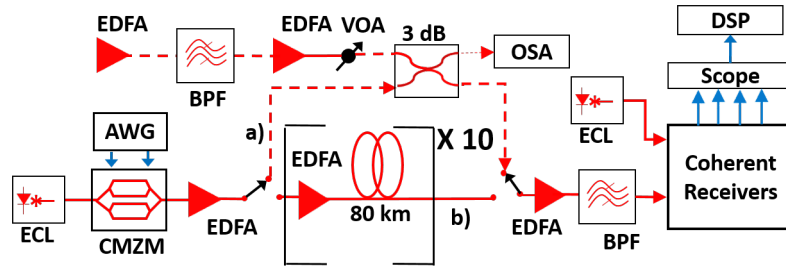


Figure 3.8: Experimental setup in: (a) back-to-back configuration (b) 800-km transmission link configuration. BPF: Band pass filter, VOA: Variable optical attenuator, CMZM: Complex Mach-Zehnder modulator, AWG: Arbitrary waveform generator, ECL: External cavity laser.

Keysight 92 GSa/s arbitrary waveform generator (AWG) into a Teraxion 20-GHz optical bandwidth IQ modulator that modulates the CW optical beam from a tunable laser (<100 kHz linewidth) set to 193.1-THz carrier frequency. A similar laser with the same linewidth was used as a local oscillator at the receiver. In the case of back-to-back configuration, the amplified signal was fed to a Finisar (U^2T) 25-GHz electrical bandwidth integrated coherent receiver after optical noise loading. The noise loading setup uses an EDFA with no input as an ASE source, a band-pass filter constraining the noise bandwidth to 200 GHz, and a second EDFA to boost the noise power. The optical noise was coupled with the optical signal with a 3-dB coupler. The coupled noise power, and thus the OSNR, is controlled with help of a variable attenuator. For the link configuration, the optical signal was passed through 10 spools of SMF-28e optical fiber, each of length 80 km. The launch power into each span is controlled by EDFAs placed before each spool, with a final EDFA placed as a pre-amplifier before the receiver. The amplified signal was optically filtered before the receiver using a BPF with bandwidth centered at the set transmission wavelength. The outputs of the coherent receiver were digitized by a Keysight 40-GSa/s, 16-GHz bandwidth real-time oscilloscope. The digital signal processing algorithms of proposed system were run offline.

Back-to-back setup

For demonstrating phase recovery for a QPSK signal, a 10-Gbaud modulated signal is generated and received in a back-to-back setup as shown in Fig. 3.8. The parallelized UKF and the parallelized LKF algorithms were implemented and the Q -factor of the recovered constellation was calculated for each algorithm. The VVPE, as a conventional method used for QPSK signals, was also implemented for comparison. The parallel structure of the VVPE is considered here for fair comparison [88]. The Q from SNR was calculated as $Q_{SNR} = 10 \log_{10}(P_s/P_n)$ where P_s is the normalized signal power and P_n is the noise power calculated from the error vector magnitude as $P_n = \text{average}(|EVM|^2)$. EVM is the absolute distance of the recovered sample on the constellation from the actual constellation point. At lower OSNRs, where the bit errors are reliably measurable, Q from the SNR matches with the Q from

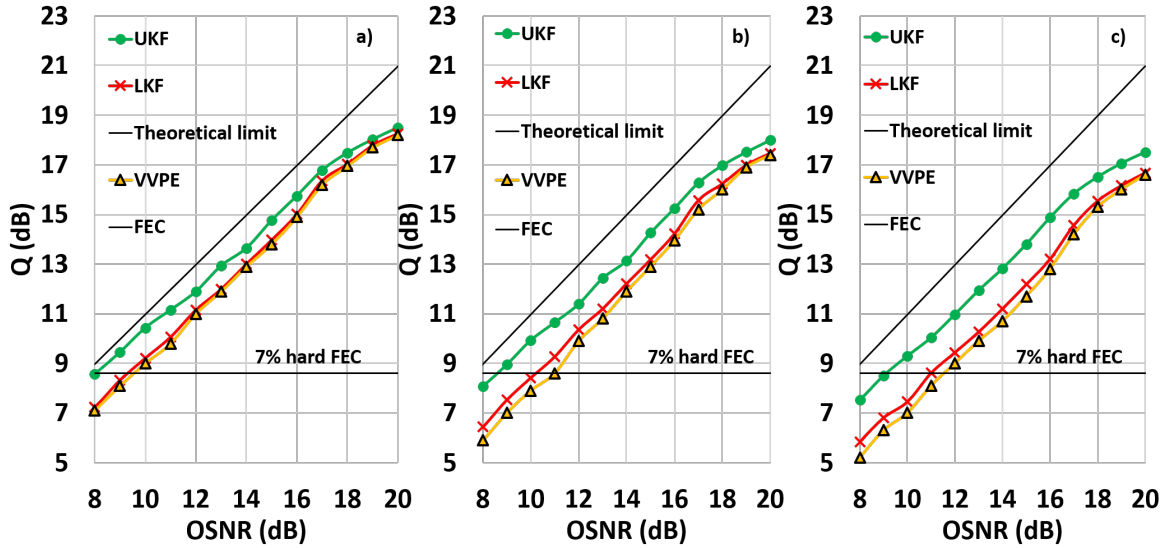


Figure 3.9: Experimental Q vs. OSNR, block lengths of: (a) 44 (b) 142 and (c) 198 samples.

BER; *i.e.* $Q_{SNR} = Q_{BER}$, where Q_{BER} for M-QAM ($M=4,16$) is given as

$$Q_{BER} = 20 \log_{10} \left(\sqrt{\frac{2(M-1)}{3}} \times \operatorname{erfc}^{-1} \left(\frac{BER \times \log_2 \sqrt{M}}{1 - \frac{1}{\sqrt{M}}} \right) \right) \quad (3.17)$$

The Q -factor for QPSK modulated signal in a back-to-back setup is plotted in Fig. 3.9 against OSNR for block lengths of 44, 142 and 198. These results demonstrate that the UKF performs better than the LKF, but with less improvement at higher OSNRs. The LKF gives marginal performance improvement over the convention Viterbi-Viterbi phase estimation (VVPE) algorithm for all block lengths. This is due to the linear observation model used in it for a nonlinear channel estimation. At low OSNRs the use of more accurate observation model, combined with the use of sigma points—more accurately capturing the signal pdf and the statistical moments of the state parameters—provides a performance advantage for the UKF over the LKF. As the OSNR increases, the amplitude noise vector in Fig. 3.7 reduces in magnitude relative to the signal vector. As such, the correction vector of the UKF approaches the correction arc of the LKF, resulting in the algorithms providing similar performance. At the FEC limit ($Q = 8.6$ dB, $BER = 3.8 \times 10^{-3}$), the UKF gives 1.2-dB, 1.5-dB and 2-dB improvement in required OSNR over the LKF for block lengths 44, 142 and 198, respectively. At optimal block length (44 samples), the UKF gives an implementation penalty of 0.3 dB, whereas it increases to 1.5 dB in case of LKF.

To investigate the effect of block length size on system performance, the block length was swept for a fixed received OSNR of 10 dB. Fig. 3.10 shows that Q reaches an optimum for block lengths of 44 samples and then steadily reduces for longer blocks. Compared with the measured Q performance when using the optimal block length, the block lengths 142 samples and 198 samples give Q penalties of 0.5 dB and 1 dB respectively.

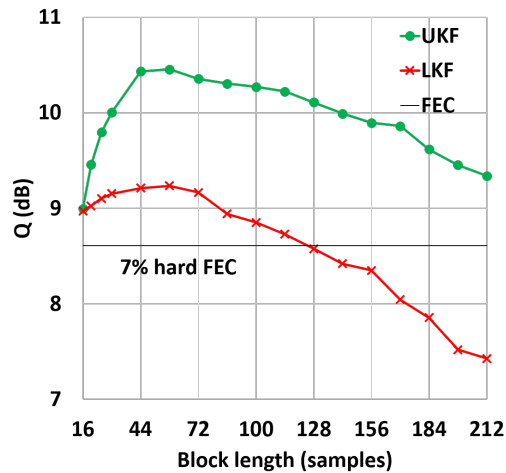


Figure 3.10: Experimental Q vs. block length, OSNR = 10 dB.

The block length and the fluctuations of the phase-mismatch within the block affects the performance as the Kalman filters estimate the slope and the midpoint of the phase-mismatch in a block based on the observations at each point in the block. Intuitively, less number of observation points in a block would lead to poorer estimates. Hence, the Q performance improves when the block length increases from 16 to 44 points per block in Fig. 3.10.

If the block length is increased beyond 44 points, the phase-mismatch undergoes fluctuations within a single block that cannot be estimated accurately in terms of slope and midpoint. In other words, the slope of the phase mismatch varies within a single block and cannot be estimated with one value, leading to poorer performance. This leads to Q performance drop beyond 44 points block length. This is against common intuition.

The optimum block length value (44 points) is dependent on the system. It will vary, depending on the type of lasers used. A system using poor quality lasers (Large frequency offsets and phase noise) will experience faster fluctuations in phase mismatch and may require shorter blocks. The optimum block length of 44 samples was observed for our system under experiment and chosen for performance comparison between different algorithms under test.

The UKF plot in Fig. 3.10 shows a sharp increase in performance up to optimum block length. This can be attributed to the UKF's capability to take into consideration higher order moments of the phase mismatch in a nonlinear system. As such, the UKFs tend to quickly approach the optimum estimates as opposed to the LKF. The LKF's plot may seem symmetrical, but that is just an outcome of its slower performance-gain characteristic with increasing block length.

Recent optical communication systems implement high-order modulation formats to increase spectral efficiency. As an example, 16-QAM is being investigated as a candidate modulation format for 400G optical transport [89]. Hence, a system using 16-QAM is also investigated to verify that the UKF and

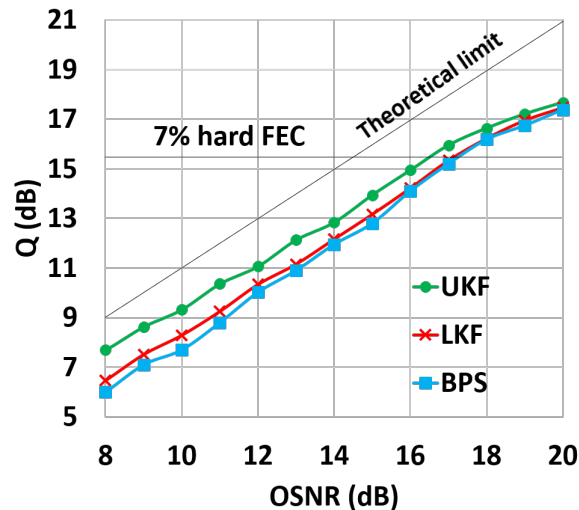


Figure 3.11: Experimental Q vs. OSNR for 16-QAM, block length = 44.

LKF can be generalized to higher-order spectrally-efficient modulation formats. A 10-GBaud, 16-QAM modulated signal was generated and recovered using the two parallelized Kalman filter algorithms. In order to adapt the system to higher-order modulation formats, only the demodulation block is changed that makes them attractive for modulation-format flexible transceivers.

Fig. 3.11 plots Q against received OSNR after using UKF and LKF on a 16-QAM signal taking 44-sample blocks. The Q for conventional BPS algorithm is also plotted for comparison. The number of test phases considered in BPS is $N_p = 16$; found to give optimal result. Similar to the QPSK case, the UKF gives higher performance gain at lower OSNRs than at higher OSNRs. However, in 16-QAM case, the improvement in required OSNR at 7% hard FEC limit ($Q=15.6$) reduces to 0.8 dB and the implementation penalty increases to 2 dB for UKF and 2.8 dB for LKF. The higher implementation penalty is as expected for 16-QAM over QPSK, and the smaller performance difference between the two Kalman filter implementations is expected at higher OSNRs (c.f. Fig. 3.7).

Parallel structures of algorithms can reduce computation time/latency of the system. One of the factors that affects the latency in parallelized Kalman filters is the block length. Fig. 3.12 shows the computation time plotted against increasing block length, in reference to that required by the parallelized LKF at optimal block length 44. The VVPE and BPS algorithms are also considered for latency comparison. As these algorithms use a sliding averaging window instead of block-wise estimation for optimal performance, the computation time required by these methods increases with window-size. At an optimal block-length of 44, the parallelized UKF has lower latency than the BPS and equal latency to the VVPE, while giving Q -performance gains against both of them. On the other hand, the LKF is more time consuming than the BPS, VVPE and the UKF at an optimal block-length of 44. Comparing Fig. 3.10 to Fig. 3.9, the UKF not only gives a gain in Q but also consumes less computation time compared with the parallelized LKF. The computation time/latency gain presented here is explained in Appendix A.

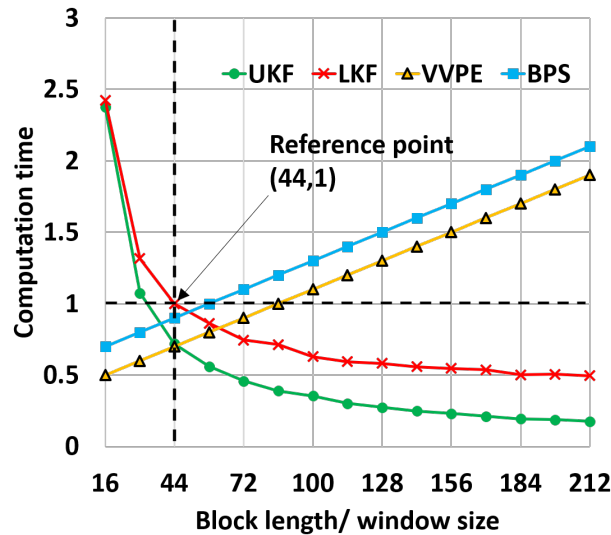


Figure 3.12: Computation time in reference to that of LKF at block length = 44

Another factor that should be considered in the computation time comparison between the LKF and UKF is the calculation of the sigma points in an UKF, which increases the number of operations. As the sigma points are independent of one-another, it is possible to parallelize their calculations; whereas the parallelization of the N addition operations required for the LKF is not possible. Thus, the UKF reduces the latency in the system, at the cost of more hardware. This is verified in the Fig. 3.12 where it can be seen that the total required computation time is reduced to 60% that of parallelized LKF with an optimal block length. This computational benefit of UKF over LKF is possible only in case of parallelized architectures, but not in the conventional serial architecture. As shown in Fig. 3.10 and Fig. 3.12, if the Q -value is sacrificed to certain extent, a considerable reduction in the computation time can be achieved. By increasing the block length from 44 to 142, Q reduces by 0.5 dB but the computation time reduces to 30% of that of block length 44. Similarly, if the block length is further increased to 198, the reduction in computation time reaches 20% that of block length 44 with reduction in Q of 1 dB.

Transmission over an 800-km optical fiber link

The signal was transferred over an 800-km fiber link with varying launch powers to assess the effects of fiber nonlinearity. Fig. 3.13 plots the Q -values of the algorithms under test using a 44-sample block length, for QPSK and 16-QAM signals, with the launch power varied.

Just as in the back-to-back case, the UKF gives a performance improvement over the LKF in the noise-dominated region. Also, the LKF gave marginal improvement over the conventional methods, like in the back-to-back case. At higher launch powers, the UKF and LKF perform similarly, since neither is able to compensate for degradations of optical nonlinearity. Although, for QPSK, the UKF gave a reduction of 2.3 dB in the required launch power at the 7% hard FEC limit over the parallelized LKF, this

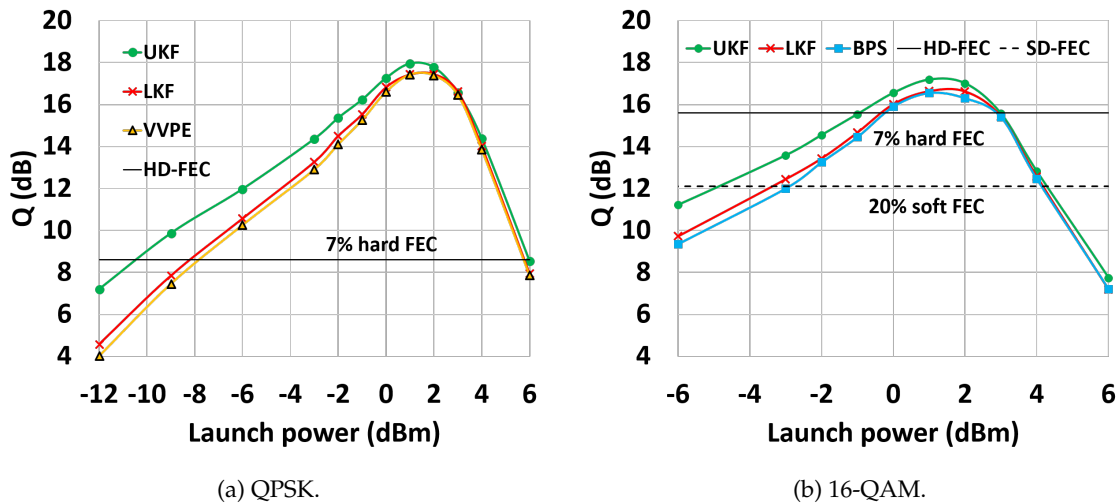
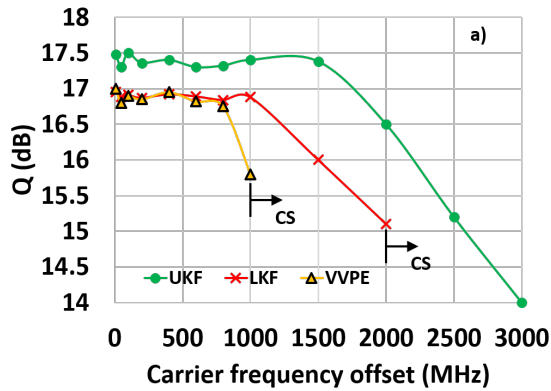


Figure 3.13: Experimental Q vs. launch power over an 800-km optical fiber link, using optimal block length.

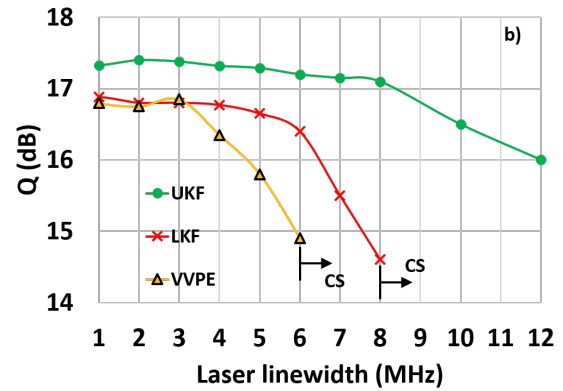
improvement was observed to be marginal (0.5 dB) for 16-QAM case. This improvement for 16-QAM increases if the 20% soft-decision FEC is used as shown in Fig. 3.13b. The soft-decision forward error correction (SD-FEC) techniques such as low-density parity check (LDPC) codes and Turbo codes are being widely explored with an intention of achieving the post-FEC bit error rate (BER) of 10^{-15} [90]. For this, the hard FEC techniques, RS(255,239), *i.e.* with 7% overhead, require a pre-FEC BER better than 3.8×10^{-3} . On the other hand, the SD-FEC techniques can achieve the desired post-FEC BER of 10^{-15} even with worse pre-FEC BERs of 2.7×10^{-2} , but require a 20% overhead [91]. The UKF requires 1.5-dB lower launch-power to achieve the pre-FEC BER of SD-FEC, resulting in UKF providing an overall improvement in terms of the reach of long-haul systems and spectral efficiency with higher-order QAM modulation schemes. Regardless of the marginal peak- Q improvement, the performance gain in low launch power region and 40% less computation time taken by parallelized UKF against the parallelized LKF makes it an attractive alternative for field links.

System tolerance against frequency offsets and linewidths

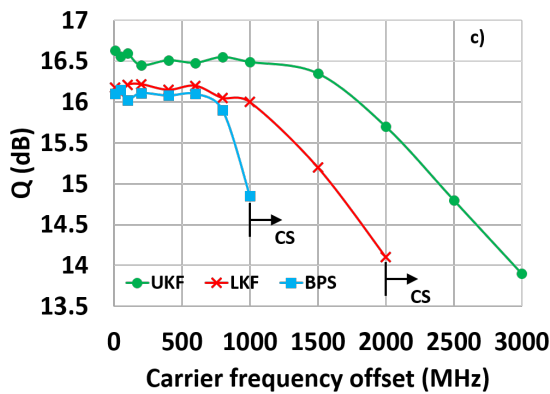
Fig. 3.14 shows the limits of CFO and linewidth up to which the UKF, LKF and the conventional methods work. Simulations were used (VPItransmissionMaker v. 9.7) for these measurements because the linewidth of the laser in the experimental setup is not configurable. The OSNR was fixed at 18 dB. This high OSNR was chosen to remove any possible effects of additive noise on the estimates. The signal distortions are mainly inflicted by the frequency offsets and phase noise. Simulating at high OSNRs, thus, gives us a better idea of the test algorithms' capabilities in carrier recovery. First, a 10-Gbaud, QPSK signal was generated and received in a back-to-back simulation. The linewidth was fixed at 200 kHz and the CFO was varied to find the tolerable CFO limit of each test algorithm. Then, the CFO was fixed at 400 MHz and the linewidth was varied. The same practice was repeated for 16-QAM modulation. It was observed that the performance of each algorithm remains constant up to certain point and then



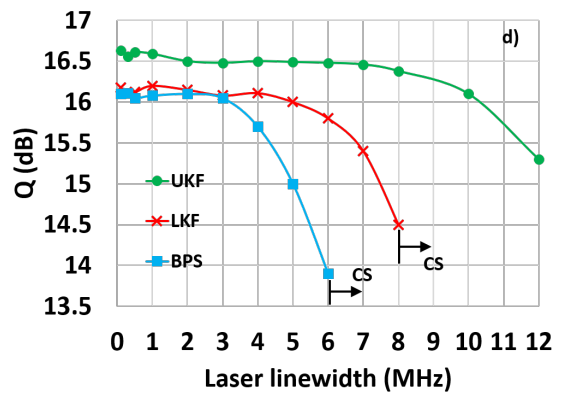
(a) Q (dB) vs. CFO (MHz) for QPSK and linewidth = 200 kHz.



(b) Q (dB) vs. linewidth (MHz) for QPSK and CFO = 400 MHz.



(c) Q (dB) vs. CFO (MHz) for 16-QAM and linewidth = 200 kHz.



(d) Q (dB) vs. linewidth (MHz) for 16-QAM and CFO = 400 MHz.

Figure 3.14: Tolerance of test algorithms for CFO and linewidth (simulations); CS: cycle slips.

drops. Eventually, it reaches a point where the system starts showing cycle slips and the number of errors shoots up. Table 3.1 shows the maximum tolerable limits of each test algorithm before experiencing cycle slips. However, the systems experience 1-2 dB Q penalty before reaching this point. Thus, the limits of CFO and linewidth without Q penalty are still lower. These limits up to which the Q penalty is within 1 dB are given in brackets in Table 3.1. An important conclusion that can be drawn from this result is that although the Kalman filters do not give high performance gain over conventional methods for high OSNRs, but their usage makes the system robust to high CFO and high laser linewidths.

Maximum tolerable limits of CFO and linewidth		
Test algorithm	Carrier frequency offset	Linewidth
Parallelized UKF	3 GHz (2 GHz)	12 MHz (11 MHz)
Parallelized LKF	2 GHz (1.5 GHz)	8 MHz (6.5 MHz)
Viterbi-Viterbi phase estimation/ Blind phase search	1 GHz (1 GHz)	6 MHz (5 MHz)

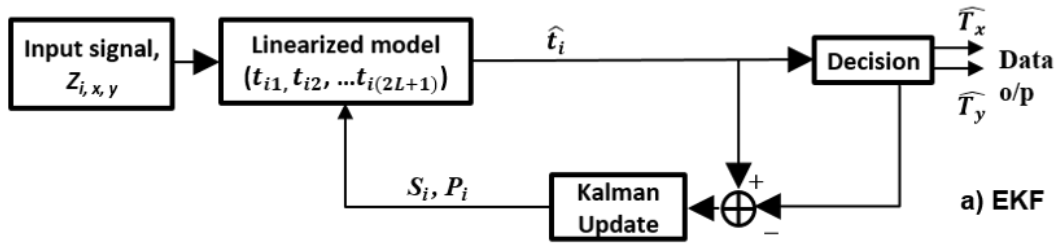
Table 3.1: Simulated maximum tolerable limits of CFO and linewidth before experiencing cycle slips for QPSK and 16-QAM signals. The values in the brackets show the tolerable limits while keeping the Q penalty less than 1 dB.

3.6 Joint phase-noise and polarization state tracking

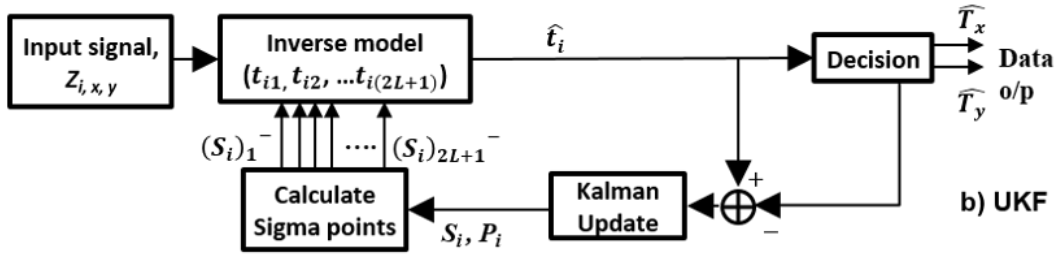
This section discusses the second application covered in the thesis using the Kalman filters which is jointly tracking the phase noise and the polarization state of the received signal. Coherent communication systems support spectrally efficient modulation schemes where data is encoded on the phase, amplitude and polarization states of the optical carrier [3]. However, the finite linewidth of the laser, used as a carrier, results in an additive random phase perturbation. Additionally, small geometric variations in optical fiber randomly rotate the state of polarization at receiver end, changing even with slight vibrations [13]. The digital coherent receiver must dynamically track the phase and polarization states of the system, in order to recover the transmitted signals with low error rates.

Commonly, with the quadrature phase shift keying (QPSK) format, adaptive filters that are based on the constant modulus algorithm (CMA) [92] are used in conjunction with the Viterbi-Viterbi phase estimation (VVPE) algorithm; the CMA takes care of the effects of polarization rotation and VVPE mitigates the effects of the phase noise. In cases of higher-order quadrature-amplitude modulation (QAM) formats, the multi-modulus algorithm (MMA) [93] with pilot-symbol-aided maximum likelihood phase estimation is often employed [94]. Kalman filters provide an alternative method, and have been proven to give optimal estimates compared with all other estimators assuming that the noise sources associated with the system are Gaussian [86]. Marshall *et al.* proposed using an extended Kalman filter (EKF) and showed faster convergence than a conventional CMA+VVPE approach [13]. Also, Linear Kalman filters (LKFs) have been used for polarization state tracking based on a radius-directed method [95]. However, this LKF did not provide joint tracking of phase and polarization, and the proposed system required significant modifications for higher-order QAM.

In this section, an unscented Kalman filter (UKF) is proposed, in place of an EKF. The UKF has been shown to accurately capture all the moments of the parameter to be estimated in contrast to only the 1st and 2nd-order moments provided by the EKF [86]. As such, the UKF gives more-accurate estimates than the EKF. However, this improvement comes at the cost of increased complexity. To address the complexity issue, modified versions of the UKF and EKF (R-UKF and R-EKF) with reduced complexities are proposed. The UKF gives a performance enhancement in comparison with the previously proposed EKF or CMA/MMA algorithms, but at the cost of increased complexity. On the other hand, the R-UKF outperforms the previous algorithms with reduced complexity, but at moderate or higher optical signal-to-noise ratios (OSNR).



(a) Extended Kalman filter block description.



(b) Unscented Kalman filter block description.

Figure 3.15: Block descriptions of the Kalman filter algorithms for nonlinear models.

3.6.1 Nonlinear observation model

The mathematical model ('observation' model) for the impairments of phase noise and polarization rotation, is given as-

$$Z = e^{j\theta} \begin{bmatrix} a + jb & c + jd \\ -c + jd & a - jb \end{bmatrix} \begin{bmatrix} T_x \\ T_y \end{bmatrix} + N \quad (3.18)$$

where, Z is the received polarization multiplexed signal, T_x and T_y are the transmitted symbols on X- and Y-polarizations respectively, $[a, b, c, d]$ are the polarization state parameters determining the polarization rotation, θ is the phase noise and N is additive Gaussian noise mostly due to amplified spontaneous emissions from EDFAs in the system. The parameters $[a, b, c, d]$ follow the Wiener process *i.e.* $a_n = a_{n-1} + \Delta a$ where n determines the time instance and Δa is Gaussian distributed [13]. The parameters b, c and d follow similar distributions. Since the parameters follow Wiener process, Wiener filters may seem to be appropriate for their estimation [8]. However, as the parameters $[a, b, c, d, \theta]$ are non-stationary, Kalman filters should give more-accurate estimates and thus prove to be optimal estimators for these parameters [83].

In spite of the benefits offered by Kalman filters, linear Kalman filters cannot be used for our application because the observation model in Eq. (3.18) is nonlinear, as the phase parameter (θ) is an exponent. As a solution to this, Marshall *et al.* proposed using an EKF that performs the linearization of the nonlinear model by taking its partial derivatives with respect to each parameter, then using this linearized model with regular LKF [13], as shown in Fig. 3.15a. However, this linearization causes inaccuracies in the parameter estimation and thus leads to sub-optimal estimates [86]. Hence, an unscented Kalman

filter (UKF) is proposed, which is able to cope with nonlinear models.

Fig. 3.15b is the block diagram of the UKF. The unknown state parameter vector to be estimated is $S=[a, b, c, d, \theta]$, $\bar{t}=[T_x, T_y]$, P_i is the *a posteriori* estimate covariance, $(S_i)_k^-$ is the k^{th} sigma point calculated, $k = 1$ to $2L+1$, and \hat{f}_i is the estimated symbol vector. The UKF algorithm for this application is given in Appendix C.

3.6.2 Modified Kalman filters for reduced complexity

As UKFs can provide more accurate estimates than EKF, using a UKF should provide a better BER performance. However, any performance improvement comes at the cost of increase complexity of the algorithm, which arises from the additional computations required for calculating the sigma points. This motivates an attempt to reduce the complexity of the Kalman filter algorithms.

To avoid singularity issues in the system, the parameters $[a, b, c, d, \theta]$ are restricted to being real valued [13]. However, due to the phase noise term ($e^{j\theta}$) in the observation model, the Kalman filter gives complex values for these parameters. Marshall *et al.* proposed splitting each complex row in the algorithm's matrices into two consecutive rows; the first row being the real part and second row being the imaginary part [13]. Although this solves the singularity problem, the overall complexity of the algorithm remains the same. This section proposes a solution: two real-valued parameters are combined into a complex-valued parameter *i.e.* take $a + jb = \tilde{a}$ and $c + jd = \tilde{c}$. As a result, the parameters to be estimated by the Kalman filter now become $S = [\tilde{a}, \tilde{c}, \theta]$. The EKF and UKF with this new reduced state vector are named as R-EKF and R-UKF respectively. Since the Kalman filter passes a complex value to each of their parameters, no splitting is required. Moreover, as the number of unknown parameters is reduced from 5 in previous versions to 3 in the modified versions, the orders of the algorithm's complex matrices reduce from 5×5 , $5 \times m$ or $m \times 5$ to 3×3 , $3 \times m$ or $m \times 3$ respectively where m can take values from 1 to 3. This lowers the number of complex multiplications in the algorithm, thus reducing the computational complexity. Additionally, since the parameters a, b, c, d always appear in pairs like $a + jb$ and $c + jd$, and never individually in the algorithm, the combining of these parameters is easily facilitated. The combined parameters, \tilde{a} and \tilde{c} still follow the Wiener process *i.e.* $\tilde{a}_n = \tilde{a}_{n-1} + \Delta\tilde{a}$ and $\tilde{c}_n = \tilde{c}_{n-1} + \Delta\tilde{c}$ where $\Delta\tilde{a} = \Delta a + j\Delta b$ and $\Delta\tilde{c} = \Delta c + j\Delta d$ and thus have a circular Gaussian distribution in the complex plane with zero means and finite variances. Table 3.2 shows the number of required complex multiplications per symbol for each algorithm and thus gives an idea of the complexity reduction with the proposed techniques.

The UKF is more computationally complex than an EKF. However, with the proposed technique to reduce complexity giving R-UKF and R-EKF, an R-UKF is less computationally complex than an EKF. The R-EKF has the least complexity of all algorithms considered in this study.

Number of complex multiplications per symbol detection		
Test algorithm	Name	Number of complex multiplications per symbol
UKF	Unscented Kalman filter	140
R-UKF	Reduced-unscented Kalman filter	90
EKF	Extended Kalman filter	95
R-EKF	Reduced-Extended Kalman filter	72

Table 3.2: Number of complex multiplications per symbol detection required by the algorithms.

3.6.3 Experimental setup

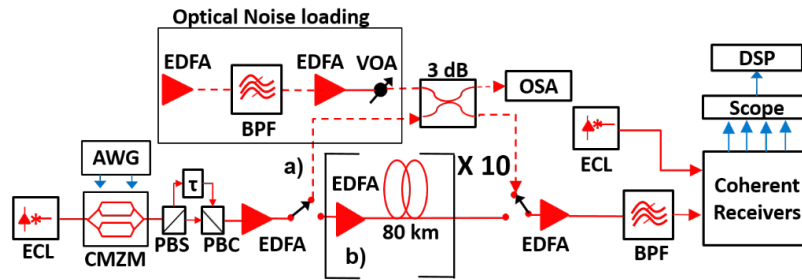


Figure 3.16: Experimental setup for a) back-to-back configuration and b) 800-km transmission link configuration; CMZM: complex Mach-Zehnder modulator, BPF: band pass filter, VOA: variable optical attenuator, ECL: external cavity laser, EDFA: erbium doped fiber amplifier.

A 20-Gbaud digital signal was generated using a Keysight 92 GSa/s arbitrary waveform generator (AWG) to drive a Teraxion 20-GHz optical bandwidth optical IQ modulator. Polarization multiplexing was emulated using an optical delay line, polarization beam splitter (PBS) and combiner (PBC) as shown in Fig. 3.16. In the back-to-back configuration, optical noise covering a 200-GHz bandwidth was added to vary the received OSNR. At the receiver end, the signal was amplified using an EDFA and filtered using a BPF with a 200-GHz bandwidth centered at the set transmission wavelength. The signal was then fed into a Finisar's (U^2T) 25-GHz electrical bandwidth integrated coherent receiver whose outputs are connected to a Keysight 40-GSa/s 28-GHz bandwidth digital signal oscilloscope (DSO). The test algorithms were run as offline DSP.

Fig. 3.17 gives the DSP flow chain performed offline. After being sampled at 40 GSa/s *i.e.* at 2 samples per symbol, the complex signals in both polarizations were passed through a static frequency domain chromatic dispersion (CD) compensation using the overlap-add method [96]. The frequency offsets in each polarization were then separately estimated using the spectral search method [97] and compensated for. The signals in each polarization were resampled to one sample per symbol before passing on to

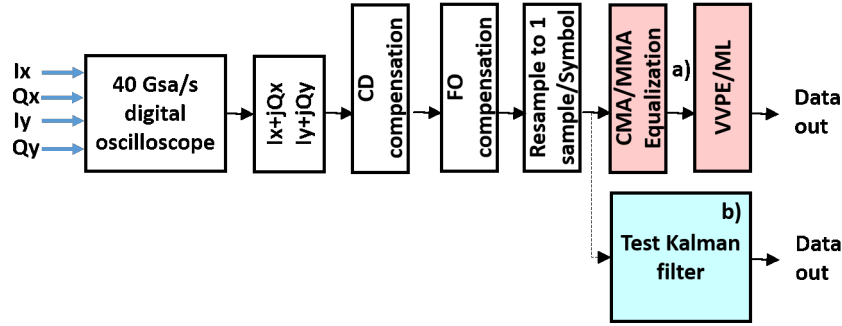


Figure 3.17: Digital signal processing flow for a) CMA+VVPE/MMA+ML b) Kalman filters under test.

the algorithms under test. The internal clock of the digital oscilloscope can be assumed to be stable, but still there are few phase perturbations added to the sampled signal. However, these perturbations can be accommodated by using additional taps in the CMA/MMA equalizers, or by optimizing the initial variances in the Kalman filters. The optimal tap length in our system was found to be 41 taps for both the CMA and MMA filters. Similarly, the Kalman filters, when aided by their decision directed nature, are able to equalize these effects by intelligently updating the parameters in the mathematical distortion model. This may even cause the Kalman filters to give complex values for real parameters to be estimated, which again supports the concept of R-UKF and R-EKF. The Kalman filters replace CMA+VVPE/ MMA+ML algorithms.

Although the R-UKF and R-EKF reduce the complexity, some changes need to be made to avoid the singularity in the system. The Jacobian matrix is-

$$J = e^{j\theta} \begin{bmatrix} Z_x & jZ_x & Z_y & j(a+jb)Z_x + j(c+jd)Z_y \\ Z_y & jZ_y & -Z_x & j(-c+jd)Z_x + j(a-jb)Z_y \end{bmatrix}. \quad (3.19)$$

For R-EKF it reduces to-

$$J = \begin{bmatrix} e^{j\theta}Z_x & e^{j\theta}jZ_y & j(e^{j\theta}\tilde{a}Z_x + e^{j\theta}\tilde{c}Z_y) \\ e^{-j\theta}Z_y^* & -e^{-j\theta}Z_x^* & j(e^{-j\theta}\tilde{c}Z_x^* - e^{-j\theta}\tilde{a}Z_y^*) \end{bmatrix} \quad (3.20)$$

For both R-UKF and R-EKF, the estimates of the parameter θ will be complex-valued. Practically, a phase cannot be complex, but in this case, the R-EKF and R-UKF gives complex outputs for θ that implies an amplitude-scaling along with a phase shift. It was found that the system avoids singularity only when that complex value is considered for θ . Taking only the real or imaginary part, or the absolute value of the complex estimate, either leads to a singularity or divergence of the filter. The explanation for this is that, since two parameters have been combined into one, the three parameters work together to enforce the received signal transformations onto desired constellation points. This causes the Kalman filters to make the θ parameter complex valued. In other words, modified Kalman filters have fewer degrees of freedom to and thus need all the parameters to be complex to maintain tracking.

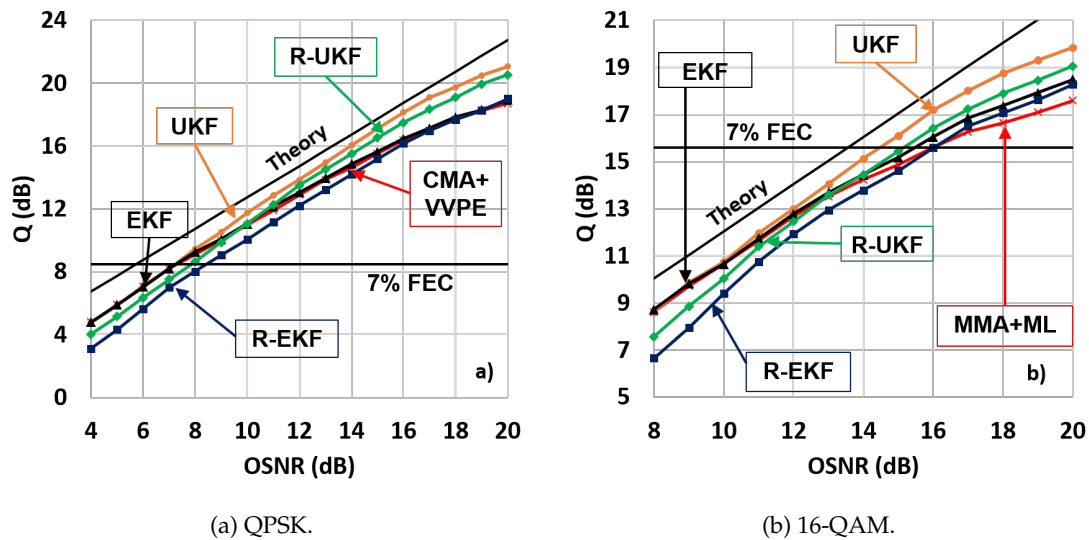


Figure 3.18: Experimental Q vs. OSNR (dB) in back-to-back configuration for 20 Gbaud QPSK and 20 Gbaud 16-QAM respectively.

While these experimental results confirm expected improvements at high OSNR, fiber communication systems are often run near their 'error-free' thresholds, commonly taken as the operating threshold for Reed-Solomon (255, 239) hard-decision forward-error correction (FEC). For the back-to-back QPSK results shown in Fig. 3.18, at low OSNR, R-UKF shows a 0.6-dB OSNR penalty at the 7% hard FEC threshold for QPSK case compared to the EKF. The implementation penalty at the hard FEC limit is 1.3 dB for the UKF, CMA+VVPE and EKF, 1.9 dB for the R-UKF and is maximum of 2.4 dB for R-EKF.

Although the R-UKF shows a reduced performance at lower OSNRs compared with the UKF and EKF for the reasons mentioned in QPSK case, it still shows a negligible OSNR penalty at the 7% hard-FEC limit compared with the EKF for the 16-QAM case. Additionally, the UKF shows an improvement of 1 dB in required OSNR at FEC limit. The implementation OSNR penalty suffered at the 7% hard-FEC limit for 16-QAM modulated signal is 0.9 dB for the UKF, 1.9 dB for the R-UKF, 2.1 dB for EKF and 2.7 dB for MMA+ML and R-EKF. Comparing with the penalties for QPSK, it can be inferred that the EKF, R-EKF and MMA+ML algorithms are not good alternatives for systems supporting both QPSK and 16-QAM. On the other hand, the UKF, with increased complexity, has a reduced implementation penalty for 16-QAM and R-UKF, with its complexity less than EKF, has a consistent implementation penalty independent of whether QPSK or 16-QAM is being received.

To understand the performance of the test algorithms in a practical transmission scenario, the signal was transmitted over 800 km. The optical signal was passed through 10 spools of SMF-28e optical fiber, each of length 80 km. The span's launch powers were controlled by EDFAs placed before each spool, with a final EDFA placed as a pre-amplifier before the receiver.

Fig. 3.19 shows the Q performance of each algorithm in tests against launch powers for both QPSK and 16-QAM. It shows that each algorithm has the same optimal launch power. In the highly nonlinear

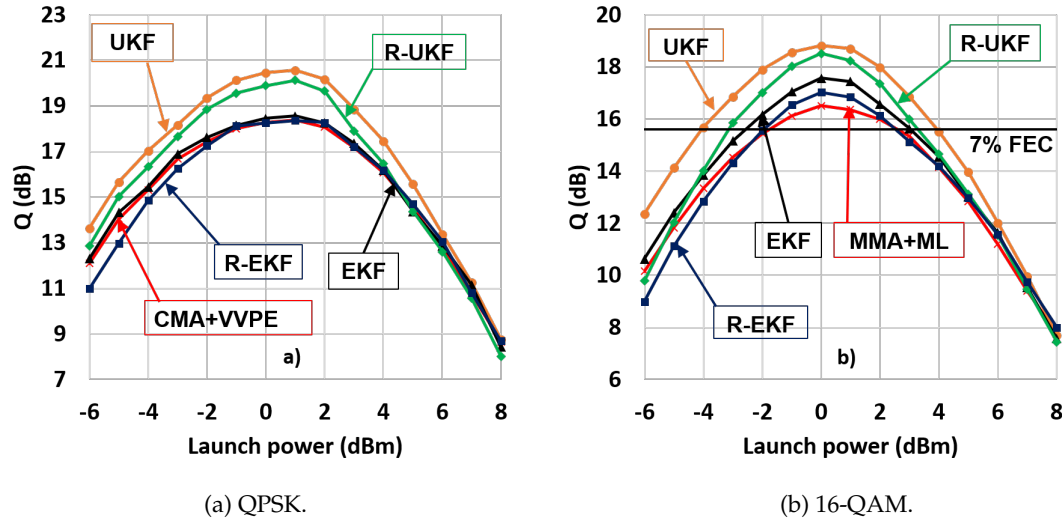


Figure 3.19: Experimental Q vs. launch power (dBm) in 800 km link configuration for 20 Gbaud QPSK and 16-QAM respectively.

transmission regime at higher powers, all the test algorithms give similar performance since the phase tracking is lost, as expected. This is because none of the algorithms are capable of compensating for rapid state changes caused by nonlinear distortion in the fiber. In the QPSK case, the EKF gives no apparent improvement over the CMA+VVPE. In case of 16-QAM, the EKF and R-EKF give marginal peak improvements over the MMA+ML as observed at higher OSNRs. At the peak Q , the signal is expected to have a high OSNR, leading to the increased performance of the UKF (2.1 dB for QPSK and 2.3 dB for 16-QAM) and R-UKF (1.8 dB for QPSK and 2.1 dB for 16-QAM) implementations CMA+VVPE/MMA+ML at optimal launch power. For the 16-QAM case, at the 7% hard FEC limit, the UKF shows 2 dB, R-UKF shows 1 dB, EKF shows 0.7 dB and R-EKF shows negligible reduction in the required launch power compared with the MMA+ML algorithm. Thus, the UKF requires the lowest launch power to achieve the required pre-FEC BER of 3.8×10^{-3} , but comes with a higher computational complexity. The R-UKF may prove to be a pragmatic option since it is less complex than the EKF and requires lower launch power to achieve the performance above FEC. The R-EKF require the highest power and thus could be a feasible option only when low complexity is of utmost importance.

3.6.4 Simulations to investigate the range of tolerable linewidth and CFO.

In addition to transmission impairments and optical noise, the finite linewidths of the lasers used in the systems can vary from device to device. The fixed-linewidth lasers (as used in our experiments) generally confine their linewidth within 100 kHz, but may exceed this value for the lasers used in dense wavelength division multiplexed (DWDM) applications. Hence, the back-to-back setup was simulated next in VPItransmissionMaker (version 9.3) software with the linewidth of both the transmitter's continuous wave (CW) laser and the receiver's local oscillator CW laser varied from 100 kHz to 1 MHz, as shown in Fig. 3.20.

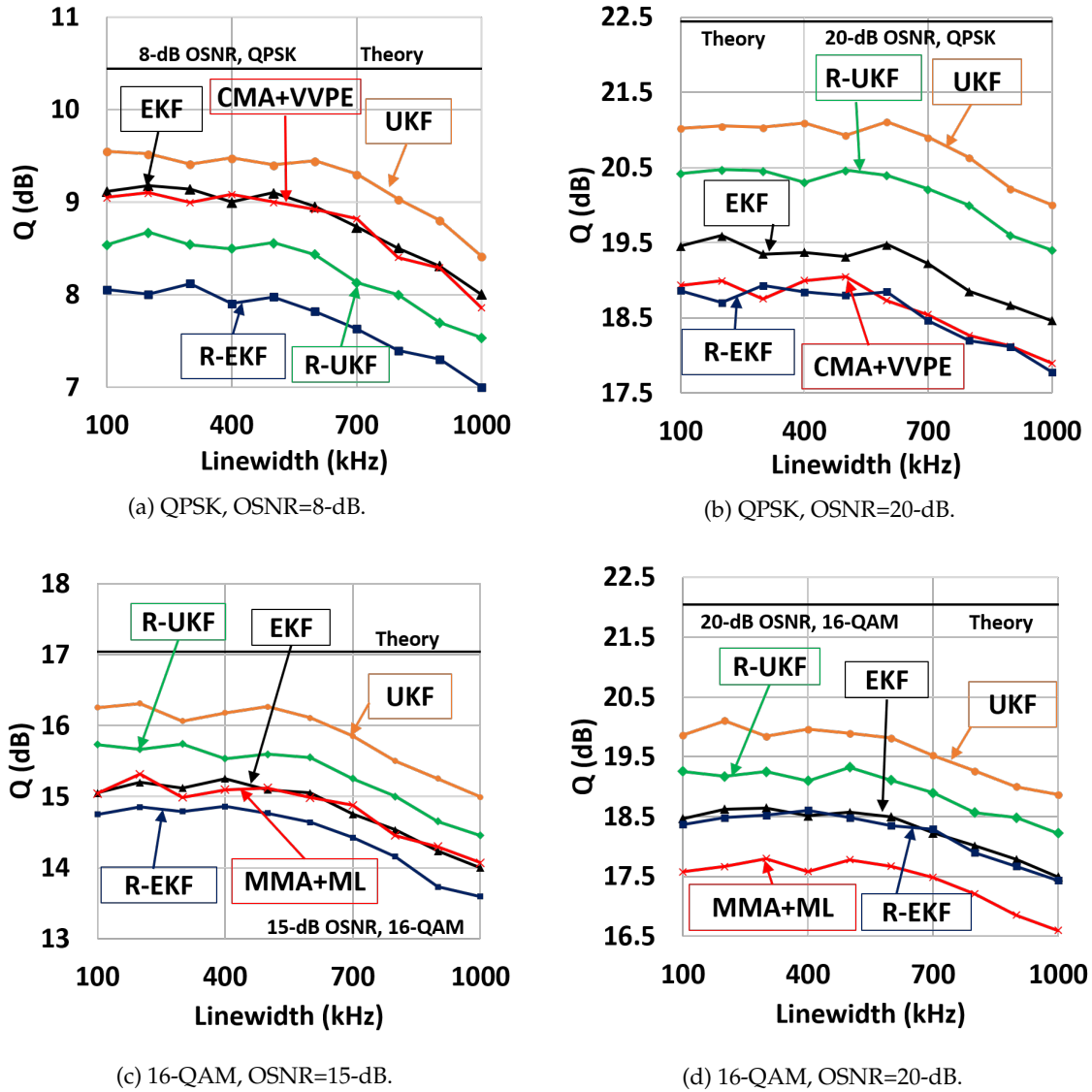


Figure 3.20: Simulated Q (dB) vs. linewidth (kHz) (simulations).

Simulations were performed with a 20-Gbaud polarization multiplexed QPSK and 16-QAM modulated signals at 20-dB OSNR and also at OSNRs close to EKFs respective 7% hard FEC limit (8 dB for QPSK and 15 dB for 16-QAM). The angular rotation rate of polarization evolution taken for simulations was 6.8 Mrad/s. This high polarization rotation velocity was taken to make a fair comparison with the simulations shown by Marshall *et al.* [13]. Additionally, fixing the polarization rotation velocity in simulations where the system is highly stressed beyond practical limits ensures the robustness of the system.

The degradation in signal Q is between 0.1 dB and 0.3 dB for all cases at 600-kHz linewidth, between 0.5 dB to 0.7 dB for 800-kHz linewidth and between 0.9 dB to 1.1 dB for 1-MHz linewidth compared with 100-kHz linewidth. As observed from the back-to-back experimental results, the Q varies by 1 dB for 1-dB change in OSNR around the hard FEC limit. Considering this and the simulation results in Fig. 3.20, it can be concluded that lasers with 1-MHz linewidth require only a 1 dB more OSNR as compared to

100-kHz linewidth lasers to maintain the performance above the hard FEC limit. Thus, the algorithms to be sufficiently robust for stressed systems with linewidths up to 1 MHz and polarization rotations up to 6.8 Mrads/s.

UKF performance gains				
Test parameter	Gain over CMA+VVPE/MMA+ML (dB)		Gain over EKF (dB)	
	QPSK	16-QAM	QPSK	16-QAM
Modulation	QPSK	16-QAM	QPSK	16-QAM
Q at 20-dB OSNR	+2	+2.2	+2	+1.5
Implementation penalty at 7% HD-FEC	0	1.5	0	1
Peak-Q	+2.1	+2.3	+2.1	+1
Required launch power at HD-FEC limit	-	+2.1	-	+1.5

Table 3.3: Performance gain observed with the unscented Kalman filter (UKF) against conventional algorithms and the extended Kalman filter (EKF).

R-UKF performance gains				
Test parameter	Gain over CMA+VVPE/MMA+ML (dB)		Gain over EKF (dB)	
	QPSK	16-QAM	QPSK	16-QAM
Modulation	QPSK	16-QAM	QPSK	16-QAM
Q at 20-dB OSNR	+1.5	+1.7	+1.5	+1
Implementation penalty at 7% HD-FEC	-0.5	+0.6	-0.5	+0.2
Peak-Q	+1.8	+2.1	+1.8	+0.8
Reduction in required launch power at HD-FEC limit	-	+1.2	-	+0.3

Table 3.4: Performance gain observed with the reduced-unscented Kalman filter (R-UKF) against conventional algorithms and the extended Kalman filter (EKF). Negative values indicate penalties.

Table 3.3 and Table 3.4 summarize the performance benefits of the UKF and R-UKF over other algorithms. Overall, these results indicate that, because it only provides a marginal performance improvement for higher modulation formats, EKF is not a good alternative to conventional CMA+VVPE/MMA+ML algorithms. On the other hand, the better performance improvement from using the UKF may come at the cost of increased complexity. For particular cases where moderate or high OSNRs in the system are available, the R-UKF seems to provide a good alternative to CMA/MMA+VVPE in terms of performance and complexity.

The techniques proposed in this chapter use Kalman filters for some of the aspects of carrier recovery. The phase noise compensation is addressed in this work but is restricted to the laser phase noise. The nonlinear phase noise tracking using Kalman filters has not been investigated. [79] and [87] have

contributed to this aspect using Kalman filters but have restricted themselves to extended Kalman filters (EKF). The ASE-induced nonlinear phase noise has been proved to show a good correlation with its delayed version. Also, the correlation strength persists up to longer delays for WDM signals with more number of channels. [98] shows that this correlation extends upto about 20 symbols for a 9-channel, 180-Gbaud signal. Thus, the currently used Kalman filters with maximum 1 symbol delay may not be optimum. A multiple-delay version of Kalman filter that considers the decisions of more than one previous symbols could be an interesting study. As a follow-up project, the performance of such multiple-delay Kalman filter can be compared with already existed multiple-delayed nonlinear filters such as the Volterra-filters. Additionally, this project may also face higher latencies due to calculations required to update Kalman gains for each delay tap. Thus, a tradeoff may be observed with performance and latencies. If the system can be parallelized, this latency issue can be reduced. However, the number of computations required to extract a symbol and the hardware complexity will definitely increase. Further investigation is required on this topic to understand the implementation feasibility of the multiple-delays Kalman filter.

Like mentioned earlier, the Kalman filters give a benefit when upgrading to higher-QAM modulation schemes. This is the result of their decision-directed nature where the system just needs to change the decision block according to the new modulation format, while rest of the system remains the same. The problem arises when the OSNRs drop and causes errors in decisions. Any decision error will cause the tracking to derail and the filter has to start over and achieve tracking again, sometimes impossible without training symbols. Nonetheless, high-order QAM systems are usually maintained at high OSNR levels and with Kalman filter's higher accuracy, they can prove to be very useful for carrier recovery in systems with very high linewidth lasers and rapid polarization rotations.

The QPSK and 16-QAM modulation schemes were investigated for the reason to understand the scalability in modulation schemes. Multicore fibers have been investigated in high data rate transmission using multiple cores as separate channels for optical communication signals [99] [100] [101]. The UKF algorithms can be expected to give similar benefits in multicore fiber systems as well, provided that the mode-coupling issue is resolved before giving different signals to the Kalman filters. The decoupling MIMO algorithms and Kalman filters can also be attempted to be combined if the interference can be mathematically modelled.

Low-cost coherent communication has been attempted in optical wide-area networks (WAN) for their high sensitivity and ease for using amplitude-phase modulation schemes [102]. In their attempts to make the coherent system low-cost, the network operators tend to use less-efficient devices such as high linewidth lasers as local oscillators. As a result, the signal experiences high frequency offsets and phase noises. To tackle these, the receiver system needs strong carrier-recovery algorithms. Thus, the UKF can

be highly beneficial for DCIs. With an additional benefit in computational complexity, even the R-UKF prove to be useful.

Kalman filters have been used in RF communications for more than 40 years now due to their optimal estimation quality and its ability to track variables that undergo non-stationary process. However, their application makes more sense for optical communications where the phase noise and frequency drifts are much higher, in terms of hundreds of kHz and hundreds of MHz respectively that calls for a strong estimation algorithm. With the use of Kalman filters, the optical systems can be made to work with low-cost lasers that give higher linewidths and frequency drifts. Hence, Kalman filters can lead to reduction in cost of deployment in coherent-optical communication systems. As low cost is one of the main reasons driving the industries to move from coherent to direct-detection, Kalman filter's can give an edge to the low-cost coherent-optical communication systems.

3.6.5 Conclusions

The Kalman filters outperform the conventional algorithms in the applications covered in this thesis and that confirms the claims about Kalman filters in the literature. They can be applied for many more applications in optical communications and beyond, as long as there is a random variable involved following the Wiener process. As the phase noise (linear or nonlinear) follows this model, Kalman filters can be used to track the phase noise individually or jointly with some other parameter that distorts the received signal. Additionally, the Kalman filter allows for estimation of multiple state parameters if the state-space equations can be formulated in algebraic matrix form. Thus, a combined nonlinearity compensation along with polarization-state and phase-noise tracking can be targeted as a future project. Unfortunately, as discussed before, the Kalman filters either require more computation time for serial-processing, or require more processing hardware in parallel-processing. A carrier recovery technique that not only reduces this complexity from DSP but removes it completely could be interesting and is investigated in the next chapter.

Optoelectronic processing approach for carrier recovery

In this chapter, a carrier frequency-offset estimator for optical OFDM systems using off-the-shelf optical components and simple digital processing is proposed as a replacement for the purely digital signal processing. Simulations show the system accuracy of $< 4\%$ estimate error within the range $[-1250 +1250]$ MHz offsets for a single polarization 28-Gbaud OFDM signal with 15% cyclic prefix. The effects of the system parameters on the performance are investigated.

Publications based on this chapter-

1. J. Jokhakar, B. Corcoran, C. Zhu and A. J. Lowery, "Electro-Optic frequency offset estimator for optical OFDM," in *European Conference and Exhibition on Optical communication (ECOC'16)*, Dusseldorf, Germany, paper W.4.SC3.12
2. J. Jokhakar, B. Corcoran, C. Zhu and A. J. Lowery, "Simple optoelectronic frequency offset estimator for optical OFDM," *Opt. Express* 25, 32161-32177 (2017).

4.1 Introduction and problem statement

Coherent optical OFDM (CO-OFDM) enables high spectral efficiency by supporting high-order complex modulation schemes and by providing a compact signal spectrum [103–106]. This allows for ultra-high speed, spectrally efficient signaling in fiber communication links. However, CO-OFDM is highly sensitive to the carrier frequency offsets (CFO) that causes a loss of orthogonality of the subcarriers, leading to errors.

Digital signal processing (DSP) at the receiver-side of a fiber optic link is often used to estimate and then compensate for the CFO. There are several different approaches taken to achieve this. A spectral peak search method can be used [97], which finds the peak in the absolute Fast-Fourier transform (FFT) spectrum of a large number of samples from the coherently received signal. Xinwei *et al.* proposed a technique that estimates the CFO based on the power variations in the null subcarriers [107] and Ming *et al.* proposed a likelihood function to be maximized [108]. An iterative frequency offset estimation method has also been proposed for OFDM signals [109]. Digital autocorrelation-based technique that uses the cyclic prefix of OFDM to estimate the CFO can also be used [110]. Training-based techniques have been proposed by Schmidl and Cox in [111] and by Minn *et al.* [112]. Such training-symbols and pilot-subcarrier based CFO estimation techniques have also been proposed by Fan *et al.*, which achieve dynamic tracking of the CFO [113]. Digital phase-locked loops (PLLs) have also been explored for CFO estimation and correction by using a carrier phase estimator [114]. Of all of these techniques, the most widely used are the spectral peak search method [97] and the digital autocorrelation method [110]. Both techniques require a large number of samples to be processed which drastically adds to the computational latency in the DSP. Any attempts to reduce the computational cost/ latency by processing fewer samples will result in loss of estimate accuracy or resolution that has deleterious effect on the BER performance. The techniques proposed by Schmidl and Cox [111] and by Minn *et al.* [112] are also widely used but, as the proposed CFO estimation method in this chapter is also blind, the blind spectral-peak search method is chosen for fair comparison.

Coming to the problem addressed in this chapter, the latency, as a figure of merit for comparison, is a critical parameter for a processing system. A small improvement in latency is important owing to its impact on certain business models. For example, the latency over the internet was widely exploited by few Wall Street traders who managed to get faster access to the stock prices than the rest by using dedicated optical fiber internet connections. A latency of a few milliseconds was translated to multi-million-dollar stock deals in favour of these few traders with high speed access. This, consequently, has fueled parallel and real-time processing research over decades. This chapter intends to address this latency issue in data-recovery by reducing the load on DSP.

Instead of replacing these algorithms with their parallel-processing counterparts, the proposed estimator completely removes the estimation algorithm. While parallelization can reduce the processing time by a given factor related to the number of parallel processes, this will increase the required high-speed (GHz-scale) digital hardware resources. To break the hardware/latency trade off from parallelization, the optoelectronic approach minimizes the latency by performing CFO estimation with an analog optoelectronic system and low-speed (MHz-scale) digital processing. To this end, an optoelectronic frequency offset estimator (OEFOE) is proposed which operates in parallel to the coherent receiver, as shown in

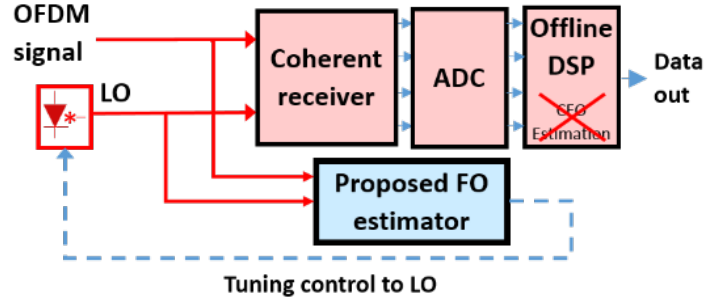


Figure 4.1: Receiver implementing the proposed estimator. ADC: Analog-to-Digital converter; LO: Local oscillator.

Fig. 4.1. This removes the computationally expensive estimation algorithms from the DSP.

All-optical or electro-optical techniques can also be employed, to avoid placing a processing burden on the DSP. These include optical injection locking (OIL) [14], optical phase-locked loops (OPLL) [115] and electro-optic phase-locked loops (EOPLL) [116]. Although these methods have their own advantages, such as simultaneous phase noise mitigation and sequential architectures, they are restricted by the complexities in OPLL, the bandwidths of the components in EOPLL or requirement of a guard band in OIL case. The proposed OEFOE gives accurate estimates for the CFO of $< 4\%$ error without requiring high speed, expensive components, while keeping the design simpler than OIL, EOPLL or an OPLL. The proposed system takes the received signal and the local oscillator (LO) signal as inputs and gives an electrical output corresponding to the frequency offset as shown in Fig. 4.1. This output is provided as a feedback to the local oscillator laser to perform the offset correction.

4.2 Coherent-optical orthogonal frequency division multiplexing

Before going into the concepts of the proposed OEFOE, a brief explanation of the coherent optical orthogonal frequency division multiplexing (CO-OFDM) is given here. This is important as CO-OFDM signal is used for numerous tests in this and the next chapter of this thesis. The OFDM, in general is widely used in RF communications for WiFi (802.11 a,g,n and forthcoming standards) and 4G cellular networks [117]. OFDM is a generic type of multi-carrier modulation (MCM) where data is loaded on multiple subcarriers of small bandwidths. Mathematically, an MCM signal can be represented as [103]-

$$s(t) = \sum_{t=-\infty}^{\infty} \sum_{k=1}^{N_{sc}} c_{ki} s_k(t - iT_s) \quad (4.1)$$

$$s_k(t) = J(t) e^{j2\pi f_k t} \quad (4.2)$$

$$J(t) = 1, \quad (0 < t \leq T_s) \quad (4.3)$$

$$= 0, \quad (t \leq 0, t > T_s)$$

where, c_{ki} is the data symbol at time instance i on k^{th} subcarrier with symbol period, T_s . The subcarriers are each centered at frequency f_k . MCM gives the benefit of using easy frequency-domain

equalization and robustness to frequency-selective multipath in wireless communication. Unfortunately, MCM needs a broad bandwidth to accommodate all the subcarriers without interference. As a solution, OFDM was suggested that again uses subcarriers but they overlap each other to conserve bandwidth [118, 119]. To prevent interference due to overlapping subcarriers, they need to be made orthogonal. Consider $\delta_{k,l}$ as the orthogonality function of the subcarriers such that

$$\delta_{k,l} = \int_0^{T_s} s_k s_l^* dt \tag{4.4}$$

From Eq. (4.2),

$$\delta_{k,l} = \frac{\sin(\pi(f_k - f_l)T_s)}{\pi(f_k - f_l)T_s} e^{2\pi(f_k - f_l)T_s} \tag{4.5}$$

Here, * represents the complex-conjugate of a variable. For orthogonality, $\delta_{k,l} = 0$. This leads to $f_k - f_l = m \frac{1}{T_s}$ for any integer m . Hence, if the frequency spacing between subcarriers is kept as described above, the subcarriers overlap but do not interfere, resulting in spectral efficiency.

OFDM requires a large number of subcarriers for robust operation. This leads to high computational complexity for large number of subcarriers. Nonetheless, from Eq. (4.1), OFDM signal can be generated by simple and computationally efficient inverse fast-Fourier transform (IFFT) on the transmitter and the data can be recovered using FFT on the receiver-side. Thus, the OFDM system becomes computationally-simpler.

The OFDM is added with a cyclic prefix that is a copy of a few samples at the start of an OFDM symbol added at the end of it. This is shown in Fig. 4.2

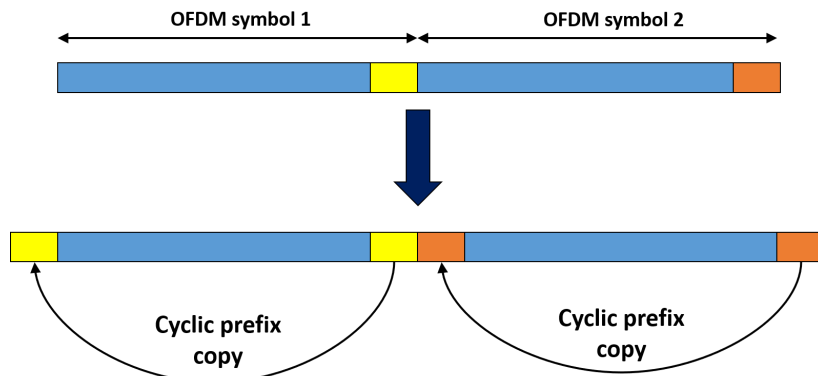


Figure 4.2: Cyclic prefix addition onto OFDM symbols.

The cyclic prefix added to the OFDM symbols makes it robust to the intersymbol-interference (ISI) due to delay spread. In extension, the cyclic prefix maintains the periodicity within an OFDM signal. As a result, the linear convolutional effect of the channel behaves as circular convolution. On removing the cyclic prefix at the receiver, this circular convolution along with the FFT removes the inter-carrier interference, provided the length of the cyclic prefix is more than the delay spread. The signal flow diagram for OFDM is shown in Fig. 4.3.

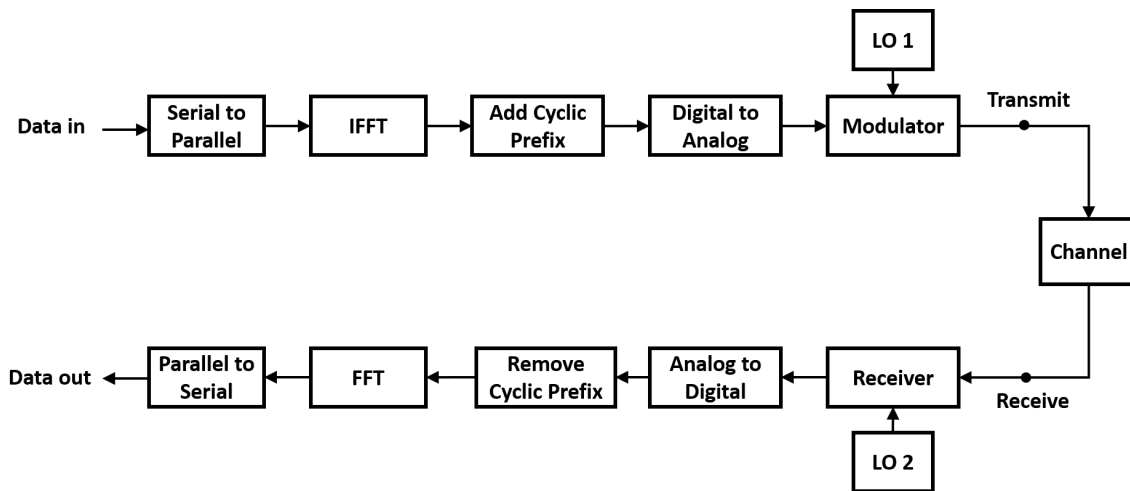


Figure 4.3: Signal flow diagram of an OFDM system. FFT: fast fourier transform, IFFT: inverse fast fourier transform, LO: local oscillator.

The delay spread multipath in wireless communication can be related to the chromatic dispersion in optical communications. Thus, the concept of OFDM was extended to optical communications, primarily to combat the chromatic-dispersion problem as first demonstrated by Lowery *et al.* in 2005 [119] for a 32x10-Gbps wavelength-multiplexed optical single-sideband OFDM transmission over 4000 kms using direct-detection. The data can be loaded on subcarriers on both the side-bands with complex IQ modulators with a linear response. The Mach-Zehnder modulators operating in their linear response region in an IQ modulator pack can be used for this with coherent receivers, that give linear relationship for optical-electrical conversion, on the receiver-side. This system was termed CO-OFDM. Shieh *et al.* demonstrated the CO-OFDM transmission for an 8-Gbps signal over 1000 kms [120]. The benefits offered by CO-OFDM are listed as follows:

1. robustness to chromatic dispersion up to certain limits (depending on the cyclic prefix length) and capability for complete mitigation in DSP.
2. Capability to mitigate the polarization-mode dispersion (PMD) in DSP.
3. Easy frequency-domain equalization and pre-compensation possible.
4. High spectral-efficiency as the orthogonal subcarriers are overlapping in frequency-domain.
5. Spectrum-shaping and easy guard-band allocation possible because of frequency-domain symbol mapping.
6. Above benefits achieved with low computational complexity as IFFT and FFT blocks are used.

4.3 Concept of optoelectronic frequency offset estimator

The underlying concept for the working of the OEFOE lies in the cyclostationarity property of OFDM signals with cyclic prefixes [110]. Consider an OFDM signal $E_s(t)$ with a cyclic prefix of period T_{CP} . Let τ_1 be the OFDM symbol period without the cyclic prefix as shown in the inset of Fig. 4.4.

Thus,

$$E_s(t) = E_s(t + \tau_1) \text{ for } t = 0 \text{ to } T_{CP} \quad (4.6)$$

Now consider the autocorrelation $R(\tau)$ of the signal $E_s(t)$ with delay τ .

$$R(\tau) = \int_0^\infty E_s(t)E_s(t + \tau)^* dt \quad (4.7)$$

Let the carrier frequency of the transmitted signal be ω_0 and carrier frequency offset Δf . Thus, the received signal Y_s and the local oscillator signal Y_L are-

$$Y_s(t) = E_s(t)e^{j\omega_0 t + \phi_1} \quad (4.8)$$

$$Y_L(t) = E_L(t)e^{j(\omega_0 t + 2\pi\Delta f)t + \phi_2} \quad (4.9)$$

where $E_L(t)$ is the amplitude of the local oscillator signal and ϕ_1, ϕ_2 are the phase offsets. The autocorrelations of $Y_s(t)$ and $Y_L(t)$ are

$$R_s(\tau) = \int_0^\infty Y_s(t)Y_s(t + \tau)^* dt = e^{-j\omega_0\tau} \int_0^\infty E_s(t)E_s(t + \tau)^* dt = e^{-j\omega_0\tau} R(\tau) \quad (4.10)$$

$$R_L(\tau) = \int_0^\infty Y_L(t)Y_L(t + \tau)^* dt = e^{-j\omega_0\tau} e^{-j2\pi\Delta f\tau} \int_0^\infty E_L(t)E_L(t + \tau)^* dt = e^{-j\omega_0\tau} e^{-j2\pi\Delta f\tau} L(\tau) \quad (4.11)$$

where $L(\tau) = \int_0^\infty E_s(t)E_s(t + \tau)^* dt$. The phase offsets ϕ_1 and ϕ_2 are affected by the laser phase noise but the integration operation and the Wiener-process nature of the phase noise negates their effect. This will be explained further. Note that $R_s(\tau)$ and $R_L(\tau)$ are not dependent on time, t , but remain constant for a given value of delay, τ , for a fixed CFO, Δf .

The ratio of $R_s(\tau)$ and $R_L(\tau)$ is:

$$D(\tau) = \frac{R_s(\tau)}{R_L(\tau)} = \frac{e^{j2\pi\Delta f\tau} R(\tau)}{L(\tau)} \quad (4.12)$$

Now, if the delay $\tau = \tau_1$ from Eqs. (4.6) and (4.7), $R(\tau_1) = \int_0^\infty E_s(t)E_s(t + \tau)^* dt$. The $R(\tau_1)$ can be written as summation of multiple OFDM symbols as follows.

$$R(\tau_1) = \sum_{n=0}^{N_{int}} \int_0^{T_{OFDM}} E_s(nT_{OFDM} + t)E_s(nT_{OFDM} + t + \tau_1)^* dt \quad (4.13)$$

where, n is OFDM symbol index and T_{OFDM} is the OFDM symbol period, including the cyclic prefix, given as $T_{OFDM} = T_{CP} + \tau_1$. For realistic system, n ranges up to a finite value N_{int} that reflects the number of OFDM symbols that need to be integrated for the proposed system to converge to the required

estimate. $R(\tau_1)$ can then be extended as

$$R(\tau_1) = \sum_{n=0}^{N_{int}} \left(\int_0^{T_{CP}} E_s(nT_{OFDM} + t) E_s(nT_{OFDM} + t)^* dt + \int_{t>T_{CP}}^{T_{OFDM}} E_s(nT_{OFDM} + t) E_s(nT_{OFDM} + t + \tau_1)^* dt \right)$$

Since the OFDM symbols are uncorrelated for $t > T_{CP}$, the second term will reduce to zero. As a result, for $\tau = \tau_1$, $R(\tau) = \sum_{n=0}^{N_{int}} \int_0^{T_{CP}} |E_s(nT_{OFDM} + t)|^2 dt$ and is real. It is important to note here that the strength of the autocorrelation is proportional to the length of cyclic prefix. Thus, longer cyclic prefixes will improve the system accuracy, as will be shown in next section. Similarly, since the amplitude of the local oscillator signal $E_L(t)$ can be taken as constant, and $L(\tau) = \int_0^{T_{CP}} |E_L(t)|^2 dt$ is also real. Thus, the only complex term in Eq. (4.12) is $e^{j2\pi\Delta f t}$ and the CFO can be calculated as-

$$\Delta f = \frac{\angle D(\tau_1)}{2\pi\tau_1} \quad (4.14)$$

4.4 System design and simulations

Two different sub-system designs are proposed here where each design has its own benefits in different implementation scenarios.

4.4.1 OEFOE Version 1

System design

The first design of the proposed optoelectronic CFO estimator (OEFOE 1) is shown in Fig. 4.4. This design is conceptually closest to the method described in the previous section, with the delayed signal and delayed LO mixing, physically occurring separately.

OEFOE 1 takes the received OFDM signal as input and splits it using a 3-dB coupler. The signal is delayed in one of the arms by a specific delay τ_1 , equal to the OFDM symbol period without the cyclic prefix (as shown in the inset of Fig. 4.4). It is assumed that the structure of the cyclic prefix of the signal in the optical network or a link is standardized and known to the receiver. Thus, the delay line's length, depending on τ_1 , can be selected accordingly. Just to make the proposed OEFOE flexible, the delay line fiber can be made detachable such that it can be replaced appropriately whenever the cyclic prefix length is changed. Problems may arise only when the system dynamically changes the cyclic prefix length.

The signal and the delayed version are then fed to a 90°-hybrid and the outputs of the hybrid are detected by slow photodiodes in balanced configuration. The output of the configuration will converge to $R_s(\tau_1)$ [121] as shown in Fig. 4.4. Simultaneously a similar setup generates a signal that converges to

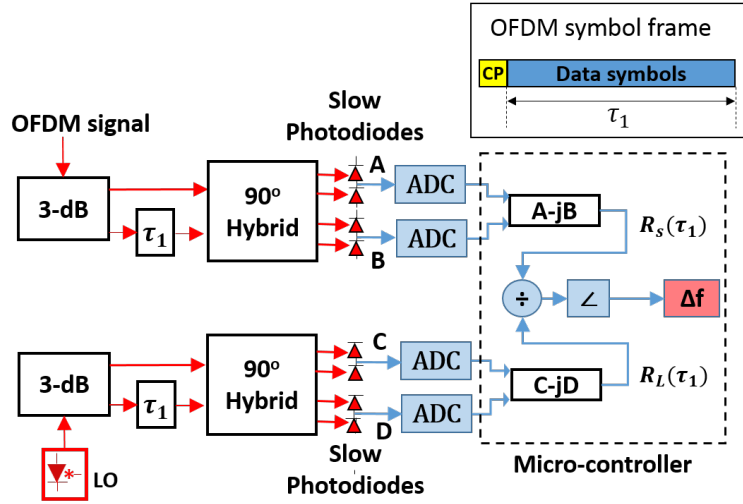


Figure 4.4: Proposed optoelectronic CFO estimator (OEFOE) design. Inset: OFDM symbol frame structure.

$R_L(\tau_1)$ as shown in Fig. 4.4. The integration operation required for $R_s(\tau_1)$ and $R_L(\tau_1)$ is performed by the slow photodiodes [122], with bandwidths governed by the parameter N_{int} . The integration time of the photodiodes has to be more than $(N_{int} \times T_{OFDM})$. Fig. 4.5 shows the OEFOE's output against time from which the convergence can be extrapolated to find the number of OFDM symbols to be integrated (N_{int}).

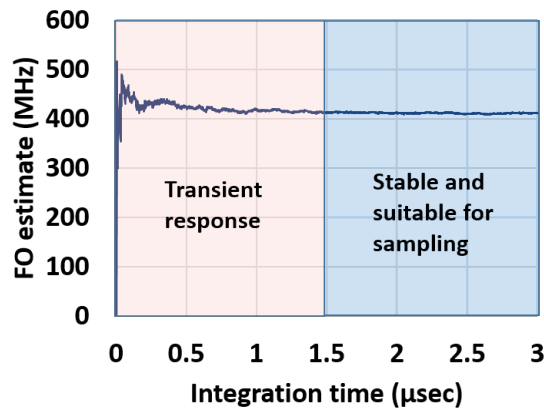


Figure 4.5: Simulated system output vs. photodiode integration time for CFO = 410 MHz.

Simulations were performed in VPItransmissionMaker software (Version 9.7) for a 28-Gbaud QPSK modulated OFDM signal of FFT length 156, 100 subcarriers and 15% cyclic prefix. The signal was oversampled at 40 Gsa/s. With this configuration, the delay τ_1 can be calculated to be 0.8 ns. Substituting $\tau_1 = 0.8$ ns in Eq. (4.14) with $\angle D(\tau_1) \in [-\pi, \pi]$, the estimation range of the OEFOE is [-625 MHz, +625 MHz]. The parameters of the optical fiber chosen for simulations are given in Table 1.

Initially, the CFO was set to 410 MHz and the output was recorded while the integration-time was swept (Fig. 4.5). It is observed that the output of the OEFOE converges to the actual CFO of 410 MHz after 1.5 μ s. Hence, the number of OFDM symbols that need to be integrated to converge to the required

Simulation parameters		
Parameter	Value	Unit
Attenuation	0.2	dB/km
Dispersion	16×10^{-6}	s/m^2
Dispersion slope	0.08×10^3	s/m^3
Group refractive index	1.47	-
Nonlinear index	2.6×10^{-20}	m^2/W
Core area	80×10^{-12}	m^2
EDFA noise figure	4	dB
Span length	100	km

Table 4.1: Parameter values taken for simulations.

estimate can be given as $N_{int} = 1.5 \times 10^{-6}/T_{OFDM}$. This dependence of convergence on the cyclic prefix is discussed in Section 4.4. In the case of fast photodiodes, the integration can be provided by bandwidth-limiting filters. However, this is not advised, as it increases the cost. The remaining operations to calculate the CFO (Eq. (4.14)) can be performed using a simple microprocessor. To do so, the electrical signals at the output of the balanced configuration need to be sampled after convergence. A single sample taken after $1.5 \mu s$ is sufficient to calculate the CFO using Eq. (4.14). Note that the actual sampling takes place after the balanced photodiodes Fig. 4.4; the trace in Fig. 4.5 just helps to visualize the convergence process.

As depicted in Fig. 4.4, OEFOE 1 could be implemented with passive off-the-shelf components such as 3-dB couplers, 90° -hybrids, and optical delay lines. Additionally, the electronic components can have low bandwidth, as only slow photodiodes and ADCs with MHz sampling rate are required. Moreover, only a small number of float-point operations are required on the samples to give the desired frequency offset estimates, which can readily be performed by a simple microcontroller.

Simulations and results for OEFOE 1

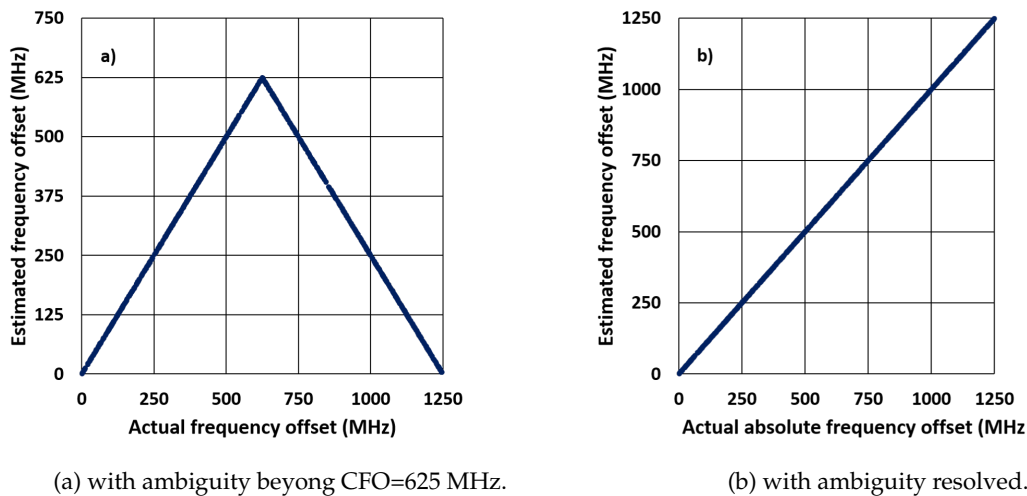


Figure 4.6: Scatterplots of Estimated CFO vs. Actual CFO (MHz).

Fig. 4.6a shows the simulated scatterplot, now with CFO sweep, estimated by the OEFOE in back-

to-back setup. The CFO is randomly chosen within the range $[-1250 \text{ MHz}, +1250 \text{ MHz}]$ for 1000 runs and estimates are calculated by both methods. As expected, the OEFOE gives accurate results with estimate errors $< 1\%$ up to $\pm 625 \text{ MHz}$. The slope of the scatter plot reverses beyond 625 MHz because of phase reversal of $\angle D(\tau_1)$ beyond π radians for positive CFO and beyond $-\pi$ radians for negative CFO. This creates an ambiguity in estimating CFO beyond $\pm 625 \text{ MHz}$ (Fig. 4.6a). To resolve this ambiguity, a known phase shift $\Delta\phi = 2\pi f_k \tau$ is added digitally to $R_s(\tau)$. f_k is known ($+2 \text{ MHz}$ in our case) giving $R_s^k(\tau) = R_s(\tau)e^{j2\pi f_k \tau}$ and leading to new frequency offset Δf_k .

If, $\Delta f < 625 \text{ MHz}$, $(\Delta f_k - \Delta f)$ will be positive owing to positive frequency shift. Similarly, if $\Delta f > 625 \text{ MHz}$, $(\Delta f_k - \Delta f)$ will be negative due to the negative slope in this region. Hence, with one additional multiplicative and subtracting operation in the microcontroller, the ambiguity can be resolved to give full estimation range of $[-1250, +1250] \text{ MHz}$ as shown in Fig. 4.6b. As these computations are to be performed on a low-clock rate microcontroller, the cost of providing these computations is orders of magnitude lower than for GHz-clock DSP ASICs used in conventional coherent communication systems. This method to resolve ambiguity will fail within the range $[623, 625] \text{ MHz}$ of the absolute actual CFO, excluding the limiting values. Despite of this failure in ambiguity resolution, the error in CFO calculation will be a maximum of 4 MHz which is still very low ($< 6.4\%$). Apart from that, the chance of the actual CFO falling within this range is low. So, in practical systems that have the CFO drifting frequently, the proposed OEFOE will have a negligible outage probability.

Implementation issues for OEFOE 1

In practical implementation of the OEFOE with discrete components as suggested above, the device's performance is affected by various parameters such as-

1. Different delays in the two optical delay lines before the 90° -hybrids in Fig. 4.4 instead of a single delay, τ_1 .
2. "Not-same" phase differences between signals at the outputs of the two 3-dB couplers in Fig. 4.4.

These parameters could be precisely controlled if OEFOE 1 was to be implemented on an integrated 'photonic chip', by providing a phase-stable platform. In the case when the OEFOE needs to be prototyped with discrete components, OEFOE 1 fails to give accurate result owing to the different delays in optical delay lines and phase differences in the 3-dB couplers. These parameters cannot be controlled or calibrated with discrete components. For such scenario of implementation with discrete components, a different design (OEFOE Version 2) is proposed in the next section.

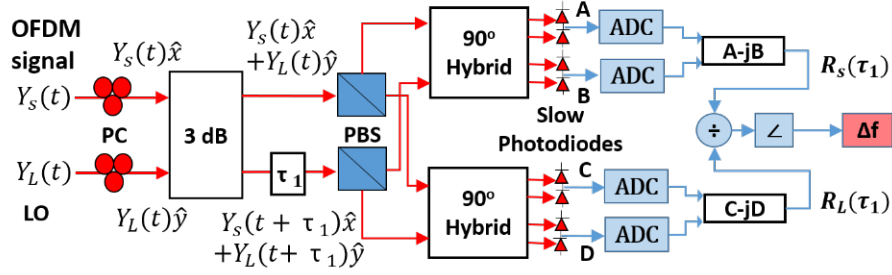


Figure 4.7: OEFOE version 2 setup. PC: polarization controller; PBS: polarization beam splitter.

4.4.2 OEFOE Version 2

A modified version of the OEFOE setup is proposed that can be prototyped with discrete components, shown in Fig. 4.7. This second version (OEFOE 2) uses only one optical delay line and one 3-dB coupler for both received and LO signals and exploits a dual-polarization coherent receiver to estimate the CFO. The received signal $Y_s(t)$ and the local oscillator signal $Y_L(t)$ are orthogonally polarized, aligned to x and y polarizations respectively using polarization controllers (PC) and combined using a 3-dB coupler. Thus, the 3-dB coupler will have signal $Y_s(t)\hat{x} + Y_L(t)\hat{y}$ on one output arm and a delayed version $Y_s(t + \tau_1)\hat{x} + Y_L(t + \tau_1)\hat{y}$ on the other arm after passing through an optical delay line, τ_1 . These signals, after splitting by polarization beam splitters (PBS), are received as $Y_s(t)\hat{x}$ and $Y_s(t + \tau_1)\hat{x}$ at the inputs of one 90°-hybrid and $Y_L(t)\hat{y}$ and $Y_L(t + \tau_1)\hat{y}$ at the inputs of other hybrid, similar to OEFOE 1 setup in Fig. 4.4. Thus, the rest of the system is the same as in Fig. 4.4, and the CFO estimates can be acquired at the output. For proper functioning of OEFOE 2, care needs to be taken that the laboratory environment is controlled and the polarization of the signal does not drift. Otherwise, OEFOE 2 will require repetitive adjustment of the polarization controllers. It can be then shown that this system is robust to phase and delay perturbations that affected OEFOE 1 design. The proposed systems in Fig. 4.4 and Fig. 4.7 resemble a coherent receiver, which is usually costly. Nonetheless, no high-speed photodiodes or high-speed ADCs are used, which are the major contributors to the high cost of the coherent receivers.

4.4.3 Effect of the phase mismatch between signals at outputs of 3-dB coupler

Let the phase mismatch between the two output arms of the 3-dB coupler be $\Delta\phi$. Thus, the inputs of the PBSs in Fig. 4 are

$$P_1(t) = e^{j\Delta\phi}(Y_s(t)\hat{x} + Y_L(t)\hat{y}) \quad (4.15)$$

$$P_2(t + \tau_1) = (Y_s(t + \tau_1)\hat{x} + Y_L(t + \tau_1)\hat{y}) \quad (4.16)$$

After being split by the PBSs, from Eqs. (4.10) and (4.11), the autocorrelation values will be

$$R_s(\tau) = e^{-j\omega_0\tau} e^{j\Delta\phi} R(\tau) \text{ and } R_L(\tau) = e^{-j\omega_0\tau} e^{-j2\pi\Delta f\tau} e^{j\Delta\phi} L(\tau). \quad (4.17)$$

As a result, after taking a ratio of $R_s(\tau)$ and $R_L(\tau)$ in the microprocessor, the $e^{j\Delta\phi}$ term is cancelled and the value of $D(\tau)$ remains the same as in Eq. (4.12). So, any phase mismatch between the signals in the output arms of the 3-dB coupler should have no effect on OEFOE 2. This is shown in Fig. 4.8

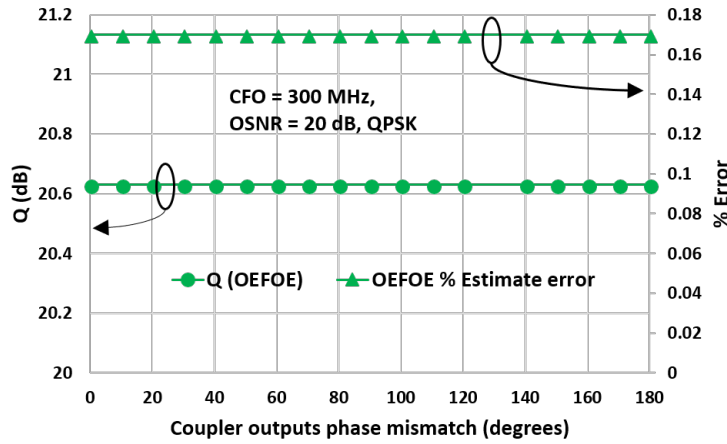


Figure 4.8: Simulated Q (dB) and estimate % error vs. coupler output phase mismatch (degrees).

4.4.4 Effects of the delay variations in the optical delay line (τ_1)

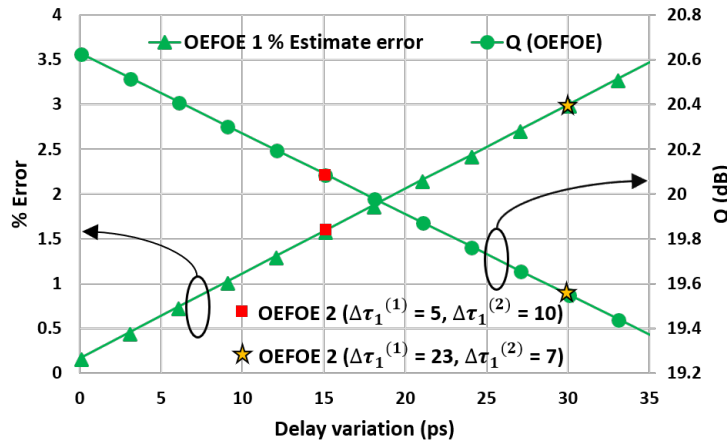


Figure 4.9: Simulated Q (dB) and estimate % error vs. delay variations (ps) in optical delay line.

For commercial SMF-28e fibers, the temperature variations in the fiber lengths can cause a delay variation up to ± 30 ps [123]. To observe the effect of delay variations, a 28-Gbaud, QPSK encoded OFDM signal of FFT length 156, 100 subcarriers and 15% cyclic prefix was generated as a test signal. As observed in Fig. 4.9, the delay variations cause a linear increase in the error and degradation of the Q performance of the system. This is observed despite of assuming perfect extinction ratio PBS whose effect will be added in the next section. With the delay variations increasing from 0 ps to 36 ps (4.5% of τ_1), the % error increases from 0.16% to 3.6% causing the Q of the recovered signal to drop from 20.6 dB to 19.35 dB i.e. by 1.25 dB. This degradation can be nullified by keeping the system in a temperature-controlled environment or by integration.

While considering the delay variation, the plots in Fig. 4.9 remains the same for both OEFOE versions, except that for OEFOE 1, the x-axis is the sum of the delay drifts ($\Delta\tau_1^{(1)} + \Delta\tau_1^{(2)}$) and for OEFOE 2, the x-axis is just $\Delta\tau_1$. It is obvious that OEFOE 1 is much more sensitive to delay drifts as it takes smaller drifts in individual delay elements to achieve a delay drift in OEFOE 2. For eg. for 0.5-dB penalty in Q , OEFOE 1 needs its delay element to drift by 15 ps, whereas it will take smaller drifts in individual delay elements of OEFOE 2 (5 and 10 or any other combination adding up to 15) to reach the same Q penalty. Two such combinations of delay drifts ($\Delta\tau_1^{(1)} = 5, \Delta\tau_1^{(2)} = 10$) and ($\Delta\tau_1^{(1)} = 23, \Delta\tau_1^{(2)} = 7$) are simulated and the results verify the discussion above. This proves that the delay variations are more problematic in OEFOE 1 as it uses two optical delay lines and the paths are independent. On the other hand, OEFOE 2 uses a single optical delay line and thus the shifts are common for both the OFDM and the LO signals. Consequently, OEFOE 2 is less affected by the delay variations than OEFOE 1, if both versions are implemented in lab using discrete components. Still, shifts in delay away from τ_1 cause inaccuracies.

4.4.5 Effect of the polarization misalignment in the polarization controllers

OEFOE Version 2 was implemented experimentally using discrete components. A 28-GBaud OFDM, QPSK signal of FFT length 156, 100 subcarriers and 15% cyclic prefix was fed from a Keysight 92 GSa/s arbitrary waveform generator (AWG) into a Teraxion optical IQ modulator. The modulated signal was split using a 3-dB coupler, where the one output was connected to a coherent receiver and the other to the proposed FO estimator. The local oscillator signal was also split in similar fashion. This splitting was done to calculate the actual frequency offset using conventional offline DSP method simultaneously, in order to verify the accuracy of the proposed FO estimator. For this offline DSP, the signal was received by a 25-GHz electrical bandwidth integrated coherent receiver connected to a Keysight 40 Gsa/s, 30-GHz bandwidth oscilloscope. The actual frequency offset was then calculated using the spectral-peak search technique.

At the same time, the proposed OEFOE setup was made in parallel as in OEFOE 2 shown in Fig. 4.7. Fortunately, the inherent internal structure of a Finisar CPRV1b2tA series integrated coherent receivers contains two PBS, two 90° hybrids and balanced photodiodes connected in the same fashion as designed in the proposed setup. Thus, it was used for detecting the optical signals. The integration process and remnant operations were performed in offline DSP for ease of proof of concept. As the Finisar integrated coherent receivers have fast photodiodes, in contrast to our requirements, the integration of the signal was done in offline DSP using digital low-pass filters.

The frequency offset of the system was allowed to drift within the range [-900 MHz, +900 MHz]. Fig. 4.10 shows the scatter plot of the absolute of estimated CFO against the actual CFO of the system

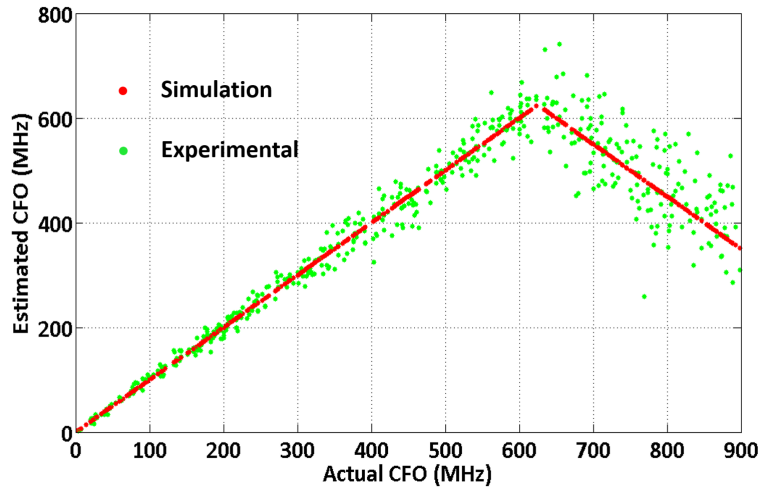
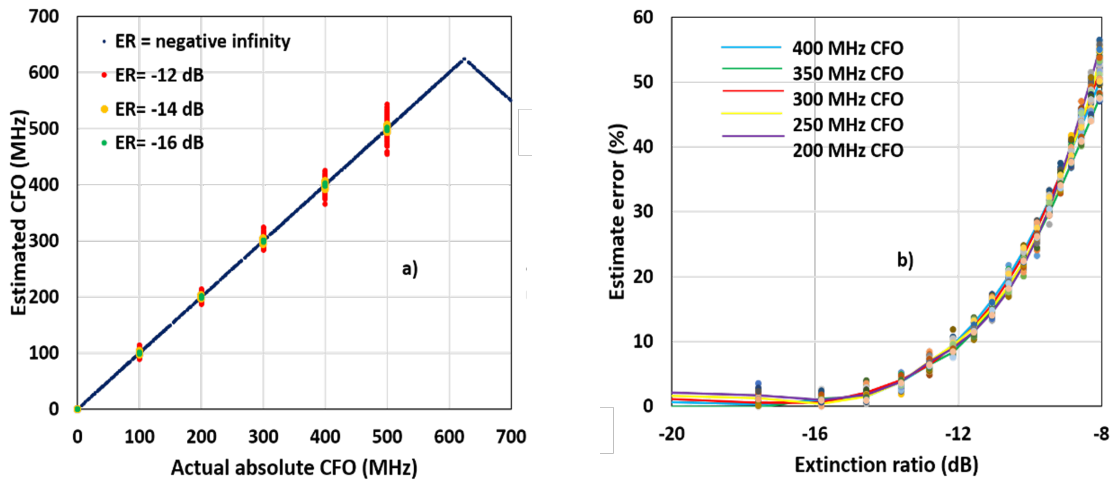


Figure 4.10: DSP estimated absolute CFO vs. proposed OEFOE Version 2 estimated absolute CFO.



(a) Simulated scatterplots of the CFO estimates for different polarization extinction ratio (ER).

(b) Estimate error (%) vs. ER (dB).

Figure 4.11: Effect of the polarization misalignment.

calculated using the spectral search method. The simulations show accurate estimation up to ± 625 MHz. The experimental results show the estimate error increasing with the frequency offsets. This increasing error was investigated and concluded to arise from polarization misalignment in the polarization controllers. This was verified in simulations as shown below.

As OEFOE 2 uses polarization diversity, the polarization alignment of the signal becomes an important factor in the performance. For accurate CFO estimations, the polarization controllers in Fig. 4.7 need to be aligned properly such that the $Y_s(t)$ and the local oscillator signal $Y_L(t)$ are orthogonally polarized on x and y polarizations respectively. In case of polarization misalignment, the system gives errors. As shown in the Fig. 4.11b the estimate errors increase nonlinearly with a decrease in the polarization extinction ratio (ER). In simulations, the polarization beam splitter is modelled to have a perfect ER, and so the change in the ER determined by the polarization misalignment θ , where $ER = -10\log_{10}(\sin^2[\theta])$.

In reality, the limited ER of the polarization beam splitters would need to be taken into account. It can be observed that the error-ratio increases rapidly from almost 0% to 50% when the polarization misalignment θ is increased from 0° (ER=-20.5 dB) to 10° (ER=-8 dB). To understand this effect, simulations were again performed by varying the ER by changing the polarization-mismatch, θ . The results are shown in Fig. 4.11a where the scatterplot shows perfect estimation for ER = $-\infty$ i.e. when $\theta = 0$ but the errors increase rapidly when the ER is slightly increased from -16 dB to -12 dB. This proves the proposed OEFOE 2 is also sensitive to the polarization alignment.

A specific OEFOE design can be chosen according to the application scenario. The OEFOE 1 design is accurate with errors $< 0.2\%$ when fabricated on an integrated photonic chip with active control of phases. On the other hand, when implemented with discrete components, OEFOE 1 performance is strongly affected by the delay variations and phase difference between outputs of 3-dB couplers. Consequently, the OEFOE 2 design is proposed that is robust to the 3-dB coupler phase differences and less sensitive to the delay variations compared with the OEFOE 1 design. Unfortunately, this design is sensitive to the polarization extinction ratio of the PBSs in the design and needs to be carefully taken care of for accurate results. The next sections discuss the parameters in the system that are common to both designs and their effects on the estimation accuracy.

4.5 Variation of performance against cyclic prefix length

As seen in Eq. (4.13), the strength of the autocorrelation depends on the limits of the integral; i.e. on the duration of the cyclic prefix (T_{CP}), that in turn determines the accuracy of the system. In other words, from Eq. (4.13), $R(\tau)$ will be more accurate when the cyclic prefix is longer. Intuitively, longer cyclic prefix, T_{CP} in proportion to T_{OFDM} , means that the autocorrelation is calculated over more symbols that increases its strength and thus the accuracy of the system. On the other hand, a longer cyclic prefix reduces spectral efficiency, showing a trade-off between Q performance and spectral efficiency.

The effect of changing cyclic prefix length can be seen in Fig. 4.12a, Fig. 4.12b and Fig. 4.12c where the OEFOE converges to the actual CFO faster for the signals with longer CP. From Fig. 4.12 it can be observed that the convergence is affected by the CP proportion (Fig. 4.12a, Fig. 4.12b and Fig. 4.12c) and not by the FFT size (Fig. 4.12d), giving us freedom when choosing the FFT size according to the channel frequency response. Moreover, the magnitude of the frequency offsets also affects the convergence as can again be observed from Fig. 4.12a, Fig. 4.12b and Fig. 4.12c. Greater frequency offsets cause slower convergence.

The convergence helps us to determine the sampling rate of the ADCs in the proposed OEFOE. For maximum trackable CFO (1250 MHz) and 15% CP, the estimation signal converges at $1.35 \mu s$. Any CP lower than 15% causes the convergence to occur only after $2.4 \mu s$. To ensure the convergence, the

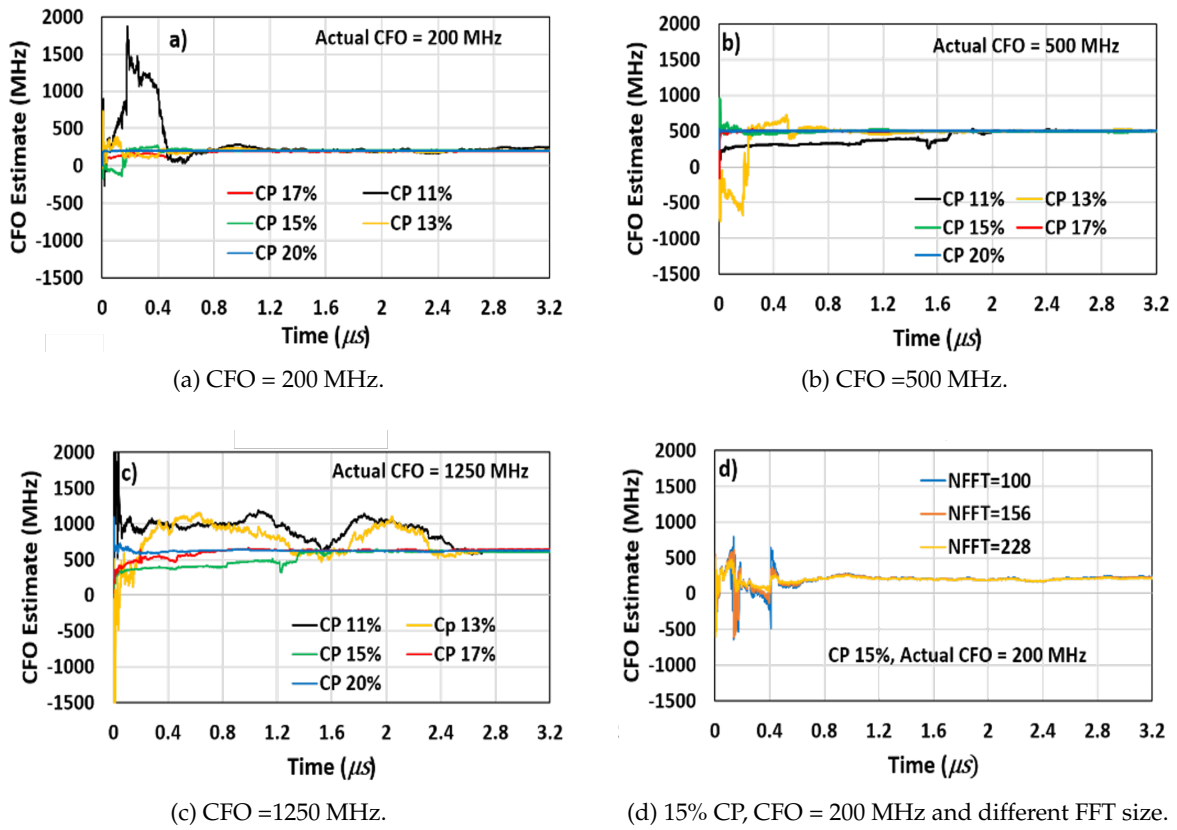


Figure 4.12: Simulated CFO estimate (MHz) vs. time (μs)

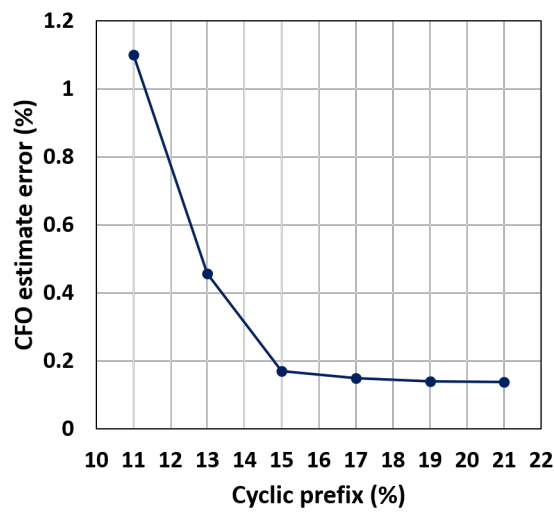


Figure 4.13: Estimate error (%) vs. Cyclic prefix (%).

electrical signals are sampled after $1.5 \mu s$ for CP set at 15%. Conversely, this means that for a sampling period of $1.5 \mu s$, the CP must be at least 15% of the OFDM symbol (without cyclic prefix).

Fig. 4.13 shows the effect of varying the CP length while retaining a sampling period of $1.5 \mu\text{s}$. The estimate error of the OEFOE remains less than 0.2% for cyclic prefix of 15% or more, while it increases rapidly if the CP is reduced below 15%. Thus, for the rest of our investigations, a 15% CP and a sampling period of $1.5 \mu\text{s}$ are chosen.

4.6 Simulated system performance

The OEFOE performance against system parameters such as the laser linewidth and OSNR is investigated further using VPItransmissionMaker software. The performance was found similar for both OEFOE versions while considering the linewidth and AWGN noise. This is intuitively obvious, as the fundamental estimation concept for both versions is the same *i.e.* based on finding the autocorrelation of the OFDM signal. Simulations were performed on OEFOE 2 design as shown in Fig. 4.14 for investigating the effects of laser linewidth and additive noise.

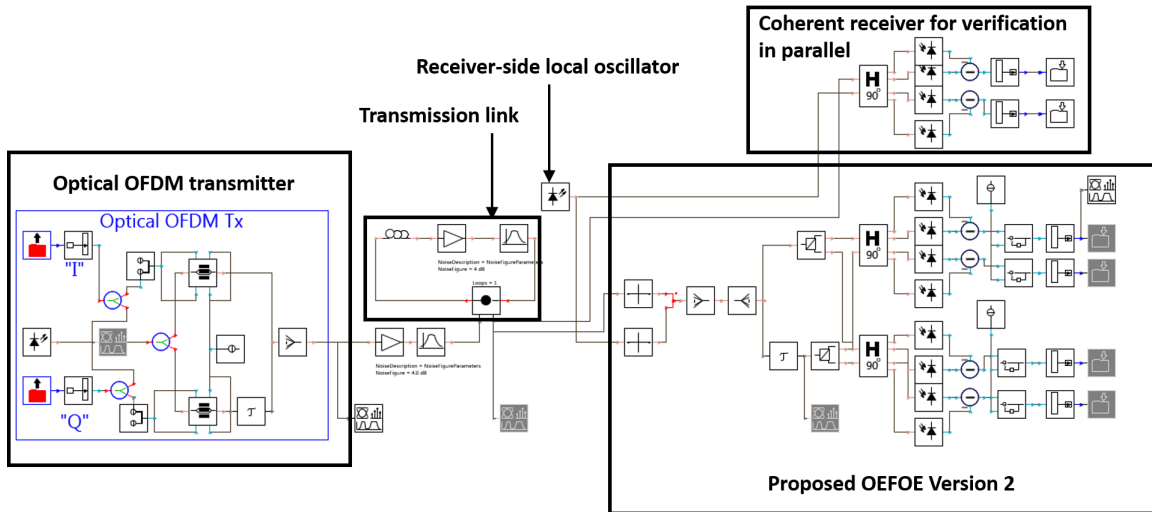


Figure 4.14: OEFOE simulation schematic in VPItransmissionMaker software.

4.6.1 Laser Linewidth

The linewidth of the lasers used in a system determine the variance of the phase noise for that system. Fig. 4.15 shows the OEFOE estimates for a CFO of 300 MHz at OSNR of 20 dB. Irrespective of the linewidths investigated (from 100 kHz to 60 MHz), the OEFOE estimated the CFO accurate to errors < 1 MHz. Thus, the proposed OEFOE system is robust to phase noise. This can be explained by the laser phase noise following a Wiener model [124]. Let $\phi(t)$ be the phase noise added to the signal at time t . Following the Wiener model [124],

$$\phi(t) = \phi(t-1) + \Delta\phi \quad (4.18)$$

where, $\phi(t) - \phi(t-1) = \Delta\phi_t$ is Gaussian distributed with zero mean and finite variance σ_t^2 .

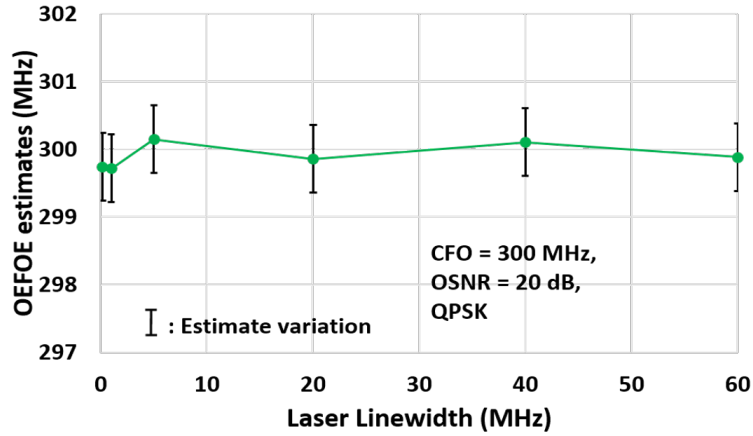


Figure 4.15: CFO estimate vs. laser linewidth (MHz) for CFO = 300 MHz.

Continuing further,

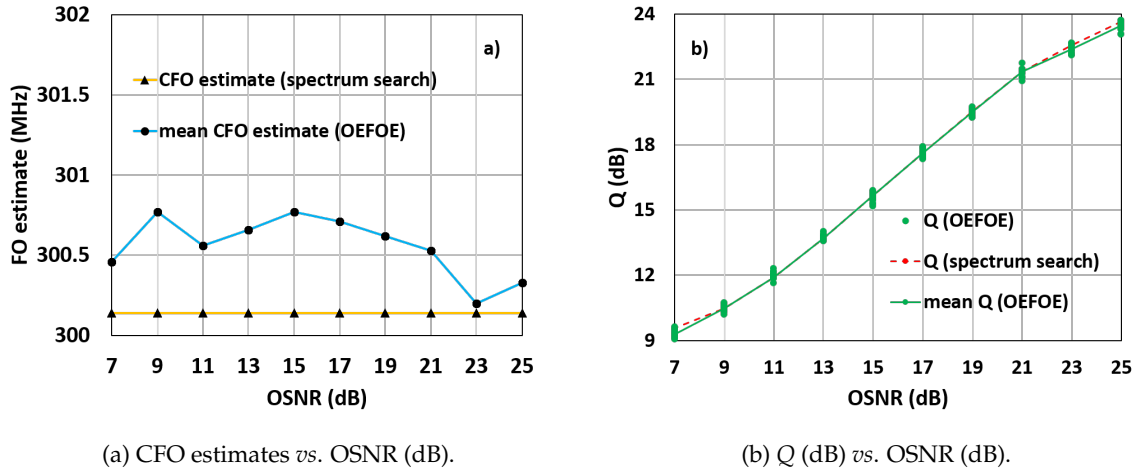
$$\phi(t-1) - \phi(t-2) = \Delta\phi_{t-1} \sim \mathcal{N}(0, \sigma_{t-1}^2) \quad (4.19)$$

$$\therefore \phi(t) - \phi(t-2) = \Delta\phi_{t-2} \sim \mathcal{N}(0, \sigma_{t-1}^2 + \sigma_t^2) \quad (4.20)$$

$$\therefore \phi(t) - \phi(t - T_{CP}) = \Delta\phi_{t-\tau_1} \sim \mathcal{N}(0, (\sigma_t^2 + \sigma_{t-1}^2 + \dots + \sigma_{t-\tau_1-1}^2)) \quad (4.21)$$

Hence, while calculating $R(\tau)$, the phases of $E_s(t)$ and $E_s(t + \tau_1)$ subtract and the integration process converges to the mean of $\Delta\phi_{t-\tau_1}$ that is zero, nulling the effect of phase noise on the CFO estimation.

4.6.2 AWGN loading



(a) CFO estimates vs. OSNR (dB).

(b) Q (dB) vs. OSNR (dB).

Figure 4.16: Effect of the AWGN noise for 28-Gbaud QPSK, FFT length=156, number of subcarriers = 100, 15% cyclic prefix and carrier frequency offset (CFO) = 300 MHz.

To test the robustness of the system to the channel noise, the OFDM signal with QPSK modulation is noise loaded with varying optical signal to noise ratio (OSNR). Fig. 4.16 compares the Q performance of the signal recovered using OEFOE with that of the signal recovered using the conventional spectral peak search method with OSNR sweep. The CFO is set to 300 MHz in the simulations. The phase mismatch

between the output arms of the 3-dB coupler and the delay variations in the optical delay line are varied randomly within the ranges $[-\pi, +\pi]$ and $[0, 30 \text{ ps}]$ respectively.

The mean CFO estimate plot from the OEFOE shows random variations independent of the OSNR. These variations are caused by the delay fluctuations in the optical delay line. Regardless, the mean estimates of the CFO from the OEFOE shows errors less than 1 MHz. The Q performance varies by a maximum of 0.8 dB around the mean Q at different OSNR. The plot of mean Q of signal recovered by OEFOE closely follows that of signal recovered by the spectral peak search method. Thus, it can be inferred that the system is robust to the noise added to the signal. This can be explained by the integration operation performed by the slow photodiodes which averages out the additive white Gaussian noise with zero mean.

4.7 Chromatic dispersion and nonlinear effects of the fiber

The OEFOE system is added in parallel to the coherent receiver setup. As a result, the input signal is perturbed with chromatic dispersion and nonlinearities when transmitted over a length of optical fiber. Additionally, the modulation format flexibility is also an important characteristic for the modern 400 Gbps optical networks handling signals with different modulation formats and needs to be examined.

4.7.1 Simulated transmission system: QPSK

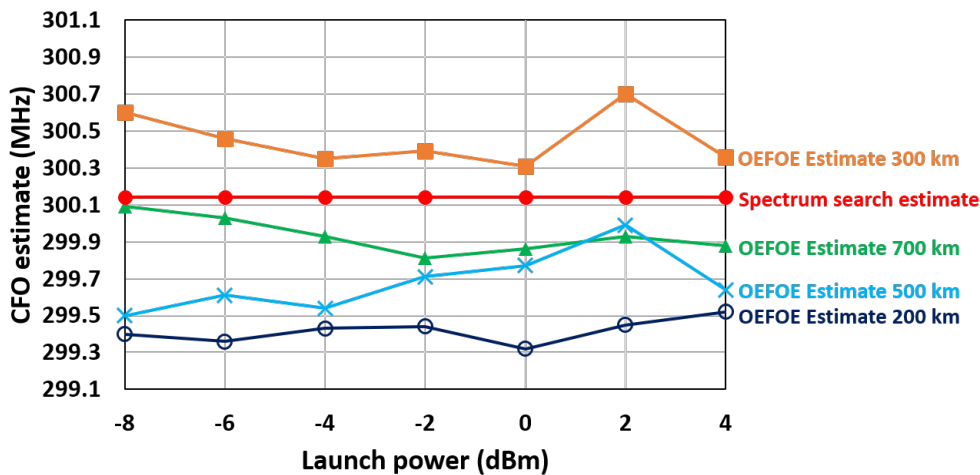


Figure 4.17: Simulated CFO estimates vs. launch power (dBm) for QPSK and carrier frequency offset (CFO) = 300 MHz.

To understand the effects of chromatic dispersion and nonlinearities of the optical fiber, the signal was simulated over transmission links of lengths from 200 km to 700 km. A recirculating loop was simulated to achieve these link lengths by varying the number of recirculations. Each loop consisted of one span of 100 km. Fig. 4.17 shows the mean OEFOE and spectral peak search estimates with varying launch powers for various transmission lengths with actual CFO fixed at 300 MHz. The plots show no

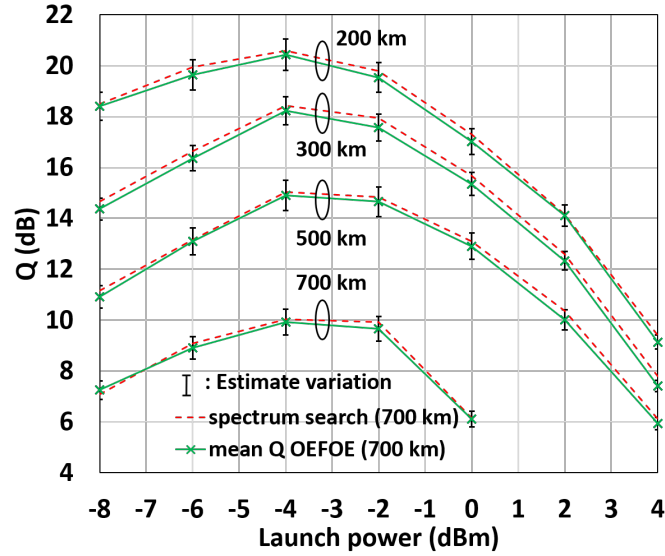


Figure 4.18: Simulated Q (dB) vs. Launch power (dBm) for 28-Gbaud QPSK signal with FFT length = 156, number of subcarriers = 100 and 15% cyclic prefix for link distances 200 km, 300 km, 500 km and 700 km.

particular dependence on transmission lengths or launch powers. The mean estimates show < 1 MHz errors compared with the spectral peak search.

Fig. 4.18 plots the Q of the signal recovered by the OEFOE compared with that of the signal recovered by the spectral peak search method with launch power sweeps and different transmission distances. The system using the proposed OEFOE gives a negligible penalty of mean 0.3 dB with 0.7-dB fluctuations due to delay variations in optical delay line and maximum penalty of 0.6 dB. These low penalties are independent of chromatic dispersion and the self-phase modulation (SPM) effect evident in the high launch power regime. Thus, the OEFOE maintains the performance despite of these impairments. The reason for robustness of OEFOE against the SPM is not completely clear. It may be possible that over the integrating period of the autocorrelation performed by the OEFOE, the SPM takes values over the range $[0 \ 2\pi]$ such that they get averaged out. However, this still needs investigation.

Since the CFO estimation by OEFOE is performed in parallel to the coherent reception, the system receives a signal that is not dispersion compensated. The fiber dispersion causes pulse spreading that leads to the inter-symbol interference (ISI). Since the interfering parts are uncorrelated, the autocorrelation removes their effects. Thus, the OEFOE is robust to the chromatic dispersion and fiber nonlinearities.

4.7.2 Simulated transmission system: 16-QAM

Higher-order QAM modulation formats have been tested for long-haul optical communication links to increase the throughput and meet the rapidly increasing needs for higher data rates. From Eq. (4.13), the autocorrelation $R(\tau)$ calculates the power of the modulating signal for the period $t = 0$ to T_{CP} . For higher-order QAMs, this power can be the same or higher than the QPSK modulating signal, depending

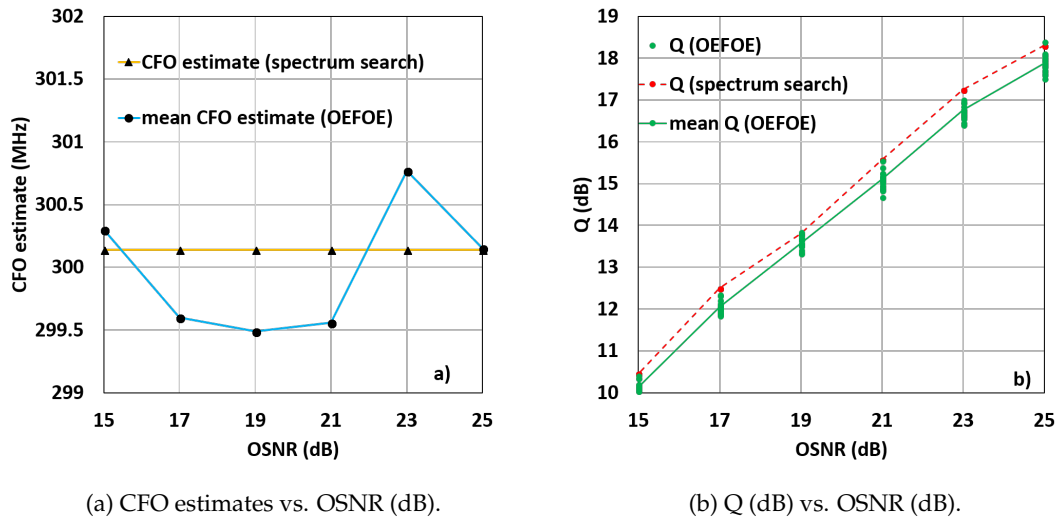


Figure 4.19: Effect of the AWGN noise for 28-Gbaud 16-QAM with FFT length = 156, number of subcarriers = 100, 15 % Cyclic prefix and carrier frequency offset (CFO) = 300 MHz.

on the data in the period. Thus, the autocorrelation $R(\tau)$ will not be weaker than that for QPSK, and may often be stronger. Moving to a higher QAM order format should not cause any degradation in the performance. This is verified in Fig. 4.19 where a 28-Gbaud, 16-QAM modulated OFDM signal was noise loaded and recovered using the OEFOE estimates. The system performance is compared with that of a system using the spectral peak search method. As expected, both the systems again perform similarly with marginal mean-Q degradation of 0.3 dB for the OEFOE-recovered signal. Like QPSK case, the Q value varied by maximum 0.7 dB.

The 16-QAM modulated signal transmission over fiber links was simulated for different lengths from 200 km to 700 km and again the Q performance of both the systems are found to be similar to each other as can be observed in Fig. 4.20. The robustness of the system can be intuitively extended to

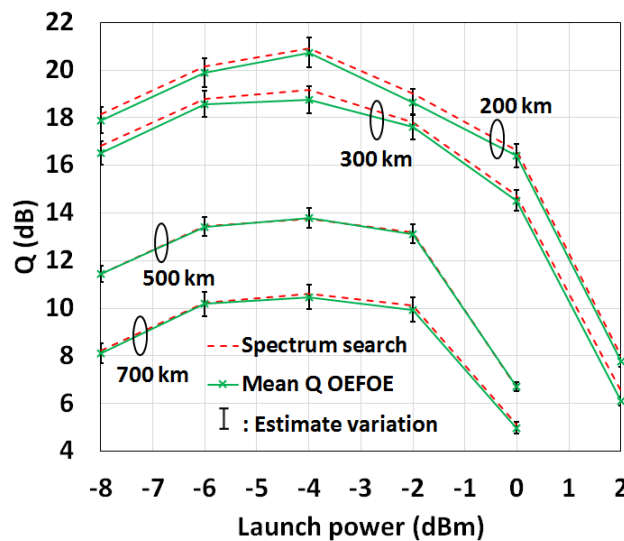


Figure 4.20: Simulated Q (dB) vs. Launch power (dBm) for 28-Gbaud 16-QAM signal with FFT length = 156, number of subcarriers = 100 and 15% cyclic prefix for link distances 200 km, 300 km, 500 km and 700 km.

mitigating cross-phase modulation (XPM) for a multichannel WDM system; however, this again remains to be investigated. Thus, the proposed designs are robust to the modulation format, laser phase noise, the additive noise, chromatic dispersion and the fiber nonlinearities on transmission, with the system implementing OEFOE giving Q performance similar to a system using spectral peak search method in DSP. However, [110] showed that the required cyclic prefix (CP) length increases with the order of the M-QAM format for accurate CFO estimation using the digital autocorrelation. It can thus be concluded that despite of similar performance, the OEFOE will require longer CP for higher-order M-QAM.

For practical implementation in deployed optical networks, the OEFOE system requires fabrication as an integrated package along with the coherent receivers. Considering this, OEFOE 1 proves to be a better option in practical scenarios as it has a simple design and does not rely on the polarization diversity. On the other hand, OEFOE 2 can be used for proof of concept demonstrations and to test any modifications or extension work. Additionally, both the systems rely on the time domain characteristic of the OFDM signals; the cyclic prefix addition can be emulated in a single carrier system as well by adding known training symbols on regular intervals (τ_1). As a result, with modification to the transmitted signal, the system can be extended to single-carrier and Nyquist-WDM systems. This can be taken as future work.

The OEFOE designs have the same topology as a dual-polarization (DP) coherent receivers, which are expensive. This may seem demotivating; but the OEFOE uses slow photodiodes and low-speed ADCs with bandwidths in range of MHz (instead of GHz bandwidth components in DP coherent receiver system). As a result, the manufacturing cost can be expected to be lower than that of the DP coherent receivers and could be further reduced if integration is used. The proposed system can be considered as a step towards achieving a DSP-free, analog-processing system that is a matter of interest for many researchers recently to reduce the power consumption by the high-speed processors. For example, an all-analog chip performing a constant modulus based adaptive equalization was proposed recently [125]. Combined with the OEFOE carrier recovery, the analog chip can achieve a power-efficient all-analog signal-processing solution that can target DSP-free coherent optical data-center interconnects (DCI) market.

The OEFOE with a feedback to the laser for frequency control was not performed in this work. Thus, the OEFOE connected with a laser and aided with required electronics to refresh the slow photodiodes after every estimation can be made in to a commercial product. However, before commercialization, it would be interesting to analyze the proposed OEFOE design fabricated on a photonic chip, to understand the cost parameter. Moreover, the feedback design needs to be analyzed as well for potential complications that could arise due to feedback delays and rapid frequency drifts.

4.7.3 Conclusions

The proposed optoelectronic frequency offset estimator gives a wide estimation range and completely removes the latency part of the CFO estimation algorithms for CO-OFDM systems. It uses off-the-shelf components and none of them need to be high speed/ high bandwidth components. The OEFOE uses the cyclic prefix properties of the OFDM systems to estimate the CFO. However, it can be extended to any other system, provided some training symbols are added repetitively on regular intervals (equivalent to τ_1). As a result, the signal will have training symbols instead of cyclic prefix and the number of symbols received and extracted still remains the same as the OFDM system. Unfortunately, the signal no longer contains orthogonal subcarriers and the system loses in spectral efficiency. The spectral efficiency can be maintained using Nyquist-WDM system and with training symbols added to it, the proposed OEFOE can be used. Essentially, the proposed OEFOE can be used in OFDM systems, Nyquist-WDM system provided training symbols are added and any other system at the cost of losing spectral efficiency. To add the training symbols repetitively is still an issue for implementation in deployed networks as it may not align with the approved standards.

One of the reasons for industries to move from coherent optical systems to direct-detection (DD) is the latency as the DD systems do not face CFO issues and do not need CFO estimation algorithms. Thus, OEFOE again gives an edge to the coherent optical communication systems as it brings down the latency to the levels of DD systems. The cost issue for coherent receivers over the DD systems still persist but the OEFOE does not significantly add to the cost of the coherent system as it consists of low-cost components.

The OEFOE works well for frequency offsets experienced by commercial lasers, but it cannot compensate for timing offsets (TO) in OFDM systems. Bolcksei showed that the autocorrelation of OFDM signal can be used to estimate the timing offset too [110]. As the OEFOE works on a similar autocorrelation technique, it may be extended to estimate the TO along with CFO. Moreover, the OEFOE does not compensate for the phase-noise aspect of the carrier recovery. An obvious extension is to explore a technique that aims at CFO and PN compensation, still performing in analog domain to prevent increasing the DSP latency. This is achieved using optical injection locking which is investigated and enhanced in the next chapter.

All-optical processing approach for carrier recovery

In this chapter, optical injection locking (OIL) for carrier recovery is explored. Two applications are investigated that either perform carrier recovery or aid it. They are-

1. The injection lock is highly sensitive to the polarizations-state of the injected signal. A sub-system that makes the OIL polarization-independent is discussed and experimentally verified.
2. The inter-channel nonlinear phase noise, dominated by cross-phase modulation is compensated for using optical injection locking. This is further enhanced by self-phase modulation cancellation using digital back-propagation.

Publications based on this chapter-

1. J. Jokhakar, B. Corcoran and A. J. Lowery, "Polarization-independent optical injection locking," in *Optical Fiber Communication Conference*, Los Angeles, USA (2017), paper Th4I.4.
2. J. Jokhakar, B. Corcoran and A. J. Lowery, "Polarization independent optical injection locking for carrier recovery in optical communication systems," *Opt. Express* 25, 21216-21228 (2017).
3. J. Jokhakar, A. J. Lowery and B. Corcoran, "Inter-channel nonlinear phase noise compensation using optical injection locking," *Opt. Express* 26, 5733-5746 (2018).
4. J. Jokhakar, B. Corcoran and A. J. Lowery, "Nonlinearity compensation using optical injection locking aided by digital back-propagation," under preparation.

5.1 Polarization-independence for optical injection locking.

5.1.1 Introduction

Optical injection locking (OIL), forces a 'slave' laser to follow the phase trend of a 'master' injected signal, and has found many applications over the past decade. These applications include: all-optical regeneration of signals [126], increasing the linear gain regime of laser [127], bandwidth enhancement of lasers [128], laser linewidth (LW) reduction [15], phase-locked mode generation for a mode-locked laser [129], optical phase-locked loops [115, 116] and carrier-recovery in coherent optical systems [14, 130–132].

In coherent optical communication systems, optical carrier recovery mitigates perturbations in the phase-encoded data, caused by the phase noise of the lasers and finite carrier-frequency offsets (CFO) between the transmitter's laser, and the receiver's local oscillator (LO). Demonstrated analog carrier-recovery methods include optical and electro optical phase locked loops (PLLs) [115]. Optical PLLs track the phase of the incoming signals and provide appropriate feedback to the remove the phase offsets [115]. Although PLLs can track both phase offsets and CFO, sub-system complexity has restricted practical implementations in communication systems. Electro-optic phase locked loops have also been proposed [116]. These systems are still relatively complex to implement, and are restricted to CFOs of 100's of MHz and phase noise bandwidths on the order of 1 MHz, by the latency of the electrical components in the feedback. In the digital domain, different signal processing techniques have been used to compensate for CFO and phase noise (e.g. [8, 92, 97, 133]). The consistent problem faced by analog and digital methods is the amount of phase noise and CFO that can be compensated for, which is either restricted by the device-bandwidths and setup-complexity in analog devices or computational complexity in DSP algorithms. These methods are useful in the best-case scenarios to linewidths on the order of 1 MHz and frequency offsets on the order of 1 GHz. In contrast, optical injection locking has been shown to achieve carrier recovery for an offset of tens of GHz [14, 130–132], without introducing latency in signal recovery in addition to providing 90% phase transfer with optical signal to noise ratios (OSNR) down to 0 dB [133]. Injection locking the receiver-side LO laser by using a residual carrier wave from the incoming signal transfers the phase noise of the signal carrier onto the LO, which enables all-optical recovery of the carrier from coherent reception [14, 130, 131].

5.1.2 Injection locking and Optical injection locking

Injection locking is an effect that affects the frequencies of signals that are coupled with each other. If multiple signals at slightly different frequencies are present in a system, but the system does not let them couple, these signals will remain independent and remain at their own frequencies. However, in case the system allows them to couple with each other, all of them will synchronize with each other and attain a

common frequency [134] [135]. This common frequency may or may not align with one of the signal's frequency.

A common example is syncing of two pendulums as observed by Christian Huygens, the inventor of pendulum clocks [136]. If two pendulums are made to oscillate on a same beam, the pendulums interact with each other. As a result, even though both may be made to oscillate on different times and from different location in space, eventually both pendulums will sync up and oscillate together as described in Fig. 5.1.

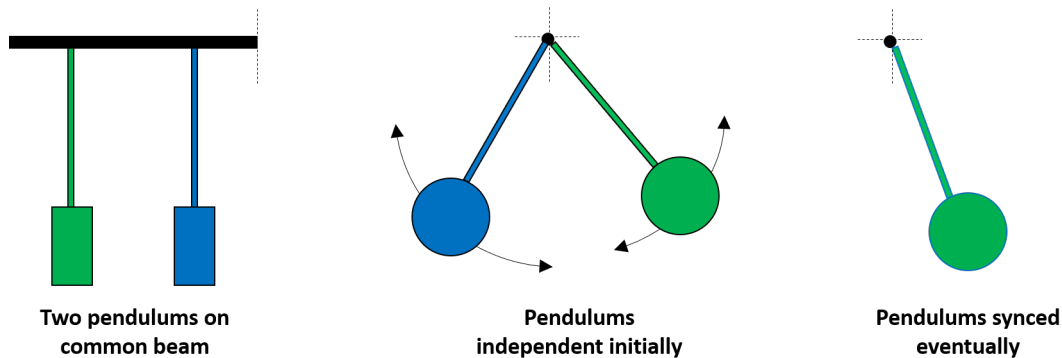


Figure 5.1: Syncing of pendulums on a common beam.

Similar concept is extended to radio-frequency signals [135] and optical lasers [137]. In a scenario of a two signals, one weak and one stronger, close to each other in frequency in a confined system that allows for their coupling will result in the stronger signal to acquire the weaker signal. In other words, the weaker signal will imitate the stronger signal in phase and frequency. This locking of weaker signal injected onto a local stronger signal is called injection locking [135] [134] [137].

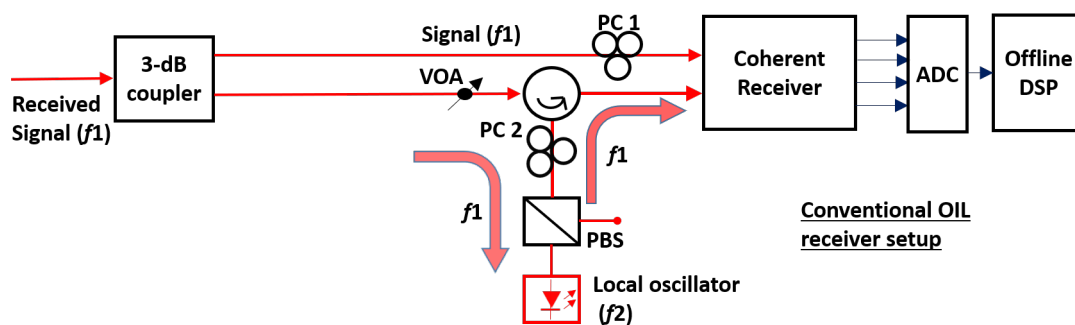


Figure 5.2: Conventional OIL setup. VOA: variable optical attenuator; PC: polarization controller; PBS: polarization beam splitter; ADC: analog-to-digital converter.

A homodyne setup as shown in Fig. 5.2 is used where the received signal is split using a 3-dB coupler with the signal in one arm fed directly to the coherent receiver and the signal in the other arm injected in the cavity of a local oscillator (LO) laser. If the free-running frequency of the LO laser (f_2) and the frequency of the injected signal (f_1) are within the locking range, defined by the power of the injected signal and laser characteristics, the LO signal locks on to the frequency of the injected signal because of

optical injection locking. This essentially removes the effects of phase noise and the CFO [14, 130–132].

The phase locking capabilities can be explained using the laser's optical field rate equation [137]-

$$\frac{dE}{dt} = \frac{1}{2}g\Delta NE(t) + kA_{inj} - j\Delta\omega\Delta t \quad (5.1)$$

where E is the electric field of the slave laser continuous wave signal. g is the linear gain coefficient, ΔN is the difference in the carrier number with the threshold, A_0 is the initial phasor magnitude and A_{inj} is the magnitude of injected signal. $\Delta\omega$ is the frequency difference between the injected and slave laser signals contributed by the CFO ($\Delta\omega_1$), PN ($\Delta\omega_2$) and the phase shifts due to changing carrier density in the laser cavity due to the injection ($\Delta\omega_3$). Hence, $\Delta\omega = \Delta\omega_1 + \Delta\omega_2 + \Delta\omega_3$. $\Delta\omega_3$ is caused by the change in refractive index in the cavity (Δn) dependent on the carrier density variations (Δn) [137]. It is derived as-

$$\Delta\omega_3 = \alpha \frac{Kv_g(dg/dn)}{2} \Delta n$$

where α is the ratio of variations in the real part of the complex refractive index to the variations in its imaginary part. K is the proportionality constant dependent on type of laser, v_g is the group velocity of the slave laser signal and dg/dn determines the variations in the imaginary part of the complex refractive index with the complex refractive index [137].

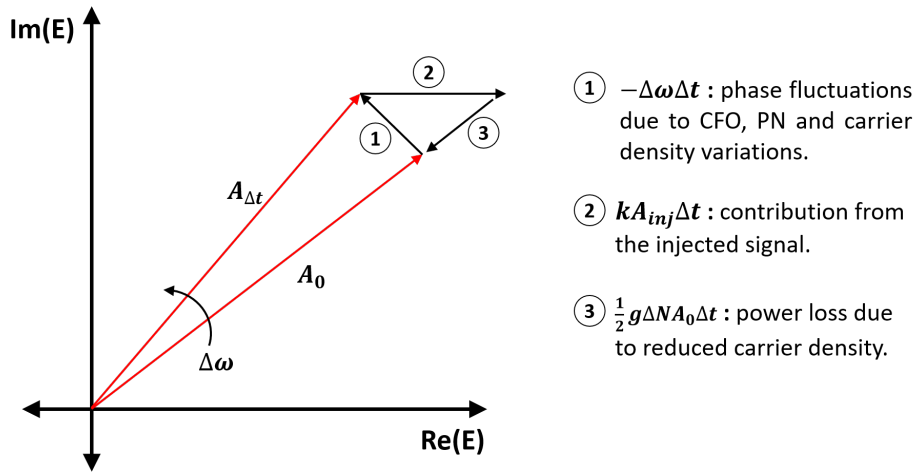


Figure 5.3: Phase model for optical injection locking based on laser rate equations.

Due to $\Delta\omega$ in the third term of Eq. (5.1), the phasor of the slave laser signal experiences a continuous phase rotation as shown in Fig. 5.3. This rotation's angular velocity depends on $\Delta\omega$ and causes the shift shown by vector 1 in Fig. 5.3. The injected power adds to the real part of the slave laser's electric field, proportional to A_{inj} reflected in the second term of Eq. (5.1). This is shown in Fig. 5.3 as vector 2. The power in the cavity increases due to the injected signal, that consumes more number of carriers in the

slave laser cavity. As a result, the carriers in the cavity reduces and the magnitude of the output signal reduce. This is represented by the vector 3 in Fig. 5.3. Under locked condition, vectors 1,2 and 3 work together to bring the slave laser signal back to original position. In other words, the vectors cancel the effect of $\Delta\omega$ and the signal undergoes no phase rotation. This leads to a locked frequency and phase condition where the output phase of the slave laser is locked to that of the injected signal [137].

5.1.3 Problem statement and proposed solution

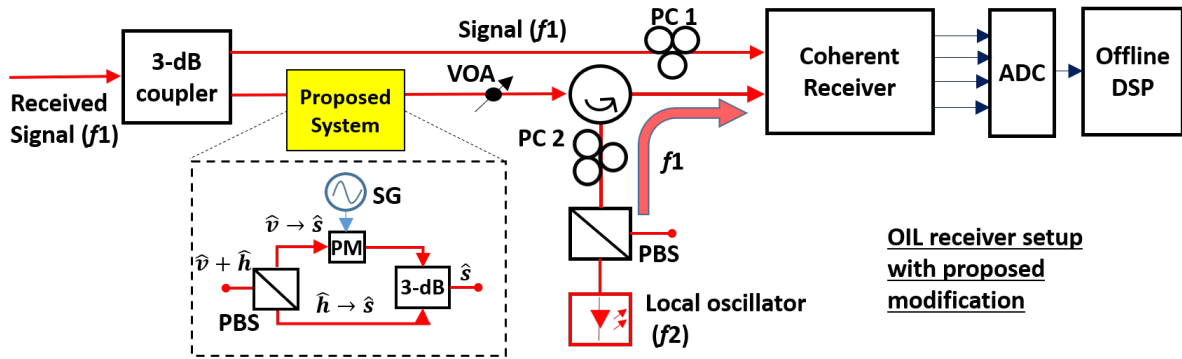


Figure 5.4: OIL setup with proposed modifications. OIL setup with the proposed modifications. SG: signal generator; PM: phase modulator.

To achieve the locked state of the OIL, the incoming signal is injected into the cavity of the slave local oscillator laser. This cavity is, however, aligned to a single state of polarization (SOP). As a result, proper locking can be achieved only if the incoming signal's state of polarization is aligned with that of the LO laser cavity and stabilized over the period of operation. In previously demonstrated OIL systems, this is achieved by alignment using the polarization controller PC2 and PBS in Fig. 5.2. Although this method works perfectly in a confined lab environment, links in underground ducts are prone to vibrations and pressure variations due to surrounding vehicular motions, human activities and general environmental variations, causing the SOP of the received signal to randomly change over time. As a result, the alignment between the LO lasing polarization and the incoming carrier will drift and may result in loss of locking for sustained polarization fades.

To prevent this loss of lock, the system needs to be constantly monitored and needs to be aligned whenever the SOP of the incoming signal changes, which requires a complex system of polarization monitoring, polarization-state control and a stable feedback loop. As an alternative, a polarization-locking module is proposed in this subsection. This module, when plugged in the OIL setup as shown in Fig. 5.4, renders the OIL independent of the incoming signal's SOP. It is demonstrated that the proposed system based on an interference mechanism maintains injection lock for any random state of polarization of the injected signal.

Experimental demonstrations in back-to-back setup and over a 20-km field trial show that the system

implementing the proposed module with the injected power as low as -25 dBm performed without a Q penalty. Experiments performed with a low output power (0.5-dBm), broad LW (40 MHz) laser at the transmitter experiences failure in the data recovery in the intradyne system, but can be successfully achieved when using the optical injection locking. In all the cases, the proposed polarization-locking module is verified to work without Q penalties compared with an injection-locked system without the module. While the system without the module repetitively lost the lock when tested over the field trial and needed timely realignment of the polarization controllers, the system with the proposed module maintained the lock all the time.

5.1.4 Proposed module design

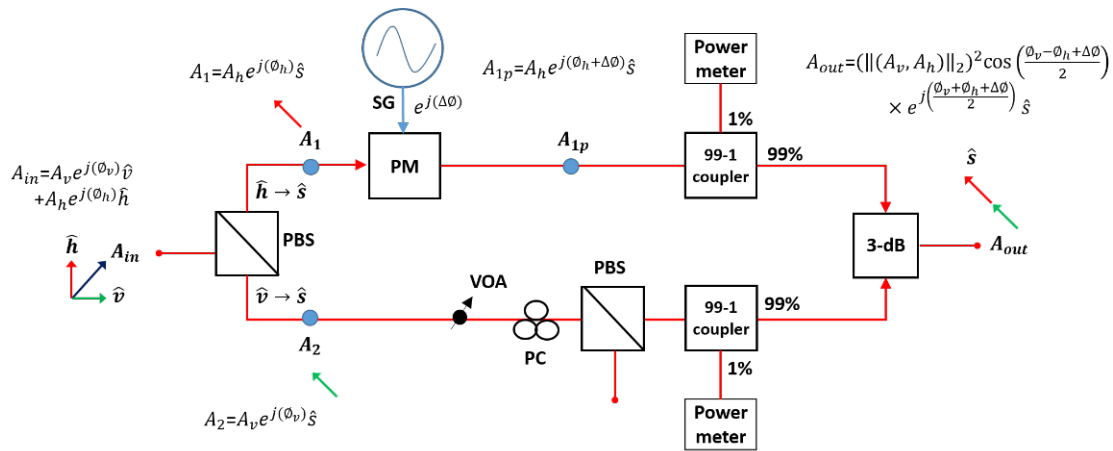


Figure 5.5: Proposed polarization-locking module design with working concept.

Consider a received signal, A_{in} in the form such that it is resolved in two components, each representing projections on orthogonal polarization states \hat{h} and \hat{v} . The signal is fed to the proposed module in Fig. 5.5.

$$A_{in} = A_v e^{j\phi_v} \hat{v} + A_h e^{j\phi_h} \hat{h} \quad (5.2)$$

The PBS in the module separates these components on to the slow axis (\hat{s}) of its two output arms. Hence both the polarization components are aligned on the slow axis,

$$A_1 = A_v e^{j\phi_v} \hat{s} \text{ and } A_2 = A_h e^{j\phi_h} \hat{s} \quad (5.3)$$

By combining A_1 (red) and A_2 (green) using a polarization-maintaining 3-dB coupler, we can convert the incoming signal's random SOP into a constant known state (\hat{s}) that can be aligned to the SOP of the LO laser using PC2. As a result, despite of the incoming signal having a random SOP, the output of the proposed module will be permanently aligned on a known state of polarization. The design in Fig. 5.5 describes the experimental setup of the proposed module.

The described concept of the polarization-locking module works perfectly except for the particular case of SOP when the signals on the \hat{h} and \hat{v} polarization axes are 180° out of phase i.e. $\phi_h - \phi_v = 180^\circ$. In such a case, interference through the 3-dB coupler will cause destructive interference, resulting in lower injected power, which can result in the LO unlocking from the signal carrier if this power fade lasts long enough. To prevent long power fades, a phase modulator was added in one arm of the proposed module as shown in Fig. 5.5. The phase modulator modulates the incoming optical signal with a low-frequency (400 kHz) sinusoidal signal generated by a signal generator (SG). The frequency of phase modulation is chosen to be higher than the speed of polarization rotations in practical systems, which can be on the order of kHz [8]. The signal in the upper arm loses power due to the phase modulator, which needs to be compensated in the other arm by a VOA and power meters, to ensure equal power signals at the input of the 3-dB coupler. As the VOA is not polarization maintaining, and the input of the 3-dB coupler needs to be aligned to a fixed polarization, additional PBS and polarization controller are used as shown in Fig. 5.5. The output signal of the phase modulator is-

$$A_{1p} = A_h e^{j(\phi_h + \Delta\phi)} \hat{s} \quad (5.4)$$

where $\Delta\phi$ is the 400-kHz sinusoidal phase modulation. An optical attenuator is used to equalize the losses in both the arms. When A_2 and A_{1p} are combined in a polarization-maintaining 3-dB coupler, we get-

$$A_{out} = \left(\|(A_h, A_v)\|_2 \right)^2 \cos\left(\frac{\phi_h - \phi_v + \Delta\phi}{2}\right) e^{j\left(\frac{\phi_h + \phi_v + \Delta\phi}{2}\right)} \hat{s} \quad (5.5)$$

Owing to the cosine term changing with $\Delta\phi$, the power out of the 3-dB coupler continuously fluctuates at 400 kHz. These low-frequency intensity fluctuations would be detrimental if passed through to the LO. In order to suppress these intensity fluctuations, the innate phase and amplitude transfer characteristics of OIL systems at low injection ratios (< -30 -dB) is exploited. Under locked conditions and within the locking range, the OIL system transfers phase modulation, replicating phase information. At the same time, the amplitude modulation can be highly suppressed [138, 139]. Consequently, the amplitude fluctuations at the output of the 3-dB coupler caused due to the low frequency (400 kHz) phase modulation ($\Delta\phi$) on one arm of the module will be suppressed, whereas the required carrier phase information will pass through. The phase modulation, $\Delta\phi$ also show up in the phase of the output which will get transferred through the OIL setup, but can be tackled, due to their low frequencies, by the phase estimation algorithms running in the DSP. Thus, the fixed SOP can be maintained at the output of the module without losing injection locking.

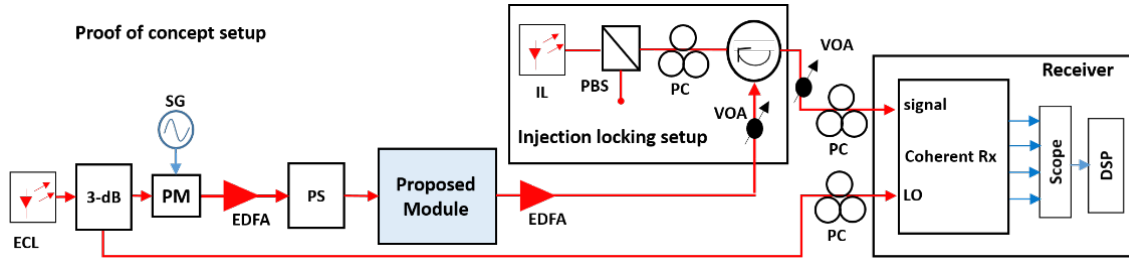
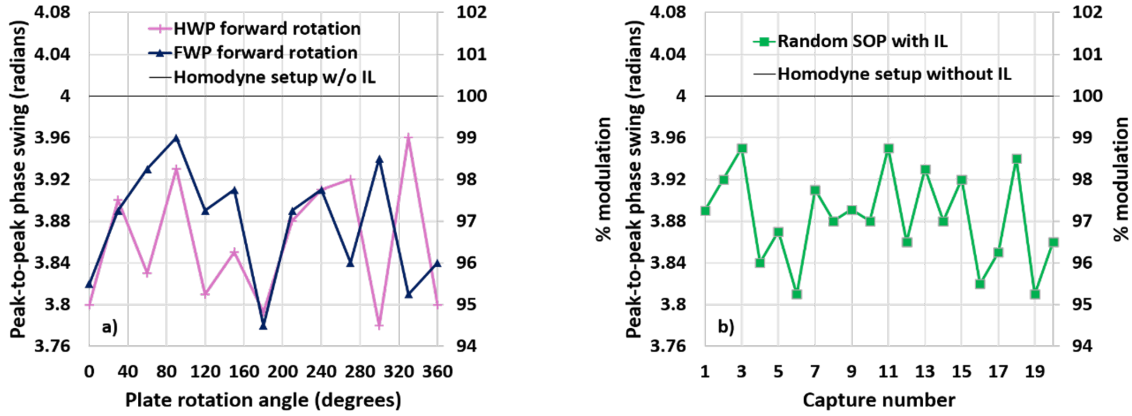


Figure 5.6: Experimental setup for proof of concept. ECL: external cavity laser; PS: polarization scrambler; IL: Injection laser; LO: local oscillator laser; Rx: Receiver.



(a) half wave plate and full wave plate rotations.

(b) 20 data captures with a random SOP.

Figure 5.7: Peak-to-peak phase swing of the recovered signal and % modulation transfer through OIL setup. SOP: state of polarization.

5.1.5 Experimental proof of concept

As a proof of concept, the transfer of a 100-MHz sinusoidal phase modulation through injection locking was observed. Here, a signal generator was used to modulate a CW laser output with an external phase modulator, as shown in Fig. 5.6. Note that this 100-MHz phase modulation is at the transmitter and not in the proposed module (there is not data transmitted yet). The polarization of the modulated optical signal was scrambled using a Novoptel EPX1000 polarization scrambler (PS) that allows controlled or random scrambling of the polarization state of the input signal. This scrambling ensured that the proposed module does not cause any suppression of the modulation or unlocking as the polarization state changes. The signal was then passed to the OIL setup through the proposed polarization-locking module with an injection ratio of -45 dB (-25 dBm at the input to the slave laser, with a 20-dBm output).

The signal was detected by a U^2T 25-GHz electrical bandwidth integrated coherent receiver and processed in DSP to recover the peak-to-peak phase swing of the signal. This peak-to-peak phase swing of the recovered signal was measured in reference to that of the signal detected in a simple homodyne setup without OIL. The polarization state of the incoming signal was varied firstly by changing the rotation angle of a half-wave plate (HWP) in the PS, then by the full-wave plate (FWP) (Fig. 5.7a), and then both of them simultaneously to cover random points on the Poincare sphere (Fig. 5.7b). Fig. 5.7a

and Fig. 5.7b show that on average, 97% of the input phase swing is transferred (see secondary y-axis) through the OIL setup independent of the polarization of the incoming signal. The variation of the phase transfer is very marginal i.e. 2% about the average. This indicates that the OIL system with the proposed module maintains the lock while transferring phase modulation regardless of the incoming state of polarization.

It is imperative that inclusion of the proposed module in the OIL should not reduce the locking bandwidth, as it may cause loss of lock in the case of low power signals. Thus, the locking bandwidth of the OIL system is investigated next, with and without the proposed module. The experimental setup is the same as in Fig. 5.6. The continuous wave ECL output is phase-modulated with a sinusoidal electrical signal whose frequency is swept from 10 MHz to 10 GHz. As the phase modulation is transferred by the OIL within the locking bandwidth, the phase swing of the output of the OIL can help in calculating the locking bandwidth. Fig. 5.8 shows the peak-to-peak swing of the received signal's sinusoidal modulated phase at the output of the OIL setup with and without the polarization-locking module. It is observed that the locking bandwidth does not change with the inclusion of the module. As the module merely changes the polarization alignment, the injection ratio remains the same in both cases and leaves the locking bandwidth unaffected.

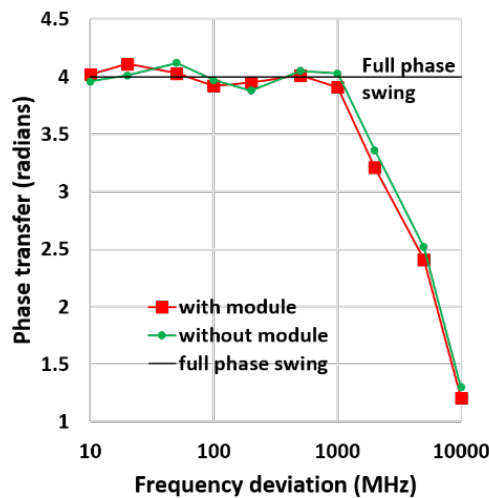


Figure 5.8: Phase transfer (radians) vs. frequency deviation (MHz).

5.1.6 Back-to-back test with injection locked self-homodyne receiver

The previous subsection proved that the proposed module allows for phase information to be transferred regardless of the incoming signal's SOP. The performance of this sub-system in a back-to-back setup is tested where injection locking is used to recover the residual carrier from a coherent OFDM signal. The experimental setup consists of a transmitter that modulates a continuous wave (CW) laser output using a complex Mach-Zehnder modulator (CMZM) driven by electrical signals from an arbitrary waveform

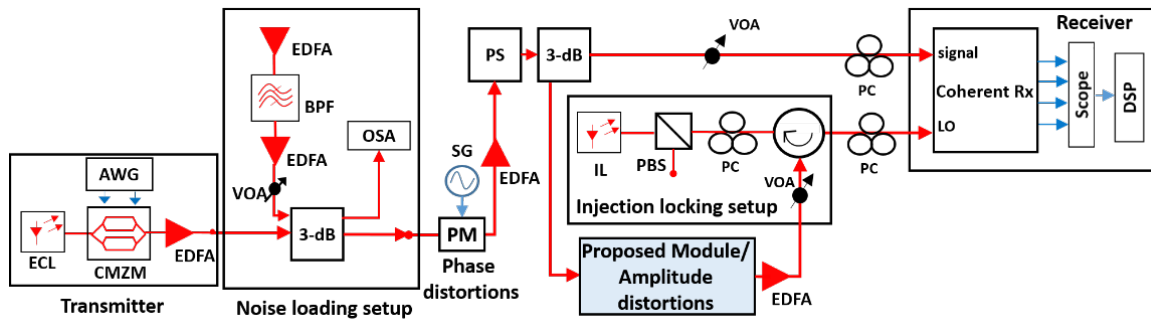


Figure 5.9: Experimental setup with proposed module and injection locking setup. CMZM: complex Mach-Zehnder modulator; EDFA: erbium doped fiber amplifier; BPF: bandpass filter; OSA: optical spectrum analyzer; DSP: digital signal processing.

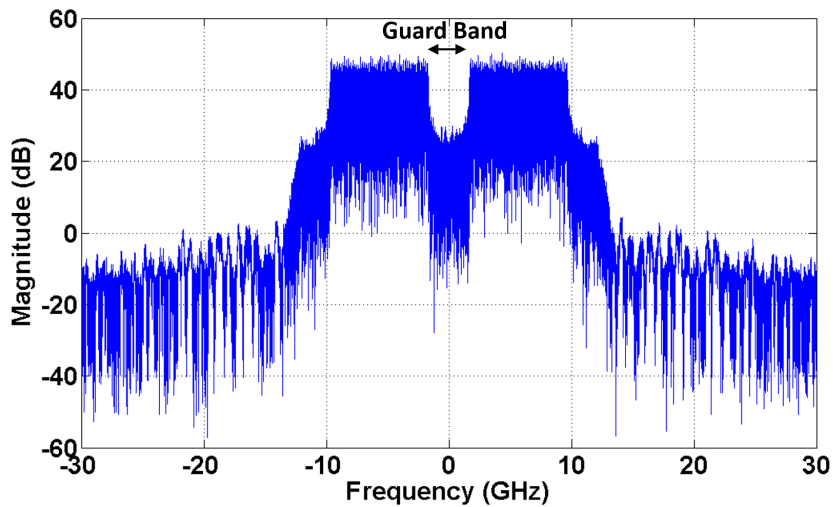
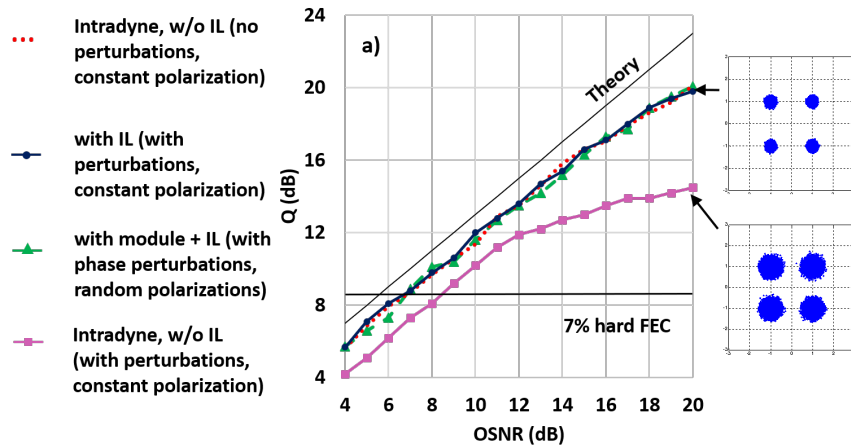
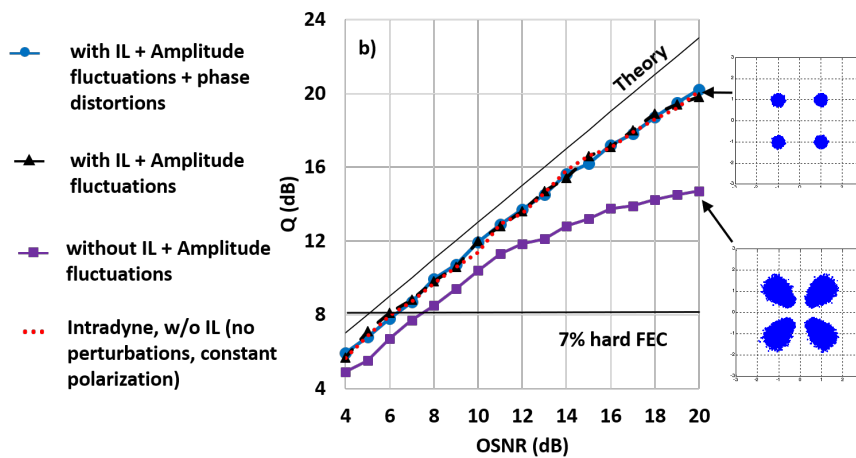


Figure 5.10: Spectrum of the generated signal with guard band.

generator as shown in Fig. 5.9. A 25-Gbaud QPSK modulated OFDM electrical signal with 100 subcarriers and 156-point FFT length was generated using a Keysight 92 GSa/s arbitrary waveform generator to drive an optical IQ modulator. A central guard band of 2.5 GHz (10 sub-carriers) was added to keep a spectral gap around the optical carrier, preventing transfer of the modulated signal through OIL (Fig. 5.10). The amplified signal from the transmitter was noise-loaded using filtered amplified spontaneous emission (ASE) noise from an EDFA covering a 200-GHz bandwidth, which was added to the signal to vary the received OSNR. The signal was artificially distorted in phase using a phase modulator. For the later part of the experiment, when a broad LW laser at the transmitter is used, the phase modulator was removed. After adding phase distortions, the polarization of the signal was scrambled using the Novoptel polarization scrambler (PS). The scrambled signal was then split using a 3-dB coupler, where one arm was connected to the proposed module followed by an OIL setup and the other arm was directly connected to the signal input of a u^2T 25-GHz electrical bandwidth integrated coherent receiver. The outputs of the coherent receiver were connected to a Keysight 40-GSa/s 28-GHz bandwidth digital signal oscilloscope (DSO). The data recovery algorithms such as the channel equalization and the residual phase recovery were run as offline DSP. To ensure that the proposed module does not cause a loss of



(a) with or without (w/o) injection locking (IL) in presence of phase distortions; Insets: Constellations of recovered signals at 22-dB OSNR with and without phase distortions.



(b) with or without (w/o) injection locking (IL) in presence of phase and amplitude distortions.

Figure 5.11: Q performance vs. OSNR (dB). Insets: Constellations of recovered signals at 22-dB OSNR with and without amplitude distortions.

performance in the system, the Q of the recovered signal was measured and plotted with OSNR sweep as shown in Fig. 5.11b. Fig. 5.11b shows that the phase distortions applied to the systems cause 5-dB degradation in Q and 1.5-dB penalty in required OSNR at 7% hard-decision FEC limit ('error free' BER = 3.8×10^{-3}) for intradyne systems compared with the injection locked system.

The phase distortions in OFDM systems cause inter-carrier interference (ICI) along with a common phase error (CPE) [140]. The phase error correction algorithms running in the DSP take care of the CPE due to the added phase distortions but cannot completely negate the effects of ICI due to the phase distortions. Hence, due to ICI and AWGN, the constellations of the recovered signals show a Gaussian spread of the constellation points, rather than a phase skew as seen in the inset of Fig. 5.11b. With the OIL, the system with phase distortions and constant signal polarization gave similar performance to that of the system without distortions, confirming that the OIL can cancel phase distortions at the receiver. This is reflected in the inset in Fig. 5.11b, where the Gaussian spread of the constellation points is reduced.

With the polarization scrambler activated, the OIL setup is injected with a signal with a random state of polarization. In order to achieve locking, the proposed module is included in the setup at this stage. However, with the polarization-locking module plugged in, the system performs similar to an intradyne system without phase distortions, with a negligible required OSNR penalty. This indicates that the phase distortions are canceled sufficiently to be useful for coherent communications systems, even for a random state of polarization of the incoming signal. Although the performances are similar, the OIL system still benefits in DSP computation as the CFO estimation and compensation algorithms are omitted for OIL.

As discussed before, the polarization-locking module may generate amplitude distortions in the signal, due to the interference in the 3-dB coupler in the module, which in turn may result in a loss of injected power and thus, the injection lock. Theoretically, these low frequency amplitude distortions are rejected by the OIL [138,139]. To systematically test this, additional amplitude distortions are added into the system to verify the AM suppression capabilities of our OIL set-up. The amplitude distortions are added replacing the proposed module with an intensity modulator driven with a 400-kHz sinusoid.

Fig. 5.11a shows that without the locking, Q drops by 5 dB at 20-dB OSNR and the required OSNR at FEC increases by 1.5 dB at hard-FEC limit. When using an injection-locked LO, the system performs similar to the reference intradyne system. This is because of the inherent rejection of low-frequency amplitude fluctuations through the OIL process. Now, with the phase fluctuations turned on and the polarization scrambler also activated, the system again performs similarly to the reference intradyne system without a loss of Q . This confirms the rejection of amplitude fluctuations, the cancellation of phase fluctuations and independence on incoming signal polarization.

5.1.7 Broad-linewidth laser experiments

The optical injection locking, being able to replicate the carrier phase information up to several GHz, should allow the use of high LW lasers in coherent communication systems. Relaxing the limits on required LW for coherent systems may enable the production of cheaper coherent transceivers, by allowing a wider range of laser fabrication tolerances, and operation at lower optical powers. The performance in a back-to-back system using a broad LW (40 MHz) low-power (0.5 dBm) laser at the transmitter was then tested. The phase modulation module was removed from the setup in Fig. 5.9, as the use of a high LW laser at the transmitter provides significant phase fluctuations. A 25-Gbaud OFDM signal was again generated with the same OFDM parameters as in previous experiment. The polarization of the injected signal was again scrambled. The system was tested for both QPSK and 16-QAM modulation formats.

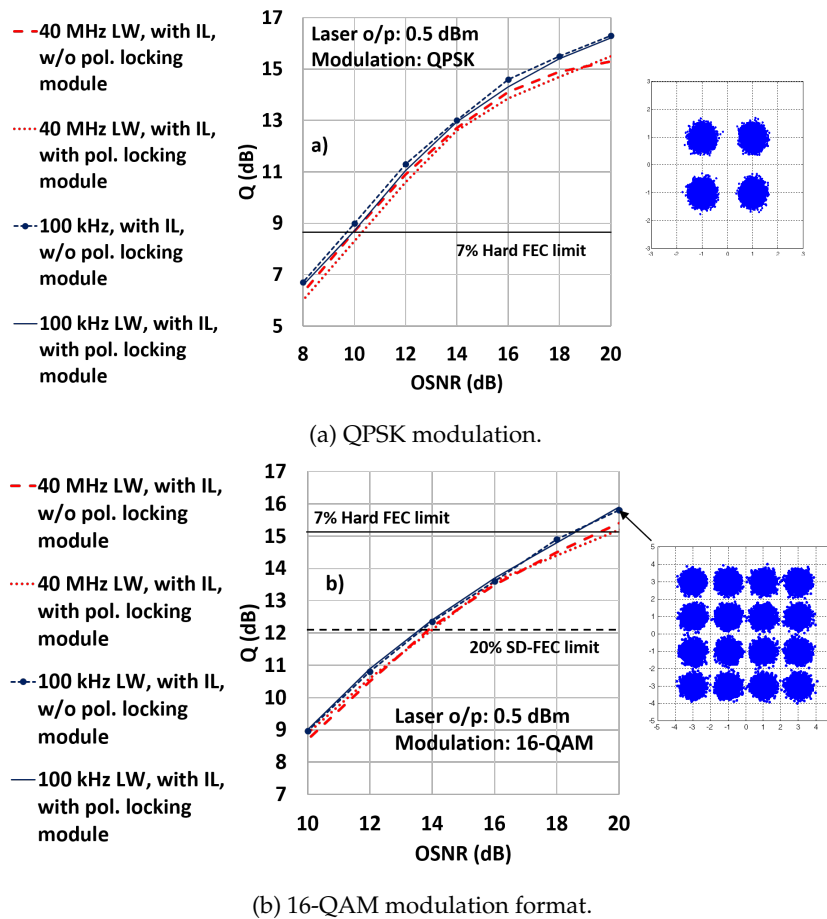


Figure 5.12: Q (dB) vs. OSNR (dB) using low performance laser (LW=40 MHz) compared with a standard laser (LW=100 kHz). Insets: Recovered constellations at 22-dB OSNR for QPSK, 16-QAM with laser LW = 40 MHz.

A reference Q curve is plotted over an OSNR sweep using a standard laser with 100-kHz LW. The output power of the standard laser was attenuated to 0.5 dBm, to match the output power of the low performance laser, so that the performance difference between these two systems could be primarily attributed to the difference in laser LWs. The performances with and without the polarization-locking module were observed to be similar, as shown in Fig. 5.12. The Q of the recovered signal reaches only 16.2 dB for QPSK at 20-dB OSNR even for a standard laser with 100 kHz LW, owing to the large OSNR penalty caused by low output power of the transmitter laser. The system was then tested using the 40-MHz LW laser. The laser gives 40-MHz broad LW despite of operating at maximum safe bias current. This low performing laser was used in the experiments to test the system under a worst-case scenario. Without injection locking, the signal at the receiver is unrecoverable, when using a spectral peak search for frequency offset compensation and training-aided maximum likelihood phase estimation. With injection locking, signal recovery is found to be possible. Fig. 5.12 shows measured performance with and without the polarization-locking module for injection locked setup. For the measurements without polarization locking module in Fig. 5.12, the system loses the injection lock when the polarization of the injected signal changes. Thus, the system needs manual calibration using polarization controllers each

time to regain the lock. On the other hand, the repetitive, manual calibration is not needed when using the proposed polarization-locking module.

Comparing the traces for systems using the low (100 kHz) and high (40 MHz) LW lasers at the transmitter, Fig. 5.12 shows that the performances are similar. Thus, it can be concluded that the OIL setup effectively cancels the phase noise due to the broad LW. At the hard FEC limit, there is a small but measurable required-OSNR penalty of 0.6 dB when using the broad LW laser, compared with the narrow LW laser. A similar performance trend was observed when using 16-QAM modulation where the system using the broad LW laser gives a marginal OSNR penalty of 1.1 dB compared with that using the narrow LW laser. Moreover, the performance for 16-QAM using the high LW laser barely reaches the hard FEC limit at 20-dB OSNR. Soft-decision thresholds can be considered for 16-QAM assuming the use of a concatenated LDPC-convolutional (LDPC-CC(18360,4,24)) code with a 20% overhead [90], giving 'error free' operation for pre-FEC BER of 2.7×10^{-2} . The OSNR penalty reduces to 0.35 dB compared with the low LW system at this soft-decision FEC limit. For both broad and narrow linewidth systems, the polarization locking module managed to maintain the injection lock despite of polarization drifts.

5.1.8 Field test over a fiber link from Monash Clayton to Caulfield campus



Figure 5.13: Map showing the test link node locations.

The system was tested over an installed 'field-trial' link from Monash University's Clayton campus to the Caulfield campus. The field link used in this experiment is a 10-km long dedicated 'dark' fiber, resulting in 20-km link transmission with a simple loop-back placed at Caulfield and an overall insertion loss of 5.8 dB.

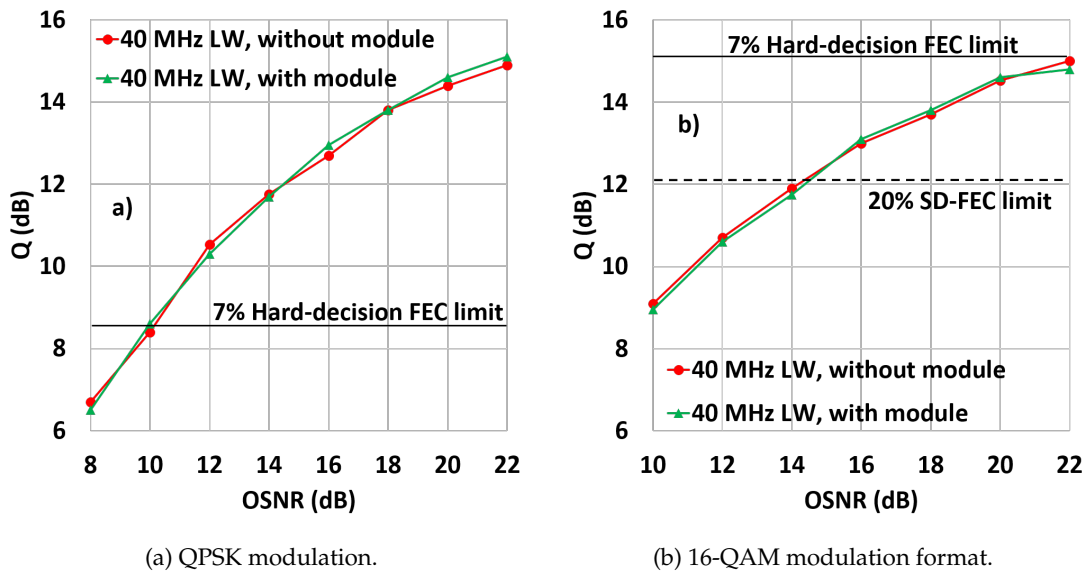


Figure 5.14: Q performance vs. OSNR (dB) for field link (20 km) using low performance laser (output power: 0.5 dBm).

The experimental setup is similar to the one shown in Fig. 5.9. The polarization scrambler and phase modulator are removed from the set-up, as random polarization rotations are provided by the field link and the phase distortions by the use of the high LW laser in the transmitter. A signal with same OFDM parameters as in previous back-to-back experiment is transmitted over the field link and received after a single round-trip with an OIL-based homodyne receiver setup.

Fig. 5.14 shows the Q of the signal recovered after transmission over the fiber link with and without the proposed module. As expected, the OIL system with the module gives similar Q performance over a wide range of OSNRs, compared with the OIL system without the module. This proves that the proposed module did not impart any performance penalties to the system. Again, as expected, the OIL system without the proposed module lost lock randomly and had to be manually realigned on multiple occasions, whereas the OIL with module maintained the lock all through the course of the experiments. The system performances for all cases with the OIL cross the forward error correction (FEC) limits, for both the 7% hard-decision FEC for QPSK, and the 20% soft-decision FEC for 16-QAM.

From the measurements, the required OSNR to maintain the performance above FEC limits is 11 dB for QPSK and 14 dB for 16-QAM. This demonstrates that coherent systems employing our polarization-insensitive OIL in installed metropolitan fiber systems can use lasers with significantly relaxed specifications (e.g. LWs up to 40 MHz, with output powers as low as 0.5 dBm). Critically, the proposed module removes the need for polarization tracking, allowing for operation with an arbitrary input polarization state.

5.2 Nonlinear interference noise cancellation using optical injection locking

5.2.1 Inter-channel nonlinear interference cancellation

Problem statement and proposed concept

The transmission reach of optical communication systems is restricted by nonlinearities in optical fibers [141]. In a multi-channel environment, these nonlinearities cause both intra-channel interference and inter-channel interference. Intra-channel nonlinear interference, such as self-phase modulation (SPM), can be compensated to a large extent by digital methods—like digital back-propagation (DBP)—which attempt to undo propagation effects by numerically solving a nonlinear Schrödinger equation [142] [143]. On the other hand, inter-channel nonlinear interference, e.g. from cross-phase modulation (XPM) and four-wave mixing (FWM), are difficult to compute accurately [144]; although, in optimized laboratory experiments, there are clear benefits from compensating inter-channel nonlinear interference [145]. DBP is also computationally intensive for inter-channel nonlinear interference due to the need to process extremely wide-bandwidth signals, and is compromised when channels are added or dropped in optically routed networks [144]. Thus, inter-channel nonlinear interference remains a problem for optically routed networks, despite significant research in developing multi-channel DBP algorithms and modelling inter-channel interference (e.g. [146] [147]).

Dar *et al.* showed that this inter-channel nonlinear interference noise (NLIN) cannot strictly be considered as circularly symmetric (CS) Gaussian noise. It can actually be dominated by phase noise in links with many short-spans: the CS Gaussian noise model is only appropriate when longer distances are covered by fewer spans [10]. For multi-channel signals with sufficient channel spacing (>30 GHz), FWM becomes negligible [148] and XPM dominates the inter-channel NLIN. The XPM model developed by Chiang *et al.* [149] indicates inter-channel phase modulation to be limited in bandwidth by dispersion-induced walk-off between the WDM channels. Thus, the spectral width of the XPM-induced phase distortion is limited in dispersion unmanaged links [150] [151] [152]. Specifically, Foo *et al.* show that the XPM bandwidth for 50-GHz channel spacing with QPSK modulation has around a 1.6-GHz full-width half-maximum with a roll-off of 2.8 dB per GHz of modulation bandwidth in a 20-span, 1600-km link [151].

There have been various approaches to compensate for inter-channel nonlinear effects; for example, phase conjugation, including using optical phase conjugation per-span [153], and phase sensitive amplifiers [133]. However, these approaches require sophisticated equipment in the field. Other approaches take advantage of the limited bandwidth of the XPM-induced phase fluctuations. For example, a low-bandwidth phase modulator, driven proportional to the combined intensity of all the WDM channels, can

be installed along the link to mitigate XPM [151]. Alternatively, pilot tone based techniques have been proposed in which the pilot tone picks up XPM along the link, enabling the XPM to be cancelled digitally at the receiver [154] [155] [156], but with added processing latency. This work shows the nonlinearity compensation capabilities of OIL and proves it to be comparable to other nonlinearity compensation methods such as optical phase conjugation or phase-sensitive amplification [153] [133]. The benefit of the OIL based compensation lies in the reduced implementation cost as compared with the above methods, as it needs hardware modifications only at the receiver. The comparable compensation capabilities show that OIL is capable to sustain and compensate for accumulated noise over the link. However, this capability is restricted to linear and nonlinear phase noise. Although OPC and PSA can compensate nonlinearity distortions up to relatively higher frequencies, they still do not make optimum solutions. Just like OIL, PSA cannot compensate for the nonlinear amplitude noise. The OPC, on the other hand, can introduce high errors if the distributed amplification is not matched properly to the accumulated nonlinearities. The walk-off in the signals may introduce bandwidth limitations in compensation capabilities of the distributed methods, just like in OIL. If this is the case, OIL may seem to be a better option.

In this section, a novel concept of using optical injection locking (OIL) to identify the XPM-induced fluctuations from the residual carrier is proposed. The identified fluctuations can then be cancelled in a coherent receiver. It is shown that, in an OFDM system with a central 2.5-GHz guard-band, OIL carrier recovery can improve peak Q by 1 dB and associated improvement in transmission reach without adding latency in the DSP, by adding optical injection locking to the receiver hardware.

The nonlinear interference noise, as discussed before, is dominated by the cross-phase modulation (XPM) for links with more number of spans of shorter lengths (< 100 km). Further, this XPM distortion is limited in bandwidth for dispersion-unmanaged links. The XPM efficiency vs. modulation frequency, ω , is [150] [151]

$$\eta_{XPM}(\omega) = \frac{\alpha^2}{(\omega\Delta\beta)^2 + \alpha^2} \left[1 + \frac{4\sin^2\left(\frac{\omega\Delta\beta L}{2}\right)e^{-\alpha L}}{(1 - e^{-\alpha L})^2} \right] \left| \frac{\sin\left(\frac{N\omega\Delta\beta L}{2}\right)}{\sin\left(\frac{\omega\Delta\beta L}{2}\right)} \right| \quad (5.6)$$

where: η_{XPM} is the XPM efficiency, α is the fiber attenuation, $\Delta\beta = D(\lambda_1 - \lambda_2)$ is the difference in the propagation constants of a continuous wave probe at wavelength λ_1 and its interferer at λ_2 . D is the chromatic dispersion parameter of the fiber. N is the number of spans in the link and L is the length of each span.

Fig. 5.15 plots the XPM efficiency for $N = 4$ and 40 spans, each of 80 km for a total length 320 km (red line) and 3200 km (blue line) respectively with 50-GHz frequency spacing and CD parameter $D = 16$ ps/nm km. The XPM efficiency increases in magnitude with the link distance due to accumulation. As transmission distance increases, the magnitude of the XPM transfer function increases as nonlinear distortions accumulate, but the bandwidth of intensity fluctuations transferred via XPM is reduced

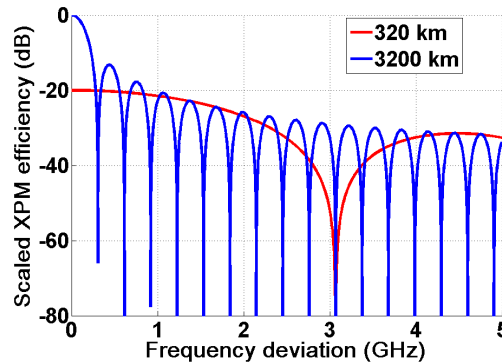


Figure 5.15: Scaled XPM efficiency (dB) vs. frequency (GHz).

(Fig. 5.15). Note that the horizontal axis in Fig. 5.15 relates to the frequency of the intensity fluctuations within the neighboring channel, not the channel spacing itself. The XPM concentration in the main lobe of the XPM efficiency spectrum reduces with the length and the XPM effects are observed to be restricted in bandwidth. This can be attributed to the walk-off caused by the CD and a large frequency spacing between the channels. As such, the XPM can be expected to provide narrowband modulation of the CW probe wavelength.

The concept of OIL based nonlinearity compensation was inspired from pilot-based nonlinearity compensation methods [154] [155] [156]. A pilot frequency tone is added in a guard band of the signal. The pilot tone acts as a CW probe signal and is subjected to the same cross-phase modulation (XPM) distortions that is suffered by the signal subcarriers across the fiber link. If this pilot tone is filtered out at the receiver, the XPM on it can be used to cancel out the XPM distortions on the signal. Du *et al.* [154], Inan *et al.* [155] and Lobato *et al.* [156] performed this filtering and cancellation digitally after coherently receiving the signal in an intradyne receiver.

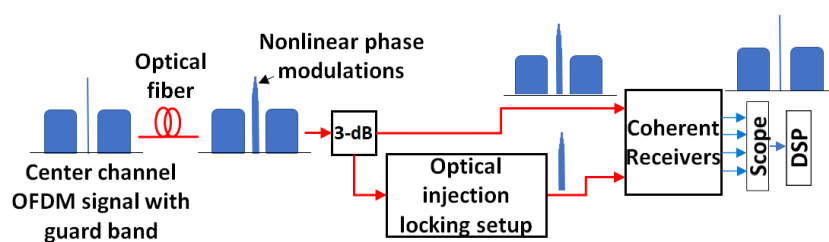


Figure 5.16: OIL-based XPM compensation concept.

The aim of this proposed technique is to achieve this XPM compensation without increasing the DSP latency. It extracts the pilot tone from the signal and uses it as a local oscillator to a coherent receiver. The XPM common to the signal and pilot cancel one another on coherent reception. To select the pilot tone in analog domain before digitization, an optical bandpass filter can be used. But the frequency drifts in the signal may lead to the OBPF band-limiting the required pilot tone or passing a portion of sidebands along with it. Thus, we need a mechanism that locks the frequency of the signal and allows

for phase transfer in a specific frequency range. This is achieved using optical injection locking as shown in Fig. 5.16. The OIL selects the residual carrier that carries the XPM modulation and uses it as local oscillator. Because OIL-based carrier recovery can replicate the phase information of the incoming signal up to several GHz, depending on the injected power (Eq. (5.7)), the recovered carrier at the output of OIL contains the phase noise information (linear and nonlinear) [14] [131]. At the same time, the output of the OIL is locked to the incoming signal carrier frequency. Thus, the OIL can be imagined as an active optical bandpass filter for phase modulation (not amplitude modulations) whose center frequency is locked on to the incoming signal's carrier frequency, avoiding the frequency drift problems in OBPF.

$$\Delta\omega_L = f_d \sqrt{R_{inj}} \sqrt{1 + \zeta^2} \quad (5.7)$$

where f_d is the slave laser cavity mode spacing, R_{inj} is the optical injection ratio and ζ is the linewidth enhancement factor of the laser cavity. The self-phase modulation (SPM) in the system is not bandlimited and occupies a relatively wider bandwidth, as $\Delta\beta \rightarrow 0$ in Eq. (4.10). The OIL suppresses the phase-transfer beyond the phase-transfer bandwidth, the proposed system cannot completely compensate for the SPM in the system. Nonetheless, the SPM can be suppressed using digital backpropagation that will be added to the OIL and investigated in next subsections.

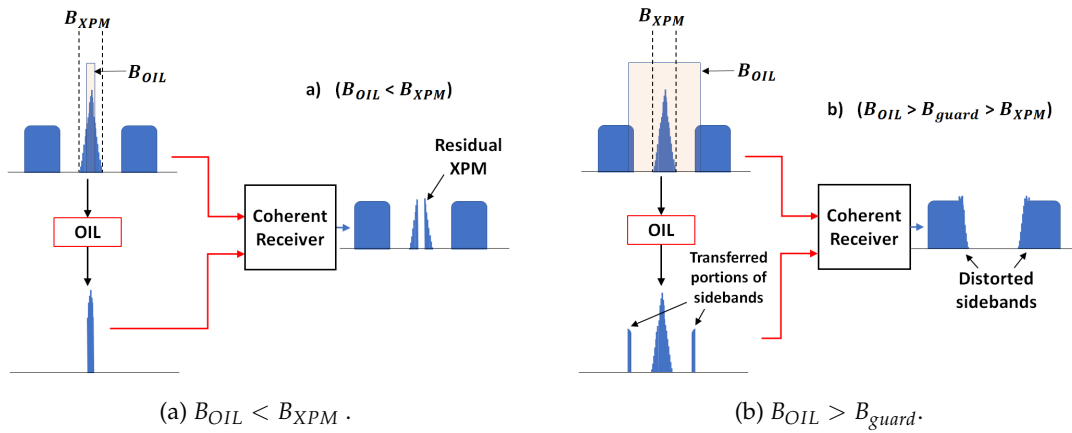


Figure 5.17: Spectral effects of OIL's phase-transfer bandwidth.

The phase-transfer bandwidth of the OIL (B_{OIL}) is critical. This is the range of frequencies within which the OIL setup passes the phase modulation to the receiver. Within this same range the amplitude modulation is highly attenuated [139]. The frequency detuning locking bandwidth, on the other hand, is a completely different parameter and should not be confused with. It defines the allowed detuning of the incoming carrier from the free-running frequency of the slave laser before locking fails entirely.

If the phase-transfer bandwidth (B_{OIL}) is less than the XPM bandwidth (B_{XPM}), the system performs sub-optimally as the detected signal still contains traces of XPM distortions at frequencies outside the OIL bandwidth (illustrated in Fig. 5.17a). Reducing the (B_{OIL}) further leads to complete loss of lock and

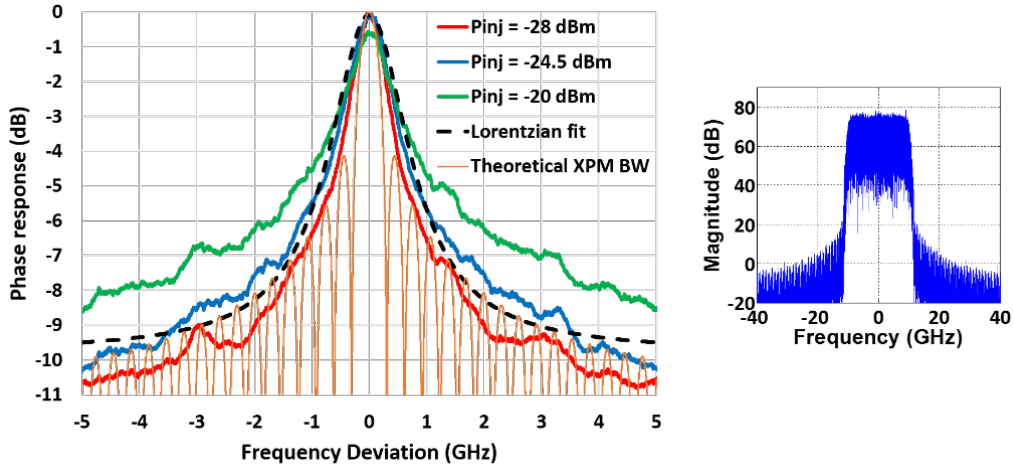


Figure 5.18: Phase transfer-function of the optical injection locking setup; P_{inj} : Injected power (dBm). Inset: 10-Gbaud modulated signal spectrum.

the system fails. At the same time, if the phase-transfer bandwidth of the OIL (B_{OIL}) is higher than the guard band frequency range (B_{guard}), it allows for some portion of the signal sidebands to pass through in the local oscillator signal and again causes distortion in the detected signal (Fig. 5.17b). Hence, there is an optimum B_{OIL} at which the proposed system needs to be operated.

The phase-transfer function of the OIL is also of importance as it reflects the frequency range and the degree of the XPM-dominated nonlinear phase noise that can be cancelled upon coherent reception. To that end, a spectrally flat wideband 20-Gbaud single-carrier QPSK-modulated signal (inset of Fig. 5.18) generated using zero-padded oversampling was injected into the OIL with various P_{inj} . The output of the OIL setup was detected in the homodyne receiver, to measure the phase modulation transfer characteristics of slave laser. This phase transfer, shown in Fig. 5.18, has a Lorentzian shape (a Lorentzian fit shown in dashed lines). B_{OIL} is related directly to the power of signal injected into the slave laser (P_{inj}) [156] i.e. the bandwidth of the phase transfer can be observed to increase with increase in P_{inj} . Fig. 5.18 also shows the theoretical XPM bandwidth for 40 spans, 3200-km link distance calculated using Eq. (5.6) and scaled to the phase transfer measurements. Ideally, these phase transfer characteristics of OIL would be flat within the B_{OIL} bandwidth to accurately transfer the XPM phase modulation. However, the Lorentzian shape of the phase transfer means that the system will attenuate higher frequency XPM components. Nonetheless, the attenuation is minimal for the main XPM lobe in Fig. 5.18 and so we can still expect significant cancellation of XPM. The attenuation can be further reduced by increasing the P_{inj} at the risk of passing portions of signal sidebands through, as highlighted in Fig. 5.18. This optimum P_{inj} or optimum injection ratio will be investigated in the next section.

Experimental setup for transmission experiments

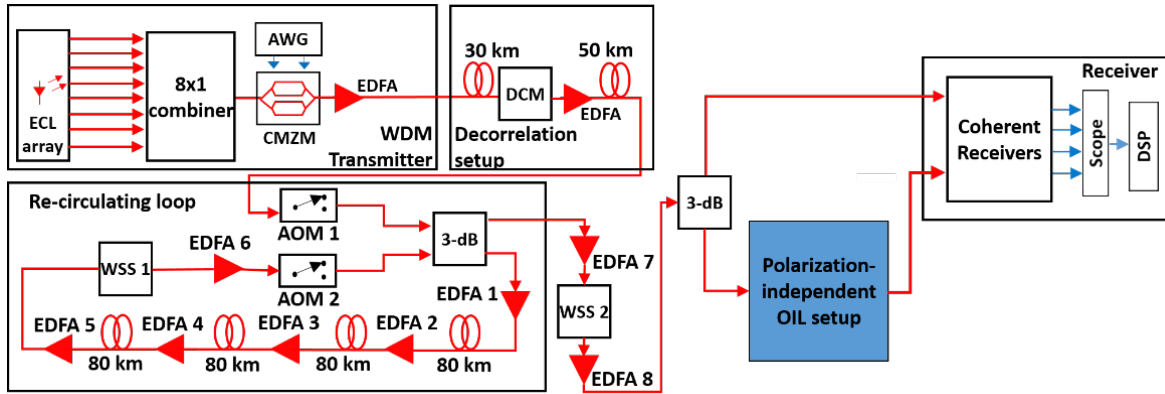


Figure 5.19: Experimental setup: AWG- arbitrary waveform generator; DCM- dispersion compensation module; EDFA- erbium doped fiber amplifier; AOM- acousto-optic modulator; WSS- wavelength selective switch (Wave-Shaper).

The optimum phase-transfer bandwidth (B_{OIL}) and, in extension, the optimum injected power (P_{inj}) were investigated for considered link distance and signal parameters. Fig. 5.19 shows the experimental setup to verify the method. An ECL array of 7 continuous wave (CW) lasers, each with 150-kHz linewidth and 15-dBm output power, was used. The center frequencies were 50-GHz apart, from 192.95 THz to 193.25 THz. The CW carriers were combined using an 8×1 polarization maintaining coupler, then modulated using a 20-GHz bandwidth IQ modulator (Complex MZM) with a 25-Gbaud OFDM signal with 100 sub-carriers from a 156-point FFT. The modulator drive was generated with a 60-Gsa/s 20-GHz bandwidth arbitrary waveform generator. A central guard-band of 2.5 GHz (10 sub-carriers) was added to prevent the transfer of the phase of the data-carrying subcarriers through the OIL set-up, providing an overall signal bandwidth of 27.5 GHz. The effective symbol rates of both the QPSK and 16-QAM is 25 Gbaud, and we assumed a 7% and 20% FEC overhead for these signals, respectively. This then gives a net rate per polarization of 46.7 Gb/s for QPSK and 83.3 Gb/s for 16-QAM. To de-correlate the neighboring channels, the multichannel signal was dispersed by ~ 14 symbols using an 80-km fiber and a Teraxion DCML dispersion compensation module, which flattens the intra-channel differential group delay within each channel, while maintaining inter-channel delay. The de-correlated WDM signal was then passed through a recirculating loop that consists of four 80-km spools of standard single-mode fiber (ITU G.652D). The number of re-circulations was controlled by two acousto-optic modulators (AOMs) to achieve transmission over multiples of 320 km. The noise bandwidth in the system was limited to 400 GHz using a WaveShaper (WSS 1). The power launched into each span was controlled by the output powers of the EDFAs numbered 1 to 5. The output of the recirculating loop was passed through WSS 2, set to pass only the central channel.

The received signal was injected into the polarization-independent OIL described in previous section. The output of the OIL was used as the local oscillator (LO) for a coherent receiver, whose outputs were

sampled by an 80 GSa/s oscilloscope feeding offline digital signal processing (DSP). The DSP used to recover the signal includes blind chromatic-dispersion compensation based on a coarse knowledge of the known distance and typical fiber dispersion using the overlap-save method, preamble-enabled frame synchronization using cross-correlation for the known preamble and received signal waveform, training-based channel estimation using the difference between the sent and received training waveforms to determine the channel response to implement static, single-tap sub-carrier equalization, and 4th-power phase estimation followed by maximum likelihood estimation for constellation recovery.

Optimum injection ratio

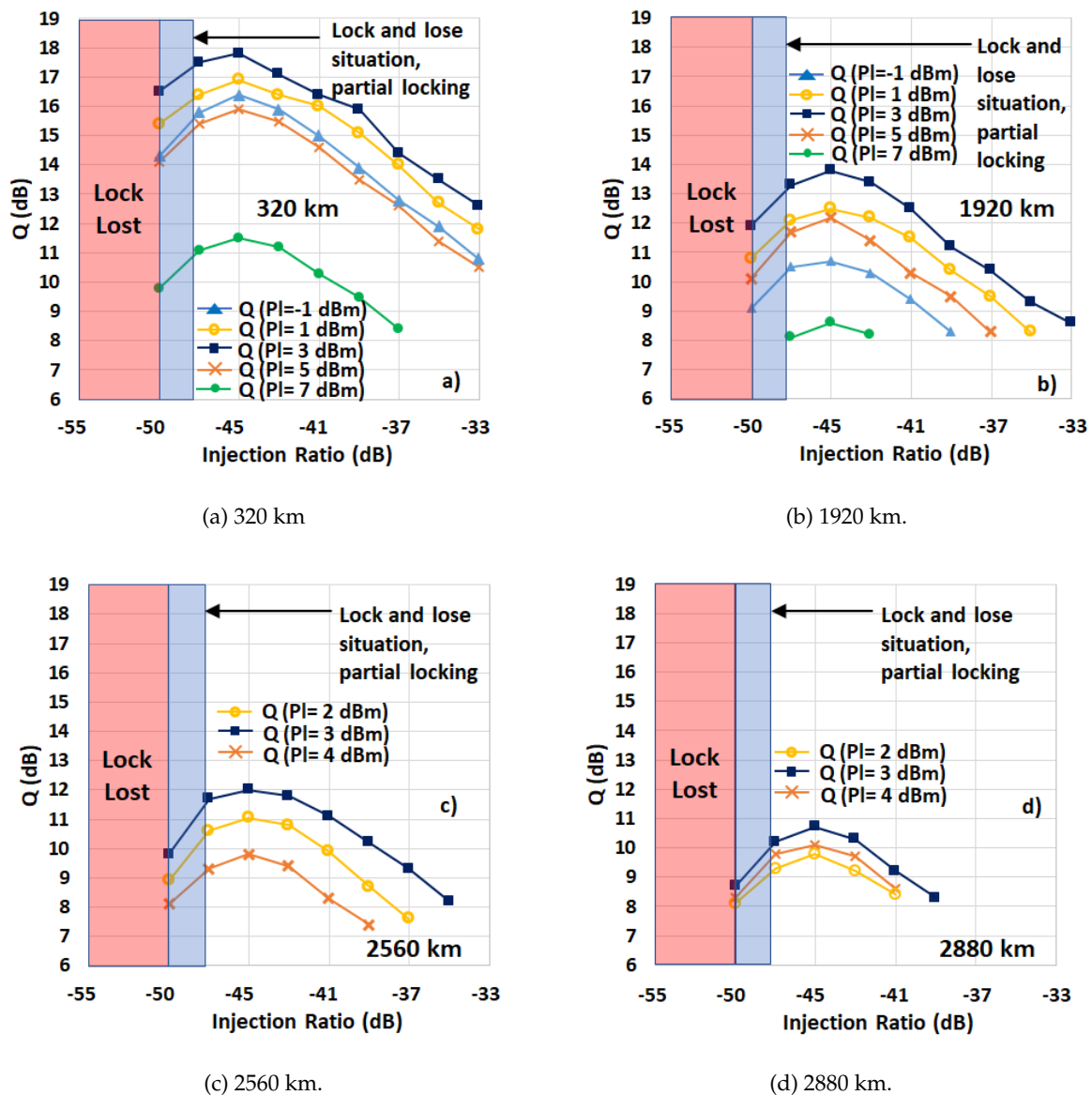


Figure 5.20: Q vs. injected power for various launch-powers and link lengths.

To confirm the optimum injection ratio, we measured the dependence of the performance of the recovered signal (using quality factor Q as a metric) on the injected power (P_{inj}) for a fixed transmission

distance. P_{inj} represents the total signal power, including the residual carrier. The injection locking extracts a residual carrier from a guard-band in the middle of the signal, with the carrier-to-signal power ratio $\ll 0$ dB, set to be close to the point where injection locking was lost. The residual carrier was produced by biasing the CMZM slightly away from the null point, in order to pass a small amount of unmodulated light through to provide the seed for injection locking.

For the measurements shown in Fig. 5.20, a distance for transmission was fixed and a receiver-side EDFA was used to ensure that the receiver is getting sufficient signal power. The injection ratio was then controlled by adjusting the P_{inj} using a VOA. Each curve on the plot was then measured for different launch-powers into the link to see the system performance in the noise limited and the nonlinear regimes.

Fig. 5.20a shows performance against injection ratio plot for a 320-km link. An optimum injection can be observed, in line with behavior predicted in Section 5.2.1. At the same time, the launch-power is also varied from -1 dBm to 7 dBm and Q plot for each launch-power is plotted. The Q increases globally from PL = -1 dBm to 3 dBm and decreases from PL = 3 dBm to 7 dBm, as expected for a nonlinear transmission system. The performance is maximum for PL = 3 dBm (dark blue squares). Along the x-axis, the performance for all curves reaches a maximum value at $P_{inj} = -24.5$ dBm, corresponding to an injection ratio of -45 dB, with the slave laser producing +20 dBm of output power in free-running mode. This would then seem to indicate that a -45 dB injection ratio is optimal over a range of transmission distances when the launch power in the link is such that the Q of the received signal is close to its maximum value.

There are several inferences we can make from this result. As the injection ratio where performance is optimized does not seem to change with either launch power or transmission distance, this suggests that the optical signal-to-noise ratio plays only a minor role in determining the optimal injection ratio. Moreover, this also suggests that chromatic and polarization mode dispersion have little impact on the injection ratio that maximizes system Q , which is understandable as the injection locking stage is polarization independent and the bandwidth of injection locking should be nominally independent of dispersion of the injected signal.

As the properties of injection locking are generally dependent on the strength of the injected tone, and even in the case of low OSNR, the power contribution of optical noise over the phase-transfer bandwidth is likely quite low, it may be expected that the injection ratio at the receiver is independent of the propagation distance. This is reflected in the relatively close match in the behaviors of the -1-dBm launch power curve at 1920 km, the 2-dBm launch power curve at 2560 km, and the 3-dBm curve at 2880 km.

At this optimum injection ratio ($P_{inj} = -24.5$ dBm), Fig. 5.18 showed that the phase response has full-width half-maximum (FWHM) of 1 GHz with 2.8 dB/GHz roll-off up to 2 GHz. The performance

drop on the low-power-side of the optimum in Fig. 5.20 is due to a reduction in the phase-transfer bandwidth of OIL (B_{OIL}) as shown in Fig. 5.17a, causing loss of phase information. If the injected power is reduced further, the system oscillates between locked and unlocked states; at lower powers, it experiences a complete loss of lock. The performance drop for injection ratios higher than the optimum is due to the increase in the phase transfer bandwidth of the OIL (B_{OIL}) more than the guard band (B_{guard}), which leads to transfer of the signal sidebands' phase on to the generated LO distorting the detected signal (Fig. 5.17b).

Similar trends are observed for longer distances as observed in Fig. 5.20b, Fig. 5.20c and Fig. 5.20d with signals transmitted over 1920 km, 2560 km and 2880 km respectively. The Q performance is again maximum for $P_L = 3$ dBm and the optimum injection ratio is again found to be -45 dB. The overall performance decreases with distance, as expected as noise and nonlinear distortions increase with transmission distance. Interestingly, it was found that the injection ratio required for optimum performance is independent of the launch-powers and the link distances. Comparing this to the expected range of XPM bandwidths for the different distances trialed, this would seem to suggest a broader phase transfer bandwidth would be preferred, for shorter distances, which should imply a change in injection ratio. The conclusion that the injection ratio—and hence phase transfer bandwidth—should be static with changing XPM bandwidth is similar to the set filter bandwidths used in [151]. This is an important and a useful property of the proposed system for optically routed networks where it is very difficult to determine the length of fiber traversed by a particular channel. In addition to this, the launch-powers may also vary in an optical network depending on the link length between subsequent repeaters, so the fact that the same optimum injection ratios are found for a variety of launch powers indicates that our method is robust to these launch power variations. As the operation of the proposed OIL-based system is independent of both transmission reach and launch power, would then seem to be suitable for use in optically routed networks, provided the injection ratio can be set (in this case to -45 dB), e.g. by using a power-controlled receiver-side EDFA.

Transmission of QPSK and 16-QAM modulated WDM signals

To gain insight on the transmission reach improvements enabled by partially compensating nonlinear distortions, a transmission distance was picked and launch power swept. Curves for different link distances are then plotted to understand the performance gain due to the nonlinearity-compensation. The injection ratio for the OIL was fixed at -45 dB, i.e. at the optimum value. The link distance was also varied to observe the maximum reach that can be achieved while the peak Q is greater than 7% hard FEC limit ($Q = 8.5$ dB, $BER = 3.8 \times 10^{-3}$).

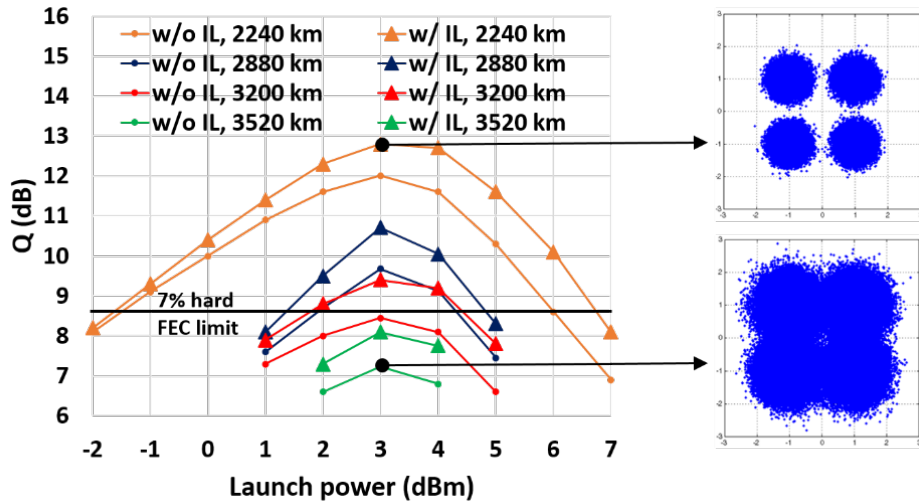
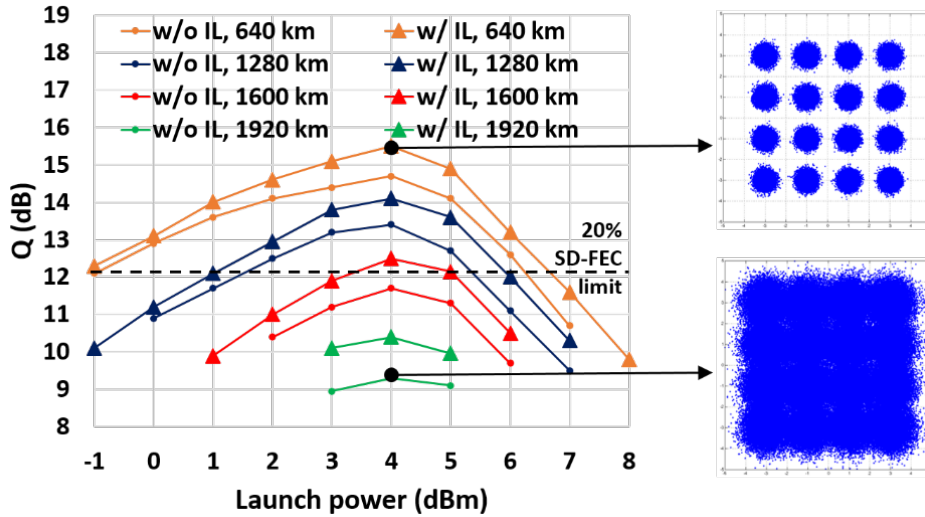
Figure 5.21: Q vs. launch-power with QPSK modulation.

Fig. 5.21 shows the performance plots for QPSK modulation. Similar to our observations in Fig. 5.20, the performance reaches the maximum at $P_L = 3$ dBm and then drops when increased further in to the nonlinear region ($P_L > 3$ dBm). The intradyne system without OIL uses a spectral peak search method for carrier frequency offset (CFO) compensation. At lower launch-powers, the OIL shows marginal improvement that increases with increase in the nonlinear effects in higher launch-power region. The performance gain for higher launch-powers verifies the compensation of the nonlinear interference by the proposed OIL setup. The performance curve for 3200 km does not reach the HD-FEC limit with the regular intradyne system, whereas, the OIL system with 3200-km link crosses the HD-FEC limit for a good range of launch-powers (2-4 dBm). In this case, the 3200-km system with OIL performs very similarly to the 2880 km system without OIL, indicating that OIL can indeed improve system reach. While the distances transmitted over are fundamentally a product of the laboratory set-up here, the relative improvement between systems with and without injection locking indicate that OIL is able to compensate for nonlinear phase noise, and that this can translate into improved system reach.

The performance for 16-QAM modulation was measured next. This is important in the context of nonlinearity compensation, because as nonlinear interference is modulation-dependent [148], the effect of nonlinearity on higher-order QAM is worse than for QPSK. Fig. 5.22 plots the measured Q for the recovered 16-QAM signal against the launch-power sweep for links of 640 km to 1920 km. The previously used HD-FEC limit was not met when transmitting 16-QAM signals over links longer than 320 km in this experiment, even for the OIL system. As a result, a 20% soft-decision FEC limit ($\text{BER} = 2.7 \times 10^{-2}$, $Q = 12.1$ dB, 20% overhead) is considered for 16-QAM modulated signals [154]. As shown in Fig. 5.22, the peak Q over 1600-km transmission for an intradyne system without OIL does not meet the pre-FEC requirements for SD-FEC, whereas with OIL system this condition is met. Again, this indicates that reach can be improved through the use of OIL, here with 16-QAM modulated signals.

Figure 5.22: Q vs. launch-power with 16-QAM modulation.

Peak- Q improvements				
Transmission distance (km)	dis-	Peak- Q improvement	Transmission distance (km)	Peak- Q improvement
2240 km		0.95	640 km	0.7
2880 km		1	1280 km	0.73
3200 km		1	1600 km	0.8
3520 km		1	1920 km	0.8

Table 5.1: Number of complex multiplications per symbol detection required by the algorithms.

Table 5.1 shows the improvement by the proposed OIL system in the peak- Q . The QPSK signals experienced 0.95-1.1 dB of improvement whereas the 16-QAM system experienced between 0.7-0.8 dB improvement in Q . A marginal increase in peak- Q -improvement with transmission distance was observed in both systems. This improvement saturates at 1 dB for QPSK and at 0.8 dB for 16-QAM.

The OIL system gave a 1-dB improvement over a regular intradyne system in the nonlinear regime for QPSK modulated signal. The best Q was always obtained at 3-dBm (4-dBm) launch-power for QPSK (16-QAM) modulated signal. The performance improvement in the nonlinear regime confirms the nonlinearity compensation by the proposed OIL-based method.

Comparing the results to digital pilot tone-based compensation methods, the proposed method gave a 0.2-dB gain in peak- Q over demonstrations of digital carrier extraction methods, which give 0.5-dB [155] [156] and 0.8-dB [154] improvements over non-compensated links. The peak- Q improvement in those systems could be limited by receiver imperfections, possibly related to the resolution of the ADCs. Moreover, the 0.2-dB improvement we observe over digital pilot recovery systems carrying QPSK was achieved without adding extra steps into the receiver-side digital signal processing (DSP), thus

avoids the introduction of extra processing latency, with reasonable increase in hardware complexity.

There are several avenues toward optimizing the performance of our system, and to establish rigorous design rules for nonlinear cross-talk suppression using this technique. In this investigation, a low carrier-to-signal-power ratio was used, that was close to what was found experimentally to be the minimum-necessary to ensure locking. However, the carrier-to-signal-power ratio could be significantly increased without significant degradation to the required OSNR at the receiver, and this may help expand the injection locking bandwidth without causing significant penalty from signal leakage. A rigorous study of this trade-off would help establish further design rules for the demonstrated system.

Compensation of inter-channel nonlinearities is proving to be a practically difficult task for multi-channel DBP [144], [145], [146], as it requires accurate models of the inter-channel interference along the link. By extracting nonlinear phase distortions optically at the receiver, we attempt to remove the requirement for accurate nonlinear channel models over wide bandwidths. In addition to this, by recovering phase distortions from the signal itself, the proposed system potentially allows for the cancellation of some stochastic nonlinear distortions that are extremely difficult to predict. For example, the proposed method should also cancel the low frequency components (those that fall within the phase transfer bandwidth of the OIL) of both the nonlinear phase noise generated due to amplified spontaneous emission's (ASE) interaction with the nonlinearities (the Gordon-Mollenauer effect).

The motivation to find alternatives to nonlinearity compensation techniques that rely on knowledge of the nonlinear fiber channel has also spurred investigations into in-line nonlinearity compensation techniques [151], [153], [154]. By requiring modification to optical equipment at the receiver-side only, our proposed system does not require modifications to equipment at multiple locations along the link, potentially simplifying implementation.

The proposed system is capable of mitigating the XPM distortion because of its limited bandwidth, but most of the wide-band SPM remains uncompensated. In contrast to wide-band inter-channel nonlinearity, DBP can significantly mitigate intra-channel nonlinear distortion (such as SPM). As such, the peak- Q and the nonlinearity tolerance can be further increased by adding a digital-backpropagation algorithm in the DSP that takes care of the SPM distortions.

Open questions remain as to whether this technique could be used to improve capacity. If only a small family of FEC options are considered, then the improvement in peak- Q afforded by OIL may be useful in using lower overhead codes (e.g. switching from 20% SD-FEC to 7% HD-FEC). If adaptive modulation or FEC codes are used, then the improvement in peak- Q may be used to improve capacity for a given transmission distance. The trade-off between peak- Q improvement and the central guard band's bandwidth need to be investigated. The proportional spectral efficiency loss for a given guard band will improve with higher bandwidth signals; here we used a 25-Gbd signal, signals with baud rates

over 60-Gbd (e.g. [157]) are becoming common, and rates up to 100-Gbd are being reported by some groups (e.g. [158]). In this work, digitally generated OFDM is chosen, because it enables guard bands to be easily defined around the residual carrier. The proposed method can, however, be generalized to any system using a guard-band, which can be investigated in future.

5.2.2 Digital backpropagation for SPM compensation cascaded with the OIL-based NLIN cancellation.

The phase distortion due to intensity fluctuations of the same signal, known as the self-phase modulation (SPM), is generally mitigated using a digital back-propagation (DBP) algorithm. DBP uses the solutions of a Nonlinear Schroedinger Equation (NSE) to trace the signal back towards transmitter to estimate the transmitted symbols. The previous section showed nonlinear interference (dominated by XPM) cancellation using optical injection locking. This technique improves the peak- Q performance of QPSK and 16-QAM modulated signals by 1 dB and 0.7 dB respectively. Despite of these gains, it cannot compensate for the wide-band SPM. Thus, in this section the OIL-based nonlinear phase noise compensation cascaded with the digital back-propagation algorithm in the DSP is investigated for the SPM cancellation over link distances up to 3520 km.

System architecture and concept

5.2.3 XPM compensation

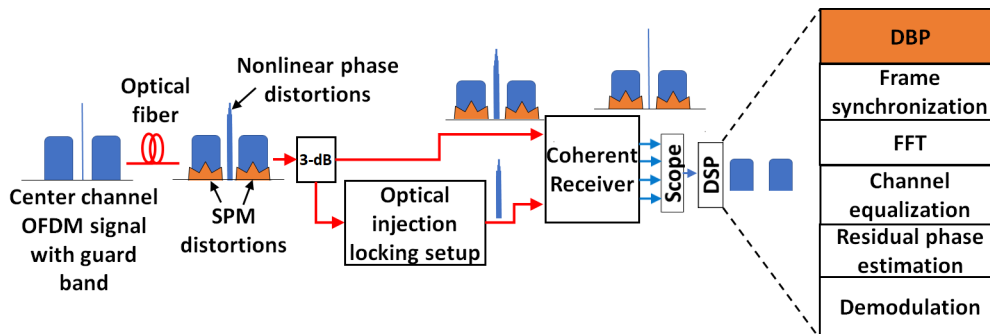


Figure 5.23: System compensating for XPM using optical injection locking and SPM using DBP (digital back-propagation).

An OFDM signal is considered in this work as it allows to a guard band to be easily created in the centre of the spectrum by allotting zeros to the central sub-carriers. A residual carrier is transmitted along with the signal. This residual carrier acts as a pilot tone and picks up the cross-phase modulation experienced by the sub-carriers. Due to the guard band (B_{guard}), the residual carrier can be filtered out and the XPM distortions can be extracted for further cancellation from the sub-carriers. As discussed in the previous section, the residual carrier can be selected out with the XPM distortions using optical injection locking (OIL) as shown in Fig. 5.23. The OIL setup allows for transfer of the phase modulation

within a certain phase-transfer bandwidth (B_{OIL}), depending on the injected power [131]. The recovered carrier with the XPM distortions at the output of the OIL is used as a local oscillator in the coherent reception of the signal. The XPM distortions get canceled due to the conjugate mixing of the XPM-carrying local oscillator and the distorted signal. The phase-transfer bandwidth needs to be chosen properly as too narrow B_{OIL} ($B_{OIL} < B_{XPM}$) leads to incomplete XPM cancellation or loss of injection lock and too broad B_{OIL} ($B_{OIL} > B_{guard}$) leads to portions of signal sidebands getting transferred to the output of the OIL. Thus, with proper injected power, the complex electrical signal at the output of the coherent receiver is free of the XPM distortions as shown in Fig. 5.23.

Digital back-propagation (DBP)

The previous section discusses the proposed XPM compensation technique using optical injection locking. Even after XPM compensation, the distortions due to self-phase modulation (SPM) still persists. For this, digital back-propagation is performed in the digital signal processing. The DBP algorithm has been widely discussed in the literature [159] [160] [161] [162] [142] [143]. The signal propagation in an optical fiber is described using a nonlinear Schroedinger equation (NLSE). The optical fiber length is divided into short steps for which the NLSE can be fragmented into linear and nonlinear parts as shown in Eq. (5.8).

$$\frac{\partial E}{\partial z} = (\hat{N} + \hat{L})E \quad (5.8)$$

$$\hat{N} = j\gamma|E|^2 \quad (5.9)$$

$$\hat{L} = -j\frac{\beta_2}{2}\frac{\partial^2}{\partial t^2} - \frac{\alpha}{2} \quad (5.10)$$

where \hat{N} and \hat{L} are the nonlinear and linear operators emulating the effect of chromatic dispersion and the nonlinearity of the fiber respectively. α , β_2 and γ are the attenuation, chromatic dispersion (CD), and nonlinear coefficients of the fiber respectively. Eq. (5.8) can be inverted in absence of noise and thus, the signal can be traced back to the transmitter to recover the actual symbol transmitted. Essentially, the split-step Fourier method is used to solve the inverse NLSE as shown below.

$$E_{Li} = IFFT(H_{Di}(\omega) \times FFT(E_i)) \quad (5.11)$$

where E_i is the signal field at the input of the i^{th} step, $H_{Di}(\omega) = \exp(-j\beta_2 h_i \omega^2 / 2)$ and h_i is the step-size of i^{th} step. $(*)$ is convolutional operation. The step-size is dependent on power and is varied along the length with shorter steps near the transmitter followed by gradually increasing step-sizes towards the receiver. This gradient step-sizes represent the actual fiber link more accurately as the signal experiences higher levels of nonlinearities near the transmitter due to higher instantaneous power levels, requiring shorter steps to find accurate solutions of the NLSE. The instantaneous power of the signal reduces

along the link due to attenuation and thus longer step-sizes can be considered towards the receiver. The step-size is calculated according to the attenuation in the fiber as-

$$h_i = \frac{-1}{\alpha} \log \frac{1 - i\delta}{1 - (i-1)\delta} \text{ and } \delta = \frac{1 - \exp(-\alpha L_{span})}{N_{steps}} \quad (5.12)$$

where L_{span} is the total span length and N_{steps} is the number of steps per span. After the linear part, the signal is passed through the nonlinear part that calculates the SPM effect on the signal as shown in Eq. (5.13).

$$E_{Ni} = E_{Li} \times \exp(\gamma h_i |E_{Li}|^2) \quad (5.13)$$

The output of the i^{th} step (E_{Ni}) is then passed through the next step till the start of the span. The final step output gives the original signal transmitted through the span.

Filtered-DBP

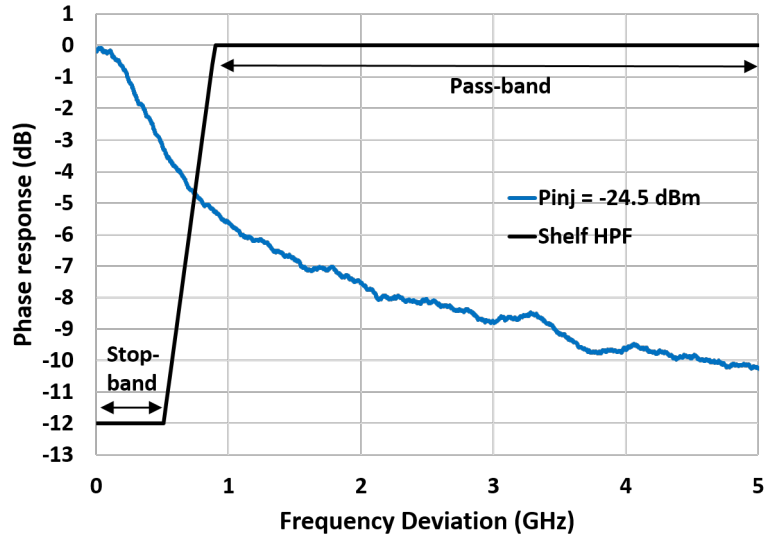


Figure 5.24: Frequency response of the high-pass filter used in filtered-DBP. HPF: high pass filter.

In conventional transmission system, the DBP works efficiently for SPM compensation. However, in our case, the regular DBP will perform sub-optimally, the reason being the OIL system has already compensated for the intra-channel nonlinear phase distortions that lie within the phase-transfer bandwidth (B_{OIL}). The regular DBP, thus, over-compensates for these intra-channel distortions at lower frequencies within B_{OIL} . To solve this issue, a filtered-DBP is proposed where a high-pass filtering of the signal is done after the nonlinear part in DBP. Consider a high-pass filter (H_{HPF}) whose frequency response is given in Fig. 5.24. The filtering operation can be shown as-

$$E_{Li-filtered} = IFFT(H_{HPF} * FFT(E_{Li})) \quad (5.14)$$

This filtering operation is inserted after Eq. (5.11) in DBP algorithm. The stop-band frequency should be chosen such that it matches the phase-transfer bandwidth of OIL (B_{OIL}). The injected power is set at

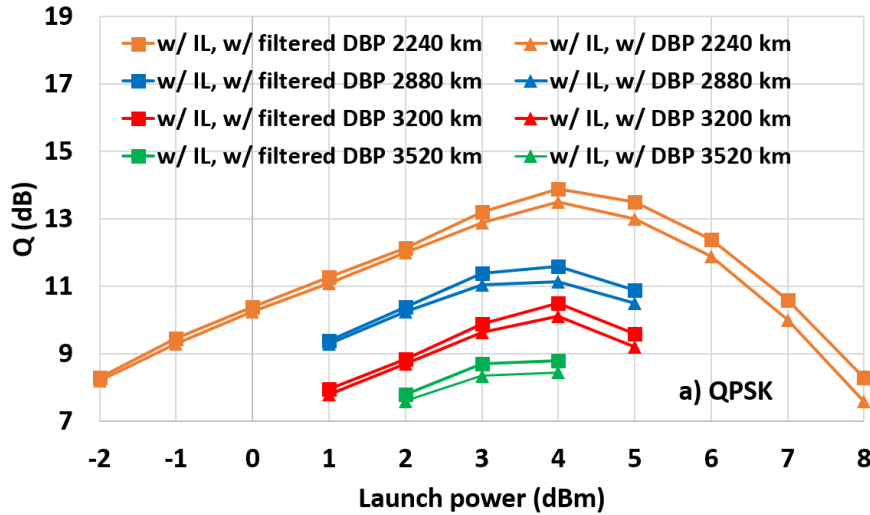
-24.5 dBm. At this optimum power, the phase transfer baseband bandwidth of the OIL was observed as shown in Fig. 5.24 (blue line). The high-pass filter is supposed to attenuate the frequencies that are passed through by the OIL. As such, the stop-band is chosen from 0 to 700 MHz and pass-band from 0.9 GHz onwards. As a result, the HPF passes those frequencies that suffer more than 5-dB attenuation by the OIL. The slope of the shelf HPF is purposely chosen as shown in Fig. 5.23. The choices of 0.7 GHz, 0.9 GHz as stopband and passband frequencies respectively were found to give optimized Q performance by repetitively checking different stop band frequencies and slope of the HPF. This result was found heuristically in our experimental setup and is not included in this thesis. Readers can pursue this project as future work for verification. If the passband frequency is reduced < 0.9 GHz and stopband is fixed at 0.7 GHz, the slope of the HPF rises quickly amplifying the ringing sidelobes in the subcarriers. This causes degradation in performance. The same problem appears if passband is fixed at 0.9 GHz and stopband is increased > 0.7 GHz. If the stopband and passband are both reduced < 0.7 GHz and < 0.9 GHz, the ringing is not amplified but the HPF does not exclude the effects of inter-channel nonlinear distortions as required. This causes overcompensation by DBP and again degrades the performance. If the stopband is fixed at 0.7 GHz and passband is increased > 0.9 GHz, the slope of HPF reduces but this increases the risk of passing the ringing-sidelobes of the subcarriers or the subcarriers themselves through (guard band = 1.25 GHz in baseband), causing performance degradation again. The same degradation effect is observed if both stopband and passband are increased > 0.7 GHz and 0.9 GHz respectively. This justifies our choice of choosing the stopband and passband frequencies that results in HPF passing all the frequencies that suffer ≥ 5 -dB attenuation from the OIL.

5.2.4 Experimental results

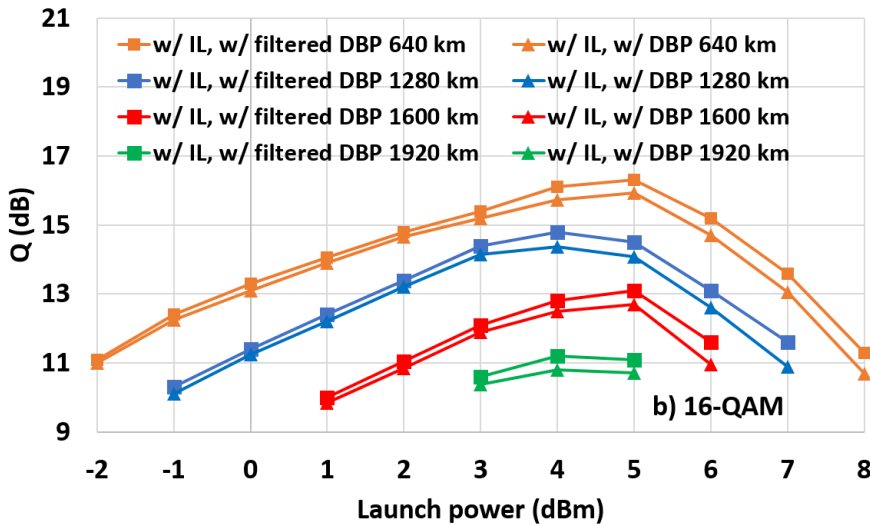
The experimental setup is same as in previous section as shown in Fig. 5.19. The sequence of DSP flow is shown in Fig. 5.23. Due to the OIL setup, the frequency offset estimation and correction is omitted. The received signal samples were passed through the DBP. For this, each span of length 80 km was divided in to 20 steps and the chromatic dispersion parameter β_2 is taken as 16 ps/(nm·km). The nonlinearity coefficient γ is calculated as

$$\gamma = \frac{2\pi n_2}{\lambda A_{eff}} \quad (5.15)$$

where $n_2 = 2.6 \times 10^{-20}$ and the effective core area, $A_{eff} = 80 \mu m$. λ is the center carrier wavelength. After back-propagation, the frame-synchronization using a pre-defined preamble is performed. The frame is passed through FFT and the OFDM symbols were extracted. The channel response was estimated and rectified from the signal using training symbols. Finally, the residual phase mismatch or phase offsets were removed by training-based maximum likelihood (ML) phase estimation algorithm to recover the transmitted symbols.



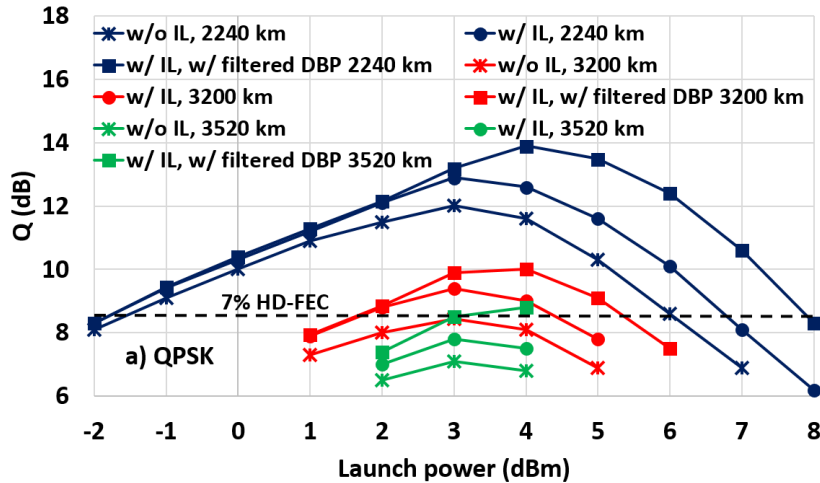
(a) QPSK.



(b) 16-QAM.

Figure 5.25: Q (dB) vs. launch power (dBm) of system with (squares) and without filtering (triangles) in DBP.

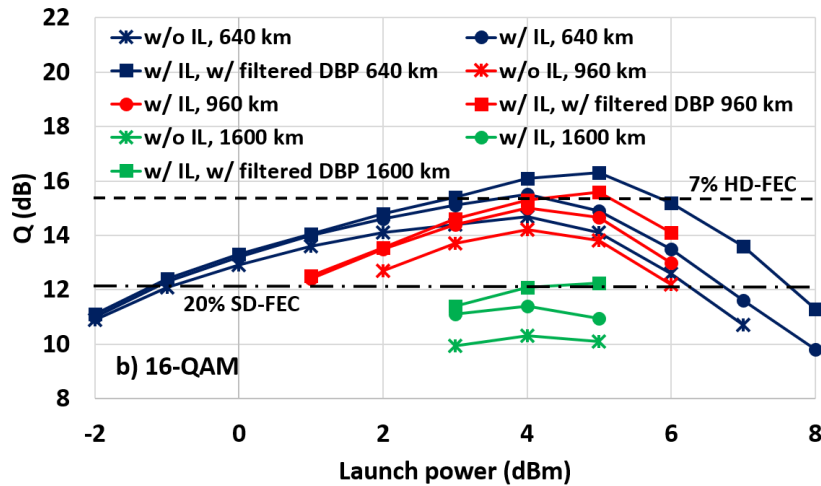
The modulated signal was initially transmitted over different transmission lengths by varying the number of times the signal loops through the recirculating loop (each loop adds 320 km to the transmission distance). The effect of filtering the signal in DBP with a shelf-HPF is shown in Fig. 5.25. For all the cases in this comparison (filtered or unfiltered DBP), the system implements OIL for XPM compensation. As mentioned in previous section, the unfiltered-DBP performs sub-optimally due to overcompensation of low-frequency intra-channel nonlinear distortions. It is observed that there is room for improvement which is achieved by the filtered DBP. The concept was tested for both QPSK and 16-QAM modulation formats. For both cases, the filtered-DBP gave a Q performance improvement of 0.4-0.5 dB in the nonlinear regime. A marginal 0.1-0.2 dB improvement in the noise-dominant low power regime is also observed. This improvement could be attributed to the ASE noise filtering effect of the HPF in the guard band region. Thus, with this optimization performed using filtered-DBP we compare the

Figure 5.26: Q vs. launch power comparison for QPSK.

overall performance improvement from OIL+filtered-DBP system over a conventional system without nonlinearity compensation.

For complete comparison, a reference curve without any nonlinearity compensation by OIL or DBP is plotted over launch power sweep (asterisk markers). In this case, the slave laser in the OIL is in free running mode i.e. there is no power injection. As a result, the frequency offsets need to be taken care of in the DSP, which is done using a spectral-peak search method. Next the received signal is injected into the OIL setup with a controlled injected power of -24.5 dBm. With the injection locking and the proposed setup for XPM compensation, an overall improvement in the Q performance of about 1 dB is observed as shown in Fig. 5.26 (circular markers) for all the transmission distances. Additionally, at 7% hard forward error correction limit ($Q=8.6$ dB, $BER = 3.8 \times 10^{-3}$), the OIL based XPM compensation makes transmission over 3200 km possible. It should be noted that OIL based recovery is not only nonlinearity compensation but partially linear phase noise compensation as well. This results in marginal gain in the linear region and improves the performance plot in low and mid-OSNR region, such that the optimum launch power may seem to remain the same. Next the filtered-DBP algorithm is added in the DSP to mitigate the SPM effects. Fig. 5.26 shows the Q performance improvement with OIL+DBP system (square markers). An additional 0.9-dB improvement in the peak- Q (1.9-dB improvement compared to reference) is observed for all the transmission distances considered. Also, a 2-dB improvement in the launch power threshold at the 7% HD-FEC limit is seen. In terms of maximum reachable transmission lengths, the system with OIL+DBP now crosses the HD-FEC threshold for distances up to 3520 km. Hence, a boost of 320 km in transmission length without errors using simple Reed Solomon RS(255,233) error-correcting codes is achieved.

Similar results are observed in the case of 16-QAM modulated signals (Fig. 5.27). The OIL-based XPM compensated increases the peak- Q by 0.7 dB, increased further by 0.9 dB when cascaded with the filtered-DBP. With OIL based XPM compensation alone the the maximum transmission distance to cross

Figure 5.27: Q vs. launch power comparison for 16-QAM.

the HD-FEC limit increases to 640 km. On addition of filtered-DBP, this maximum reach further increases to 960 km. In case when 20% soft-decision FEC is considered, the maximum transmission reach that can be achieved without errors using soft decision LDPC codes concatenated by convolutional codes is 1600 km for 16-QAM. By adding the filtered-DBP in the system, a 1-dB improvement in the required launch power is observed at peak- Q for both modulation formats, thus allowing for the signals to be launched at higher powers for longer distances. Overall, the OIL+DBP system proves to be capable of boosting the transmission reach and the Q performance by compensating for the XPM-dominated nonlinear phase noise and the SPM accumulated by the signal on transmission over longer distances.

There are expected trade-offs between the width of the guard-band employed to host the residual carrier, and performance, especially when considering the overall capacity. At higher injection ratios, the leakage of data sidebands into the recovered carrier reduce performance. Clearly, with a wide guard-band, this effect could be reduced, but at the cost of lost capacity. This change in guard-band is also likely to influence the optimal carrier-to-signal power ratio. An argument can also be made that the spectral benefits achieved by using OFDM may be lost by adding a guard band. A full investigation of this trade-off between the spectral benefit for the applied OFDM parameters, the width of guard band and channel capacity would benefit from using mutual information as a metric.

Fig. 5.15 shows that the XPM effect drops by 20 dB within 1-GHz modulation bandwidth for 3200 km links. For 320-km links, though XPM is quite low, but it stays almost constant up to 2.5 GHz. On the other hand, the phase transfer bandwidth of OIL for a flat-spectrum signal shows a lorentzian shape and is not flat (Fig. 5.18). The width of this Lorentzian shape increases with the injected power, up to the point when the OIL system enters the chaotic regime. As a result, the OIL will completely or partly, transfer the XPM phase distortions to be cancelled further, according to the link length and injected power. As such, for complete or better cancellation of XPM, shorter links will require more injected power than

the longer links. This change of required injected power according to link lengths could be an issue in optical WDM networks where it is difficult to determine the length that individual channel has traversed. Further investigation on required injected power against link length, thus, needs to be performed.

The nonlinear inter-channel noise (NLIN) addressed in this thesis is a specific case when the XPM dominates the NLIN for many short spans for long overall link. However, the NLIN contributes to amplitude noise and polarization rotations too along with phase distortions [163]. The amplitude noise is dominant over the polarization rotations and phase distortions for low channel spacing between the WDM channels. Moreover, the OIL system transfers only the phase distortions for further cancellation and not the amplitude distortions. As a result, the proposed OIL-based NLIN cancellation can tackle only the phase distortion part of NLIN. The OIL setup will not be affected by the polarization-rotations induced by nonlinear interactions because we use the polarization-independence module. Nonetheless, these polarization rotations will cause cross-polarization effects in the received signal and has to be negated in the offline DSP. Further investigation of the proposed OIL-based NLIN compensation against link lengths, channel spacing and number of spans will enlighten us more on this system. These are some issues that would need to be investigated before turning the proposed system for feasible commercial implementation over field links and optical networks.

5.2.5 Conclusions

The OIL-based carrier recovery has been researched for decades now. This chapter proposed techniques to make the OIL-based carrier recovery practical to implement in field links. The experimental verifications and the field tests proved the reliability of the proposed concepts. The OIL-based carrier recovery was made independent of the signal's polarization, which is a big issue in field links. Moreover, the OIL was used for nonlinearity compensation in addition to carrier recovery. Thus, the proposed technique reduces the DSP latency as the CFO estimation and inter-channel nonlinearity compensation algorithms are no longer required. The OIL also partially compensates for the laser phase noise as against the OEFOE in previous chapter. This benefit, however, comes at the cost of increased hardware complexity. Thus, trade-offs exist between system's computation/hardware complexity and system's latency in data-recovery over the various techniques explored in this thesis.

Conclusions

In this thesis, different approaches and methods have been investigated that work to achieve or aid carrier recovery in optical communications systems. The proposed methods target one or more aspects of carrier recovery; some techniques provide additional utilities. This is shown in Table 6.1. The proposed methods are discussed across Chapters 3-5.

Proposed techniques and compensation capabilities			
Technique	Carrier frequency offset	Phase noise	Additional utility
Parallelized Kalman filters for single carrier system	✓	✓	✗
Joint polarization-state and phase noise tracking	✗	✓	Polarization state tracking
Optoelectronic frequency offset estimator	✓	✗	✗
Polarization-independent optical injection locking	✓	✓(Partial)	Maintained injection lock with drifting polarization
Optical injection locking based nonlinearity compensation	✓	✓(Partial)	Nonlinear phase noise compensation

Table 6.1: Proposed techniques with their compensation capabilities.

Chapter 1 discussed the problems addressed in this thesis covered under the broad topic of carrier recovery in optical communications. A brief explanation about the effects of these problems such as carrier frequency offset, phase noise and nonlinear interference noise was given. Also, the techniques proposed to mitigate these effects were briefly discussed along with their pros and cons.

Chapter 2 talked about the important inventions and research in the field of communications and carrier recovery that led to the present techniques. The chapter started with techniques proposed for carrier recovery in wireless radio frequency communication systems followed by many of them being inherited for optical communication systems and then techniques developed specially for optical communications.

Chapter 3 focused on the digital signal processing approach for carrier recovery. Kalman filters, being proved as the optimum estimators were investigated. They were investigated for two applications namely, parallel processing architecture for carrier recovery and joint phase-noise and polarization state tracking. For the first application, a blind, unscented Kalman filter implemented as parallelized architecture for carrier recovery in single-carrier optical systems was proposed. Its performance was compared with previously proposed parallelized LKF. For block lengths optimized for Q performance, the UKF reduces the computation time by 1.7 times than that of parallelized LKF. At the same time, the UKF requires 1.2 dB and 0.8 dB lower OSNR at the 7% hard FEC limit compared with the LKF for both QPSK and 16-QAM modulated signals respectively. These improvements in computation time and required OSNR were observed to be better for longer blocks. The proposed system was verified to perform successfully over an 800-km long-haul link, where the UKF gives 2.3-dBm improvement in the required launch power at hard FEC limit over LKF that reduces with the order of modulation. This study shows that in the case of parallelized architectures, for specific applications of carrier recovery in optical communication systems, an unscented Kalman filter can prove to be a better option than a linear Kalman filter. The benefit, however, comes at the cost of increased processing hardware requirements.

For the second application, an unscented Kalman filter was investigated and compared with the previously proposed extended Kalman filter for joint polarization state tracking and phase noise mitigation. A comparison was also made with conventional blind CMA algorithms for QPSK and MMA for 16-QAM modulation formats. It was shown through experiments that the proposed UKF for joint polarization and phase tracking outperforms the previously proposed EKF algorithm and the conventional CMA+VVPE/MMA+ML algorithms at the cost of increased complexity. The EKF showed no improvement over CMA+VVPE algorithm on a QPSK modulated signal throughout the OSNR range investigated and very marginal improvement over MMA+ML algorithm for higher QAM modulation formats at high OSNRs. The reduced-complexity versions of the UKF and EKF, R-UKF and R-EKF were also proposed for this application. The R-UKF outperformed both EKF and CMA +VVPE/MMA+ML for moderate and higher OSNRs (i.e. >10 dB for QPSK and >13 dB for 16-QAM), while requiring fewer computations than the EKF. Although the R-EKF was less complex than the EKF, its performance was compromised for target OSNRs (i.e. <18 dB for QPSK and <16 dB for 16-QAM). After transmission over an 800-km optical fiber link, all of the algorithms attained their peak performance at same launch powers;

the UKF and R-UKF outperformed the other algorithms, whose performances were similar except for low launch power region where the EKF showed marginal improvement over CMA+VVPE and R-EKF. In the case of 16-QAM signals, the UKF required the lowest launch power at the 7% hard FEC limit followed by R-UKF, EKF, R-EKF and MMA+ML. Overall, the Kalman filters gave flexibility against changes in modulation formats as compared with the conventional systems. An UKF gave optimum performance over all other algorithms at the cost of increased computational complexity. In case of systems that require lower complexity, an R-UKF proved to be an appropriate choice if its OSNR requirements are met. Here, the R-UKF proved to be optimum with its gains in computational complexity and performance. Less computational complexity can be translated to less hardware requirements, but very less can be said about the latency of the system as that would depend on the processing architecture design.

Chapter 4 focused on the frequency offset aspect in carrier recovery of optical communication systems. An optoelectronic carrier-frequency offset estimator that replaces the computationally expensive estimation DSP algorithms was designed and tested using simulations. The system was designed in two versions, one suitable to integration on a photonic chip while the other suitable to be implemented in a lab with discrete equipments. Both the versions use passive optical components and avoid the use of high-speed photodiodes or high-speed analog-to-digital converters. For a 28-Gbaud OFDM signal ($N=156$, 100 subcarriers), the system can estimate CFO up to ± 1250 MHz with estimate errors $< 4\%$. The simulations with varying cyclic prefix lengths suggested the CP length to be fixed $\geq 15\%$ to maintain the errors $< 1\%$. The system was found to be robust to the chromatic dispersion, laser linewidth, self-phase modulation, AWGN noise in the channel and the launch powers in a transmission link. Hence, the system provides an efficient way towards reducing the load on digital signal processing. The reduction in the DSP latency can be expected to be about 6-8%, depending on the CFO estimation algo, with a slight increase in hardware complexity.

Chapter 5 looked into the all-optical processing approach of optical injection locking for carrier recovery. In the first half of the chapter, the proposed methods helped the sustainability of the OIL-based carrier recovery rather than performing it. A pluggable module was proposed that, when attached before the OIL setup, rendered the OIL independent of the incoming signal's polarization state. This was achieved without any considerable loss in the Q performance. The system was tested over a 20-km field link, using a 40-MHz LW, 0.5-dBm transmitter laser. The random fluctuations in the polarization of the signal due to random events in the surroundings of the link were taken care of by the proposed module. The resulting continuously-locked OIL setup cancelled the phase noise effects of the broad LW laser. Thus, the complete setup with the proposed module along with the IL relaxed the constraints on the laser specifications and proved to be capable for practical implementation, which was difficult until now due to the polarization-sensitivity of OIL's mechanism.

In the second half, an all-optical processing approach for nonlinear phase noise compensation, using optical injection locking, was proposed. The concept was experimentally verified on an OFDM signal in a WDM system. The method resulted in 1-dB (QPSK) and 0.7-dB (16-QAM) improvement in Q in the nonlinear power regime, compared with a conventional intradyne receiver. With an injection ratio of -45 dB, the transmission reach of the system was increased by 1 loop of the recirculating loop (320 km) in the experimental setup before hitting the FEC limit. Thus, the proposed system can extend the transmission distance of optical communication networks, only requiring a sub-system modification at the receiver to avoid changes to fiber transmission infrastructure. Similar to the optoelectronic approach, the all-optical processing approach also gave latency gains with increase in hardware complexity.

The Q -performance improvements of the proposed methods in this thesis are shown in Fig. 6.1. The improvements are given in comparison with the respective conventional methods used for the different applications.

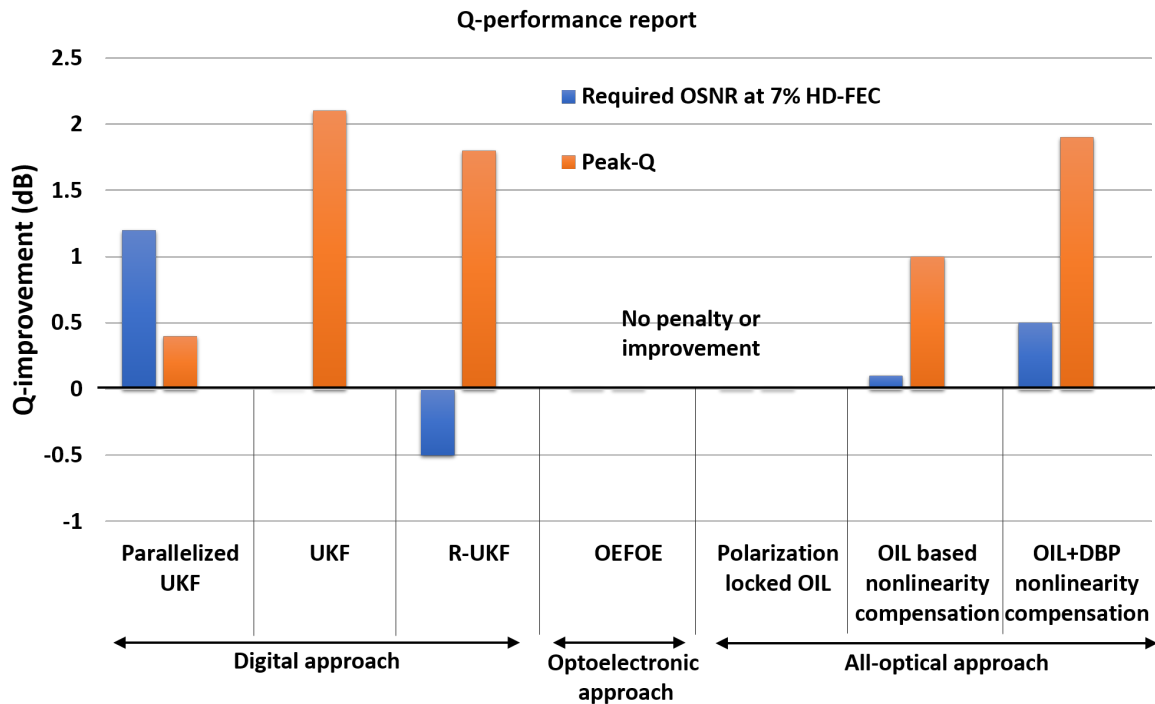


Figure 6.1: Q -performance report of the proposed carrier-recovery methods.

Performance report 👍 : Gain, 👎 : Penalty			
Technique	Q performance	Latency	Complexity
Parallelized Kalman filters for single carrier system	👍	👍	👎
Joint polarization-state and phase noise tracking	👍 👎 (low OSNRs in R-UKF)	👎 (for UKF) 👍 (for R-UKF)	👎 (for UKF) 👍 (for R-UKF)
Optoelectronic frequency offset estimator	Unchanged	👍	👍 (Computational) 👎 (Hardware)
Polarization-independent optical injection locking	Unchanged	👍	👍 (Computational) 👎 (Hardware)
Optical injection locking based nonlinearity compensation	👍	👍	👍 (Computational) 👎 (Hardware)

Table 6.2: Performance of the proposed techniques with respect to the requirement aspects.

From all these methods investigated, a common revelation appears. Various performance parameters such as the Q performance, latency, hardware complexity or computational complexity are involved for selecting an approach. The choice may vary for different application scenarios. All the techniques in the literature or proposed in this thesis give gains in one or more of these parameters at the cost of some other parameter. This can be seen in Table 6.2. A technique that gives benefits in all these parameters does not exist yet. Attempts can only be made to approach that ideal solution that may or may not exist. Though this research-journey towards optical carrier recovery has slowed down in past few years, it has yet not reached its ultimate, ideal destination.

Appendix

7.1 Appendix A: Parallelized unscented Kalman filter architecture and algorithm

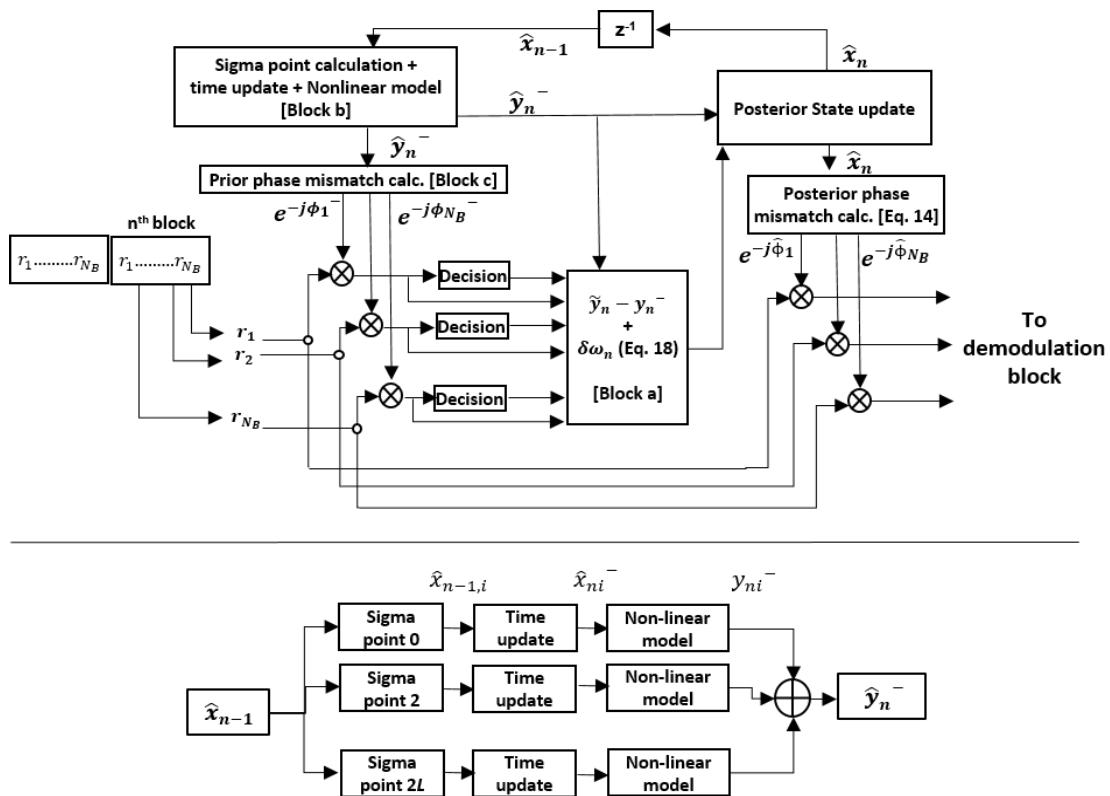


Figure 7.1: (a) Architecture of parallelized unscented Kalman filter. (b) Internal structure of Block A.

The unscented Kalman filters, unlike the linear Kalman filters, can perform for nonlinear models [86]. The UKF predicts the estimates by choosing a specific number of sigma points from the previous estimates and passing each of them through the nonlinear observation model, the output of which gives more accurate predictions of the unknown parameters for current time instance. Fig. 7.1 shows the architecture of the parallelized UKF system. The step-by-step processing algorithm of this structure is given as follows.

Unscented Kalman filter algorithm

Given: $\hat{x}_{k-1} = [\hat{\theta}_{k-1} \ \hat{\omega}_{k-1}]$, the estimates from $(k-1)^{th}$ block and the covariance matrix P_{k-1} . Here, θ_k and ω_k are the midpoint and the slope of the phase mismatch in k^{th} block respectively.

Prediction stage

From the previous block estimates \hat{x}_{k-1} the sigma points are calculated (Fig. 3.21(b)).

Calculate Sigma points:

i^{th} sigma point: $\hat{x}_{k-1,i} = \hat{x}_{k-1} + \sqrt{(L+\lambda)(P_{k-1})_{ii}}$; for $i=1 \dots L$

i^{th} sigma point: $\hat{x}_{k-1,i} = \hat{x}_{k-1} - \sqrt{(L+\lambda)(P_{k-1})_{ii}}$; for $i=L+1 \dots 2L$

where: $\lambda = L(10^{-3} - 1)$ is the scaling parameter, L is the number of parameters to be estimated. Here, $L=2$ as two parameters, θ and ω are being estimated. $(P_{k-1})_i$ is the i^{th} column of P_{k-1} .

Time Update:

$$\hat{x}_{k,i}^- = A\hat{x}_{k-1,i}; \quad i = 1 \dots 5. \quad (7.1)$$

where: $A = \begin{bmatrix} 1 & N_B \\ 0 & 1 \end{bmatrix}$. The time updated sigma points are each passed through the nonlinear observation model as

$$y_{k,i}^- = [e^{j\hat{x}_{k,i}^-(0)} \ \hat{x}_{k,i}^-(1)]^T; \quad i = 1 \dots 5. \quad (7.2)$$

$$\hat{y}_k^- = \sum_{i=1}^5 w_i y_{k,i}^- \quad (7.3)$$

$$P_k^- = \sum_{i=1}^5 w_i^c (y_{k,i}^- - \hat{y}_k^-)(y_{k,i}^- - \hat{y}_k^-)^* + Q \quad (7.4)$$

where $\alpha^2 = 10^{-3}$ determines the spread of sigma points and β is used to incorporate prior knowledge of the distribution ($\beta = 2$ is optimum for Gaussian distribution [86]). The weights in Eqs. (7.3) and (7.4) are given as $w_1 = \lambda/(L+\lambda)$; $w_1^c = \lambda/(L+\lambda) + 1 - \alpha^2 + \beta$; $w_{2\dots 5} = w_{2\dots 5}^c = 1/2(L+\lambda)$ [86]; and the covariance $Q = \begin{bmatrix} 0 & 0 \\ 0 & 10^{-3} \end{bmatrix}$. These sigma points, being independent of each other can be calculated in parallel. Thus, the complete process of calculating \hat{y}_k^- from \hat{x}_{k-1} in Block A of Fig. 3.21(a) can be parallelized as shown in Fig. 3.21(b). The phase mismatch at each sample for current k^{th} block is then predicted in Block B of Fig. 3.21(a) using-

$$\phi_n^- = \hat{y}_k^-(0) + \left(n - \frac{N_B + 1}{2} \right) \hat{y}_k^-(1); \quad n = 1 \dots N_B \quad (7.5)$$

Update stage

The state parameters are updated in this stage as follows (see Fig. 3.21(a)).

$$s_{n,k} = r_{n,k}e^{-j\phi_n^-}; \quad d_{n,k} = \text{decision}(s_{n,k}) \quad (7.6)$$

where $r_{n,k}$ is the n^{th} sample of k^{th} block of the received signal. The final updated state parameters are calculated as

$$\hat{x}_k = \hat{x}_{k-1} + K_k \begin{bmatrix} \tilde{y}_k - \hat{y}_k^- \\ \delta\omega_k \end{bmatrix} \quad (7.7)$$

$$P_k = (I_{2 \times 2} - K_k)P_k^- \quad (7.8)$$

where the innovation, $\delta\omega_k$ is given as $\delta\omega_k = \frac{\text{Im} \left[\sum_{n=1}^{N_B} \left(n - \frac{N_B+1}{2} \right) s_{n,k} d_{n,k}^* \right]}{\text{Re} \left[\sum_{n=1}^{N_B} \left(n - \frac{N_B+1}{2} \right)^2 s_{n,k} d_{n,k}^* \right]}$ and

$$\tilde{y}_k = s_{(N_B=1/2),k} \times (d_{(N_B=1/2),k})^* \quad (7.9)$$

The LKF calculates the innovation of θ *i.e.* $\delta\theta_k$ along with $\delta\omega_k$ in block **a**. As this is avoided in UKF, it benefits in latency. The Kalman gain is $K_k = P_k^- (P_k^- + R)^{-1}$ and the covariance matrix $R = \begin{bmatrix} 10^{-3} & 0 \\ 0 & 10^{-4} \end{bmatrix}$. The covariance matrices are taken from [12] and improved upon by trial and error to optimize Q . The estimates $\hat{x}_k = [\hat{\theta}_k \hat{\omega}_k]$ in Eq. (7.7) are then used to calculate the phase mismatches of each sample in the k^{th} signal block by interpolation, again using Eq. (3.13). The received signal samples are then compensated for these mismatches and sent for demodulation.

7.2 Appendix B: Chosing co-ordinate system for joint phase-noise and polarization-state observation model

The conventional mathematical model or Jones matrix for any birefringent material is given as [164]

$$M = \begin{bmatrix} e^{j\eta/2}\cos^2\vartheta + e^{-j\eta/2}\sin^2\vartheta & (e^{j\eta/2} - e^{-j\eta/2})e^{-j\Phi}\cos\vartheta\sin\vartheta \\ (e^{j\eta/2} - e^{-j\eta/2})e^{j\Phi}\cos\vartheta\sin\vartheta & e^{-j\eta/2}\cos^2\vartheta + e^{j\eta/2}\sin^2\vartheta \end{bmatrix} \quad (7.10)$$

where, η is the relative phase retardation induced between the fast axis and the slow axis, ϑ is the orientation of the fast axis with respect to the horizontal axis and Φ is the circularity *i.e.* $\Phi = 0$ for linear retarders and $\Phi = \pm\pi/2$ for circular retarders. It can be observed that M forms a scaled unitary matrix that agrees with the properties of a Jones matrix.

The elements of Jones matrix, M , are complex and can be written in phasor form as Xe^{jY} or in Cartesian form as $a + jb$. In this work, the Cartesian form is chosen for the Jones matrix as follows-

$$M = \begin{bmatrix} a + jb & c + jd \\ -c + jd & a - jb \end{bmatrix} \quad (7.11)$$

The reason for choosing the Cartesian form lies in context to using the Kalman filters that require the parameters (to be estimated) to follow the Wiener process, *i.e.* an unknown parameter z should follow $z_{n+1} = z_n + \Delta z$. The suffix denotes the time instance and Δz is normal distributed such that $\Delta z \sim \mathcal{N}(0, \sigma_z^2)$. Since the real and imaginary parts of the elements of M follow Wiener procedure [13], cartesian form is considered.

It may be possible that some researchers may favour to use the phasor form instead of Cartesian for reasons of their own. Nonetheless, it can be proved that using the phasor form does not work in Kalman filters. Consider the matrix element $a + jb$ with equivalent phasor form Xe^{jY} where a and b follow the Wiener process *i.e.* $a_{n+1} = a_n + \Delta a$ and $b_{n+1} = b_n + \Delta b$. Thus, in order to use Xe^{jY} in Kalman filters, X and Y should also follow Wiener process.

$$X_n = \|a_n + jb_n\| = \sqrt{a_{n-1}^2 + b_{n-1}^2 + \Delta a^2 + \Delta b^2 + j2a\Delta a + 2b\Delta b} \quad (7.12)$$

$$X_n = X_{n-1} \left(\sqrt{1 + \frac{\Delta a^2 + \Delta b^2 + j2a\Delta a + 2b\Delta b}{X_{n-1}^2}} \right) \quad (7.13)$$

Now consider $\Delta X = X_n - X_{n-1}$.

$$\Delta X = X_{n-1} \left(\sqrt{1 + \frac{\Delta a^2 + \Delta b^2 + j2a\Delta a + 2b\Delta b}{X_{n-1}^2}} - 1 \right) \quad (7.14)$$

The term $(\Delta a)^2 + (\Delta b)^2$ is exponential distributed and $(2a\Delta a + 2b\Delta b)$ is Gaussian distributed, Δa and Δb being Gaussian distributed. Thus, the addition of an exponential and Gaussian distribution is definitely not Gaussian. As a result, ΔX is not Gaussian distributed and X does not follow Wiener process, making phasor form Xe^{jY} unsuitable for Kalman filters.

Intuitively, since X is a non-zero magnitude, $X_n - X_{n-1} = (X_n - r)$ for $X_{n-1} =$ any positive number ' r '. Thus, the range within which $\Delta X = X_n - X_{n-1}$ can take values is $[-r, \infty]$. In order to make the distribution of X_n to take values within range $[-\infty, \infty]$, X_{n-1} has to take value ∞ that is not possible in practical systems. This contradicts the properties of Gaussian distribution that has the limits $[-\infty, \infty]$. As a result, again, ΔX is not Gaussian distributed and X does not follow Wiener process, making phasor form Xe^{jY} unsuitable for Kalman filters.

7.3 Appendix C: Unscented Kalman filter algorithm for joint phase noise and polarization-state tracking

Algorithm 5 Alg.5: UKF for joint phase noise and polarization-state tracking

Given:

L: Number of unknown parameters to be estimated

L=5 for UKF and EKF; L=3 for R-UKF and R-EKF.

$$\lambda = L(10^{-3} - 1)$$

$$\alpha^2 = 10^{-3}$$

$$\beta = 2$$

$$w_1 = \lambda / (L + \lambda)$$

$$w_1^c = \lambda / (L + \lambda) + 1 - \alpha^2 + \beta$$

$$w_{2 \dots (2L+1)} = w_{2 \dots (2L+1)}^c = 1/2(L + \lambda)$$

$$S_1 = [0, 0, \dots, 0]_{1 \times L}^T$$

$$P_1 = [0]_{L \times L}$$

$$A = I_{L \times L}$$

$$Q = 10^{-5}$$

$$R = 10^{-1}$$

for $k = 1 : N$ **do**

▷ For N signal samples

Time update equations:

A.5.1: $S_k^- = AS_{k-1}$

A.5.2: $P_k^- = AP_{k-1}A^T + Q$

Calculate sigma points:

A.5.3: $(S_k)_i^- = S_k^- + \sqrt{(L + \lambda)(P_k^-)_i}$; for $i=1 \dots L$

A.5.4: $(S_k)_i^- = S_k^- - \sqrt{(L + \lambda)(P_k^-)_i}$; for $i=L+1 \dots 2L$

▷ $(P_k^-)_i$ is the i^{th} column of the matrix P_k^-

A.5.5: $S_{kf} = \sum_{i=1}^{2L+1} w_i (S_k)_i^-$

Measurement update equations:

For UKF:

A.5.6: $t_{k,i} = e^{-j[(S_k)_i^-(5)]} \begin{bmatrix} (S_k)_i^-(1) + j(S_k)_i^-(2) & (S_k)_i^-(3) + j(S_k)_i^-(4) \\ -(S_k)_i^-(3) + j(S_k)_i^-(4) & (S_k)_i^-(1) - j(S_k)_i^-(2) \end{bmatrix} \begin{bmatrix} Z_x \\ Z_y \end{bmatrix}$

For R-UKF:

A.5.7: $t_{k,i} = e^{-j[(S_k)_i^-(3)]} \begin{bmatrix} (S_k)_i^-(1) & (S_k)_i^-(2) \\ -(S_k)_i^-(2)^* & (S_k)_i^-(1)^* \end{bmatrix}$

A.5.8: $\hat{t}_k = \sum_{i=1}^{2L+1} w_i t_{k,i}$

A.5.9: $P_{tt} = \sum_{i=1}^{2L+1} w_i^c (t_{k,i} - \hat{t}_k)(t_{k,i} - \hat{t}_k)^* + R$

A.5.10: $P_{ts} = \sum_{i=1}^{2L+1} w_i^c ((S_k)_i^- - S_{kf})(t_{k,i} - \hat{t}_k)^*$

A.5.11: $K_k = P_{ts} P_{tt}^{-1}$

A.5.12: $S_k = S_{kf} + K_k(\hat{t}_k - \text{decision}(\hat{t}_k))$

A.5.13: $P_k = P_k^- - K_k P_{tt} K_k^*$

end

7.4 MATLAB codes

7.4.1 UKF for joint polarization-state and phase-noise tracking code.

The following code executes an unscented Kalman filter for specific application of joint SOP and PN tracking. The code takes 'sig_in' as an input signal array of dimensions "2xN" where each row represents samples taken in each of the X and Y polarizations. N is the total number of samples taken. The output 'sig_out' also holds the same format. M is the modulation order of M-QAM. The values of 'R', 'Q' and other initial parameters are chosen such that they achieve the optimum performance. They may vary for other setups. The initial decisions should be correct to achieve accurate tracking. If not, training symbols can be used. However, they were not observed necessary in our experiments.

```
function [sig_out]=UKF_SOP_PN(sig_in)
%%-----initialisation-----
S0=[0.01;0;0;0;0];
P0=0;
A=eye(5);
polvar=10^-1;
thetavar=10^-8;
Q=[polvar 0 0 0 0;0 polvar 0 0 0;0 0 polvar 0 0;0 0 0 polvar 0;...
  0 0 0 0 thetavar];
R=10^-1;
alphasqr=10^-3;
beta=2;
lamda=5*(alphasqr-1);
wm0=lamda/(5+lamda);
wc0=wm0+(1-alphasqr+beta);
wm1=1/(2*(5+lamda));
wm2=wm1;
wcl=wm1;
wc2=wm1;
%%UKF code
for jj=1:length(sig_in,M)
  %%-----time update-----
  Sminus=A*S0;
  Pminus=A*P0*A'+Q;
  %%-----Calculate Sigma points-----
  sig0=Sminus;
  sig1=Sminus+(sqrt((5+lamda).*(Pminus(:,1)))));
  sig2=Sminus+(sqrt((5+lamda).*(Pminus(:,2)))));
  sig3=Sminus+(sqrt((5+lamda).*(Pminus(:,3)))));
  sig4=Sminus+(sqrt((5+lamda).*(Pminus(:,4)))));
  sig5=Sminus+(sqrt((5+lamda).*(Pminus(:,5)))));
  sig6=Sminus-(sqrt((5+lamda).*(Pminus(:,1)))));
  sig7=Sminus-(sqrt((5+lamda).*(Pminus(:,2)))));
  sig8=Sminus-(sqrt((5+lamda).*(Pminus(:,3)))));
  sig9=Sminus-(sqrt((5+lamda).*(Pminus(:,4)))));
  sig10=Sminus-(sqrt((5+lamda).*(Pminus(:,5)))));

  sighatminus=(wm0*sig0+wm1*sig1+wm2*sig2+wm2*sig3+wm2*sig4+wm2*sig5+wm2...
  *sig6+wm2*sig7+wm2*sig8+wm2*sig9+wm2*sig10);

  %%-----Transfer sigma points through the nonlinear model-----
  v0=exp(1i*sig0(5))*[sig0(1)+1i*sig0(2) sig0(3)+1i*sig0(4);...
    -sig0(3)+1i*sig0(4) sig0(1)-1i*sig0(2)]*[sig_in(1,jj);sig_in(2,jj)];
```

```

v1=exp(1i*sig1(5))*[sig1(1)+1i*sig1(2) sig1(3)+1i*sig1(4); ...
    -sig1(3)+1i*sig1(4) sig1(1)-1i*sig1(2)]*sig_in(:,jj);
v2=exp(1i*sig2(5))*[sig2(1)+1i*sig2(2) sig2(3)+1i*sig2(4); ...
    -sig2(3)+1i*sig2(4) sig2(1)-1i*sig2(2)]*sig_in(:,jj);
v3=exp(1i*sig3(5))*[sig3(1)+1i*sig3(2) sig3(3)+1i*sig3(4); ...
    -sig3(3)+1i*sig3(4) sig3(1)-1i*sig3(2)]*sig_in(:,jj);
v4=exp(1i*sig4(5))*[sig4(1)+1i*sig4(2) sig4(3)+1i*sig4(4); ...
    -sig4(3)+1i*sig4(4) sig4(1)-1i*sig4(2)]*sig_in(:,jj);
v5=exp(1i*sig5(5))*[sig5(1)+1i*sig5(2) sig5(3)+1i*sig5(4); ...
    -sig5(3)+1i*sig5(4) sig5(1)-1i*sig5(2)]*sig_in(:,jj);
v6=exp(1i*sig6(5))*[sig6(1)+1i*sig6(2) sig6(3)+1i*sig6(4); ...
    -sig6(3)+1i*sig6(4) sig6(1)-1i*sig6(2)]*sig_in(:,jj);
v7=exp(1i*sig7(5))*[sig7(1)+1i*sig7(2) sig7(3)+1i*sig7(4); ...
    -sig7(3)+1i*sig7(4) sig7(1)-1i*sig7(2)]*sig_in(:,jj);
v8=exp(1i*sig8(5))*[sig8(1)+1i*sig8(2) sig8(3)+1i*sig8(4); ...
    -sig8(3)+1i*sig8(4) sig8(1)-1i*sig8(2)]*sig_in(:,jj);
v9=exp(1i*sig9(5))*[sig9(1)+1i*sig9(2) sig9(3)+1i*sig9(4); ...
    -sig9(3)+1i*sig9(4) sig9(1)-1i*sig9(2)]*sig_in(:,jj);
v10=exp(1i*sig10(5))*[sig10(1)+1i*sig10(2) sig10(3)+1i*sig10(4); ...
    -sig10(3)+1i*sig10(4) sig10(1)-1i*sig10(2)]*sig_in(:,jj);

vhatminus=(wm0*v0+wm1*v1+wm2*v2+wm2*v3+wm2*v4+wm2*v5+wm2*v6+wm2*v7+wm2*v8+
wm2*v9+wm2*v10);

Pvv=wc0*(v0-vhatminus)*conj(v0'-vhatminus')+wc1*(v1-vhatminus)*conj(v1'-
vhatminus')+wc2*(v2-vhatminus)*conj(v2'-vhatminus')...
+wc2*(v3-vhatminus)*conj(v3'-vhatminus')+wc2*(v4-vhatminus)*conj(v4'-
vhatminus')+wc2*(v5-vhatminus)*conj(v5'-vhatminus')...
+wc2*(v6-vhatminus)*conj(v6'-vhatminus')+wc2*(v7-vhatminus)*conj(v7'-
vhatminus')+wc2*(v8-vhatminus)*conj(v8'-vhatminus')...
+wc2*(v9-vhatminus)*conj(v9'-vhatminus')+wc2*(v10-vhatminus)*conj(v10'-
vhatminus')+R;

Psv=wc0*(sig0-sihatminus)*conj(v0'-vhatminus')+wc1*(sig1-
sihatminus)*conj(v1'-vhatminus')+wc2*(sig2-sihatminus)*conj(v2'-
vhatminus')+wc2*(sig3-sihatminus)*conj(v3'-vhatminus')+wc2*(sig4-
sihatminus)*conj(v4'-vhatminus')+wc2*(sig5-sihatminus)*conj(v5'-
vhatminus')+wc2*(sig6-sihatminus)*conj(v6'-vhatminus')+wc2*(sig7-
sihatminus)*conj(v7'-vhatminus')+wc2*(sig8-sihatminus)*conj(v8'-
vhatminus')+wc2*(sig9-sihatminus)*conj(v9'-vhatminus')+wc2*(sig10-
sihatminus)*conj(v10'-vhatminus');

hhatminus=qamdemod(vhatminus,M);
hhatminus1=qammod(hhatminus,M);
%%-----Calculate Kalman gain-----
Kalmangain=Pvv/Psv;
%%-----Update estimates-----
S0=(Sminus+Kalmangain*(hhatminus1-vhatminus));
P0=Pminus-Kalmangain*Pvv*Kalmangain';
%%Use the estimates to recover the signal-----
sigout(:,jj)=exp(1i*S0(5))*[S0(1)+1i*S0(2) S0(3)+1i*S0(4);-S0(3)+1i*S0(4)
S0(1)-1i*S0(2)]*[sig_in(1,jj);sig_in(2,jj)];
end
end

```

7.4.2 R-UKF for joint polarization-state and phase-noise tracking code.

%The following code executes a reduced-unscented Kalman filter (R-UKF) for %specific application of joint SOP and PN tracking. The code takes 'sig_in' %as an input signal array of dimensions "2xN" where each row represents %samples taken in each of the X and Y polarizations. N is the total number of %samples taken. The output 'sig_out' also holds the same format. M is the %modulation order of M-QAM.

```
function [sig_out]=UKF_SOP_PN(sig_in)
%%-----initialisation-----
S0=[0.01;0;0];
P0=0;
A=eye(3);
polvar=10^-1;
thetavar=10^-8;
Q=[polvar 0 0;0 polvar 0;0 0 thetavar];
R=10^-1;
alphasqr=10^-3;
beta=2;
lamda=3*(alphasqr-1);
wm0=lamda/(3+lamda);
wc0=wm0+(1-alphasqr+beta);
wm1=1/(2*(3+lamda));
wm2=wm1;
wc1=wm1;
wc2=wm1;
%%UKF code
for jj=1:length(sig_in,M)
    %%-----time update-----
    Sminus=A*S0;
    Pminus=A*P0*A'+Q;
    %%-----Calculate Sigma points-----
    sig0=Sminus;
    sig1=Sminus+(sqrt((3+lamda).*(Pminus(:,1)))));
    sig2=Sminus+(sqrt((3+lamda).*(Pminus(:,2)))));
    sig3=Sminus+(sqrt((3+lamda).*(Pminus(:,3)))));
    sig4=Sminus-(sqrt((3+lamda).*(Pminus(:,1)))));
    sig5=Sminus-(sqrt((3+lamda).*(Pminus(:,2)))));
    sig6=Sminus-(sqrt((3+lamda).*(Pminus(:,3)))));
    sighatminus=(wm0*sig0+wm1*sig1+wm2*sig2+wm2*sig3+wm2*sig4+wm2*sig5+wm2*
        sig6);

    %%-----Transfer sigma points through the nonlinear model-----
    v0=exp(1i*sig0(3))*[sig0(1) sig0(2);-conj(sig0(2)) ...
        conj(sig0(1))]*[sig_in(1,jj);sig_in(2,jj)];
    v1=exp(1i*sig1(3))*[sig1(1) sig1(2);-conj(sig1(2)) ...
        conj(sig1(1))]*[sig_in(1,jj);sig_in(2,jj)];
    v2=exp(1i*sig2(3))*[sig2(1) sig2(2);-conj(sig2(2)) ...
        conj(sig2(1))]*[sig_in(1,jj);sig_in(2,jj)];
    v3=exp(1i*sig3(3))*[sig3(1) sig3(2);-conj(sig3(2)) ...
        conj(sig3(1))]*[sig_in(1,jj);sig_in(2,jj)];
    v4=exp(1i*sig4(3))*[sig4(1) sig4(2);-conj(sig4(2)) ...
        conj(sig4(1))]*[sig_in(1,jj);sig_in(2,jj)];
    v5=exp(1i*sig5(3))*[sig5(1) sig5(2);-conj(sig5(2)) ...
        conj(sig5(1))]*[sig_in(1,jj);sig_in(2,jj)];
```

```

v6=exp(1i*sig6(3))*[sig6(1) sig6(2);-conj(sig6(2)) ...
                    conj(sig6(1))]*[sig_in(1,jj);sig_in(2,jj)];
vhatminus=(wm0*v0+wm1*v1+wm2*v2+wm2*v3+wm2*v4+wm2*v5+wm2*v6;

Pvv=wc0*(v0-vhatminus)*conj(v0'-vhatminus')+wc1*(v1- vhatminus)*conj(v1'-
vhatminus')+wc2*(v2-vhatminus)*conj(v2'-vhatminus')....
+wc2*(v3-vhatminus)*conj(v3'-vhatminus')+wc2*(v4-vhatminus)*conj(v4'-
vhatminus')+wc2*(v5-vhatminus)*conj(v5'-vhatminus')....
+wc2*(v6-vhatminus)*conj(v6'-vhatminus')+R;

Psv=wc0*(sig0-sihatminus)*conj(v0'-vhatminus')+wc1*(sig1-
sihatminus)*conj(v1'-vhatminus')+wc2*(sig2-sihatminus)*conj(v2'-
vhatminus')+wc2*(sig3-sihatminus)*conj(v3'-vhatminus')+wc2*(sig4-
sihatminus)*conj(v4'-vhatminus')+wc2*(sig5-sihatminus)*conj(v5'-
vhatminus')+wc2*(sig6-sihatminus)*conj(v6'-vhatminus');

hhatminus=qamdemod(vhatminus,M);
hhatminus1=qammod(hhatminus,M);
%%-----Calculate Kalman gain-----
Kalmangain=Pvv/Psv;
%%-----Update estimates-----
S0=(Sminus+Kalmangain*(hhatminus1-vhatminus));
P0=Pminus-Kalmangain*Pvv*Kalmangain';
%%Use the estimates to recover the signal-----
sigout(:,jj)=exp(1i*S0(3))*[S0(1) S0(2);-conj(S0(2)) ...
                           conj(S0(1))]*[sig_in(1,jj);sig_in(2,jj)];
end
end

```

Published papers

Optics Letters

Parallelized unscented Kalman filters for carrier recovery in coherent optical communication

JOKHAKAR JIGNESH,^{1,*} BILL CORCORAN,^{1,2} AND ARTHUR LOWERY^{1,2}

¹Electro-Photonics Laboratory, Department of Electrical and Computer Systems Engineering, Monash University, Clayton, VIC 3800, Australia

²Centre for Ultrahigh-Bandwidth Devices for Optical Systems (CUDOS), Australia

*Corresponding author: jignesh.jokhakar@monash.edu

Received 18 March 2016; revised 12 May 2016; accepted 19 May 2016; posted 23 May 2016 (Doc. ID 261039); published 11 July 2016

We show that unscented Kalman filters can be used to mitigate local oscillator phase noise and to compensate carrier frequency offset in coherent single-carrier optical communication systems. A parallel processing architecture implementing the unscented Kalman filter is proposed, improving upon a previous parallelized linear Kalman filter (LKF) implementation. © 2016 Optical Society of America

OCIS codes: (060.1660) Coherent communications; (060.2330) Fiber optics communications.

<http://dx.doi.org/10.1364/OL.41.003253>

Coherent detection in optical communication systems has allowed for both expanded capacity through access to complex optical modulation formats and greater reach through the ability to mitigate signal transmission impairments [1]. Coupled with digital signal processing techniques at the receiver, chromatic dispersion and polarization mode dispersion can be compensated [2]. Signal-processing solutions are required for carrier recovery, which compensates for frequency offset (FO) between the signal carrier and the receiver local oscillator, as well as random phase noise (PN) due to phase drifts between the finite linewidth lasers.

Carrier recovery techniques can be broadly split into two categories: “blind” and “aided” techniques. Blind carrier recovery uses known intrinsic properties of the transmitted signal, e.g., the the Viterbi–Viterbi algorithm for quadrature-phase-shift-keyed (QPSK) signals, which can be used for phase noise compensation and frequency offset estimation [3]. A Viterbi–Viterbi algorithm has been proposed that uses a Weiner filter to update the weights [4]; however, since the statistical properties of the phase noise vary with time, Weiner filters do not give optimum estimates. For higher-order quadrature-amplitude modulation (QAM), different recovery algorithms need to be employed, e.g., radial decision-directed methods [2]. Decision-directed maximum-likelihood-based estimators [5] require perhaps the least drastic reconfiguration with different modulation formats, at the cost of computational complexity. Aided techniques, on the other hand, use predefined preambles, pilot symbols, or pilot frequency tones to allow for

frequency estimation and phase tracking, sacrificing some bandwidth efficiency [6–8].

As an alternative to these techniques, the Kalman filter is a “blind” technique for carrier recovery. Kalman filters can use a simple “slicer” [9] for decision-directed operation, with the slicer providing similar modulation-format flexibility to maximum-likelihood techniques but with considerably lower complexity. Moreover, Kalman filters have been shown to converge faster than least-mean squares or constant-modulus algorithm [9], and as an unbiased estimation technique [10], can minimize output signal variance toward an optimal minimum mean-squared error [9]. However, the performance improvement from Kalman filters comes at the cost of increased computational complexity, which can result in unwanted latency in systems.

Recently, a parallelized architecture implementing a linear Kalman filter (LKF) was proposed to perform carrier recovery [11] to improve computation speeds toward real-time implementation. In this Letter, we propose an improved Kalman filtering system, using a parallelized architecture to implement an unscented Kalman filter (UKF) [9]. While UKFs in serial architecture require more computational effort than LKFs, by exploiting parallelization, we show that UKFs can outperform LKFs in terms of computation time and system performance. Our proposed parallelized UKF gives a 1.2 and 0.8 dB improvement in required optical signal-to-noise ratio (OSNR) for QPSK at the 7% hard FEC (RS 255, 239) limit over the parallelized LKF for QPSK and 16 QAM modulated signals, respectively. Additionally the UKF needs only 60% of the computation time of LKF. Moreover, by comparing the performance of the candidate Kalman filters for both QPSK and 16 QAM modulated signals, we show that our proposed UKF can function with higher-order QAM modulation without drastic changes to the system. The proposed algorithm was also tested in an 800 km fiber transmission system and showed similar performance when using either a UKF or a LKF.

In parallelized implementations of both the UKF and LKF, the received sampled signal is divided into fixed-length blocks. Each block is processed in parallel by the Kalman filter to get the estimate of the slope of the phase mismatch in the k th block (ω_k) and the value of the mismatch at the midpoint of the k th block (θ_k). Thus, the state parameter vector to be estimated by

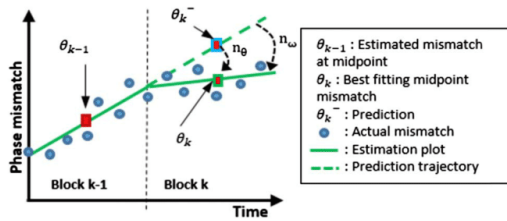


Fig. 1. Diagram showing the phase-tracking concept of the parallelized schemes.

the Kalman filters is $x_k = [\theta_k \ \omega_k]^T$. The estimated phase mismatch at each sample in the block, as shown in Fig. 1, is then calculated as $\phi_{m,k} = \theta_k + (m - \frac{N+1}{2})\omega_k$, where $\phi_{m,k}$ is the phase mismatch at the m th sample of the k th block, with each block having a length N . The parallelized Kalman filter runs once per block instead of for every sample in the case of sample-by-sample (serial) architecture.

In the case of the parallelized LKF proposed in [11], the state update equations are $\theta_{k+1} = N \cdot \omega_k + \theta_k$ and $\omega_{k+1} = \omega_k + n_f$, where N is the block length. The quantity n_f denotes the “process noise” (i.e., change in mismatch slope) between consecutive blocks. The observation model considered in case of LKF is [11] $\hat{\theta}_k = \theta_k + n_\theta$ and $\hat{\omega}_k = \omega_k + n_\omega$, where $\hat{\theta}_k$ and $\hat{\omega}_k$ are the actual values for the phase mismatch midpoint and slope, respectively, and n_θ and n_ω are the observation noises (i.e., prediction errors) associated with these state parameters, respectively. To accurately estimate the phase mismatch, the Kalman filtering algorithm attempts to minimize the observation noises (n_θ and n_ω). These quantities are illustrated graphically in Fig. 1.

Kalman filters are prediction-update-type estimators where a prediction of the state parameter vector x_k is done at time instance $k-1$ given as \hat{x}_k^- . Using \hat{x}_k^- , a prediction of the measurement at time k , y_k^- is calculated. In the next step, we reach time instance k and make the actual measurement \tilde{y}_k . The final estimate of the Kalman filter at time instance k is then calculated using $\hat{x}_k = \hat{x}_k^- + K_k(\tilde{y}_k - y_k^-)$, where K_k is the Kalman gain. The filter is said to be locked to the changes in state parameters when the prediction ($\hat{x}_k - \hat{x}_k^-$) approaches zero. This can be achieved by minimizing $(\tilde{y}_k - y_k^-)$.

In case of the LKF proposed in [11], it is assumed that the state parameters are themselves the observations, i.e., $\tilde{y}_k = [\hat{\theta}_k \ \hat{\omega}_k]^T$. Thus, it is assumed that the actual phase mismatch at the midpoint of the block can be accurately inferred from measurements, which may not be strictly true. Moreover, the amplitude noise in the observed signal is not considered, further perturbing the measurement. To address these problems, we propose a new observation model [Eq. (1)] that uses a complex observation noise (n_y) as opposed to the scalar observation noise (n_θ) used in the LKF, such that

$$\tilde{y}_k = e^{j\theta_k} + n_y \quad \text{and} \quad \hat{\omega}_k = \omega_k + n_\omega, \quad (1)$$

where n_y is the complex observation noise (incorporating both phase, n_θ , and amplitude noise, n_a), as shown in Fig. 2. Moreover, the parameter \tilde{y}_k is the directly measured received sample at the midpoint of the k th block, stripped of its modulation by a slicer, as shown in Fig. 2(c), as opposed to $\hat{\theta}_k$ which

is inferred from measurements in [11]. The inclusion of the complex term n_y allows for correction of both amplitude and phase variations, so it is key to improving system performance at lower OSNRs. Since the observation model is now nonlinear a LKF cannot no longer be used, so we use an unscented Kalman filter (UKF) [9]. While LKFs propagate predictions of the mean and variance of the state parameters through the observation model to update the Kalman filter [11], a UKF instead uses a set of “sigma points” [9] that are specifically chosen to capture the statistical moments (and hence the probability distribution function) of the state parameters x_k and are then propagated through the observation model. The mean and variance of these propagated sigma points are then used to update the Kalman filter. In addition to the changes to the observation model shown in Eq. (1), we also modify the state update equations as

$$\theta_{k+1} = N\omega_k + \theta_k + n_j \quad \text{and} \quad \omega_{k+1} = \omega_k + n_f. \quad (2)$$

Here, adding n_j attempts to improve the state update by including a term for laser phase noise.

Figures 2(a) and 2(b), respectively, show a graphical representation of the corrections that the linear and unscented Kalman filters apply and the block representation of the UKF, which is similar to that in [11] except for the calculation of $(\tilde{y}_k - y_k^-)$ instead of $\delta\theta_k$ in LKF. If the received signal is stripped of its modulation, the residual component is of the form $y_k = e^{j\theta_k} + n$. Moreover, the LKF attempts to minimize the arc n_θ , so instead of trying to approach y_k , it tries to approach $e^{j\theta_k}$ by minimizing the phase difference n_θ . The UKF attempts to minimize the vector n_y to approach y_k in Fig. 2(b), which gives a more accurate estimate of the mismatch. For the UKF, the Kalman gain of the UKF is a complex value, giving a phase shift as well as scaling. We compare the performance of the UKF to the LKF below. We note that a similar state space model was proposed recently in [12] which uses an “extended” Kalman filter (EKF) implementation. The inherent benefits of the UKF over the EKF [9] predict that our UKF provides higher system performance than an EKF.

The proposed system was verified experimentally in back-to-back configuration and over an 800-km optical fiber transmission link (Fig. 3). A 10-GBaud signal from an arbitrary waveform generator (AWG) drives a 20-GHz optical bandwidth complex modulator, which modulates light from a tunable laser (<100 kHz linewidth at 193.1 THz). A laser with the same linewidth is used as a local oscillator at the receiver. A final EDFA is used as a pre-amplifier and the signal filtered before reception.

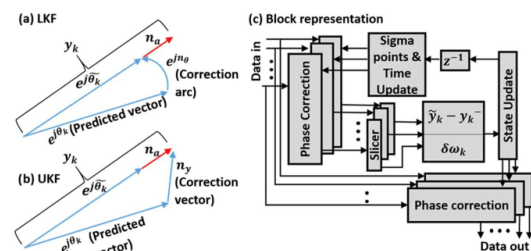


Fig. 2. Graphical representations of (a) the linear Kalman filter and (b) the unscented Kalman filter. n_a , amplitude noise vector; $e^{j\theta_k}$, vector due to CFO, TO, and PN. (c) Block representation of the UKF.

The outputs of the coherent receiver are digitized by a 40-GSa/s, 16-GHz bandwidth real-time oscilloscope and resampled to two samples per symbol. In the back-to-back case, the received OSNR was varied through optical noise loading. The noise loading setup consists of an EDFA as a noise source, a 200 GHz bandwidth band-pass filter, and a second EDFA to boost the noise power. The optical noise is coupled with the optical signal by a 3-dB coupler, with the OSNR controlled with a variable attenuator. For the link, the optical signal passes through 10x80 km fibers, with launch power controlled by EDFAs placed before each span. The test algorithms of the proposed system were run offline.

A 10 GBaud modulated signal and receive in a back-to-back setup, as shown in Fig. 3. The parallelized UKF and LKF algorithms were implemented and the Q -factor was calculated for each algorithm. We calculate Q from SNR as $Q = 10 \log_{10}(\text{SNR}_{\text{rec}})$, where SNR_{rec} is the signal-to-noise ratio of the received signal at the output of the carrier recovery algorithm. At lower OSNRs, where the bit errors are reliably measurable, the Q from the SNR matches with the Q from the BER [13]. The Q -factor for the QPSK signal back-to-back is plotted in Fig. 4. Figures 4(a)–4(c) show the Q factor plots for different block lengths, demonstrating that the UKF performs better than the LKF, with less improvement at higher OSNRs. At low OSNRs the more accurate observation model, combined with the use of sigma points provides a performance advantage for the UKF over the LKF. As the OSNR increases, the amplitude noise vector in Fig. 2 reduces in magnitude relative to the signal vector. As such, the correction vector of the UKF approaches the correction arc of the LKF, resulting in the algorithms providing similar performance. At the forward error correction (FEC) limit ($Q = 8.6$ dB, $\text{BER} = 3.8 \times 10^{-3}$), the UKF gives 1.2 dB, 1.5 dB, and 2 dB improvement in the required OSNR over the LKF for block lengths 44, 142, and 198, respectively. At the

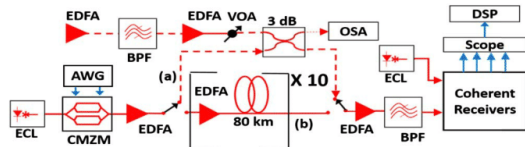


Fig. 3. Experimental setup in (a) the back-to-back configuration and (b) the 800 km transmission link configuration. BPF, bandpass filter; VOA, variable optical attenuator; CMZM, complex Mach-Zehnder modulator; AWG, arbitrary waveform generator; ECL, external cavity laser.

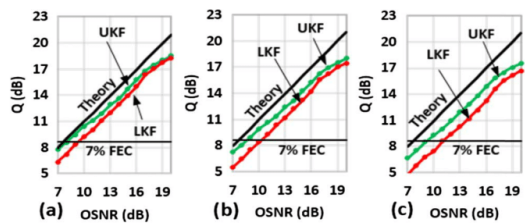


Fig. 4. Q versus OSNR, with block lengths of (a) 44, (b) 142, and (c) 198 samples.

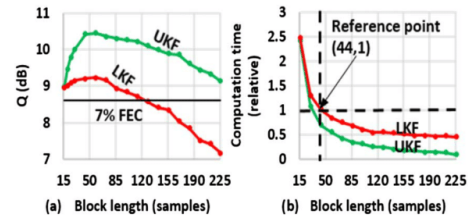


Fig. 5. (a) Q -value versus block length, with OSNR = 10 dB. (b) Computation time referenced to that of LKF at a block length of 44.

optimum block length (44 samples), the UKF gives an implementation penalty of 0.3 dB, whereas it increases to 1.5 dB in case of LKF.

To investigate the effects of block length on performance, we sweep block length for a fixed received OSNR of 10 dB. Figure 5(a) shows that Q reaches an optimum for block lengths of 44 samples. Compared with the measured Q performance when using the optimal block length, the block lengths 142 samples and 198 samples give Q penalties of 0.5 dB and 1 dB, respectively. Block lengths below the optimum, where there are not enough samples to properly estimate the slope of the phase mismatch trajectory, cause reductions in Q . For longer blocks, the slope of the phase mismatch can vary considerably within a block, again giving rise to errors and reductions in Q , as seen in Fig. 5(a).

The block length also affects the computation time. Figure 5(b) shows the computation time against that required by the parallelized LKF at optimum block length 44. Comparing Figs. 5(a) and 5(b), the UKF not only gives a gain in Q but also consumes less computation time compared with the parallelized LKF. The computation gain comes from the extra N addition operations required by the LKF in order to calculate the prediction error for phase mismatch for the k th block ($\delta\theta_k$), which is used to update the state parameter vector x_k [11]. Since the phase mismatch is not directly observable from the received signal, the LKF calculates the error vector from the mean of phase errors that requires N addition operations. When implementing a UKF, these N addition operations are avoided since the observations in this case are the received signal samples stripped of their modulation (\tilde{y}_k) and not the phase mismatch.

However, the calculation of the sigma points in an UKF increases the number of operations. As the sigma points are independent of one another, it is possible to parallelize their calculations; whereas the parallelization of the N addition operations required for the LKF is not possible. Thus, the UKF reduces the latency in the system, at the cost of more hardware. This is verified in Fig. 5(b), where the total required computation time for the UKF is 1.7 times lower than for the parallelized LKF with optimal block lengths. This computational benefit of UKF over LKF is possible only in case of parallelized architectures but not for conventional serial architectures. It should be noted from Fig. 5 that it is possible to trade off complexity for performance by changing block length.

Recent optical communication systems implement high-Fig. 5 order modulation formats to increase spectral efficiency. A 16 QAM is being investigated for 400G optical transport [14]. Hence, we additionally used 16 QAM to verify that the UKF

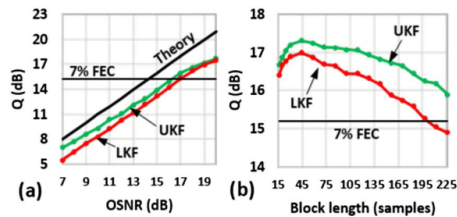


Fig. 6. (a) Q versus OSNR for 16 QAM, block length = 44. (b) Q versus block length for 16-QAM, OSNR = 19 dB.

and LKF can be generalized to higher-order formats. A 10 GBaud 16 QAM signal was generated and recovered using algorithms in test. In order to adapt the system to higher-order formats, only the demodulation block is changed which makes the Kalman filters attractive for modulation-format flexible transceivers.

Figure 6(a) plots Q against the received OSNR after using UKF and LKF on a 16 QAM signal taking 44 sample blocks. Similar to the QPSK case, the UKF gives higher performance gain at lower OSNRs than at higher OSNRs. However, in the 16 QAM case, the improvement in the required OSNR at a 7% hard FEC limit ($Q = 15.2$) reduces to 0.8 dB, and the implementation penalty increases to 2 dB for the UKF and 2.8 dB for the LKF.

By varying the block length at 19 dB OSNR, Q was again measured to be optimum at a block length of 44 samples. Thus, comparing the results for QPSK and 16 QAM systems, the proposed system shows similar trends independent of the modulation format. However, at the same time, the performance gain for UKF over LKF reduces for higher QAM modulation formats at OSNRs required to keep Q above the FEC limit. Overall, although the performance gain in using a UKF over a LKF at optimized block length is not very large for higher QAM formats, the improvement in computation time moving from a LKF to a UKF implementation is considerable.

Figure 7 plots the Q -values of the algorithms under test after transmission over 800 km with the launch power varied. We use a 44-sample block length for QPSK and 16-QAM signals.

At higher launch powers, the UKF and LKF performed similarly since neither is able to compensate for degradations of optical nonlinear effects. Although the UKF gave 2.3 dBm improvement for the QPSK case in the required launch power over the parallelized LKF at the FEC limit, this improvement was marginal (0.3 dBm) for the 16 QAM case. Nonetheless, the computation time of parallelized UKF is still 60% of that of parallelized LKF. As such, the real advantage of using a parallelized UKF may be in reduced latency. The complete experiment was found to experience frequency offsets ranging from 0 to 630 MHz, and multiple observations led to the conclusion that the proposed systems are robust within this range.

In conclusion, we have proposed a blind, unscented Kalman filter with a parallelized architecture for carrier recovery in optical systems and compared the performance with a previous parallelized LKF. For block lengths optimized for Q performance, the UKF reduces the computation time by 1.7 times than that of parallelized LKF and requires 1.2 dB and 0.8 dB

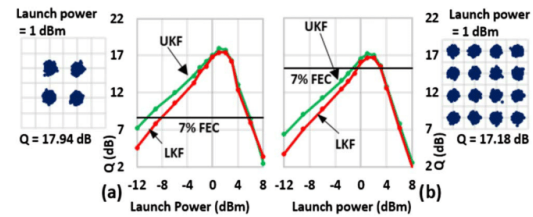


Fig. 7. Q versus launch power for (a) QPSK and (b) 16 QAM, over an 800 km optical fiber link, using an optimal block length.

lower OSNR at the 7% hard FEC limit compared to the LKF for both QPSK and 16 QAM modulated signals, respectively. These improvements in computation time and required OSNR were observed to be better for longer blocks. The proposed system was verified to perform successfully over an 800 km long-haul link, where the UKF gives 2.3 dBm improvement in the required launch power at the hard FEC limit over LKF that reduces with the order of modulation. This study shows that in the case of parallelized architectures, for specific applications of carrier recovery in optical communication systems, an unscented Kalman filter can prove to be a better option than a linear Kalman filter.

Funding. Australian Research Council (ARC) (CE110001018, FL130100041).

Acknowledgment. VPIphotonics (www.vpiphotonics.com) for support under their University Program.

REFERENCES

1. M. Nakazawa, K. Kikuchi, and T. Miyazaki, *High Spectral Density Optical Communication Technologies* (Springer-Verlag, 2010), Vol. 6.
2. S. J. Savory, *Opt. Express* **16**, 804 (2008).
3. I. Fatadin, D. Ives, and S. J. Savory, *Opt. Express* **21**, 10166 (2013).
4. M. G. Taylor, *J. Lightwave Technol.* **27**, 901 (2009).
5. D. Gaudenzi, T. Garde, and V. Vanghi, *IEEE Trans. Commun.* **43**, 3090 (1995).
6. T. Pfau, S. Hoffman, and R. Noe, *J. Lightwave Technol.* **27**, 989 (2009).
7. M. G. Taylor, "Algorithms for coherent detection," in *Optical Fiber Communication Conference and Exposition (OFC) and National Fiber Optic Engineers Conference (NFOEC)*, San Diego, California, USA, 2010, paper OThL4.
8. D. Zhao, L. Xi, X. Tang, W. Zhang, Y. Qiao, and X. Zhang, *Opt. Express* **23**, 24822 (2015).
9. E. A. Wan and R. van der Merwe, "The unscented Kalman filter for nonlinear estimation," in *Proceedings of IEEE Adaptive Systems for Signal Processing, Communications, and Control Symposium Conference*, Alberta, Canada, 2000, p. 153.
10. S. Kay, *Fundamentals of Statistical Signal Processing: Estimation Theory* (Wiley, 1993), Vol. 1.
11. T. Inoue and S. Namiki, *Opt. Express* **22**, 15376 (2014).
12. L. Pakala and B. Schmauss, *Opt. Express* **24**, 6391 (2016).
13. M. Selmi, Y. Jaouen, and P. Ciblat, "Accurate digital frequency offset estimator for coherent PolMux QAM transmission systems," in *Proceedings of European Conference and Exhibition on Optical Communications (ECOC)*, Vienna, Austria, 2009, paper P3.08.
14. "Technology options for 400G implementation," OIF-Tech-Options-400G-01.0, July, 2015 (white paper).

Unscented Kalman filters for polarization state tracking and phase noise mitigation

JOKHAKAR JIGNESH,^{1,*} BILL CORCORAN,^{1,2} CHEN ZHU,¹ AND ARTHUR LOWERY^{1,2}

¹*Electro-Photonics Lab, Department of Electrical and Computer Systems Engineering, Monash University, Clayton, VIC 3800, Australia*

²*Centre of Ultrahigh-bandwidth Devices for Optical Systems (CUDOS), Australia*
*jignesh.jokhakar@monash.edu

Abstract: Simultaneous polarization and phase noise tracking and compensation is proposed based on an unscented Kalman filter (UKF). We experimentally demonstrate the tracking under noise-loading and after 800-km single-mode fiber transmission with 20-Gbaud QPSK and 16-QAM signals. These experiments show that the proposed UKF outperforms both conventional blind tracing algorithms and a previously proposed extended Kalman filter, at the cost of higher complexity. Additionally, we propose and test modified Kalman filter algorithms to reduce computational complexity.

© 2016 Optical Society of America

OCIS codes: (060.1660) Coherent communications; (060.2330) Fiber optics communications.

References and links

1. D. S. Millar and S. J. Savory, "Blind adaptive equalization of polarization-switched QPSK modulation," *Opt. Express* **19**(9), 8533–8538 (2011).
2. M. G. Taylor, "Phase estimation methods for optical coherent detection using digital signal processing," *J. Lightwave Technol.* **27**(7), 901–914 (2009).
3. E. A. Wan and R. van der Merwe, "The unscented Kalman filter for nonlinear estimation", in *Proc. IEEE Adaptive Systems for Signal Processing, Communications, and Control Symposium Conference* (2000), (2000), pp. 153–158.
4. T. Marshall, B. Szafraniec, and B. Nebendahl, "Kalman filter carrier and polarization-state tracking," *Opt. Lett.* **35**(13), 2203–2205 (2010).
5. Y. Yang, G. Cao, K. Zhong, X. Zhou, Y. Yao, A. P. T. Lau, and C. Lu, "Fast polarization-state tracking scheme based on radius-directed linear Kalman filter," *Opt. Express* **23**(15), 19673–19680 (2015).
6. J. Jokhakar, B. Corcoran, C. Zhu, and A. J. Lowery, "Unscented Kalman filters for polarization state tracking and phase noise mitigation," in *Proc. of Optical Fiber Communication Conference*, OSA Technical Digest (online) (Optical Society of America, 2016), paper Tu2A.4.
7. S. Kay, *Fundamentals of Statistical Signal Processing, Volume 1: Estimation Theory* (Wiley, 1993).
8. T. Xu, G. Jacobsen, S. Popov, M. Forzati, J. Mårtensson, M. Mussolin, J. Li, K. Wang, Y. Zhang, and A. T. Friberg, "Frequency-domain chromatic dispersion equalization using overlap-add methods in coherent optical system," *J. Opt. Commun.* **32**(2), 131–135 (2011).
9. M. Selmi, Y. Jaouen, and P. Ciblat, "Accurate digital frequency offset estimator for coherent PolMux QAM transmission systems," in *Proc. of European Conference and Exhibition on Optical Communication* (2009), pp. 1–2.
10. OIF-Tech-Options-400G-01.0 – Technology Options for 400G Implementation (July 2015) (White paper). Available: <http://www.oiforum.com/wp-content/uploads/OIF-Tech-Options-400G-01.0.pdf>.
11. R. A. Shafik, M. S. Rahman, and A. H. M. R. Islam, "On the extended relationships among EVM, BER and SNR as performance metrics," in *Proc. of International Conference on Electrical and Computer Engineering* (2006), pp. 408–411.
12. H. Louchet, K. Kuzmin, and A. Richter, "Improved DSP algorithms for coherent 16-QAM transmission," in *Proceedings of European Conference and Exhibition on Optical Communication* (2008), pp. 57–58.
13. C. Zhu, A. V. Tran, S. Chen, L. B. Du, T. Anderson, A. J. Lowery, and E. Skafidas, "Frequency-domain blind equalization for long-haul coherent pol-mux 16-QAM system with CD prediction and dual-mode adaptive algorithm," *IEEE Photonics J.* **4**(5), 1653–1661 (2012).
14. S. Zhang, P. Y. Kam, C. Yu, and J. Chen, "Decision-aided carrier phase estimation for coherent optical communications," *J. Lightwave Technol.* **28**(11), 1597–1607 (2010).
15. D. Chang, F. Yu, Z. Xiao, N. Stojanovic, F. N. Hauske, Y. Cai, C. Xie, L. Li, X. Xu, and Q. Xiong, "LDPC convolutional codes using layered decoding algorithm for high speed coherent optical transmission," in *Proc. of*

- Optical Fiber Communication Conference*, OSA Technical Digest (Optical Society of America, 2012), paper OW1H.4.
16. X. Zhou, L. E. Nelson, P. Magill, R. Isaac, B. Zhu, D. W. Peckham, P. I. Borel, and K. Carlson, "High spectral efficiency 400 Gb/s transmission using PDM time-domain hybrid 32–64 QAM and training-assisted carrier recovery," *J. Lightwave Technol.* **31**(7), 999–1005 (2013).
 17. A. Alvarado, E. Agrell, D. Lavery, R. Maher, and P. Bayvel, "Replacing the soft-decision FEC limit paradigm in the design of optical communication systems," *J. Lightwave Technol.* **33**(20), 4338–4352 (2015).
 18. R. Driggers, *Encyclopedia of Optical Engineering, Volume 2*, (Marcel Dekker Inc. 2003).
 19. H. G. Berry, G. Gabrielse, and A. E. Livingston, "Measurement of the Stokes parameters of light," *Appl. Opt.* **16**(12), 3200–3205 (1977).

1. Introduction

Coherent communication systems support spectrally efficient modulation schemes where data is encoded on the phase, amplitude and polarization states of the optical carrier. However, the finite linewidth of the laser, used as a carrier, results in an additive random phase perturbation. Additionally, small geometric variations in optical fiber randomly rotate the state of polarization at receiver end, changing even with slight vibrations. The digital coherent receiver must dynamically track the phase and polarization states of the system, in order to recover the transmitted signals fully.

Commonly, with quadrature phase shift keying (QPSK) format, adaptive filters that are based on the constant modulus algorithm (CMA) [1] is used in conjunction with the Viterbi-Viterbi phase estimation (VVPE) algorithm, where the CMA takes care of the effects of polarization rotation and VVPE mitigates the effects of the phase noise. In cases of higher quadrature-amplitude modulation (QAM) formats, multi-modulus algorithm (MMA) or Weiner filter based estimation with pilot-symbol-aided maximum likelihood phase estimation is employed [2]. Kalman filters provide an alternative method, and have been proven to give optimum estimates compared with all other estimators assuming that the noise sources associated with the system are Gaussian [3]. Recently, Marshall *et al.* proposed to use a Kalman filter; extended Kalman filter (EKF) to be more precise, and showed faster convergence than conventional CMA + VVPE approach [4]. Also, Linear Kalman filters (LKFs) have been used for polarization state tracking based on a radius-directed method [5]. However, this LKF did not provide joint tracking of phase and polarization, and the proposed system requires significant modifications when shifting to higher order QAM.

In this paper we propose to use, in place of an EKF, an 'unscented' Kalman filter (UKF) that has been shown to accurately capture all the moments of the parameter to be estimated in contrast to only the 1st and 2nd-order moments provided by the EKF [3]; thus, it gives more-accurate estimates. However, this improvement in performance from the UKF comes at the cost of increased complexity, leading us to discuss modified versions of the UKF and EKF (R-UKF and R-EKF) with reduced complexities [6]. This paper is an extension to our previous work in [6], operating at higher baud rates and investigating operation with both QPSK and 16-QAM modulation formats. The UKF was found to provide performance enhancement in comparison with the previously proposed EKF or CMA/MMA algorithms but at the cost of increased complexity, whereas the R-UKF outperformed the previous algorithms with reduced complexity but at moderate or higher optical signal-to-noise ratios (OSNR).

Section 2 discusses the phase and polarization observation model and unscented Kalman filters in detail. Section 3 proposes modifications to reduce the complexities of Kalman filter algorithms. Section 4 describes the experimental setup and shows the performance of each algorithm for back-to-back noise loading as well as 800-km fiber optical link configuration for 20G-baud QPSK and 16-QAM modulated signals. We present our conclusions in Section 5. The appendices provide the unscented Kalman filter algorithm proposed in this paper and an intuitive and detailed discussion of the mathematical model.

2. Kalman filters

Unlike the CMA or other adaptive filter algorithms such as least mean square (LMS), recursive least square (RLS) *etc.* that calculate the tap coefficients of a digital finite impulse response filter towards reducing a cost function, Kalman filters use a mathematical model of transmission impairments to mitigate their effects. In other words, instead of estimating the correct coefficients of the taps in filter, Kalman filters attempt to estimate the accurate values of the parameters in the mathematical model of distortions. Since these parameters are random, the MMSE criterion is considered instead of the maximum likelihood (ML) [7]. When the noises associated with the mathematical model have Gaussian distributions, Kalman filters can provide optimal estimates in terms of minimum variance [3]. The mathematical model ('observation' model) for the impairments of phase noise and polarization rotation, is given as

$$Z = e^{j\theta} \begin{pmatrix} a + jb & c + jd \\ -c + jd & a - jb \end{pmatrix} \begin{pmatrix} T_x \\ T_y \end{pmatrix} + N \quad (1)$$

where, Z is the received polarization multiplexed signal, T_x and T_y are the transmitted symbols on X and Y polarizations respectively, $[a, b, c, d]$ are the polarization state parameters determining the polarization rotation, θ is the phase noise parameter and N is the additive Gaussian noise term mostly due to amplified spontaneous emissions from EDFAs in the system. A more detailed discussion about the observation model is given in Appendix B. The parameters $[a, b, c, d]$ follow the Wiener process i.e. $a_n = a_{n-1} + \Delta a$ where n determines the time instance and Δa is Gaussian distributed [4]. The parameters b, c and d follow similar distribution. Since the parameters follow Wiener process, Weiner filters may seem to be appropriate for their estimation [2]. However, as the parameters $[a, b, c, d, \theta]$ are non-stationary, Kalman filters should give more-accurate estimates and thus prove to be optimum estimators for these parameters [7].

The Kalman filter used here estimates the parameters $[a, b, c, d, \theta]$ and performs the inverse of the mathematical model on the received signal. The estimates of $[T_x, T_y]$ can now be calculated using maximum likelihood, T_x and T_y being deterministic points of constellations.

In spite of the benefits offered by Kalman filters, linear Kalman filters cannot be used for our application because the observation model in Eq. (1) is non-linear, as the phase parameter (θ) is an exponent. As a solution to this, Marshall *et al.* proposed using an EKF that performs the linearization of the non-linear model by taking its partial derivatives with respect to each parameter, then using this linearized model with regular LKF [4], as shown in Fig. 1(a). However, this linearization causes inaccuracies in the parameter estimation and thus only leads to sub-optimal estimates [3]. Hence, we propose to use an 'unscented' Kalman filter (UKF), which is able to cope with nonlinear models.

The UKF calculates $(2L + 1)$ sigma points, where L is the number of parameters, to accurately capture all the moments of the probability density function (PDF) of the parameters, then passes them through the actual model without linearization [3]. The sigma points, propagated through the actual model, capture the PDF of the signal at the output of the model more accurately than the EKF that just performs the scaling of the mean and variance of the PDF. As a result, UKF should provide better performance than the EKF [3].

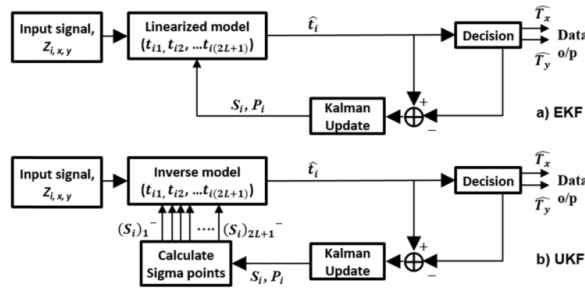


Fig. 1. Block representation of extended Kalman filter (EKF) and unscented Kalman filter (UKF).

Figure 1(b) is the block diagram of the UKF. The unknown state parameter vector to be estimated is $\mathcal{S} = [a, b, c, d, \theta]$, $t = [T_x \ T_y]$, P_i is the *a posteriori* estimate covariance, $(S_i)_k^-$ is the k^{th} sigma point calculated, $k = 1$ to $2L + 1$, and \hat{t}_i is the estimated symbol vector. The UKF algorithm for our application is given in Appendix A.

3. Modified Kalman filters

As UKFs can provide more accurate estimates compared with EKFs, using a UKF should provide a system performance improvement. However, this performance improvement comes at the cost of increase complexity of the algorithm that arises from the additional computations required for calculating the sigma points. This has motivated us to attempt to reduce the complexity of the Kalman filter algorithms we use.

To avoid singularity issues in the system, the parameters $[a, b, c, d, \theta]$ are restricted to being real valued [4]. However, due to the phase noise term ($e^{j\theta}$) in the observation model, the Kalman filter gives complex values for these parameters. Marshall *et al.* proposed splitting each complex row in the algorithm matrices into two consecutive rows; the first row being the real part and second row being the imaginary part [4]. Although this solves the singularity problem, the overall complexity of the algorithm remains the same. As a solution to this, we propose to combine two real-valued parameters into a complex-valued parameter i.e. take $a + jb = \tilde{a}$ and $c + jd = \tilde{c}$. As a result, the parameters to be estimated by the Kalman filter now become $\mathcal{S} = [\tilde{a}, \tilde{c}, \theta]$. We name the EKF and UKF, with this new reduced state vector, as R-EKF and R-UKF respectively. Since the Kalman filter passes a complex value to each of their parameters, no splitting is required. Moreover, as the number of unknown parameters reduces from 5 in previous versions to 3 in the modified versions, the orders of the algorithm's complex matrices reduce from 5×5 , $5 \times m$ or $m \times 5$ to 3×3 , $3 \times m$ or $m \times 3$ where m can take values within $\{1,3\}$. This reduces the number of complex multiplications in the algorithm, thus reducing the computational complexity. Additionally, since the parameters a, b, c, d always appear in pairs like $a + jb$ and $c + jd$, and never individually in the algorithm, the combining of these parameters is easily facilitated. The combined parameters, \tilde{a} and \tilde{c} still follow the Weiner process i.e. $\tilde{a}_n = \tilde{a}_{n-1} + \Delta\tilde{a}$ and $\tilde{c}_n = \tilde{c}_{n-1} + \Delta\tilde{c}$ where $\Delta\tilde{a} = \Delta a + j\Delta b$ and $\Delta\tilde{c} = \Delta c + j\Delta d$ and thus have a circular Gaussian distribution in the complex plane with zero means and finite variances. Table 1 shows the number of required complex multiplications per symbol for each algorithm and thus gives an idea of the complexity reduction with the proposed techniques.

The UKF is more computationally complex than an EKF. However, with the proposed technique to reduce complexity giving R-UKF and R-EKF, an R-UKF is less computationally

complex than an EKF and the R-EKF shows has the least complexity of all algorithms considered in this study.

Table 1. Number of complex multiplications per symbol detection required by the algorithms.

Algorithm	Name	Number of complex multiplications per symbol
UKF	Unscented Kalman filter	140
R-UKF	Reduced - Unscented KF	90
EKF	Extended Kalman filter	95
R-EKF	Reduced - Extended KF	72

4. Experimental setup

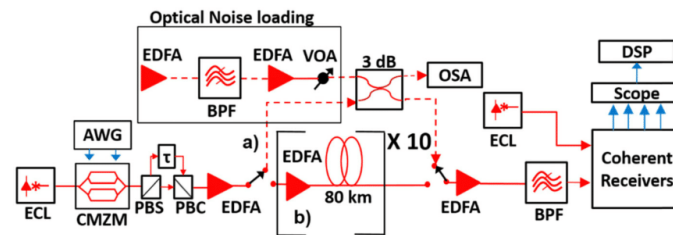


Fig. 2. Experimental setup for a) back-to-back configuration and b) 800-km transmission link configuration; CMZM: complex Mach-Zehnder modulator, BPF: band pass filter, VOA: variable optical attenuator, ECL: external cavity laser, EDFA: erbium doped fiber amplifier.

20-Gbaud digital signals were generated using an arbitrary waveform generator (AWG) to drive an optical IQ modulator. Polarization multiplexing was emulated using an optical delay line, polarization beam splitter (PBS) and combiner (PBC) as shown in Fig. 2. In the 'back-to-back' configuration, optical noise covering a 200-GHz bandwidth was added to vary the received OSNR. At the receiver end, the signal was amplified using an EDFA and filtered using a BPF with a 200-GHz bandwidth centered at the set transmission wavelength, then fed into a 25-GHz electrical bandwidth integrated coherent receiver. The outputs of the coherent receiver were connected to a 40-GSa/s 28-GHz bandwidth digital signal oscilloscope (DSO). The test algorithms were run as offline DSP.

Figure 3 gives the DSP flow chain performed offline. After being sampled at 40 GSa/s i.e. at 2 samples per symbol, the complex signals in both polarizations were passed through a static frequency domain chromatic dispersion (CD) compensation using overlap-add method [8] for optical fiber link configuration. The frequency offsets in each polarization were then separately estimated using spectral search method [9] in all cases and compensated for. The signals in each polarization are then resampled to one sample per symbol before passing on to the algorithms under test. The internal clock of the DSO can be assumed to be stable, but still there are few phase distortions added in the sampled signal. However, these distortions can be taken care of by longer length taps in CMA/MMA equalizers or by optimizing the initial variances in the Kalman filters. The optimum tap length in our system was found to be 41 taps for both CMA and MMA filters. Similarly, the Kalman filters aided by their decision directed nature are able to equalize these effects by intelligently updating the parameters in the mathematical distortion model. This may even cause the Kalman filters to give complex values for real parameters to be estimated which again supports the concept of R-UKF and R-EKF. As shown in Fig. 3, the Kalman filters replace CMA + VVPE/ MMA + ML algorithms.

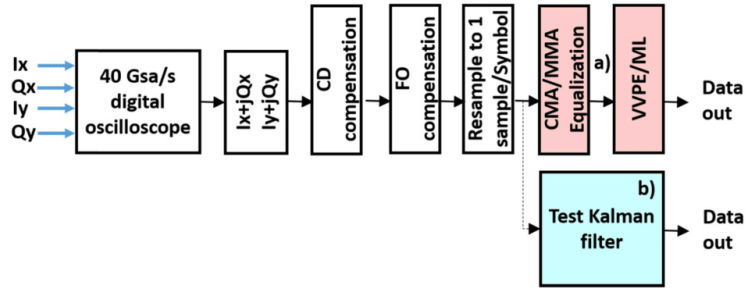


Fig. 3. Digital signal processing flow for a) CMA + VVPE/MMA + ML b) Kalman filters under test.

While QPSK is used for 100Gb/s channels for optical transport, future 400Gb/s channels are likely to use 16QAM as a modulation scheme [10]. Thus, the performance of our proposed systems have been measured for 20 Gbaud 16-QAM and QPSK signals. The signal quality factor (Q) after recovered by the test algorithms was measured. At lower OSNRs where sufficient errors were measured (above the FEC limit), the Q -value calculated from the constellation variance (Q_{SNR}) is equal to the Q -value calculated from the finite BER (Q_{BER}) where Q_{BER} for any M-QAM modulation format is [11]

$$Q_{\text{BER}} = 20 \log_{10} \left(\sqrt{\frac{2(M-1)}{3}} \times \text{erfc}^{-1} \left(\frac{\text{BER} \times \log_2 \sqrt{M}}{\left(1 - \frac{1}{\sqrt{M}}\right)} \right) \right) \quad (2)$$

Although the R-UKF and R-EKF reduce the complexity, some changes need to be made to avoid the singularity in the system. The Jacobian matrix is

$$J = e^{j\theta} \begin{bmatrix} Z_x & jZ_x & Z_y & jZ_y & j(a+jb)Z_x + j(c+jd)Z_y \\ Z_y & -jZ_y & -Z_x & jZ_x & j(-c+jd)Z_x + j(a-jb)Z_y \end{bmatrix} \quad (3)$$

For R-EKF it reduces to

$$J = \begin{bmatrix} e^{j\theta} Z_x & e^{j\theta} Z_y & j(e^{j\theta} \tilde{a} Z_x + e^{j\theta} \tilde{c} Z_y) \\ e^{-j\theta} Z_y^* & -e^{-j\theta} Z_x^* & j(e^{-j\theta} \tilde{c} Z_x^* - e^{-j\theta} \tilde{a} Z_y^*) \end{bmatrix} \quad (4)$$

For the R-EKF, the data symbol estimated in Y polarization is the conjugate of the actual transmitted symbol. For both R-UKF and R-EKF, the estimates of the parameter θ will be complex. We noted that the system avoids singularity only when that complex value is considered. Taking only the real or imaginary part, or the absolute value of the complex estimate, either leads to singularity or divergence of the filter. The explanation for this is that, since we have combined two parameters into one, the three parameters work together to enforce the received signal transformations onto desired constellation points. This causes the Kalman filters to make the θ parameter complex valued. In other words, modified Kalman filters have fewer degrees of freedom to achieve the desired results and thus need all the parameters to be complex. Additionally, in our system, the values for observation noise variance σ_z^2 and process noise variance σ_p^2 giving optimum performance were found to be

10^{-1} and 10^{-8} for EKF and UKF, and 5×10^{-1} and 10^{-4} for R-EKF and R-UKF respectively. This increased variance leads to a lower performance at poor OSNRs.

4.1 Experimental results

Figure 4 shows the performance of the proposed algorithms in terms of signal quality factor (Q) against received OSNR. At high OSNR for the QPSK case, the UKF and R-UKF both outperform the EKF, showing an increase in Q by 1.7-dB and 1.4-dB respectively at 20-dB OSNR. Similarly, for the 16-QAM case in Fig. 4, the UKF and R-UKF give 1.4-dB and 1-dB improvement over EKF at 20-dB OSNR. The unscented transformation used in UKF and R-UKF leads to more-accurate capture of the *a priori* and *a posteriori* estimate error covariances [12], and hence we get these benefits of UKF and R-UKF over EKF.

Figure 4 also shows the UKF and R-UKF performance compared with the conventional constant-modulus algorithm (CMA) (41 taps) and Viterbi and Viterbi phase estimation (VVPE) algorithm [1]. The number of taps were chosen to be in accordance to optimum Q performance observed as discussed before. In this case, the UKF and R-UKF give up to 2-dB and up to 1.5-dB improvements in received signal Q at 20-dB OSNR, respectively. In the 16-QAM case, the VVPE algorithm is not a strong phase estimation tool due to higher noise susceptibility of the 16-QAM signal. Thus, a multi-modulus algorithm (MMA) [13] with pilot-based maximum likelihood (ML) technique aided technique [14] is an alternate method to estimate the constellation symbols [2]. Figure 4 shows that for 16-QAM case, the EKF and R-EKF now give considerable 0.7-dB and 0.6-dB performance gains over MMA + ML techniques, respectively, at 20-dB OSNR, which was not observed in QPSK case with CMA + VVPE algorithm. Additionally, the UKF and R-UKF continue their trends and give 2.2-dB and 1.7-dB improvements over MMA + ML scheme. These improvements are because of a more intelligent update of the Kalman gain using the *a priori* and *a posteriori* estimate error covariance against the constant step size of CMA/MMA. The improvement over CMA/MMA is not as much in the EKF since the linearization process disturbs the accuracy of the estimate co-variances.

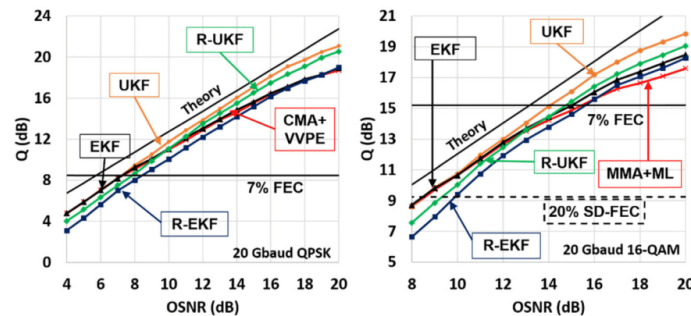


Fig. 4. Q -value vs. OSNR in back-to-back configuration for 20 Gbaud QPSK and 20 Gbaud 16-QAM respectively.

While these simulations of the system performance at high OSNR confirm expected improvements, fiber communication systems are often run near their 'error-free' thresholds, commonly taken as the operating threshold for Reed-Solomon (255, 239) hard-decision forward-error correction (FEC). For the back-to-back QPSK results shown in Fig. 4, at low OSNR, due to higher co-variances needed by the R-UKF, this algorithm shows a 0.6-dB OSNR penalty at the 7% hard FEC threshold for QPSK case compared to the EKF. The implementation penalty at the hard FEC limit is 1.3-dB for the UKF, CMA + VVPE and EKF, 1.9-dB for the R-UKF and is maximum of 2.4-dB for R-EKF.

Although the R-UKF shows reduced performance at lower OSNRs compared with the UKF and EKF for the reasons mentioned in QPSK case, it still shows negligible OSNR penalty at the 7% hard-FEC limit compared with the EKF for the 16-QAM case. Additionally, the UKF shows an improvement of 1-dB in required OSNR at FEC limit. The implementation OSNR penalty suffered at the 7% hard-FEC limit for 16-QAM modulated signal is 0.9-dB for the UKF, 1.9-dB for the R-UKF, 2.1-dB for EKF and 2.7-dB for MMA + ML and R-EKF. Comparing with the penalty values for QPSK, it can be inferred that the EKF, R-EKF and MMA + ML algorithms are not good alternatives for systems supporting both QPSK to 16-QAM. On the other hand, the UKF, with increased complexity, has a reduced implementation penalty for 16-QAM and R-UKF, with its complexity less than EKF, has a consistent implementation penalty independent of whether QPSK or 16-QAM is being received.

Recent research in optical communication focuses on 400G systems that require higher-order QAM modulation formats and powerful error correcting techniques for making long distance transmission possible at these high data rates. The soft-decision forward error correction (SD-FEC) techniques such as low-density parity check (LDPC) codes and Turbo codes are being widely explored with an intention of achieving the post-FEC bit error rate (BER) of 10^{-15} [15]. For this, the hard FEC techniques, RS(255,239), *i.e.* with 7% overhead, require a pre-FEC BER better than 3.8×10^{-3} . On the other hand, the SD-FEC techniques can achieve the desired post-FEC BER of 10^{-15} even with worse pre-FEC BERs of 2.7×10^{-2} , but require a 20% overhead [16]. At this 20% SD-FEC limit for 16-QAM modulated signal, the UKF, EKF and the MMA + ML algorithms give similar performances, whereas, the R-UKF and R-EKF give OSNR penalties of 0.8-dB and 1.3-dB respectively. Hence, for higher pre-FEC BERs, the reduction in complexity in R-UKF and R-EKF comes at the cost of increase in OSNR penalty compared with other algorithms. So for 16-QAM with a 20% FEC overhead, the comparative performance of the algorithms used here is similar to the case of a 7% FEC overhead for QPSK. Nonetheless, for systems that are designed for better pre-FEC BER, the R-UKF can prove to be a good alternative to the EKF. We note that a given pre-FEC BER as a SD-FEC threshold may not be the most accurate metric [17], but this does provide us with an approximate bound for comparison.

To understand the performance of the test algorithms in a practical transmission scenario, the signal was transmitted over 800 km. The optical signal was passed through 10 spools of optical fiber, each of length 80 km. The span's launch powers were controlled by EDFAs placed before each spool, with a final EDFA placed as a pre-amplifier before the receiver.

Figure 5 shows the Q performance of each algorithms in test with varying launch power for both QPSK and 16-QAM modulated signals. It shows that each algorithm has the same optimal launch power. At higher powers, the highly nonlinear transmission regime, they give similar performance since the phase tracking is lost as expected, as none of the algorithms are capable of compensating for fast state changes caused by non-linear distortions in the fiber. In the QPSK case, the EKF gave no apparent improvement over the CMA + VVPE, whereas in case of 16-QAM, as observed at higher OSNRs, the EKF and R-EKF give marginal peak improvement over the MMA + ML. At the peak Q , we expect the signal to have a high OSNR, leading to the increased performance of the UKF (2.1-dB for QPSK and 2.3-dB for 16-QAM) and R-UKF (1.8-dB for QPSK and 2.1-dB for 16-QAM) implementations CMA + VVPE/MMA + ML at optimal launch power. For the 16-QAM case, at the 7% hard FEC limit, the UKF showed 2-dB, R-UKF showed 1-dB, EKF showed 0.7-dB and R-EKF showed negligible improvement in the required launch power compared with the MMA + ML algorithm. Thus, the UKF requires the lowest launch power to achieve the required pre-FEC BER of 3.8×10^{-3} but comes with higher computational complexity. The R-UKF may prove to be a pragmatic option since it is less complex than the EKF and requires lesser launch power to achieve the performance above FEC. The R-EKF require the highest power and thus could be a feasible option only when low complexity is of utmost importance.

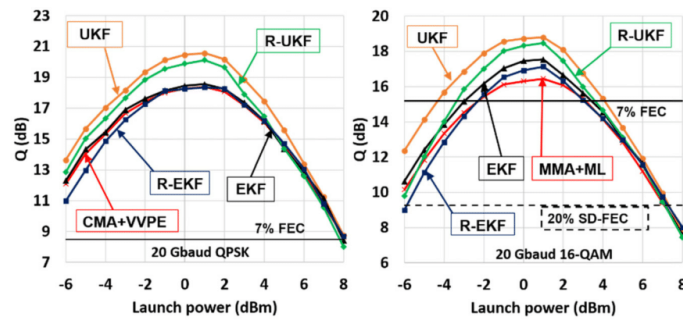


Fig. 5. Q -value vs. launch power (dBm) in 800 km link configuration for 20 Gbaud QPSK and 16-QAM respectively.

4.2 Simulation results

In addition to transmission impairments and optical noise, the finite linewidth of the lasers used in the systems can vary from device to device. Although tuneable external cavity lasers (as used in our experiments) generally confine their linewidth within 100 kHz, for DWDM applications laser linewidths may exceed this value. Hence, we simulated the back-to-back setup in VPTransmissionMaker v. 9.3 software with the linewidth of both the transmitter's continuous wave (CW) laser and the receiver's local oscillator CW laser varied from 100 kHz to 1 MHz as shown in Fig. 6.

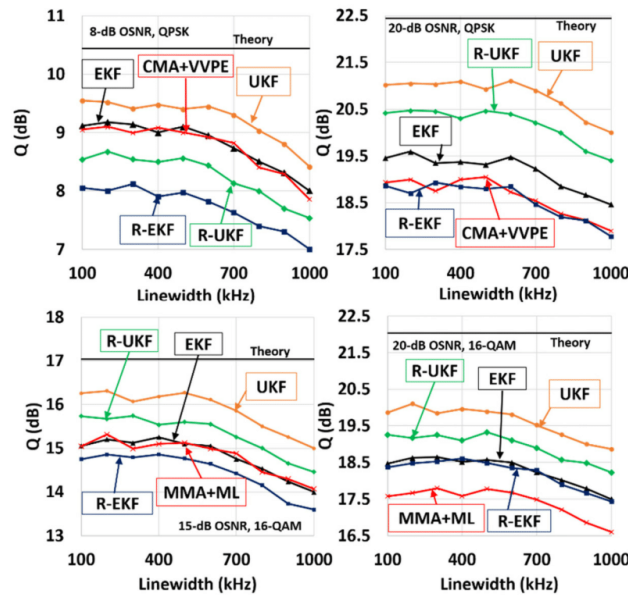


Fig. 6. Q (dB) vs. linewidth (kHz) for 8 dB OSNR, QPSK; 20 dB OSNR, QPSK; 15 dB OSNR, 16 QAM and 20 dB OSNR, 16 QAM respectively.

Simulations were performed with a 20-Gbaud polarization multiplexed QPSK and 16-QAM modulated signals at 20-dB OSNR and also at OSNRs close to EKFs respective 7% hard FEC limit (8-dB for QPSK and 15-dB for 16-QAM). The angular rotation rate of polarization evolution taken for simulations is 6.8 Mrad/s. This high polarization rotation velocity was taken to make a fair comparison with the simulations shown by Marshall *et al.* in [4]. Additionally, fixing the polarization rotation velocity in simulations where the system is highly stressed beyond practical limits ensures the robustness of the system.

The degradation in signal Q is between 0.1-dB and 0.3-dB for all cases explored at laser linewidth values of 600 MHz, between 0.5-dB to 0.7-dB for linewidth value of 800 MHz and a 0.9-dB to 1.1-dB degradation occurring with laser linewidth values of 1 MHz compared to the performance with 100-kHz linewidths. As observed from the back-to-back experimental results, the performances show 1-dB variation with a 1-dB change in OSNR around the hard FEC limit. Considering this and the simulation results in Fig. 6, it can be concluded that lasers with 1 MHz linewidths require only a 1-dB increase in the OSNR as compared to that required for lasers with 100 kHz linewidths. Thus, the algorithms to be sufficiently robust for stressed systems with linewidths up to 1 MHz and polarization rotations up to 6.8 Mrads/s.

The observation model in Eq. (1) does not consider the differential group delay (DGD), *i.e.* the effects of polarization mode dispersion (PMD). To understand the robustness of the system to PMD, simulations were performed with 20-Gbaud modulated signals over 800 km, with the PMD parameter of the fiber varied from 0.028 to 0.084. This is equivalent to sweeping the PMD from 25 ps (less than one symbol duration) to 75 ps (more than 1 symbol) for a 20-Gbaud signal. The results are shown in Fig. 7. A standard SMF-28 fiber tends to give maximum of 28-ps DGD over 800 km distance that relates to negligible performance penalty for both the QPSK and 16-QAM signals. A penalty of 1-dB occurred for a DGD of 65 ps for all cases corresponding to links of 2000 km of standard SMF-28 fiber. Hence, the algorithms could be implemented in practice. Additionally, the proposed systems were tested with artificially added absolute frequency offsets up to 1 GHz showed variations in the performances of the test algorithms within 0.4-dB, verifying the robustness to frequency offsets.

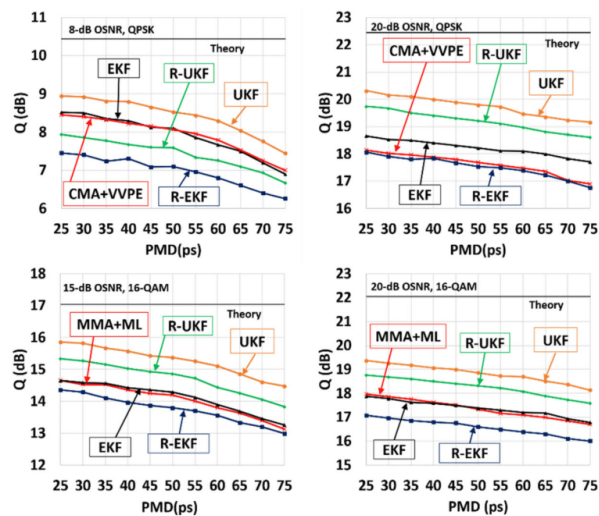


Fig. 7. Q (dB) vs. PMD (ps) for 8 dB OSNR, QPSK; 20 dB OSNR, QPSK; 15 dB OSNR, 16 QAM and 20 dB OSNR, 16 QAM respectively.

The intelligent update of the Kalman gain based on the statistical information aided with the decision-directed nature of the Kalman filters makes the Kalman filters to perform in spite of DGD being slightly higher than 1 symbol. However, we do observe performance degradation as shown in Fig. 7. If the DGD is increased further, we can expect that the system will at some point completely lose track, resulting in a sharp drop in performance. Also, the FIR filters used for CMA/MMA in this work were symbol-period spaced. A performance comparison of the Kalman filters under test with that of fractionally-space time domain equalizers (FS-TDE) remains to be explored. Additionally, the maximum tolerable residual CD after overlap-add static CD compensation also remains to be investigated which can be taken up as future work.

Overall, these results indicate that, because it only provides a marginal performance improvement for higher modulation formats, EKF is not a good alternative to conventional CMA + VVPE/MMA + ML algorithms, whereas, the better performance improvement from using the UKF may come at the cost of increased complexity. For particular cases where moderate or high OSNRs in the system are available, the R-UKF seems to provide a good alternative to CMA/MMA + VVPE in terms of performance and complexity.

5. Conclusions

We have investigated and compared two types of Kalman filters for joint polarization state tracking and phase noise mitigation: unscented Kalman filters and previously proposed extended Kalman filters. A comparison was also made with conventional blind CMA algorithms for QPSK and MMA for 16-QAM modulation formats. We have shown through experiments that our proposed UKF for joint polarization and phase tracking outperforms the previously proposed EKF algorithm and the conventional CMA + VVPE/MMA + ML algorithms at the cost of increased complexity. The EKF used shows no improvement over CMA + VVPE algorithm when tracking polarization and phase on a QPSK modulated signal throughout the OSNR range investigated and very marginal improvement over MMA + ML algorithm for higher QAM modulation formats at high OSNRs.

We have proposed reduced-complexity versions of the UKF and EKF, R-UKF and R-EKF, for joint polarization and phase noise tracking. The R-UKF outperforms both EKF and CMA + VVPE/MMA + ML for moderate and higher OSNRs (i.e. >10-dB for QPSK and >13-dB for 16-QAM), while requiring fewer computations than the EKF. Although the R-EKF is less complex than the EKF, its performance is compromised for target OSNRs (i.e. <18 dB for QPSK and <16 dB for 16-QAM). After transmission over an 800-km optical fiber link, all of the algorithms attain their peak performance at same launch powers; the UKF and R-UKF outperform the other algorithms, whose performances are similar except for low launch power region where the EKF shows marginal improvement over CMA + VVPE and R-EKF. In the case of 16-QAM signals, the UKF requires the lowest launch power at the 7% hard FEC limit followed by R-UKF, EKF, R-EKF and MMA + ML.

Overall, the Kalman filters give flexibility against changes in modulation formats as compared with the conventional systems. An UKF gives optimum performance over all other algorithms at the cost of increased complexity. In case of systems that require for lower complexity, an R-UKF proves to be an appropriate choice if its OSNR requirements are met.

Appendix A: Unscented Kalman filter algorithm

$$S_0 = [0, 0, \dots, 0]_{1 \times L}^T$$

$$P_0 = [0]_{L \times L}$$

L = 5 for UKF and EKF; L = 3 for R-UKF

$$A = I_{L \times L}$$

$$S_i^- = AS_{i-1}^-$$

$$P_i^- = AP_{i-1}^- A^T + Q$$

Calculate Sigma points:

$$(S_i)_k^- = S_i^- + \sqrt{(L + \lambda)(P_i^-)_k} \quad \text{where, } \lambda = L(10^{-3} + 1) \text{ and } (P_i^-)_k \text{ is the } k^{\text{th}} \text{ column of}$$

$$P_i^- \cdot (S_i)_f = \sum_{k=0}^{2L} \omega_k^{(m)} (S_i)_k^-$$

$$t_{ik} = e^{j\{(S_i)_k^-(s)\}} \begin{bmatrix} \{(S_i)_k^-(1)\} + j\{(S_i)_k^-(2)\} & \{(S_i)_k^-(3)\} + j\{(S_i)_k^-(4)\} \\ \{-(S_i)_k^-(3)\} + j\{(S_i)_k^-(4)\} & \{(S_i)_k^-(1)\} - j\{(S_i)_k^-(2)\} \end{bmatrix} \begin{bmatrix} Z_x \\ Z_y \end{bmatrix}$$

$$\hat{t}_i = \sum_{k=0}^{2L} \omega_k^{(m)} t_{ik}$$

$$P_{tt} = \sum_{k=0}^{2L} \omega_k^{(c)} (t_{ik} - \hat{t}_i)(t_{ik} - \hat{t}_i)^* + R \quad P_{tt} = \sum_{k=0}^{2L} \omega_k^{(c)} (t_{ik} - \hat{t}_i)(t_{ik} - \hat{t}_i)^* + R$$

$$P_{ts} = \sum_{k=0}^{2L} \omega_k^{(c)} ((S_i)_k^- - (S_i)_f)(t_{ik} - \hat{t}_i)^*$$

$$\omega_0^{(m)} = \lambda / (L + \lambda)$$

$$\omega_0^{(c)} = \{\lambda / (L + \lambda)\} + (1 - \alpha^2 + \beta)$$

For Gaussian distribution of parameters, $\beta = 2$

$$\text{Kalman gain: } (G_i) = P_{ts} P_{tt}^{-1}$$

$$S_i = (S_i)_f + G_i [\hat{t}_i - \text{decision}(\hat{t}_i)]$$

$$P_i = P_i^- - G_i P_{tt} G_i^*$$

Appendix B: Description of the mathematical observation model

The conventional mathematical model or Jones matrix for any birefringent material is given as [18]

$$M = \begin{bmatrix} e^{j\eta/2} \cos^2 \vartheta + e^{-j\eta/2} \sin^2 \vartheta & (e^{j\eta/2} - e^{-j\eta/2}) e^{-j\phi} \cos \vartheta \sin \vartheta \\ (e^{j\eta/2} - e^{-j\eta/2}) e^{j\phi} \cos \vartheta \sin \vartheta & e^{-j\eta/2} \cos^2 \vartheta + e^{j\eta/2} \sin^2 \vartheta \end{bmatrix} \quad (5)$$

where, η is the relative phase retardation induced between the fast axis and the slow axis, ϑ is the orientation of the fast axis with respect to the horizontal axis and ϕ is the circularity i.e. $\phi = 0$ for linear retarders and $\phi = \pm \pi/2$ for circular retarders. It can be observed that M forms a scaled unitary matrix that agrees with the properties of a Jones matrix.

The elements of Jones matrix, M are complex and can be written in phasor form as Xe^{jY} or in Cartesian form as $a+jb$. In our work, we chose the Jones matrix to be in Cartesian form as

$$M = \begin{bmatrix} a + jb & c + jd \\ -c + jd & a - jb \end{bmatrix} \quad (6)$$

The reason for choosing the Cartesian form lies in context to using the Kalman filters that require the parameters (to be estimated) to follow the Weiner process, i.e. an unknown

parameter z should follow $z_{n+1} = z_n + \Delta z$ where the suffix denotes the time instance and Δz is normal distributed such that $\Delta z \sim \mathcal{N}(0, \sigma_z^2)$. Since the real and imaginary parts of the elements of M follow Weiner procedure [4], Cartesian form is considered.

It may be possible that some researchers may favour to use the phasor form instead of Cartesian for reasons of their own. However, we prove here that using the phasor form does not work in Kalman filters. Consider the matrix element $a+jb$ with equivalent phasor form Xe^{jY} where a and b follow the Weiner process i.e $a_{n+1} = a_n + \Delta a$ and $b_{n+1} = b_n + \Delta b$. Thus, in order to use Xe^{jY} in Kalman filters, X and Y should also follow Weiner process.

$$\begin{aligned} \text{Now, } X_n &= \|a_n + jb_n\| \\ &= \sqrt{a_{n-1}^2 + b_{n-1}^2 + (\Delta a)^2 + (\Delta b)^2 + j(2a\Delta a + 2b\Delta b)} \end{aligned} \tag{7}$$

$$X_n = X_{n-1} \left(\sqrt{1 + \frac{(\Delta a)^2 + (\Delta b)^2 + j(2a\Delta a + 2b\Delta b)}{X_{n-1}^2}} \right) \quad (\text{from (7)}) \tag{8}$$

Now consider $\Delta X = X_n - X_{n-1}$

$$\Delta X = X_{n-1} \left(\sqrt{1 + \frac{(\Delta a)^2 + (\Delta b)^2 + j(2a\Delta a + 2b\Delta b)}{X_{n-1}^2}} - 1 \right) \tag{9}$$

The term $\{(\Delta a)^2 + (\Delta b)^2\}$ is exponential distributed and $(2a\Delta a + 2b\Delta b)$ is Gaussian distributed, Δa and Δb being Gaussian distributed. Thus, the addition of an exponential and Gaussian distribution is definitely not Gaussian. As a result, ΔX is not Gaussian distributed and X does not follow Weiner process, making phasor form Xe^{jY} unsuitable for Kalman filters.

Intuitively, since X is a non-zero magnitude, $X_n - X_{n-1} = (X_n - r)$ for $X_{n-1} =$ any positive number ' r '. Thus, the range within which $\Delta X = X_n - X_{n-1}$ can take values is $[-r, \infty]$. In order to make the distribution of X_n to take values within range $[-\infty, \infty]$, X_{n-1} has to take value ∞ that is not possible in practical systems. This contradicts the properties of Gaussian distribution that has the limits $[-\infty, \infty]$. As a result, again, ΔX is not Gaussian distributed and X does not follow Weiner process, making phasor form Xe^{jY} unsuitable for Kalman filters.

Relevance to Poincare sphere

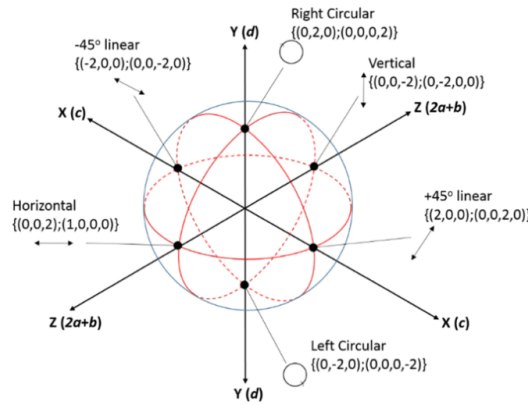


Fig. 8. Poincare sphere showing different polarizations with Stokes parameter and equivalent $[a, b, c, d]$ parameters in the form $\{(S1, S2, S3);(a, b, c, d)\}$.

The a, b, c, d parameters being the real and imaginary parts of M , they can be written as $a = \cos(\eta/2)$; $b = \sin(\eta/2) \cos \vartheta$; $c = 2 \sin(\eta/2) \sin \vartheta \sin \varnothing$; $d = 2 \sin(\eta/2) \cos \vartheta \sin \varnothing$. Calculating the values of these parameters for different polarizations from the corresponding values of Π , ϑ and \varnothing , the relevance of a, b, c, d parameters to Poincare sphere can be deduced as shown in Fig. 8.

Thus, it can be concluded that c and d denote the X and Y co-ordinates of the Poincare sphere, *i.e.* the normalized S1 and S2 Stokes parameters in Fig. 8 respectively, whereas the Z co-ordinate of the sphere (normalized S3) is denoted by $(2a+b)$ [19]. Hence, any polarization state on or within the Poincare sphere can be denoted in the form of a, b, c, d parameters and equivalent Jones matrix M can be derived from Eq. (6).

Funding

Australian Research Council's (ARC) Centre of Excellence and Laureate Fellowship schemes (CE110001018, FL130100041).

Acknowledgment

We thank VPIphotonics (www.vpiphotonics.com) for their support under the university program.

Simple optoelectronic frequency-offset estimator for coherent optical OFDM

JOKHAKAR JIGNESH,^{1,*} BILL CORCORAN,^{1,2} CHEN ZHU,^{1,3} AND ARTHUR LOWERY^{1,2}

¹*Electro-Photonics Lab, Department of Electrical and Computer Systems Engineering, Monash University, Clayton, VIC 3800, Australia*

²*Centre of Ultrahigh-bandwidth Devices for Optical Systems (CUDOS), Australia*

³*Now with Nokia Bell Labs, 600 Mountain Ave, Murray Hill, NJ 07974, USA*

*jignesh.jokhakar@monash.edu

Abstract: We propose a carrier frequency-offset estimator for optical OFDM systems using off-the-shelf optical components and simple digital processing as a replacement for the purely digital signal processing using the cyclostationarity property of optical OFDM signals with cyclic prefix. Simulations show the system accuracy of <4% estimate error within the range [-1250 + 1250] MHz offsets for a single polarization 28-Gbaud OFDM signal with 15% cyclic prefix. The effects of the system parameters on the performance are investigated.

© 2017 Optical Society of America under the terms of the [OSA Open Access Publishing Agreement](#)

OCIS codes: (060.1660) Coherent communications; (060.2330) Fiber optics communications; (130.0250) Optoelectronics.

References and links

1. W. Shieh, H. Bao, and Y. Tang, "Coherent optical OFDM: theory and design," *Opt. Express* **16**(2), 841–859 (2008).
2. A. J. Lowery and L. B. Du, "Optical orthogonal division multiplexing for long haul optical communications: A review of the first five years," *Opt. Fiber Technol.* **17**(5), 421–438 (2011).
3. M. Selmi, Y. Jaouen, and P. Ciblat, "Accurate digital frequency offset estimator for coherent PolMux QAM transmission systems," in *European Conference on Optical Communication*, 2009, Vienna, Austria, paper P3.08.
4. X. Du, J. Zhang, C. Yu, and P. Kam, "Blind carrier frequency offset estimation for coherent optical OFDM Systems," in *Advanced Photonics 2016 (IPR, NOMA, Sensors, Networks, SPPCom, SOF)*, OSA Technical Digest (online) (Optical Society of America, 2016), paper SpW2G.3.
5. M. Li, J. Zhao, and L. K. Chen, "Blind maximum-likelihood frequency offset estimation for coherent fast OFDM receivers," *2013 18th OptoElectronics and Communications Conference held jointly with 2013 International Conference on Photonics in Switching (OECC/PS)*, 2013, Kyoto, Japan, Paper TuPr-11.
6. A. Dweik, A. Hazmi, S. Younis, B. Sharif, and C. Tsimenidis, "Blind iterative frequency offset estimator for orthogonal frequency division multiplexing systems," in *IET Communications* **4**(16), 2008–2019 (2010).
7. H. Böleskei, "Blind estimation of symbol timing and carrier frequency offset in wireless OFDM systems," *IEEE Trans. J. Comm.* **49**(6), 988–1000 (2001).
8. T. M. Schmidl and D. C. Cox, "Robust frequency and timing synchronization for OFDM," *IEEE Trans. Commun.* **45**, 1613–1621 (1997).
9. H. Minn, V. K. Bhargava, and K. B. Letaief, "A robust timing and frequency synchronization for OFDM systems," *IEEE Trans. Wirel. Commun.* **2**(4), 822–839 (2003).
10. S. H. Fan, J. Yu, D. Qian, and G. K. Chang, "A fast and efficient frequency offset correction technique for coherent optical orthogonal frequency division multiplexing," *J. Lightwave Technol.* **29**(13), 1997–2004 (2011).
11. C. Xie and G. Raybon, "Digital PLL based frequency offset compensation and carrier phase estimation for 16-QAM coherent optical communication systems," in *European Conference on Optical Communication*, 2012, Amsterdam, Netherlands, paper Mo.1. A.2.
12. N. Nambath, M. Anghan, N. B. Thaker, R. Ashok, R. Kamran, A. K. Mishra, and S. Gupta, "First Demonstration of an All Analog Adaptive Equalizer for Coherent DP-QPSK Links," in *Optical Fiber Communication Conference*, 2017, Los Angeles, USA, paper M3D.5.
13. Z. Liu, J. Kim, D. Wu, D. Richardson, and R. Slavik, "Homodyne OFDM with optical injection locking for carrier recovery," *J. Lightwave Technol.* **33**(1), 34–41 (2014).
14. M. Lu, H. Park, J. Parker, E. Block, A. Sivananthan, Z. Griffith, L. Johansson, M. Rodwell, and L. Coldren, "A heterodyne optical phase-locked loop for multiple applications," in *Optical Fiber Communication conference*, 2013, Anaheim, USA, paper OW3D.1.
15. L. Naglic, L. Pavlovic, B. Bategelj, and M. Vidmar, "Improved phase detector for electro-optical phase-locked loops," *Electron. Lett.* **44**(12), 758–761 (2008).

16. J. Jokhakar, B. Corcoran, C. Zhu, and A. J. Lowery, "Electro-optic frequency offset estimator for optical OFDM," in *European Conference on Optical Communication*, 2016, Dusseldorf, Germany, paper P1.SC3.31.
17. J. Li, R. Schmogrow, D. Hillerkuss, P. C. Schindler, M. Nazarathy, C. Schmidt-Langhorst, S. B. Ezra, I. Tselniker, C. Koos, W. Freude, and J. Leuthold, "A self-coherent receiver for detection of PolMUX coherent signals," *Opt. Express* **20**(19), 21413–21433 (2012).
18. T. Fujita, Y. Toba, Y. Miyoshi, and M. Ohashi, "Optical analog multiplier based on phase sensitive amplification," in *Optoelectronics and Communication conference*, 2013, Kyoto, Japan, Paper TuPS-8.
19. Datasheet "Corning SMF-28e Optics Fiber Product Information." Available: http://www.tlc.unipr.it/cucinotta/cfa/datasheet_SMF28e.pdf.
20. M. Khanzadi, "Modelling and estimation of phase noises in oscillators with coloured noise sources," Ph.D. dissertation, Dept. of Signals and Systems, Chalmers Univ. of Technology, Goteborg, Sweden, 2013.
21. W. Shieh and K. P. Ho, "Equalization-enhanced phase noise for coherent-detection systems using electronic digital signal processing," *Opt. Express* **16**(20), 15718–15727 (2008).

1. Introduction

Coherent optical OFDM (CO-OFDM) allows for high spectral efficiency by supporting high-order complex modulation schemes and by providing a compact signal spectral [1,2]. This allows for ultra-high speed, spectrally efficient signaling in fiber communication links. However, CO-OFDM is highly sensitive to the carrier frequency offsets (CFO) that causes a loss of orthogonality of the subcarriers, leading to errors.

Digital signal processing (DSP) at the receiver side of a fiber optic link is often used to estimate and then compensate for the CFO. There are several different approaches taken to achieve this. A spectral peak search method can be used [3], which finds the peak in the absolute Fast-Fourier transform (FFT) spectral of a large number of samples from the coherently received signal. Xinwei *et al.* proposed a technique that estimates the CFO based on the power variations in the null subcarriers [4] and Ming *et al.* proposed a likelihood function [5] to be maximized. An iterative frequency offset estimation method has been proposed in [6] for OFDM signals. Digital autocorrelation based technique that uses the cyclic prefix of OFDM to estimate the CFO can also be used [7]. Training-based techniques have been proposed by Schmidl and Cox in [8] and by Minn *et al.* in [9]. Such training-symbols and pilot-subcarrier based CFO estimation techniques have also been proposed by Fan *et al.*, which achieve dynamic tracking of the CFO [10]. Digital phase-locked loops (PLLs) have also been explored for CFO estimation and correction by using a carrier phase estimator [11]. Of all of these techniques, the most widely used techniques are the spectral peak search method [3] and the digital autocorrelation method [7]. Both techniques require a large number of samples to be processed which drastically adds to the computational latency in the DSP. Any attempts to reduce the computational cost/ latency by processing less number of samples will result in loss of estimate accuracy or resolution that has deleterious effect on the OFDM performance. The techniques proposed by Schmidl and Cox in [8] and by Minn *et al.* in [9] are also widely used but, as the proposed CFO estimation method in this paper is also blind, we choose the blind spectral-peak search method for fair comparison.

The latency, as a figure of merit for comparison, is a decisive parameter for a processing system. A small improvement in latency is important owing to its impact on certain business models. For example, the latency over the internet was widely exploited by few Wall Street traders who managed to get faster access to the stock prices than the rest by using dedicated optical fiber internet connections. A latency of a few milliseconds was translated to multi-million-dollar stock deals in favour of these few traders with high speed access. This, consequently, has fueled parallel and real-time processing research over decades. This paper intends to address this latency issue in data-recovery by reducing the load on DSP.

Instead of replacing these algorithms with their parallel-processing counterparts, we propose to completely remove the estimation algorithm. While parallelization can reduce the processing time by a given factor related to the number of parallel processes, this will increase the required high-speed (GHz-scale) digital hardware resources. To break the hardware/latency trade off from parallelization, we instead propose to minimize latency by performing CFO estimation with an analog optoelectronic system and low-speed (MHz-scale)

digital processing. This aim provides another step toward all-analogue signal processing for low latency coherent communications [12].

To this end, we propose an optoelectronic frequency offset estimator (OEFOE) that operates in parallel to the coherent receiver, as shown in Fig. 1, and allows for removal of the computationally expensive estimation algorithms from the DSP.

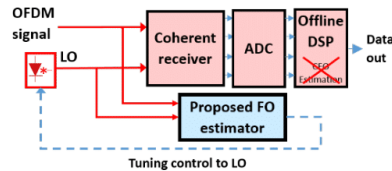


Fig. 1. Receiver implementing the proposed estimator. ADC: Analog-to-Digital converter; LO: Local oscillator.

All-optical or electro-optical techniques can also be employed, to avoid placing a processing burden on the DSP. These include optical injection locking (OIL) [13], optical phase-locked loops (OPLL) [14] and electro-optic phase-locked loops (EOPLL) [15]. Although these methods have their own advantages, such as simultaneous phase noise mitigation and sequential architectures, but they are restricted by the complexities in OPLL, bandwidths of the components in EOPLL or requirement of a guard band in OIL case. The proposed OEFOE gives accurate estimates for the CFO of $< 4\%$ error without requiring high speed, expensive components, while keeping the design simpler than OIL, EOPLL or an OPLL. While we have shown that it is possible to get accurate frequency offset estimates from an OEFOE using off-the-shelf components (as presented at ECOC'16 [16]), in this paper we use simulations to perform an in-depth analysis of the effects of various system parameters on estimate accuracy. The system takes the received signal and the local oscillator (LO) signal as inputs and gives an electrical output corresponding to the frequency offset as shown in Fig. 1. This output is provided as a feedback to the local oscillator laser to perform the offset correction.

Section 2 outlines the mathematical underpinning for the operation of the proposed OEFOE. Section 3 presents two versions of the OEFOE depending on the implementation scenario and gives simulation results considering parameters specific to each version design. Section 4 shows the effects of system parameters common to both designs, and investigates the Q performance after transmission over various distances with QPSK or 16-QAM modulated signals. Finally, the conclusions are made in Section 5.

2. Concept of optoelectronic frequency offset estimation for OFDM

The underlying concept for the working of the OEFOE lies in the cyclostationarity property of OFDM signals with cyclic prefixes [7]. We show mathematically how this leads to frequency offset estimation. Consider an OFDM signal $E_s(t)$ with a cyclic prefix of period T_{CP} . Let τ_1 be the OFDM symbol period without the cyclic prefix as shown in the inset of Fig. 2(a).

Thus,

$$E_s(t) = E_s(t + \tau_1) \text{ for } t = 0 \text{ to } T_{CP}. \quad (1)$$

Now consider the autocorrelation $R(\tau)$ of the signal $E_s(t)$ with delay τ .

$$\therefore R(\tau) = \int_0^\infty E_s(t) E_s(t + \tau)^* dt. \quad (2)$$

Let the carrier frequency of the transmitted signal be ω_0 and carrier frequency offset Δf . Thus, the received signal Y_s and the local oscillator signal Y_L are

$$Y_s(t) = E_s(t)e^{j\omega_0 t + \phi_1}. \quad (3)$$

$$Y_L(t) = E_L(t)e^{j(\omega_0 + 2\pi\Delta f)t + \phi_2}. \quad (4)$$

where $E_L(t)$ is the amplitude of the local oscillator signal and ϕ_1, ϕ_2 are the phase offsets. The autocorrelations of $Y_s(t)$ and $Y_L(t)$ are

$$\begin{aligned} R_s(\tau) &= \int_0^\infty Y_s(t)Y_s^*(t+\tau) dt \\ &= e^{-j\omega_0\tau} \int_0^\infty E_s(t)E_s^*(t+\tau) dt \\ &= e^{-j\omega_0\tau} R(\tau). \end{aligned} \quad (5)$$

$$\begin{aligned} R_L(\tau) &= \int_0^\infty Y_L(t)Y_L^*(t+\tau) dt \\ &= e^{-j\omega_0\tau} e^{-j2\pi\Delta f\tau} \int_0^\infty E_L(t)E_L^*(t+\tau) dt \\ &= e^{-j\omega_0\tau} e^{-j2\pi\Delta f\tau} L(\tau). \end{aligned} \quad (6)$$

where. The phase offsets ϕ_1 and ϕ_2 are affected by the laser phase noise but the integration process and the Wiener process nature of the phase noise negates their effect. This will be explained further in section 5.1. Note that $R_s(\tau)$ and $R_L(\tau)$ are not dependent on the time parameter, t , but remain constant for a fixed value, τ , for a fixed CFO, Δf .

The ratio of $R_s(\tau)$ and $R_L(\tau)$ is:

$$D(\tau) = \frac{R_s(\tau)}{R_L(\tau)} = \frac{e^{j2\pi\Delta f\tau} R(\tau)}{L(\tau)}. \quad (7)$$

Now, if the delay $\tau = \tau_1$ from Eqs. (1) and (2), $R(\tau_1) = \int_0^\infty E_s(t)E_s^*(t+\tau_1) dt$.

The $R(\tau_1)$ can be written as summation of multiple OFDM symbols as follows

$$R(\tau_1) = \sum_{n=0}^{\infty} \int_{t=0}^{t=T_{OFDM}} E_s(nT_{OFDM} + t)E_s^*(nT_{OFDM} + t + \tau_1) dt. \quad (8)$$

where, n determines the OFDM symbol index and T_{OFDM} is the OFDM symbol period given as $T_{OFDM} = T_{CP} + \tau_1$. For realistic system, n ranges up to a finite value N_{int} that reflects the number of OFDM symbols that need to be integrated for the proposed system to converge to the required estimate. $R(\tau_1)$ can then be extended as

$$R(\tau_1) = \sum_{n=0}^{N_{int}} \left(\int_0^{T_{CP}} E_s(nT_{OFDM} + t)E_s^*(nT_{OFDM} + t) dt + \int_{T_{CP}}^{T_{OFDM}} E_s(nT_{OFDM} + t)E_s^*(nT_{OFDM} + t + \tau_1) dt \right).$$

Since the OFDM symbols are uncorrelated for $t > T_{CP}$, the second term will reduce to zero. As a result, for $\tau = \tau_1$, $R(\tau) = \sum_{n=0}^{N_{int}} \int_0^{T_{CP}} |E_S(nT_{OFDM} + t)|^2 dt$ and is real. It is important to note here that the strength of the autocorrelation is proportional to the length of cyclic prefix. Thus, longer cyclic prefixes will improve the system accuracy, as will be shown in next section. Similarly, since the amplitude of the local oscillator signal $E_L(t)$ can be taken as constant, $L(\tau) = \int_0^{T_{CP}} |E_L(t)|^2 dt$ and is also real. Thus, the only complex term in Eq. (7) is $e^{j2\pi\Delta f\tau}$ and the CFO can be calculated as

$$\Delta f = \frac{\angle D(\tau_1)}{2\pi\tau_1} \tag{9}$$

So, by mixing both the signal & local oscillator with delayed copies of themselves and then integrating the resulting waveforms, we are able to gain an estimate of the frequency. This mixing and integration can be done using 90° hybrids and slow photodiodes respectively and whole estimation can thus be performed in analog domain.

3. System design and simulations

In this paper, we propose two sub-system designs to provide the required mixing for the OEFOE, where each design has its own benefits in different implementation scenarios.

3.1 OEFOE version 1

3.1.1 System design

The first design of the proposed optoelectronic CFO estimator (OEFOE 1) is shown in Fig. 2(a). This design is conceptually closest to the method described in the previous section, with the delayed signal and delayed LO mixing occurring physically separately.

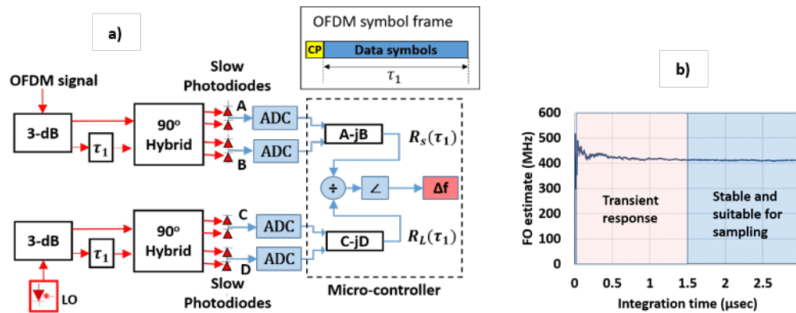


Fig. 2. a) Proposed optoelectronic CFO estimator (OEFOE) design. Inset: OFDM symbol frame structure. b) System output with photodiode integration time for CFO = 410 MHz.

OEFOE 1 takes the received OFDM signal as input and splits it using a 3-dB coupler. The signal is delayed in one of the arms by a specific delay τ_1 , equal to the OFDM symbol period without the cyclic prefix (as shown in the inset of Fig. 2(a)). We assume that the structure of the cyclic prefix of the signal in the optical network or a link is standardized and known to the receiver. Thus, the delay line's length (τ_1) can be spliced accordingly. Just to make the proposed OEFOE flexible, the delay line fiber can be made detachable such that it can be

replaced appropriately whenever the cyclic prefix length is changed. Problems may arise only when the system dynamically changes the cyclic prefix length.

The signal and the delayed version are then fed to a 90° -hybrid and the outputs of the hybrid are detected by slow photodiodes in balanced configuration. The output of the configuration will converge to $R_s(\tau_1)$ [17] as shown in Fig. 2(a). Simultaneously a similar setup generates a signal that converges to $R_L(\tau_1)$ as shown in Fig. 2(a). The integration operation required for $R_s(\tau_1)$ and $R_L(\tau_1)$ is performed by the slow photodiodes [18], with a response time governed by the parameter N_{int} . The integration time of the photodiodes has to be more than $(N_{int} \times T_{OFDM})$. Figure 2(b) shows the OEFOE's output against time from which the convergence can be extrapolated to find the number of OFDM symbols to be integrated (N_{int}).

Simulations were performed in VPITransmissionMaker for a 28-Gbaud QPSK modulated OFDM signal and 15% cyclic prefix. The experimental verification was shown previously in [16]. In this paper we perform simulations to understand the effects of various parameters involved in the system. It was observed that the output converges to the actual CFO of 410 MHz after 1.5 μ s. Hence, the number of OFDM symbols that need to be integrated to converge to the required estimate can be given as $N_{int} = 1.5e-6/T_{OFDM}$. This dependence of convergence on the cyclic prefix is discussed in Section 4. In the case of fast photodiodes, the integration can be provided by bandwidth-limiting filters. However, this is not advised as it increases the cost. The remaining operations to calculate the CFO (Eq. (9)) can be performed using a simple microprocessor. To do so, the electrical signals at the output of the balanced configuration need to be sampled after convergence. A single sample taken after 1.5 μ s is sufficient to calculate the CFO using Eq. (9). Note that the actual sampling takes place after the balanced photodiodes in Fig. 2(a); the trace in Fig. 2(b) just helps to visualize the convergence time.

As depicted in Fig. 2(a), OEFOE 1 could be implemented with passive off-the-shelf components such as 3-dB couplers, 90° -hybrids, and optical delay lines. Additionally, the electronic components can have low bandwidth, as only slow photodiodes and ADCs with MHz sampling rate are required. Moreover, only a small number of float-point operations are required on the samples to give the desired frequency offset estimates, which can readily be performed by a simple microcontroller. Given these desirable qualities, we next simulate OEFOE 1.

3.1.2 Simulations and results for the OEFOE 1

The OEFOE 1 design in Fig. 2(a) was simulated in VPITransmissionMaker software (Version 9.7). A 28-Gbaud OFDM signal of FFT length 156, 100 subcarriers and 15% cyclic prefix was generated and oversampled at 40-GSa/s sampling rate. With this configuration, the delay τ_1 can be calculated to be 0.8 ns. Substituting $\tau_1 = 0.8$ ns in Eq. (9) with $\angle D(\tau_1) \in [-\pi, \pi]$, we find the estimation range of the OEFOE to be [-625 MHz + 625 MHz].

Figure 3(a) shows the scatterplot of the CFO estimated by the OEFOE in back-to-back setup compared with the spectral-peak search method. The CFO was randomly chosen within the range [-1250 MHz + 1250 MHz] for 1000 runs and estimates were calculated by both methods. As expected, the OEFOE gives accurate results with estimate errors < 1% up to ± 625 MHz. The slope of the scatter plot reverses beyond 625 MHz because of phase reversal of $\angle D(\tau_1)$ beyond π radians for positive CFO and beyond $-\pi$ radians for negative CFO, creating an ambiguity in estimating CFO beyond ± 625 MHz (Fig. 3(a)). To resolve this ambiguity we add a known phase shift $\Delta\phi = 2\pi f_k \tau$ digitally to $R_s(\tau)$ where f_k is known (+ 2 MHz in our case) giving $R_s^k(\tau) = R_s(\tau)e^{j2\pi f_k \tau}$ and leading to Δf^k . If, $\Delta f < 625$ MHz, $\Delta f^k - \Delta f$ will be positive owing to positive frequency shift and if $\Delta f > 625$ MHz,

$\Delta f^k - \Delta f$ will be negative due to the negative slope in this region. Hence, with one additional multiplicative and subtracting operation in the microcontroller, the ambiguity can be resolved to give full estimation range of $[-1250 + 1250]$ MHz as shown in Fig. 3(b). As these computations are to be performed on a low-clock rate microcontroller, the cost of providing this computations is orders of magnitude lower than for GHz-clock DSP ASICs used in conventional coherent communication systems. This method to resolve ambiguity will fail within the range $[623 \text{ } 625]$ MHz of the absolute actual CFO, excluding the limiting values. However, despite of this failure in ambiguity resolution, the error in CFO calculation will be a maximum of 4 MHz which is still very low ($< 6.4\%$). Apart from that, the chance of the actual CFO falling within this range is low. So, in practical systems that have the CFO drifting frequently, the proposed OEFOE will have a negligible outage probability.

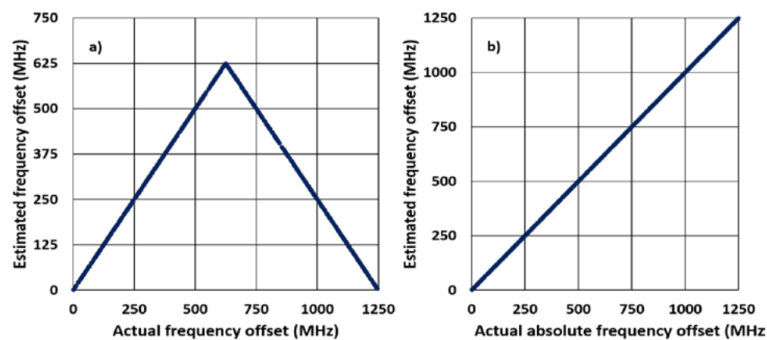


Fig. 3. Scatterplots of Estimated CFO vs. Actual CFO (MHz) for a) with ambiguity beyond 625 MHz CFO and b) ambiguity resolved.

3.1.3 Implementation issues for the OEFOE 1

In practical implementation of the OEFOE with discrete components as suggested above, the device's performance is affected by various parameters such as:

- 1) different delays in the optical delay lines before the hybrids in Fig. 2(a) instead of a single delay, τ_1 .
- 2) different phase differences between signals at the outputs of the 3-dB couplers in Fig. 2(a).

These parameters could be precisely controlled if OEFOE 1 was to be implemented on an integrated 'photonic chip', by providing a phase-stable platform. In the case when the OEFOE needs to be prototyped with discrete components, the OEFOE 1 fails to give accurate result owing to the parameters mentioned above that cannot be controlled or calibrated any more. For such scenario of implementation with discrete components, we propose a different design, Version 2, as discussed in the next section.

3.2 OEFOE version 2

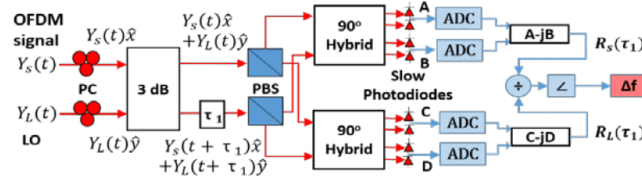


Fig. 4. Modified setup. PC: polarization controller; PBS: polarization beam splitter.

3.2.1 System design

We propose a modified version of the OEFOE setup that can be prototyped with discrete components. This second version (OEFOE 2) uses only one optical delay line and one 3-dB coupler for both received and LO signals and exploits a dual-polarization coherent receiver to estimate the CFO. The received signal $Y_s(t)$ and the local oscillator signal $Y_L(t)$ are orthogonally polarized, placed on x and y polarizations respectively using polarization controllers (PC) and combined using a 3-dB coupler. Thus, the 3-dB coupler will have signal $Y_s(t)\hat{x} + Y_L(t)\hat{y}$ on one output arm and a delayed version $Y_s(t + \tau_1)\hat{x} + Y_L(t + \tau_1)\hat{y}$ on the other arm after passing through an optical delay line, τ_1 . These signals, after splitting by polarization beam splitters (PBS) are received as $Y_s(t)\hat{x}$ and $Y_s(t + \tau_1)\hat{x}$ at the inputs of one 90°-hybrid and $Y_L(t)\hat{y}$ and $Y_L(t + \tau_1)\hat{y}$ at the inputs of other hybrid, similar to the OEFOE 1 setup in Fig. 2(a). Thus, the rest of the system is the same as in Fig. 2(a), and we can acquire the CFO estimates at the output. We can then show that this system is robust to phase and delay perturbations that effected the OEFOE 1 design. The proposed systems in Figs. 3 and 4 resemble a coherent receiver, which is usually costly; however, we do not use the high-speed photodiodes or high-speed ADCs, which are the major contributors to the high cost of the coherent receivers.

3.2.2 Effects of the phase difference between signals at outputs of the 3-dB coupler

Let the phase mismatch between the two output arms of the 3-dB coupler be $\Delta\phi$. Thus, the inputs of the PBSs in Fig. 4 are

$$P_1(t) = e^{j\Delta\phi} (Y_s(t)\hat{x} + Y_L(t)\hat{y}). \tag{11}$$

$$P_2(t + \tau_1) = Y_s(t + \tau_1)\hat{x} + Y_L(t + \tau_1)\hat{y}. \tag{12}$$

After being split by the PBSs, from Eqs. (5) and (6), the autocorrelation values will be

$$R_s(\tau) = e^{-j\omega_0\tau} e^{j\Delta\phi} R(\tau) \text{ and } R_L(\tau) = e^{-j\omega_0\tau} e^{-j2\pi\Delta f\tau} e^{j\Delta\phi} L(\tau). \tag{13}$$

As a result, after taking a ratio of $R_s(\tau)$ and $R_L(\tau)$ in the microprocessor, the $e^{j\Delta\phi}$ term is cancelled and the value of $D(\tau)$ remains the same as in Eq. (7). So, any phase mismatch between the signals in the output arms of the 3-dB coupler should have no effect on OEFOE 2.

3.2.3 Effects of the delay variations in the optical delay line (τ_1)

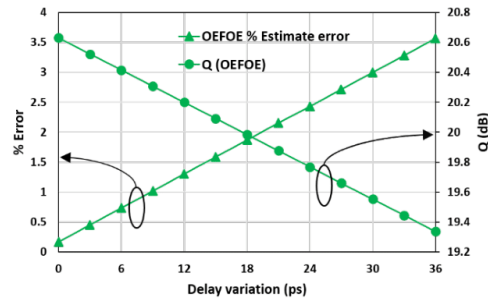


Fig. 5. Q (dB) and estimate % error vs. delay variations (ps) in optical delay line.

For commercial SMF-28e fibers, the temperature variations in the fiber lengths we use to implement our system can cause a delay variation up to ± 30 ps [19], corresponding to a $\sim 4\%$ variation away from the required delay value. Again, we use a 28-Gbaud, QPSK encoded OFDM signal of FFT length 156, 100 subcarriers and 15% cyclic prefix as a test signal. As observed in Fig. 5, the delay variations cause a linear increase in the error and degradation of the Q performance of the system. This is observed despite of assuming perfect extinction ratio PBS whose effect will be added in the next section. With the delay variations increasing from 0 ps to 36 ps (4.5% or τ_1), the % error increases from 0.16% to 3.6% causing the Q of the recovered signal to drop from 20.6 dB to 19.35 dB i.e. by 1.25 dB. This degradation, however, can be nulled by keeping the system in a temperature-controlled environment or by integration. The delay variations are more problematic in the OEFOE 1 as it uses two optical delay lines and the paths are independent. On the other hand, OEFOE 2 uses a single optical delay line and thus the shifts are common for both the OFDM and the LO signals. Thus, OEFOE 2 is less affected by the delay variations than OEFOE 1, if both versions are implemented in lab using discrete components. Still, shifts in delay away from τ_1 cause inaccuracies.

3.2.4 Effect of the polarization misalignment in the polarization controllers

As the OEFOE 2 uses polarization diversity, the polarization alignment of the signal becomes an important factor in the performance. For accurate CFO estimations, the polarization controllers in Fig. 4 need to be aligned properly such that the $Y_s(t)$ and the local oscillator signal $Y_L(t)$ are orthogonally polarized on x and y polarizations respectively. In case of polarization misalignment, the system gives errors. As shown in the Fig. 6(b) the estimate errors increase nonlinearly with a decrease in the polarization extinction ratio (ER). In simulations, the polarization beam splitter is modelled to have a perfect ER, and so the change in the ER determined by the polarization misalignment θ , where $ER = -10\log_{10}(\sin^2[\theta])$.

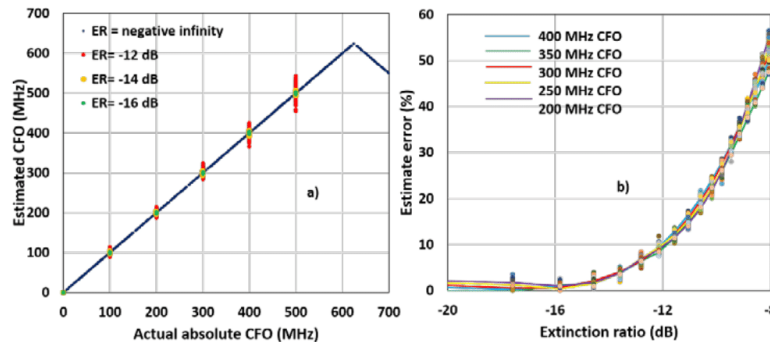


Fig. 6. a) Scatterplots of the CFO estimates for different polarization extinction ratio (ER) and b) Estimate error (%) vs. ER (dB).

In reality, the limited ER of the polarization beam splitters would need to be taken into account. It can be observed that the errors increase rapidly from almost 0% to 50% when the polarization misalignment θ is increased from 0° (ER = -20.5 dB) to 10° (ER = -8 dB). This is reflected in Fig. 6(a) wherein the scatterplot shows perfect estimation for ER = $-\infty$ i.e. when $\theta = 0$ but the errors increase rapidly when the ER is slightly increased from -16 dB to -12 dB. This shows the proposed OEFOE 2 is also sensitive to the polarization alignment of the polarization controllers and should be properly taken care of while performing the experiments.

A specific OEFOE design can be chosen according to the application scenario. The OEFOE 1 design is accurate with $< 0.2\%$ errors when fabricated on an integrated photonic chip with controllable design parameters. On the other hand, when implemented with discrete components, the OEFOE 1 performance is majorly affected by the delay variations and phase difference between outputs of 3-dB couplers. Consequently, the OEFOE 2 design is proposed that is robust to the 3-dB coupler phase differences and less sensitive to the delay variations compared with the OEFOE 1 design. However, this design is sensitive to the polarization extinction ratio of the PBSs in the design and needs to be carefully taken care of for accurate results. The next sections discuss the parameters in the system that are common to both designs and their effects on the estimation accuracy.

4. Variation of performance against cyclic prefix length

As seen in Eq. (8), the strength of the autocorrelation depends on the limits of the integral; i.e. on the duration of the cyclic prefix (T_{CP}) that in turn determines the accuracy of the system. In other words, from Eq. (8), $R(\tau)$ will be more accurate when the cyclic prefix is longer. Intuitively, longer cyclic prefix, T_{CP} means that the autocorrelation is calculated over more symbols that increases its strength and thus the accuracy of the system. However, a longer cyclic prefix reduces spectral efficiency, showing a trade-off between Q performance and spectral efficiency.

The effect of changing cyclic prefix length can be seen in Fig. 7(a)-7(c) where the OEFOE converges to the actual CFO faster for the signals with longer CP. From Fig. 7(a)-7(d) it can be observed that the convergence is affected by the CP proportion (a-c) and not by the FFT size (Fig. 7(d)), giving us freedom when choosing the FFT size according to the channel frequency response. Moreover, the magnitude of the frequency offsets also affects the convergence as can again be observed from Fig. 7(a)-7(c); with greater frequency offsets causing slower convergence.

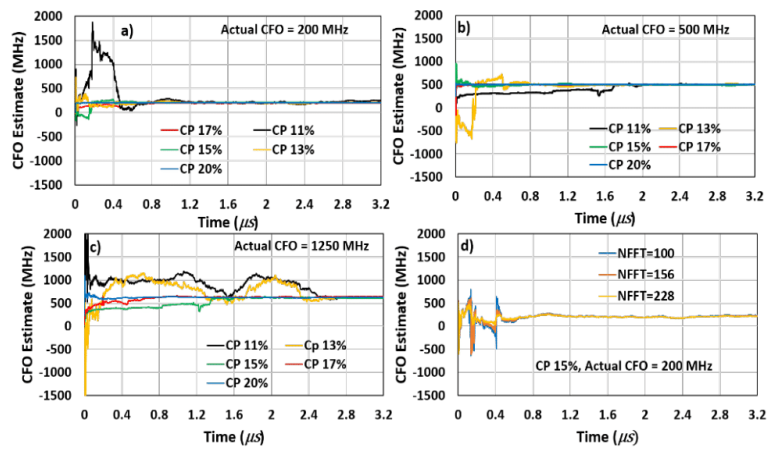


Fig. 7. CFO estimate (MHz) vs. time (μs) for: a) actual CFO = 200 MHz and different cyclic prefix (CP); b) actual CFO = 500 MHz and different cyclic prefix; c) actual CFO = 1250 MHz and different cyclic prefix and d) 15% CP with actual CFO = 200 MHz and different FFT size (NFFT).

The convergence helps us to determine the sampling rate of the ADCs in the proposed OEFOE. We observe that for maximum trackable CFO (1250 MHz) and 15% CP the estimation signal converges at $1.35 \mu s$. Any CP lower than 15% causes the convergence to occur after $2.4 \mu s$. To ensure the convergence, we sample the electrical signals after $1.5 \mu s$ for CP set at 15%. Conversely, this means that for a sampling period of $1.5 \mu s$, the CP must be at least 15%.

Figure 8 shows the effect of varying the CP length while retaining a sampling period of $1.5 \mu s$. The estimate error of the OEFOE remains less than 0.2% for cyclic prefix of 15% or more, while it increases rapidly if the CP is reduced below 15%. Thus, for the rest of our investigations, we will work with a CP of 15% and a sampling period of $1.5 \mu s$.

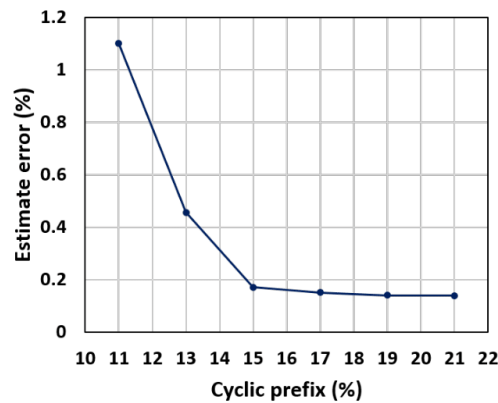


Fig. 8. Estimate error (%) vs. Cyclic prefix (%).

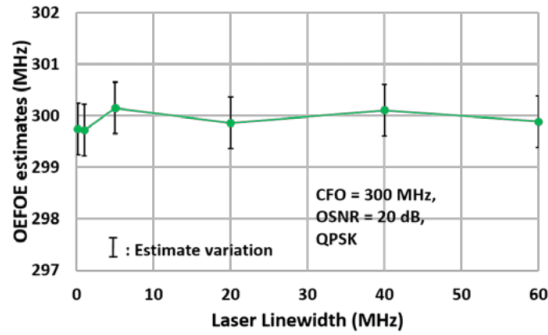


Fig. 9. CFO estimate vs. laser linewidth (MHz) for CFO = 300 MHz.

5. Simulated system performance

We next investigate OEFOE performance against system parameters, such as laser linewidth and OSNR, before simulating performance after transmission through 200 to 700 km fiber links.

5.1 Laser linewidth

The linewidth of the lasers used in a system determine the variance of the phase noise for that system. Figure 9 shows the OEFOE estimates for a CFO of 300 MHz at OSNR of 20 dB, irrespective of the linewidths investigated (from 100 kHz to 60 MHz), accurate to < 1 MHz. Thus, the proposed OEFOE system is robust to phase noise. This can be explained by the laser phase noise following a Wiener model [20]. Let $\varphi(t)$ be the phase noise added to the signal at time t . Following the Wiener model [20],

$$\varphi(t) = \varphi(t-1) + \Delta\varphi. \quad (14)$$

where, $\varphi(t) - \varphi(t-1) = \Delta\varphi_t$ is Gaussian distributed with zero mean and finite variance $\sigma_{\Delta\varphi_t}^2$. Continuing further,

$$\varphi(t-1) - \varphi(t-2) = \Delta\varphi_{t-1} \sim N(0, \sigma_{\Delta\varphi_{t-1}}^2). \quad (15)$$

$$\therefore \varphi(t) - \varphi(t-2) = \Delta\varphi_{t-2} \sim N(0, (\sigma_{\Delta\varphi_{t-1}}^2 + \sigma_{\Delta\varphi_t}^2)). \quad (16)$$

Eventually,

$$\therefore \varphi(t) - \varphi(t - T_{CP}) = \Delta\varphi_{t-T_{CP}} \sim N(0, (\sigma_{\Delta\varphi_t}^2 + \sigma_{\Delta\varphi_{t-1}}^2 + \dots + \sigma_{\Delta\varphi_{t-T_{CP}+1}}^2)). \quad (17)$$

Hence, while calculating $R(\tau)$, the phases of $E_s(t)$ and $E_s(t + \tau_1)$ subtract and the integration process converges to the mean of $\Delta\varphi_{t-\tau_1}$ that is zero, nulling the effect of phase noise on the CFO estimation.

5.2 AWGN loading

To test the robustness of the system to the channel noise, the OFDM signal was QPSK modulated and noise loaded with varying optical signal to noise ratio (OSNR). Figure 10 compares the Q performance of the signal recovered using OEFOE with that of the signal recovered using the conventional spectral peak search method with OSNR sweep. We again use a test signal of QPSK encoded OFDM at a rate of 28-Gbaud, with FFT length 156, 100

occupied subcarriers and a 15% cyclic prefix. The CFO is set to 300 MHz in the simulations. The phase mismatch between the output arms of the 3-dB coupler and the delay variations in the optical delay line are varied randomly within the ranges $[-\pi, +\pi]$ and $[0, 30]$ ps respectively.

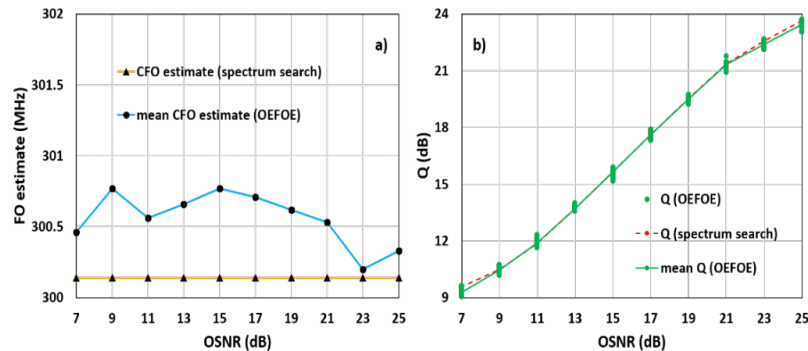


Fig. 10. a) CFO estimates vs. OSNR (dB) and b) Q (dB) vs. OSNR (dB) for 28-Gbaud QPSK, FFT length = 156, number of subcarriers = 100, 15% cyclic prefix and carrier frequency offset (CFO) = 300 MHz.

The mean CFO estimate plot from the OEFOE shows random variations independent of the OSNR. These variations are caused by the delay fluctuations in the optical delay line. Regardless, the mean estimates of the CFO from the OEFOE shows errors less than 1 MHz. The Q performance varies by maximum 0.8 dB around the mean Q at different OSNR. The plot of mean Q of signal recovered by OEFOE closely follows that of signal recovered by the spectral peak search method. Thus, it can be inferred that the system is robust to the noise added to the signal. This can be explained by the integration operation performed by the slow photodiodes that average out the additive white Gaussian noise with zero mean.

5.3 Chromatic dispersion and nonlinear effects of the fiber

The OEFOE system is added in parallel to the coherent receiver setup. As a result, the input signal is perturbed with chromatic dispersion and nonlinearities when transmitted over a length of optical fiber. As such it becomes important to test the OEFOE over a transmission link. Additionally, the modulation format flexibility is also an important characteristic for the modern 400G optical networks handling signals with different modulation formats and needs to be examined.

5.3.1 Simulated transmission system: QPSK

To understand the effects of chromatic dispersion and nonlinearities of the optical fiber, the signal was simulated over transmission links of lengths from 200 km to 700 km. A recirculating loop was simulated to achieve these link lengths by varying the number of recirculations. Each loop consisted of one span of 100 km. Figure 11 shows the mean OEFOE and spectral peak search estimates with varying launch powers for various transmission lengths with actual CFO fixed at 300 MHz. The plots show no particular pattern with increasing transmission lengths or launch powers. The mean estimates show < 1 MHz errors compared with the spectral peak search.

Figure 12 shows the plots of the Q of the signal recovered by the OEFOE compared with that of the signal recovered by the spectral-peak search method with launch power sweeps and different transmission distances. The system using the proposed OEFOE gives a

negligible penalty of mean 0.3-dB with 0.7-dB fluctuations due to delay variations in optical delay line and maximum penalty of 0.6-dB. These low penalties are independent of chromatic dispersion and the self-phase modulation (SPM) effect evident in the high launch power regime. Thus, the OEFOE maintains the performance despite of these impairments.

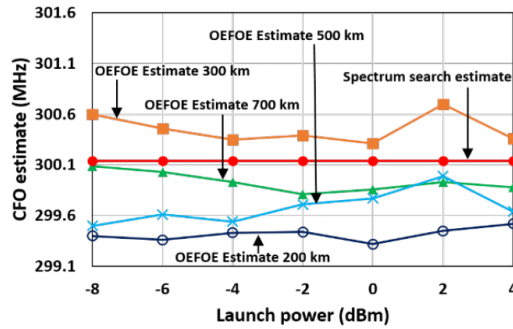


Fig. 11. Simulated CFO estimates vs. Launch power (dBm) for QPSK with launch power = -4 dBm and carrier frequency offset (CFO) = 300 MHz.

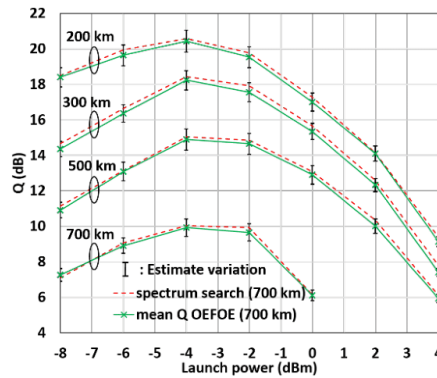


Fig. 12. Simulated Q (dB) vs. Launch power (dBm) for 28-Gbaud QPSK signal with FFT length = 156, number of subcarriers = 100 and 15% cyclic prefix for link distances 200 km, 300 km, 500 km and 700 km.

Since the CFO estimation by OEFOE is performed in parallel to the coherent reception, the system receives a signal that is not dispersion compensated. The fiber dispersion causes pulse spreading that leads to the inter-symbol interference (ISI). Since the interfering parts are uncorrelated, the autocorrelation removes their effects. Thus, the OEFOE is robust to the chromatic dispersion as well as the nonlinearities in the optical fiber. The parameters of the optical fiber chosen for simulations are given in Table 1.

Table 1. Simulation Parameters

Parameter	Value
Attenuation	0.2 dB/km
Dispersion	16×10^{-6} s/m ²
Dispersion slope	0.08×10^3 s/m ³
Group refractive index	1.47
Nonlinear index	2.6×10^{-20} m ² /W
Core area	80×10^{-12} m ²
EDFA noise figure	4-dB
Span length	100 km

5.3.2 Simulated transmission system: 16-QAM

Higher-order QAM modulation formats have been tested for long-haul optical communication links to increase the throughput and meet the rapidly increasing needs for data rates. From Eq. (8), the autocorrelation $R(\tau)$ calculates $|E_s(t)|^2$ i.e. the power of the modulating signal for the period $t = 0$ to T_{CP} . For higher-order QAMs, this power can be the same or higher than the QPSK modulating signal, depending on the data in the period. Thus, the autocorrelation $R(\tau)$ will not be weaker than that for QPSK, and may often be stronger. Hence, moving to a higher QAM order format should not cause any degradation in the performance. This is verified in Fig. 13 where a 28-Gbaud 16-QAM modulated OFDM signal is noise loaded and recovered using the OEFOE estimates. The system performance is compared with that of a system using the spectral peak search method. As expected, both the systems again perform similarly with marginal mean- Q degradation of 0.3 dB for the OEFOE-recovered signal. Like QPSK case, the Q value varied by maximum 0.7-dB due to the fluctuations in optical delay line with maximum penalty of 0.8-dB.

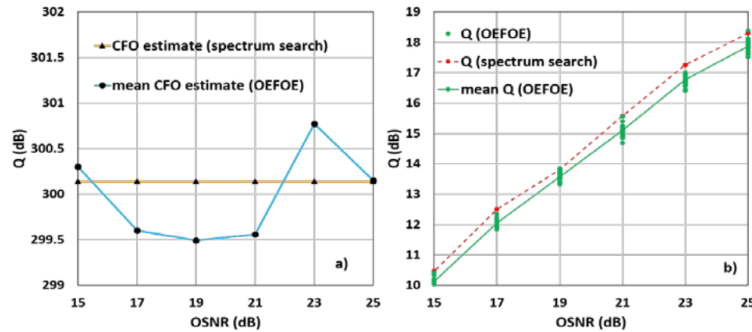


Fig. 13. Simulated a) CFO estimates vs. OSNR (dB) and b) Q (dB) vs. OSNR (dB) for 28-Gbaud 16-QAM with FFT length = 156, number of subcarriers = 100, 15% Cyclic prefix and carrier frequency offset (CFO) = 300 MHz.

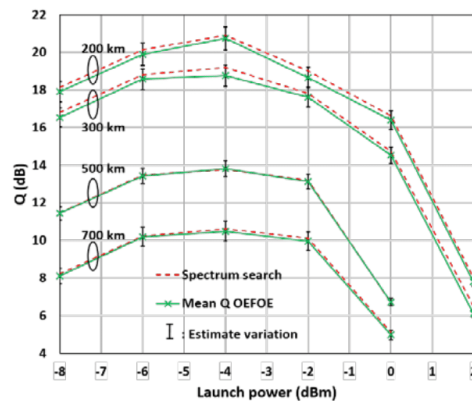


Fig. 14. Simulated Q (dB) vs. Launch power (dBm) for 28-Gbaud 16-QAM with FFT length = 156, number of subcarriers = 100, 15% Cyclic prefix for link distances 200 km, 300 km, 500 km and 700 km.

The 16-QAM modulated signal transmission over fiber links was simulated for different lengths from 200 km to 700 km and again the Q performance of both the systems were found to be similar to each other as can be observed in Fig. 14. The robustness of the system can be intuitively extended to the cross-phase modulation (XPM) for a multichannel WDM system; however, this remains to be investigated. Thus, the proposed designs are robust to the modulation format, laser phase noise, the additive noise, chromatic dispersion and the fiber nonlinearities on transmission, with the system implementing OEFOE giving Q performance similar to a system using spectral-peak search method in DSP. However, as Ref [7], showed that the required cyclic prefix (CP) length for accurate CFO estimation using the digital autocorrelation increases with the order of the M-QAM format. We can, thus, conclude that despite of similar performance, the OEFOE will require longer CP for higher-order M-QAM when $M > 64$.

Finally, we discuss the equalization-enhanced phase noise (EPPN). The EPPN is caused by the electronic dispersion-compensation and adds to the impairments from the laser phase noise [21]. The digital CFO estimators have been noted to suffer in performance due to this EPPN. On the other hand, OEFOE's performance remains unaffected by EPPN as it operates in the analogue domain before electronic dispersion compensation, the EPPN will not be present at the input of the OEFOE. Thus, the OEFOE is robust to EPPN too, a quality that is not present in DSP-based CFO compensation methods.

For practical implementation in deployed optical networks, the OEFOE system requires fabrication as an integrated package along with the coherent receivers. Considering this, the OEFOE 1 proves to be a better option in practical scenario as it provides a simpler design and does not rely on the polarization diversity. On the other hand, OEFOE 2 can be used for proof of concept demonstrations and to test any modifications or extension work. Additionally, both the systems rely on the time domain characteristic of the OFDM signals i.e. the cyclic prefix addition that can be emulated in a single carrier system as well by adding known training symbols on regular interval (τ_1). As a result, with modification in the transmitted signal, the system can be extended to single-carrier and Nyquist-WDM systems. This can be taken as a future work. The OEFOE designs have the same topology as a dual-polarization (DP) coherent receivers which are expensive that may seem demotivating. However, we use slow photodiodes and low-speed ADCs with bandwidths in range of MHz (instead of GHz bandwidth components in DP coherent receiver system). Thus, the manufacturing cost can be

expected to be much lower than that of the DP coherent receivers and could be further reduced if integration is used. The proposed system can be considered as a step towards achieving a DSP-free, analog-processing system that is a matter of interest for many researchers recently to reduce the power consumption by the high-speed processors. For example, an all-analog chip performing a constant modulus based adaptive equalization was proposed recently [12]. Combined with the OEFOE carrier recovery, the analog chip can achieve a power-efficient all-analog signal-processing solution that can target DSP-free coherent optical data-center interconnects (DCI) market.

6. Conclusions

An optoelectronic carrier-frequency offset estimator that replaces the computationally expensive estimation DSP algorithms is designed and tested using simulations. The system was designed in two versions, one suitable to integration on a photonic chip while the other suitable to be implemented in a lab with discrete equipments. Both the versions use passive optical components and avoid the use of high-speed photodiodes or high-speed analog-to-digital converters. For a 28-Gbaud OFDM signal ($N = 156$, 100 subcarriers), the system can estimate CFO up to ± 1250 MHz with estimate errors $< 4\%$. The simulations with varying cyclic prefix lengths suggested the CP length to be fixed $\geq 15\%$ to maintain the errors $< 1\%$. The system was found to be robust to the chromatic dispersion, laser linewidth, self-phase modulation, AWGN noise in the channel and the launch powers in a transmission link. Hence, the system proves to be an alternative to computationally expensive digital CFO estimation algorithms, providing a way towards reducing the DSP latency.

Funding

Australian Research Council's Laureate Fellowship scheme (FL130100041).

Acknowledgment

We thank VPIphotonics (www.vpiphotonics.com) for their support under the university program.

Polarization independent optical injection locking for carrier recovery in optical communication systems

JOKHAKAR JIGNESH^{1,*} BILL CORCORAN,^{1,2} JOCHEN SCHRÖDER,³ AND ARTHUR LOWERY^{1,2}

¹*Electro-Photonics Lab., Dept. of Electrical and Computer Systems Engineering, Monash University, Clayton, VIC 3800, Australia*

²*Centre of Ultrahigh-bandwidth Devices for Optical Systems (CUDOS), Australia*

³*Photonics Lab, Chalmers University of Technology, Göteborg, Sweden*

*jignesh.jokhakar@monash.edu

Abstract: An optical injection locking (IL) system that is independent of the incoming signal's polarization is demonstrated for carrier recovery in coherent optical communication systems. A sub-system that enables polarization independence is discussed and experimentally verified. The system is tested over a 20-km test field link using a broad-linewidth laser (40 MHz), and shows the suppression of phase noise when using the carrier recovered by injection locking as the local oscillator.

© 2017 Optical Society of America

OCIS codes: (060.1660) Coherent communications; (060.2330) Fiber optics communications; (140.3520) Lasers, injection-locked; (070.1170) Analog optical signal processing.

References and links

1. A. Umbach, G. Unterborsch, R. P. Braun, and G. Grobkopf, "Stable optical source and high-speed photodetector used for remote fiber-optic 64-GHz mm wave generation," in *Optical Fiber Communication Conf. (OFC '98)*, San Jose, (1998), 260–261.
2. H. K. Sung, T. Jung, D. Tishinin, K. Y. Liou, W. T. Tsang, and M. C. Wu, "Optical injection-locked gain-lever distributed Bragg reflector lasers with enhanced RF performance," in *Proc. of 2004 IEEE Int. Topical Meeting on Microwave Photonics, Ogunquit (2004)*, paper MWP.04.
3. H. L. T. Lee, R. J. Ram, O. Kjebon, and R. Schatz, "Bandwidth enhancement and chirp reduction in DBR lasers by strong optical injection," in *Conf. Lasers and Electro-Optics (CLEO 2000)*, Nice (2000), paper CMS4.
4. O. Lidoine, P. Gallion, C. Chabran, and G. Debarge, "Locking range, phase noise and power spectrum of an injection-locked semiconductor laser," *IEE Proc., J Optoelectron.* **137**(3), 147–154 (1990).
5. S. Uvin, S. Keyvaninia, F. Lelarge, G. Duan, B. Kuyken, and G. Roelkens, "Narrow line width frequency comb source based on an injection-locked III–V-on-silicon mode-locked laser," *Opt. Express* **24**(5), 5277–5286 (2016).
6. M. Lu, H. Park, J. Parker, E. Block, A. Sivanathan, Z. Griffith, L. Johansson, M. Rodwell, and L. Coldren, "A heterodyne optical phase-locked loop for multiple applications," *Optical Fiber Communication Conf. (OFC)*, Anaheim, paper OW3D.1 (2013).
7. L. Naglic, L. Pavlovic, B. Bategelj, and M. Vidmar, "Improved phase detector for electro-optical phase-locked loops," *Electron. Lett.* **44**(12), 758–761 (2008).
8. Z. Liu, D. J. Richardson, and R. Slavik, "Optical injection locking based carrier recovery for coherent signal reception," in *Asia Communications and Photonics Conf.(ACP)*, paper AM3I.3, Hongkong (2015).
9. Z. Liu, J. Kim, D. S. Wu, D. J. Richardson, and R. Slavik, "Homodyne OFDM with optical injection locking for carrier recovery," *J. Lightwave Technol.* **33**(1), 34–41 (2015).
10. O. Lidoine, P. Gallion, and D. Erasme, "Analysis of a homodyne receiver using an injection locked semiconductor laser," *J. Lightwave Technol.* **9**(5), 659–665 (1991).
11. E. Dale, W. Liang, D. Eliyahu, A. A. Savchenkov, V. S. Ilchenko, A. B. Matsko, D. Seidel, and L. Maleki, "On phase noise of self-injection locked semiconductor lasers," in *Proc. SPIE 8960, Laser Resonators, Microresonators, and Beam Control XVI*, 89600X (2014).
12. S. L. I. Olsson, B. Corcoran, C. Lundström, E. Tipsuwannakul, S. Sygletos, A. D. Ellis, Z. Tong, M. Karlsson, and P. A. Andrekson, "Injection locking-based pump recovery for phase-sensitive amplified links," *Opt. Express* **21**(12), 14512–14529 (2013).
13. M. Selmi, Y. Jaouen, and P. Ciblat, "Accurate digital frequency offset estimator for coherent PolMux QAM transmission systems," in *Proc. of European Conf. on Optical Communication (ECOC)*, paper P3.08, Vienna (2009).

#300541

<https://doi.org/10.1364/OE.25.021216>

Journal © 2017

Received 21 Jun 2017; revised 11 Aug 2017; accepted 11 Aug 2017; published 22 Aug 2017

14. D. S. Millar and S. J. Savory, "Blind adaptive equalization of polarization-switched QPSK modulation," *Opt. Express* **19**(9), 8533–8538 (2011).
15. M. G. Taylor, "Phase estimation methods for optical coherent detection using digital signal processing," *J. Lightwave Technol.* **27**(7), 901–914 (2009).
16. J. Jokhakar, B. Corcoran, and A. J. Lowery, "Polarization-independent optical injection locking," in *Optical Fiber Communication Conf. (OFC)*, paper Th4I.4, Los Angeles (2017).
17. M. Mazur, A. Lorences-Riesgo, M. Karlsson, and P. A. Andrekson, "10 tb/s self-homodyne 64-qam superchannel transmission with 4% spectral overhead," in *Optical Fiber Communication Conf. (OFC)*, paper Th3F.4, Los Angeles (2017).
18. R. Noé, B. Koch, V. Mirvoda, and D. Sandel, "Endless optical polarization control and PMD compensation," in *Optical Fiber Communication Conf. (OFC)*, paper OThJ1, San Diego (2010).
19. A. Fragkos, A. Bogris, D. Syvridis, and R. Phelan, "Amplitude Noise Limiting Amplifier for Phase Encoded Signals Using Injection Locking in Semiconductor Lasers," *J. Lightwave Technol.* **30**(5), 764–771 (2012).
20. R. Lodenkamper, T. Jung, R. L. Davis, L. J. Lembo, M. C. Wu, and J. C. Brock, "RF performance of optical injection locking," *Proc. SPIE* **3463**, 227–236 (1998).
21. R. A. Shafik, Md. S. Rahman, A. H. M. R. Islam, "On the extended relationships among EVM, BER and SNR as performance metrics," in *Proc. of International Conf. on Electrical and Computer Engineering* (2006), Dhaka, Bangladesh, 408–411.
22. P. Robertson and S. Kaiser, "Analysis of the effects of phase-noise in orthogonal frequency division multiplex (OFDM) systems," in *Proc. of IEEE International Conf. on Communications. (ICC)*, Seattle, WA, (1995), **vol.3** pp. 1652–1657.
23. M. Noroozi, A. Zahedi, and H. Bakhshi, "Compensation of phase noise in OFDM systems using a CPE and channel estimation scheme," in *Proc. of Int. Symp. on Performance Evaluation of Computer and Telecommunication Systems*, Edinburgh (2008), pp. 197–201.
24. D. Chang, F. Yu, Z. Xiao, N. Stojanovic, F. N. Hauske, Y. Cai, C. Xie, L. Li, X. Xu, and Q. Xiong, "LDPC convolutional codes using layered decoding algorithm for high speed coherent optical transmission," in *Proc. of Optical Fiber Communication Conf. (OFC)*, paper OW1H.4, Los Angeles (2012).

1. Introduction

Optical injection locking (IL), which forces a 'slave' laser to follow the phase trend of a 'master' injected signal, has found many applications over the past decade. These applications include: all-optical regeneration of signals [1], increasing the linear gain regime of laser [2], bandwidth enhancement of lasers [3], laser linewidth (LW) reduction [4], phase-locked mode generation for a mode-locked laser [5], optical phase-locked loops [6,7] and carrier-recovery in coherent optical systems [8–11].

In coherent optical communication systems, optical carrier recovery mitigates perturbations in the phase-encoded data, caused by the phase noise of the lasers and finite carrier-frequency offsets (CFO) between the transmitter's laser, and the receiver's local oscillator (LO). Demonstrated analog carrier-recovery methods include optical and electro optical phase locked loops (PLLs) [6]. Optical PLLs track the phase of the incoming signals and provide appropriate feedback to the remove the phase offsets [6]. Although PLLs can track both phase offsets and CFO, sub-system complexity has restricted practical implementations in communication systems. Electro-optic phase locked loops have also been proposed [7]. These systems are still relatively complex to implement, and are restricted to CFOs of 100's of MHz and phase noise bandwidths on the order of 1 MHz, by the latency of the electrical components in the feedback. In the digital domain, different signal processing techniques have been used to compensate for CFO and phase noise (e.g [12–15]). The consistent problem faced by analog and digital methods is the amount of phase noise and CFO that can be compensated for, which is either restricted by the device-bandwidths and setup-complexity in analog devices or computational complexity in DSP algorithms. These methods are useful in the best-case scenarios to LWs on the order of 1 MHz and frequency offsets on the order of 1 GHz. In contrast, optical injection locking has been shown to achieve carrier recovery for an offset of tens of GHz [8–11], without introducing latency in signal recovery in addition to providing > 90% phase transfer with optical signal to noise ratios (OSNR) down to 0 dB [12]. Injection locking the receiver-side LO laser by using a residual carrier wave from the incoming signal transfers the phase noise of the signal carrier onto the LO, which enables all-optical recovery of the carrier from coherent reception [8–10].

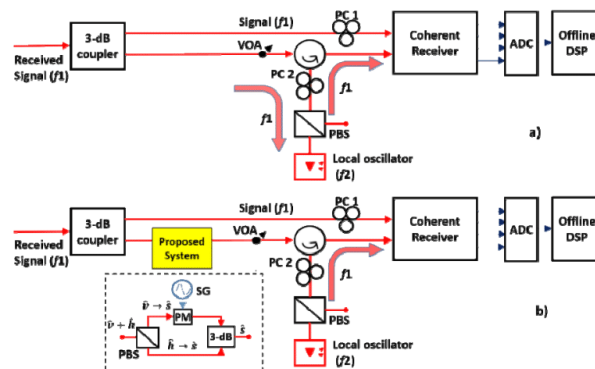


Fig. 1. Receiver system: a) conventional IL setup; b) IL setup with the proposed modifications. VOA: variable optical attenuator; PC: polarization controller; PBS: polarization beam splitter; SG: signal generator; ADC: analog-to-digital converter; PM: phase modulator.

A homodyne setup as shown in Fig. 1(a) is used where the received signal is split using a 3-dB coupler with the signal in one arm fed directly to the coherent receiver and the signal in the other arm injected in the cavity of a local oscillator (LO) laser. If the free-running frequency of the LO laser (f_2) and the frequency of the injected signal (f_1) are within the locking range, defined by the power of the injected signal and laser characteristics, the LO signal locks on to the frequency of the injected signal, essentially removing the effects of phase noise and the CFO [8–11].

To achieve the locked state of the IL, the incoming signal is injected into the cavity of the slave local oscillator laser. This cavity is, however, aligned to a single state of polarization (SOP). As a result, proper locking can be achieved only if the incoming signal's state of polarization is aligned with that of the LO laser cavity and stabilized over the period of operation. In previously demonstrated IL systems, this is achieved by alignment using the polarization controller PC2 and PBS in Fig. 1(a). Although this method works perfectly in a confined lab environment, links in underground ducts are prone to vibrations and pressure variations due to surrounding vehicular motions, human activities and general environmental variations, causing the SOP of the received signal to randomly change over time. As a result, the alignment between the LO lasing polarization and the incoming carrier will drift and may result in loss of locking for sustained polarization fades. To prevent this, the system needs to be constantly monitored and needs to be aligned whenever the SOP of the incoming signal changes, which requires a complex system of polarization monitoring, polarization-state control and a stable feedback loop. As an alternative, in this paper, we propose and demonstrate a polarization-locking module that, when plugged in the IL setup as shown in Fig. 1(b), renders the IL independent of the incoming signal's SOP. This is an extension of the work presented in the OFC 2017 conference [16].

We demonstrate that our system based on an interference mechanism maintains injection lock for any random state of polarization of the injected signal. The proposed polarization-locking module may cause the system to go in to a deep fade due to its interfering mechanism, and eventually result in loss of lock. To prevent this, phase modulation was added to frequently push the system away from the points of deep fades. The consequential amplitude fluctuations, caused by the interfering mechanism and the phase modulations, were considered and shown to be sufficiently suppressed by the IL's amplitude transfer characteristics. Experimental demonstrations in back-to-back setup and over a 20-km field trial showed that the system implementing the proposed module with the injected power as low as -25 dBm performed without Q penalty, similar to a conventional intradyne system

with a narrow LW (100 kHz) laser. Experiments were also performed with a low-output-power (0.5 dBm), broad-LW (40 MHz) laser at the transmitter, for which the data recovery failed in the intradyne system, but was successfully achieved when using the injection locked system. At this broad linewidth, the blind phase estimation algorithms fail due to cycle slips. Training-based phase estimation could work for this broad linewidth but at the cost of increased overhead. On the other hand, a self-homodyne receiver (with injection locking in our case) aided with blind phase estimation, can perform equally well or better than the training based phase estimation for such broad linewidths [17]. In all the cases, the proposed polarization-locking module was verified to work without Q penalties or locking bandwidth compared with an injection-locked system without the module. However, the system without the module repetitively lost the lock when tested over the field trial and needed timely realignment of the polarization controllers, which was solved in the system implementing the proposed module.

Section 2 discusses the design and working of the proposed polarization-locking module. Section 3 describes the proof of concept experiments and results. The experiment with an optical OFDM signal in a back-to-back setup is shown in Section 4 where the system with proposed module was verified to work without Q penalties in spite of fluctuating polarization rotation, phase and amplitude perturbations. Section 5 discusses the broad-LW experiments where the injection locking manages to recover the data when using a broad-LW laser. Section 6 covers the field trial experiment over a 20-km test link. Section 7 concludes the paper with the inferences made from the experimental results.

2. Proposed module design and modifications to IL setup

To make the injection locking independent of the incoming signal’s SOP, a module was designed that can be plugged in before the IL setup, as shown in Fig. 1(b); the module design is shown in Fig. 2.

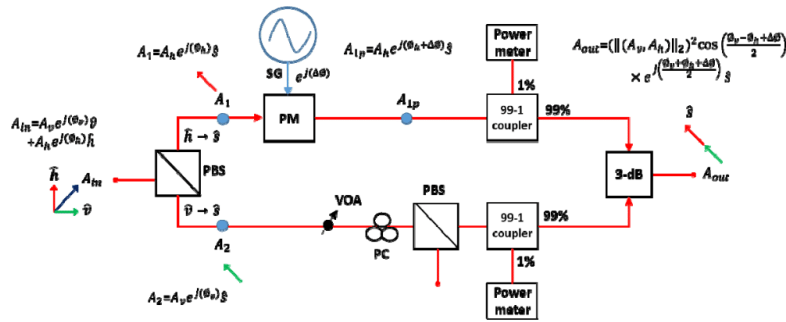


Fig. 2. Proposed polarization-locking module design with working concept.

Consider a signal (A_{in}) at the input of the proposed module (left, Fig. 2), which has a random SOP that can be resolved into finite components in the vertical \hat{v} (red) and horizontal \hat{h} (green) polarization axes,

$$A_{in} = A_v e^{j\theta_v} \hat{v} + A_h e^{j\theta_h} \hat{h} \tag{1}$$

The PBS in the module separates these components on to the slow axis (\hat{s}) of its two output arms (i.e. horizontal component to the top arm in Fig. 2 at Point A_1 , vertical component to the bottom arm at Point A_2). Hence both the polarization components are aligned on the slow axis.

$$A_1 = A_h e^{j\phi_h} \hat{s} \text{ and } A_2 = A_v e^{j\phi_v} \hat{s} \quad (2)$$

Conceptually, if we were to then simply combine A_1 (red) and A_2 (green) using a polarization-maintaining 3-dB coupler, we can convert the incoming signal's random SOP in to a constant known state (\hat{s}). As a result, despite of the incoming signal having a random SOP, the output of the polarization-locking module will be permanently aligned on a known state of polarization. However, any phase difference between A_1 and A_2 leads to a fade in amplitude if the output of the coupler. When the SOP of the signal is such that the \hat{h} and \hat{v} polarization components are opposite phase, interference through the 3-dB coupler will cause destructive interference. If the module is then placed before injection locking, this destructive interference will result in lower injected power, which can result in the LO unlocking for long fades.

To prevent long power fades, a phase modulator was added in one arm of the proposed module as shown in Fig. 2. The phase modulator modulates the incoming optical signal with a low-frequency (400 kHz) sinusoidal signal generated by a signal generator (SG). The frequency of phase modulation is chosen to be higher than the speed of polarization rotations in practical systems, which can be on the order of kHz [18]. This then converts potentially long, uncontrolled power fades into a relatively rapid (400 kHz) amplitude modulation.

In practice, the signal in the upper arm of Fig. 2 is attenuated due to the insertion loss of the phase modulator; this attenuation is balanced in the other arm by a VOA, to ensure equal powers at the two inputs of the 3-dB coupler. Because in our experiment the VOA is not polarization maintaining, and the inputs of the 3-dB coupler need to be aligned to the same fixed polarization, an additional PBS and polarization controller are used, as shown in Fig. 2. This complexity can be reduced by using all polarization maintaining components. Referring back to Fig. 2, the output of the phase modulator can then be represented as

$$A_{1p} = A_h e^{j(\phi_h + \Delta\phi)} \hat{s} \quad (3)$$

where, in our experiments, $\Delta\phi$ is a 400-kHz sinusoidal phase modulation. When A_2 and A_{1p} are combined in a polarization-maintaining 3-dB coupler, we get

$$A_{out} = (\|A_h, A_v\|_2)^2 \cos\left(\frac{\phi_h - \phi_v + \Delta\phi}{2}\right) e^{j\left(\frac{\phi_h + \phi_v + \Delta\phi}{2}\right)} \hat{s} \quad (4)$$

The equations are derived without considering the losses in the upper of the polarization-locking module. Owing to the cosine term changing with $\Delta\phi$, the power out of the 3-dB coupler continuously fluctuates at 400 kHz. These low-frequency intensity fluctuations would be detrimental if passed through to the LO. In order to suppress these intensity fluctuations, we exploit the innate phase and amplitude transfer characteristics of IL systems at low injection ratios (< -30 -dB). Under locked conditions and within the locking range, the IL system transfers phase modulation, replicating phase information. At the same time, the amplitude modulations can be highly suppressed [19,20]. Consequently, the amplitude fluctuations at the output of the 3-dB coupler caused due to the low frequency phase modulation ($\Delta\phi$) on one arm of the module will be suppressed, whereas the required carrier phase information will pass through. The phase modulation, $\Delta\phi$ also show up in the phase of the output which will get transferred through the IL setup. However, this phase modulation can be compensated for by the phase estimation algorithms running in the DSP, as the frequency (400-kHz) is much lower than the symbol rate. Thus, the fixed SOP can be maintained at the output of the module without losing injection locking.

3. Proof of concept

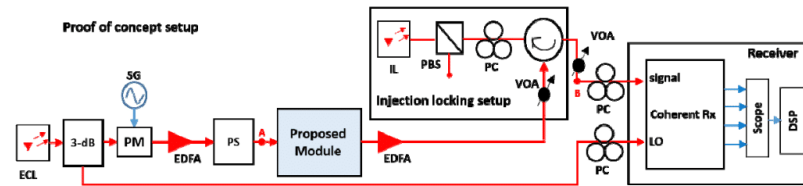


Fig. 3. Experimental setup for proof of concept. ECL: external cavity laser; PS: polarization scrambler; IL: Injection laser; LO: local oscillator laser; Rx: Receiver.

As a proof of concept, we investigate the transfer of a 100-MHz sinusoidal phase modulation through injection locking. Here, a signal generator is used to modulate a CW laser output with an external phase modulator, as shown in Fig. 3. Note that this 100-MHz phase modulation is used to investigate the transfer of phase information through the injection locking process, and is applied externally at the transmitter. As described in the previous section, the polarization-locking module uses 400-kHz phase modulation to reduce polarization fades. The same technique is again used in the experiments described in this section. The polarization of the modulated optical signal was scrambled using a Novoptel EPX1000 polarization scrambler (PS) that allows controlled or random scrambling of the polarization state of the input signal. This scrambling ensured that the proposed module does not cause any suppression of the modulation or unlocking as the polarization state changes. The signal was then passed to the IL setup through the proposed polarization-locking module with an injection ratio of -45 dB (-25 dBm at the input to the slave laser, with a 20-dBm output). The phase modulated signal was then detected by a 25-GHz electrical bandwidth integrated coherent receiver and processed in DSP to recover the peak-to-peak phase swing of the signal.

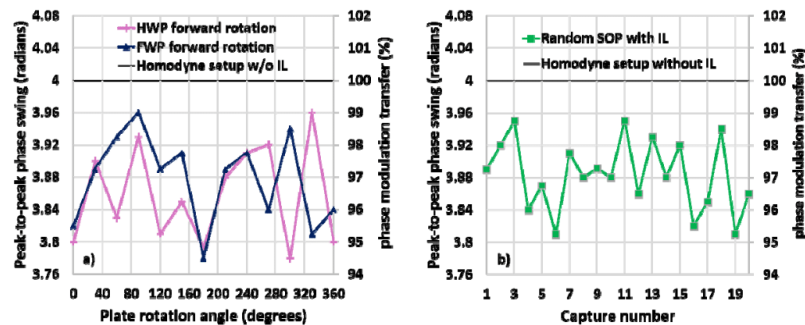


Fig. 4. Peak-to-peak phase swing of the recovered signal and % modulation transfer through IL setup vs.: a) rotation angle of half-wave plate and full-wave plate of the polarization scrambler (PS); b) for 20 data captures each with a random state of polarization (SOP).

In order to ascertain how well phase modulation is transferred through the injection locking stage, we compared the peak-to-peak phase swing of the recovered signal with and without the injection locking stage. For a reference measurement, we passed the signal directly out of the phase modulator (Point A, Fig. 3) to the signal input of the coherent receiver (Point B, Fig. 3). This phase modulator provides a reference swing of 4 radians peak-to-peak ($= 1.27\pi$ radians). We then compared this with the phase swing when the signal is passed through a polarization scrambler, our polarization-locking module, and the injection

locking stage before the coherent receiver. The reference measurement and the phase swing with the system in place are plotted in Fig. 4, marked on the left vertical axis. The ratio of phase swing measured with this system in place to the reference measurement without gives us a measure of the modulation transfer through our system, plotted on the right vertical axes of Figs. 4(a) and 4(b) as a percentage.

To show that the polarization-locking module makes the injection locking process insensitive to the polarization state of the incoming signal, we first varied the rotation angle of a half-wave plate (HWP) in the PS, then the full-wave plate (FWP), and then both of them simultaneously to cover random points on the Poincaré sphere. Figures 4(a) and 4(b) show that on average, 97% of the input phase swing was transferred (see secondary y-axis) through the IL setup independent of the polarization of the incoming signal (x-axis) with a 2% variation about the average. This indicates that the IL system with the polarization-locking module maintains the lock while transferring phase modulation regardless of the incoming state of polarization.

It is imperative that inclusion of the polarization-locking module in the OIL should not reduce the locking bandwidth, as it may cause loss of lock in the case of low power signals. Thus, the locking bandwidth of the OIL system was investigated with and without the polarization-locking module. The experimental setup is the same as in Fig. 3. The continuous wave ECL output was phase-modulated with a sinusoidal electrical signal whose frequency was swept from 10 MHz to 10 GHz. As the phase modulations are transferred by the OIL within the locking bandwidth, the phase swing of the output of the OIL can help in calculating the locking bandwidth. Figure 5 shows the peak-to-peak swing of the received signal's sinusoidal modulated phase at the output of the OIL setup with and without the polarization-locking module. It is observed that the locking bandwidth does not change with the inclusion of the module. This is an expected result, as the module merely changes the polarization alignment, and so the injection ratio remains the same in both cases, leaving the locking bandwidth unaffected.

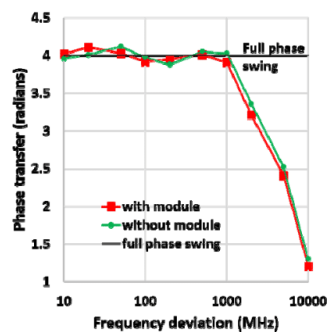


Fig. 5. Phase transfer (radians) vs. frequency deviation (MHz).

4. Back-to-back test with injection locked self-homodyne receiver

The previous section proved that the polarization-locking module allows for phase information to be transferred regardless of the incoming signal's SOP. We now test the performance of this sub-system in a back-to-back setup where injection locking is used to recover the residual carrier from a coherent OFDM signal. The experimental setup consists of a transmitter that modulates a continuous wave (CW) laser output using a complex Mach-Zehnder modulator (CMZM) driven by electrical signals from an arbitrary waveform generator as shown in Fig. 6. A 25-Gbaud QPSK modulated OFDM electrical signal with 100 subcarriers and 156-point FFT length was generated using an arbitrary waveform generator to

drive an optical IQ modulator. A central guard band of 2.5 GHz (10 sub-carriers) was added to keep a clear spectrum containing the optical carrier, preventing transfer of the modulated signal through IL. The amplified signal from the transmitter is noise-loaded using filtered amplified spontaneous emission (ASE) noise from an EDFA covering a 200-GHz bandwidth, which was added to the signal to vary the received OSNR.

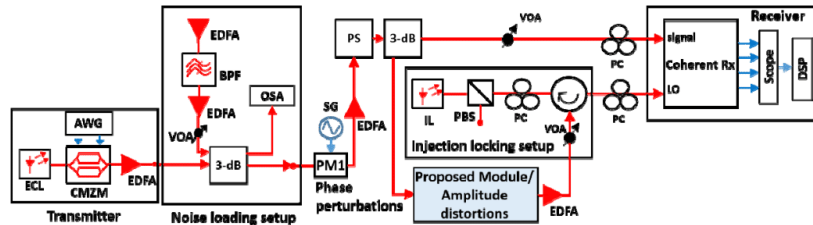


Fig. 6. Experimental setup with proposed polarization-locking module and injection locking setup. CMZM: complex Mach-Zehnder modulator; EDFA: erbium doped fiber amplifier; BPF: bandpass filter; OSA: optical spectrum analyzer; DSP: digital signal processing.

To ensure that the IL replicates the low frequency phase modulations, and that the phase perturbations cancel out in a homodyne receiver setup, the noise-loaded signal was distorted in phase using a phase modulator (PM1 in Fig. 6). For the later part of the experiment, when we used a broad LW laser at the transmitter, the phase modulator was removed. After adding phase perturbations, the polarization of the signal is scrambled using the Novoptel polarization scrambler (PS). The scrambled signal was then split using a 3-dB coupler, where one arm is connected to the polarization-locking module followed by an IL setup and the other arm was directly connected to the signal input of a 25-GHz electrical bandwidth integrated coherent receiver. The outputs of the coherent receiver were connected to a 40-GSa/s 28-GHz bandwidth digital signal oscilloscope (DSO). The data recovery algorithms such as the channel equalization and the residual phase recovery were run as offline DSP.

Figure 7(a) shows performance of injection locking and intradyne systems with or without phase perturbations added to the signal. At lower OSNRs where sufficient errors were measured, the Q -value calculated from the error vector magnitude (Q_{SNR}) is equal to the Q -value calculated from the finite BER (Q_{BER}) where Q_{BER} for any M-QAM modulation format is [21]

$$Q_{\text{BER}} = 20 \log_{10} \left(\sqrt{\frac{2(M-1)}{3}} \times \text{erfc}^{-1} \left(\frac{\text{BER} \times \log_2 \sqrt{M}}{\left(1 - \frac{1}{\sqrt{M}}\right)} \right) \right). \quad (5)$$

Figure 7(a) plots the performance versus OSNR for the intradyne system without any added phase perturbations (red dotted line), to provide a reference. When phase perturbations are added at the transmitter, and the receiver is in the intradyne configuration (i.e. without injection locking), the Q degrades by 5-dB in Q and an additional 1.5-dB OSNR is required at the 7% hard-decision FEC limit ('error free' BER = 3.8×10^{-3}). Using the injection locking stage to recover the phase perturbed carrier from the signal compensates the phase fluctuations, as shown in Fig. 7(a) by the match of the curve marked by blue circles with the undistorted intradyne reference (red dots). Moreover, when the polarization of the incoming signal is randomly rotated and using the proposed module for polarization independence (Fig. 7(a), green triangles), the system performance is again the same as the undistorted intradyne reference. To ensure that polarization independent injection locking can also perform without penalty, we include our polarization-locking module, and activated the polarization

scrambler. The performance of this system is plotted as green triangles in Fig. 7(a), and shows a negligible required OSNR penalty at the FEC limit, when compared to the undistorted intradyne reference (red dots). This indicates that the phase fluctuations are sufficiently canceled to be useful for coherent communications systems, even for a random state of polarization of the incoming signal. Moreover, the OIL system provides an additional overall benefit by reducing DSP complexity, because the CFO estimation and compensation algorithms are omitted for OIL.

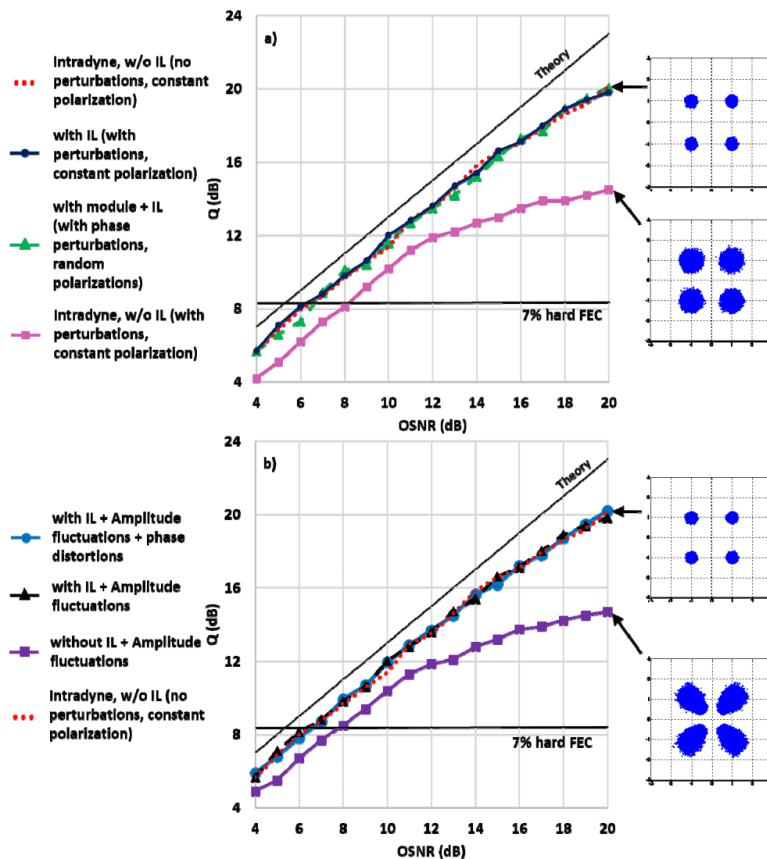


Fig. 7. Q performance vs. OSNR: a) with or without (w/o) injection locking (IL) in presence of additional phase perturbations; b) with or without (w/o) injection locking (IL) in presence of additional amplitude fluctuations; Insets: Constellations of recovered signals at 22-dB OSNR with and without phase/amplitude perturbations.

The phase perturbations in OFDM systems cause inter-carrier interference (ICI) along with a common phase error (CPE) [22, 23]. The phase error correction algorithms running in the DSP take care of the CPE but cannot completely negate the effects of ICI due to the phase perturbations. Hence, due to ICI and AWGN, the constellations of the recovered signals show circularly symmetric Gaussian spreads of the constellation points, rather than a phase skew as

seen in the inset of Fig. 7(a). With the IL, the system with phase perturbations and constant signal polarization gave similar performance to that of the system without perturbations, confirming that the IL can cancel phase perturbations at the receiver. This is reflected in the inset in Fig. 7(a), where the Gaussian spread of the constellation points is significantly reduced.

As discussed in Section 1, the polarization-locking module may generate amplitude fading in the signal, due to the interference in the 3-dB coupler in the module, which in turn may result in a loss of injected power and thus, the injection lock. Theoretically, these low-frequency amplitude fluctuations are rejected by the IL [19, 20]. To systematically test this, we added additional amplitude fluctuations into our system to verify the AM suppression capabilities of our IL set-up. The amplitude fluctuations were added replacing the polarization-locking module with an intensity modulator driven with a 400-kHz sinusoid.

Figure 7(b) shows that without the locking, compared with intradyne system without perturbations: Q drops by 5-dB at 20-dB OSNR and the required OSNR at FEC increases by 1.5-dB at hard-FEC limit. When using an injection-locked LO, the system performs similarly to the reference intradyne system. This is because of the inherent rejection of low-frequency amplitude fluctuations through the IL process. Now, with the phase fluctuations turned on and the polarization scrambler also activated, the system again performs similarly to the reference intradyne system without a loss of Q , confirming the rejection of amplitude fluctuations, the cancellation of phase fluctuations and independence on incoming signal polarization.

5. Broad-linewidth laser experiments

The optical injection locking, being able to replicate the carrier phase information up to several GHz, should allow the use of broad LW lasers in coherent communication systems. Relaxing the limit on required LW for coherent systems may lower the cost of coherent transceivers, by allowing a wider range of fabrication tolerances, and operation at lower optical powers. We tested performance in a back-to-back system as in the previous section, here using a broad LW (40 MHz) low-power (0.5 dBm) laser at the transmitter. The phase modulation module was removed from the setup in Fig. 6, as the use of a broad LW laser at the transmitter provides significant phase fluctuations. A 25-Gbaud OFDM signal was again generated with the same OFDM parameters as in previous experiment. The polarization of the injected signal was again scrambled. The system was tested for both QPSK and 16-QAM modulation formats.

A reference Q curve was plotted over an OSNR sweep using a laser with 100-kHz LW. Its output power was attenuated to 0.5 dBm, to match the output power of the low-performance laser, so that the performance difference between these two systems could be primarily attributed to the difference in laser LWs. The performances with and without the polarization-locking module were similar, as shown in Fig. 8. The Q of the recovered signal reaches only 16.2 dB for QPSK at 20-dB OSNR even for the 100-kHz LW laser, owing to the OSNR penalty caused by low output power of the laser. The system was then tested using the 40-MHz LW laser. This laser had a 40-MHz LW, despite operating at its specified maximum bias current. This low-performing laser was used in the experiments to test the system under worst-case scenario. Without injection locking, the signal at the receiver was unrecoverable, even when using a spectral peak search for frequency offset compensation and training-aided maximum likelihood phase estimation. With injection locking, signal recovery was possible. Figure 8 shows the measured performance with and without the polarization-locking module in the injection locked setup. For the measurements without polarization locking, the system lost lock when the polarization of the injected signal changed, then required manual adjustment of the polarization controllers to regain the lock. On the other hand, this manual intervention was not needed when the polarization-locking module was used.

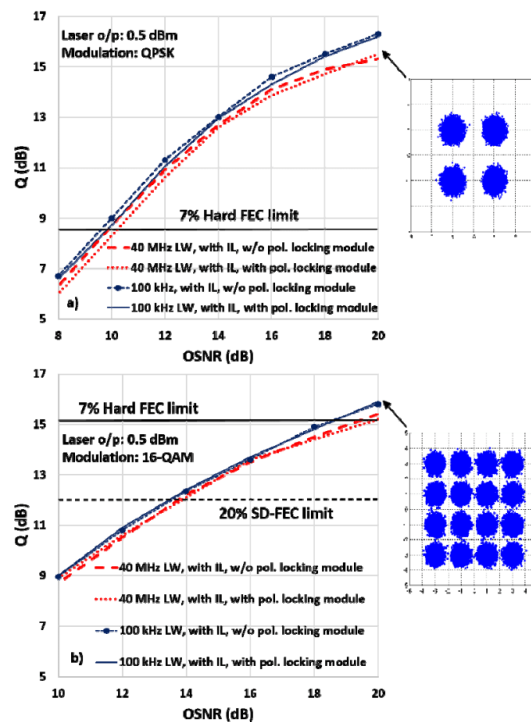


Fig. 8. Q (dB) vs. OSNR (dB) using a low performance laser (LW = 40 MHz) compared with a standard laser (LW = 100 kHz) for injection locking the local oscillator with and without polarization-locking module for a) QPSK modulation and b) 16-QAM modulation. Insets: Recovered constellations at 22-dB OSNR for QPSK, 16-QAM with LW = 40 MHz.

Comparing the traces for systems using the narrow (100 kHz) and broad (40 MHz) LW lasers at the transmitter, Fig. 8 shows that the IL setup effectively cancels the phase noise due to the broad LW, as the performance was observed to be similar to that of the system using the narrow LW laser. There is a small but measurable required-OSNR penalty of 0.6 dB when using the broad LW laser, compared with the narrow LW laser at the hard FEC limit. A similar performance trend was observed when using 16-QAM modulation where the system using the broad LW laser gives a marginal OSNR penalty of 1.1 dB, compared with that using the narrow LW laser, both at the limit of hard-decision FEC (15.2 dB). Moreover, the performance using the broad LW laser for 16-QAM barely reaches the hard FEC limit at 20-dB OSNR. Nonetheless, soft-decision thresholds can be considered for 16-QAM assuming the use of a concatenated LDPC-convolutional (LDPC-CC(18360,4,24)) code with a 20% overhead [24], giving 'error free' operation for pre-FEC BER of 2.7×10^{-2} . The OSNR penalty reduces to 0.35-dB compared with the narrow LW system at this soft-decision FEC limit. For both the broad and narrow linewidth systems, the polarization locking module was able to maintain the injection lock despite of polarization drifts.

6. Field test over a fiber link from Monash Clayton to Caulfield campus

The system was tested over an installed 'field-trial' link from Monash University's Clayton campus to the Caulfield campus. The field link used in this experiment is a 10-km long dedicated 'dark' fiber, resulting in 20-km link transmission with a simple loop-back placed at Caulfield and an overall insertion loss of 5.8 dB (Fig. 9).

The experimental setup is similar to the one shown in Fig. 6. The polarization scrambler and phase modulator are removed from the set-up, as random polarization rotations are provided by the field link and the phase perturbations by the use of the broad LW laser in the transmitter. A signal with same OFDM parameters as in previous back-to-back experiment was transmitted over the field link and received after a single round-trip with an IL-based homodyne receiver setup. Figure 10 shows the Q of the signal recovered after transmission over the fiber link with and without the polarization-locking module. As expected, the IL system with the module gave similar Q performance over a wide range of OSNRs, compared with the IL system without the module. This proved that the polarization-locking module did not impart performance penalties to the system. Again, as expected, the IL system without the polarization-locking module lost lock randomly and had to be manually realigned on multiple occasions, whereas the IL with module maintained the lock all through the course of the experiments. The system performances for all cases with the IL cross the forward error correction (FEC) limits, for both the 7% hard-decision FEC for QPSK, and the 20% soft-decision FEC for 16-QAM.



Fig. 9. Map of south-east Melbourne, showing the test link node locations.

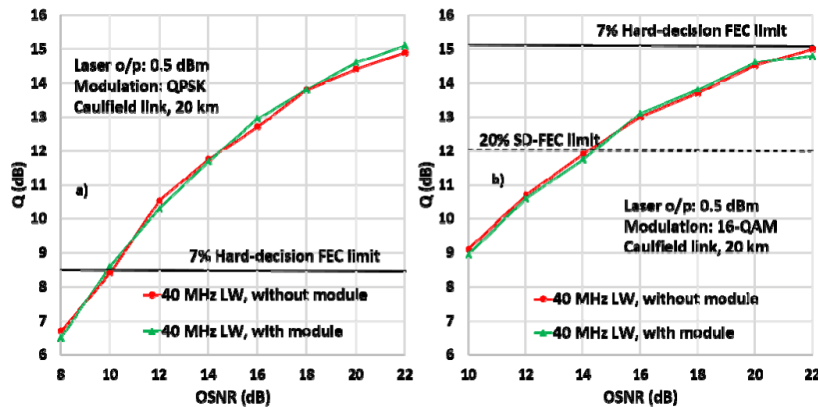


Fig. 10. Q (dB) vs. OSNR (dB) using low performance laser for a) QPSK modulation and b) 16-QAM modulation format.

From the measurements, we infer the required OSNR is 11 dB for QPSK and 14 dB for 16-QAM, demonstrating that coherent systems, employing our polarization-insensitive IL in installed metropolitan fiber systems, can use lasers with significantly relaxed specifications (e.g. LWs up to 40 MHz, with output powers as low as 0.5-dBm). Critically, the polarization-locking module removes the need for polarization tracking, allowing for operation with an arbitrary input polarization state.

7. Conclusions

An optical injection locking (IL) setup is modified with a module that, when added to the IL setup, allows locking independent of the injected signal's polarization. The proposed polarization-locking module enabled the optical injection locking (IL) setup to maintain the lock for all states of polarization of the injected signal without any considerable loss in the Q performance. The system was also tested over a 20-km field link, using a 40-MHz LW 0.5-dBm transmitter laser. The random fluctuations in the polarization of the signal due to random events in the surroundings of the link was taken care of by the proposed polarization-locking module. The resulting continuously-locked IL setup cancelled the phase noise effects of the broad LW laser. Thus, the complete setup with the polarization-locking module along with the IL relaxed the constraints on the laser specifications and proved to be capable for practical implementation, which was difficult until now due to the polarization-sensitivity of IL's locking mechanism.

Funding

Australian Research Council's (ARC) Centre of Excellence Laureate Fellowship schemes (CE110001018, FL130100041).

Acknowledgement

We thank VPIphotonics (www.vpiphotonics.com) for their support under the university program.

Inter-channel nonlinear phase noise compensation using optical injection locking

JOKHAKAR JIGNESH,^{1,*} ARTHUR LOWERY,^{1,2} AND BILL CORCORAN^{1,2}

¹*Electro-Photonics Lab., Dept. of Electrical and Computer Systems Engineering, Monash University, Clayton, VIC 3800, Australia*

²*Centre of Ultrahigh-bandwidth Devices for Optical Systems (CUDOS), Australia*

*jignesh.jokhakar@monash.edu

Abstract: We propose optical injection locking (OIL) to enable compensation of the inter-channel nonlinear phase noise, which is dominated by cross-phase modulation (XPM). In this paper, injection locking is used to create a local oscillator for a homodyne receiver from a residual carrier. The locking is fast enough to follow XPM-phase distortion, but slow enough to reject the signal bands, which are spaced slightly away from the pilot. The homodyne receiver thus partially cancels XPM, as it is common to the signals and the pilot. An experimental 7-channel WDM system gives 1-dB (0.7-dB) improvement in the peak Q of the center channel, for QPSK (16-QAM) modulated OFDM subcarriers, and increased the transmission reach by 320 km. The optimum performance was achieved at an injection ratio of -45 dB, with the injected power as low as -24.5 dBm.

© 2018 Optical Society of America under the terms of the [OSA Open Access Publishing Agreement](#)

OCIS codes: (060.2330) Fiber optics communications; (060.2920) Homodyning; (140.3520) Lasers, injection-locked.

References and links

1. P. P. Mitra and J. B. Stark, "Nonlinear limits to the information capacity of optical fibre communications," *Nature* **411**(6841), 1027–1030 (2001).
2. E. Ip and J. M. Khan, "Compensation of dispersion and nonlinear impairments using digital backpropagation," *J. Lightwave Technol.* **26**(20), 3416–3425 (2008).
3. E. Ip, "Nonlinear compensation using backpropagation for polarization-multiplexed transmission," *J. Lightwave Technol.* **28**(6), 939–951 (2010).
4. R. Dar and P. J. Winzer, "On the limits of digital back-propagation in fully loaded WDM systems," *IEEE Photonics Technol. Lett.* **28**(11), 1253–1256 (2016).
5. E. Temprana, E. Myslivets, V. Ataie, B. P.-P. Kuo, N. Alic, V. Vusirikala, V. Dangui, and S. Radic, "Demonstration of coherent transmission reach tripling by frequency-referenced nonlinearity pre-compensation in EDFA-only SMF link," in *42nd European Conf. on Optical Communication, (ECOC)*, Dusseldorf, Germany, 2016, pp. 1–3.
6. E. F. Mateo, F. Yaman, and G. Li, "Efficient compensation of inter-channel nonlinear effects via digital backward propagation in WDM optical transmission," *Opt. Express* **18**(14), 15144–15154 (2010).
7. L. Zhu, F. Yaman, and G. Li, "Experimental demonstration of XPM compensation for WDM fibre transmission," *Electron. Lett.* **46**(16), 1140–1141 (2010).
8. R. Dar, M. Feder, A. Mecozzi, and M. Shtaif, "Accumulation of nonlinear interference noise in fiber-optic systems," *Opt. Express* **22**(12), 14199–14211 (2014).
9. X. Chen and W. Shieh, "Closed-form expressions for nonlinear transmission performance of densely spaced coherent optical OFDM systems," *Opt. Express* **18**(18), 19039–19054 (2010).
10. T. K. Chiang, N. Kagi, M. E. Marhic, and L. G. Kazovsky, "Cross-phase modulation in fiber links with multiple optical amplifiers and dispersion compensators," *J. Lightwave Technol.* **14**(3), 249–260 (1996).
11. R. Dar, M. Feder, A. Mecozzi, and M. Shtaif, "Properties of nonlinear noise in long, dispersion-uncompensated fiber links," *Opt. Express* **21**(22), 25685–25699 (2013).
12. B. Foo, B. Corcoran, and A. Lowery, "Optoelectronic method for inline compensation of XPM in long-haul optical links," *Opt. Express* **23**(2), 859–872 (2015).
13. Z. Tao, W. Yan, S. Oda, T. Hoshida, and J. C. Rasmussen, "A simplified model for nonlinear cross-phase modulation in hybrid optical coherent system," *Opt. Express* **17**(16), 13860–13868 (2009).
14. M. E. McCarthy, M. A. Z. Al Kahteeb, F. M. Ferreira, and A. D. Ellis, "PMD tolerant nonlinear compensation using in-line phase conjugation," *Opt. Express* **24**(4), 3385–3392 (2016).
15. S. L. I. Olsson, B. Corcoran, C. Lundström, T. A. Eriksson, M. Karlsson, and P. A. Andrekson, "Phase-sensitive amplified transmission links for improved sensitivity and nonlinearity tolerance," *J. Lightwave Technol.* **33**(3), 710–721 (2015).

16. L. B. Y. Du and A. J. Lowery, "Pilot-based XPM nonlinearity compensator for CO-OFDM systems," *Opt. Express* **19**(26), B862–B867 (2011).
17. B. Inan, S. Randel, S. L. Jansen, A. Lobato, S. Adhikari, and N. Hanik, "Pilot-tone-based nonlinearity compensation for optical OFDM systems," *36th European Conf. and Exhibition on Optical Communication (ECOC)*, Torino, 2010, paper Tu.4.A.6.
18. A. Lobato, B. Inan, S. Adhikari, and S. L. Jansen, "On the efficiency of RF-Pilot-based nonlinearity compensation for CO-OFDM," *2011 Optical Fiber Communication Conf. (OFC)*, Los Angeles, CA, 2011, paper OTuF2.
19. Z. Liu, J. Y. Kim, D. S. Wu, D. J. Richardson, and R. Slavík, "Homodyne OFDM with optical injection locking for carrier recovery," *J. Lightwave Technol.* **33**(1), 34–41 (2015).
20. O. Lidoyne, P. Gallion, and D. Erasme, "Analysis of a homodyne receiver using an injection locked semiconductor laser," *J. Lightwave Technol.* **9**(5), 659–665 (1991).
21. J. Jignesh, B. Corcoran, J. Schröder, and A. Lowery, "Polarization independent optical injection locking for carrier recovery in optical communication systems," *Opt. Express* **25**(18), 21216–21228 (2017).
22. A. Fragkos, A. Bogris, D. Syvridis, and R. Phelan, "Amplitude noise limiting amplifier for phase encoded signals using injection locking in semiconductor lasers," *J. Lightwave Technol.* **30**(5), 764–771 (2012).
23. O. Lidoyne, P. Gallion, C. Chabran, and G. Debarge, "Locking range, phase noise and power spectrum of an injection-locked semiconductor laser," *IEE Proc., Optoelectron.* **137**(3), 147–154 (1990).
24. R. A. Shafik, Md. S. Rahman, A. H. M. R. Islam, "On the extended relationships among EVM, BER and SNR as performance metrics," in *Proc. of International Conf. on Electrical and Computer Engineering* (2006), Dhaka, Bangladesh, pp. 408–411.
25. D. Chang, F. Yu, Z. Xiao, N. Stojanovic, F. N. Hauske, Y. Cai, C. Xie, L. Li, X. Xu, and Q. Xiong, "LDPC convolutional codes using layered decoding algorithm for high speed coherent optical transmission," in *Proc. of Optical Fiber Communication Conference (OFC)*, (2012), paper OW1H.4.
26. R. Rios-Müller, J. Renaudier, P. Brindel, A. Ghazisaeidi, I. Fernandez, P. Tran, C. Simonneau, L. Schmalen, and G. Charlet, "Spectrally-efficient 400-Gb/s single carrier transport over 7200 km," *J. Lightwave Technol.* **33**(7), 1402–1407 (2015).
27. G. Raybon, A. Adamiecki, P. J. Winzer, C. Xie, A. Konczykowska, F. Jorge, J.-Y. Dupuy, L. L. Buhl, S. Chandrashekar, A. S. Draving, M. Grove, K. Rush, B. Zhu, and D. W. Peckham, "All-ETDM 107-Gbaud PDM-16QAM (856-Gb/s) transmitter and coherent receiver," in *Proc. of European Conference and Exhibition on Optical Communication (ECOC)*, (2013), London, paper PD2.D.3.

1. Introduction

The transmission reach of optical communication systems is restricted by nonlinearities in optical fibers [1]. In a multi-channel environment, these nonlinearities cause both intra-channel interference and inter-channel interference. Intra-channel nonlinear interference, such as self-phase modulation (SPM), can be compensated to a large extent by digital methods—like digital back-propagation (DBP)—which attempt to undo propagation effects by numerically solving a nonlinear Schrödinger equation [2,3]. On the other hand, inter-channel nonlinear interference, e.g. from cross-phase modulation (XPM) and four-wave mixing (FWM), are difficult to model with significant precision for effective compensation, based on full-field digital propagation [4]; although, in optimized laboratory experiments, there are clear benefits from compensating inter-channel nonlinear interference [5]. Digital methods based on virtual propagation are also computationally intensive for inter-channel nonlinear interference, due the need to process extremely wide-bandwidth signals. They are also compromised when channels are added or dropped in optically routed networks [4]. Thus, inter-channel nonlinear interference remains a problem for optically routed networks, despite significant research in developing multi-channel DBP algorithms and modelling inter-channel interference (e.g [6,7]). Dar *et al.* showed that this inter-channel nonlinear interference noise (NLIN) cannot strictly be considered as circularly symmetric (CS) Gaussian noise, but can be dominated by phase noise in systems with many short-spans: the CS Gaussian noise model is only appropriate when longer distances are covered by fewer spans [8]. For multi-channel signals with sufficient channel spacing (>30 GHz), FWM becomes negligible [9] and XPM dominates the inter-channel NLIN. The XPM model developed in [10] indicates a reduction in the bandwidth of inter-channel phase modulation by dispersion-induced walk-off between the WDM channels, which depends on the channel spacing. Thus, the spectral width of the XPM-induced phase distortion is limited in dispersion-unmanaged links [11–13]. Specifically [12], shows that the XPM bandwidth for 50-GHz channel spacing with QPSK modulation is

~1.6-GHz full-width half-maximum, with a roll-off of 2.8 dB per GHz of modulation bandwidth in a 20-span, 1600-km link.

There have been various approaches to compensate for inter-channel nonlinear effects; for example, phase conjugation, including using optical phase conjugation per-span [14], and phase sensitive amplifiers [15]. However, these approaches require sophisticated equipment in the field. Other approaches take advantage of the limited bandwidth of the XPM-induced phase fluctuations. For example, a low-bandwidth phase modulator, driven proportional to the combined intensity of all of the WDM channels, can be installed along the link to mitigate XPM [12]. Alternatively, pilot-tone based techniques have been proposed, in which the pilot tone picks up XPM along the link, enabling the XPM to be cancelled digitally at the receiver [16–18], but with added processing latency.

In this paper, we propose using optical injection locking (OIL) to identify the XPM-induced fluctuations from the residual carrier, which can then be cancelled in a coherent receiver. We show that in an OFDM system with a central 2.5-GHz guard-band, OIL carrier recovery can improve peak Q by 1-dB and associated improvement in transmission reach without adding latency in the DSP, by adding optical injection locking to the receiver hardware.

Section 1 describes the concept of nonlinearity compensation using optical injection locking. Section 3 discusses the experimental setup used for the concept verification and the results observed for various injected power, link distances and modulation schemes. Finally, Section 4 draws the conclusions.

2. Concept

The nonlinear phase noise, as discussed in the previous section, is dominated by the cross-phase modulation (XPM) for systems with more number of spans of shorter lengths (< 100 km). Further, this XPM distortion is limited in bandwidth for dispersion-unmanaged links. The XPM efficiency vs. modulation frequency, ω , is [10–12]

$$\eta_{XPM}(\omega) = \frac{\alpha^2}{(\omega\Delta\beta)^2 + \alpha^2} \left[1 + \frac{4 \sin^2\left(\frac{\omega\Delta\beta L}{2}\right) e^{-\alpha L}}{(1 - e^{-\alpha L})^2} \right] \left| \frac{\sin\left(\frac{N\omega\Delta\beta L}{2}\right)}{\sin\left(\frac{\omega\Delta\beta L}{2}\right)} \right|. \quad (1)$$

where: η_{XPM} is the XPM efficiency, α is the fiber attenuation, $\Delta\beta = D(\lambda_1 - \lambda_2)$ is the difference in the propagation constants of a continuous wave probe at wavelength λ_1 and its interferer at λ_2 ; D is the chromatic dispersion parameter of the fiber; N is the number of spans in the link and L is the length of each span. Figure 1a plots the XPM efficiency for $N = 4$ and 40 spans, each of 80 km for a total length 320 km (red line) and 3200 km (blue line) respectively. The frequency spacing is 50 GHz. The CD parameter $D = 16$ ps/nm km. Note that the horizontal axis in Fig. 1a relates to the frequency of the intensity fluctuations within the neighboring channel, not the channel spacing itself.

We observe that the XPM efficiency increases in magnitude with the link distance due to accumulation. As transmission distance increases, the magnitude of the XPM transfer function increases as nonlinear distortions accumulate, but the bandwidth of intensity fluctuations transferred via XPM is reduced (Fig. 1a). The XPM concentration in the main lobe of the XPM efficiency spectrum reduces with the length and the XPM effects becomes restricted in bandwidth. This can be attributed to the walk-off caused by the CD and a large-frequency spacing between the channels. As such, we can expect the XPM to phase modulate the CW probe wavelength only at relatively low frequencies.

The concept of OIL based nonlinearity compensation was inspired from pilot-based nonlinearity compensation methods [16–18]. A pilot frequency tone is added in a guard band of the signal. The pilot tone acts as a CW probe signal and is subjected to the same cross-

phase modulation (XPM) distortions that is suffered by the signal subcarriers across the fiber link. As such, if this pilot tone is filtered out at the receiver, the XPM on it can be used to cancel out the XPM distortions on the signal. Refs [16–18], performed this filtering and cancellation digitally after coherently receiving the signal in an intradyne receiver.

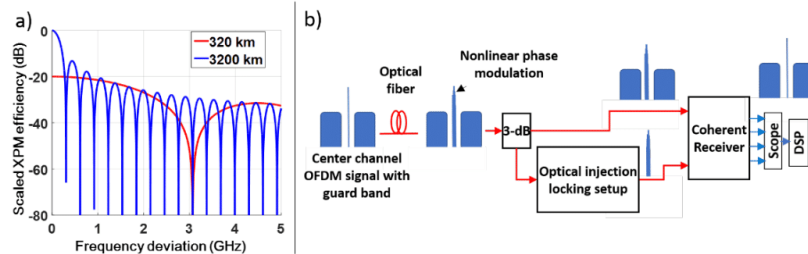


Fig. 1. a) Scaled XPM efficiency (dB) vs. frequency (GHz), b) OIL-based nonlinear phase noise compensation.

In this work, our intention was to achieve this XPM compensation without increasing the DSP latency. We need to select the pilot tone and use it as a local oscillator to a coherent receiver so that the XPM common to the signal and pilot cancel one another before digitization of the signal. To select the pilot tone in analog domain before digitization, we could use an optical bandpass filter, but frequency drifts in the signal may lead to the OBPF amplitude-modulating the extracted pilot tone, or passing portions of signals sidebands along with it. Thus, we need a mechanism that locks to the frequency of the signal and allows for phase transfer in a specific bandwidth. This motivates us to use optical injection locking, as shown in Fig. 1b. The OIL selects the XPM-modulated pilot (a residual carrier) so it can be used as a local oscillator in a coherent receiver. Because OIL-based carrier recovery can replicate the phase information of the incoming signal up to several GHz, depending on the injected power, the recovered carrier at the output of OIL contains the phase noise information (linear and nonlinear) [19–21]. At the same time, the output of the OIL frequency locks to the incoming signal carrier frequency. Thus, the OIL acts as an optical bandpass filter for phase modulation (not amplitude modulations), whose center frequency is locked on to the incoming signal's carrier frequency, avoiding the frequency drift problems in passive OBPF.

The self-phase modulation (SPM) in the system is not bandlimited and occupies a relatively wider bandwidth, as $\Delta\beta \rightarrow 0$ in Eq. (1). The OIL suppresses the phase-transfer beyond the phase-transfer bandwidth, the proposed system cannot completely compensate for the SPM in the system. As such, we do not expect our approach to significantly compensate for intra-channel distortions, such as the nonlinear interactions between the OFDM subcarriers. In our work, we choose digitally generated orthogonal frequency division multiplexing (OFDM), because it enables guard bands to be easily defined around the residual carrier. Our method can, however, be generalized to any system using a guard-band.

3. Polarization-independent injection locking

3.1 Polarization-independent injection locking sub-system

Figure 2 shows the experiment in detail. The received signal is split: half to a coherent homodyne receiver, and half injected in the cavity of a local oscillator (LO) laser via a circulator. The OIL slave LO laser was a Gooch and Housego EM650 distributed feedback laser. If the free-running frequency of the LO laser (f_2) and the frequency of the injected signal (f_1) are within the locking range, the LO signal locks on to the frequency of the injected signal, essentially suppressing its phase noise and removing the CFO.

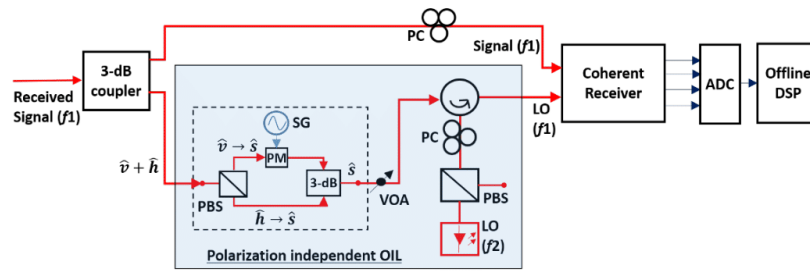


Fig. 2. Optical injection locking setup with polarization locking module used in this experiment. PBS- polarization beam splitter; PC- polarization controller; SG: signal generator, VOA: variable optical attenuator, ADC: analog-digital convertor, DSP: digital signal processing.

This OIL cavity is aligned to a defined of polarization (SOP). As a result, proper locking can be achieved only when the incoming signal's state of polarization is aligned with that of the LO laser cavity. We proposed a module in [21] that, when added before the circulator (dashed box in Fig. 2), makes the OIL system independent of the incoming signal's polarization *i.e.* the module outputs a signal with a constant SOP. This signal, \hat{s} is then aligned with the LO cavity using a polarization controller, thus maintaining the injection lock despite of polarization drifts in the link. The blue box in Fig. 2 shows the complete polarization-independent OIL setup. The polarization controller in the signal path was used in preliminary set-up measurements to ensure polarization independence of the injection-locking module, but left in a random state for the rest of the experiment.

The results presented in [21] show that this polarization-injection locking system, when used with a self-homodyne receiver, in a back-to-back configuration over a range of OSNRs, performs almost identically to using an ECL as local oscillator in a standard intradyne receiver. This shows that the optical injection locking stage shows no obvious advantage in terms of compensating for laser phase noise when using high-precision (~ 100 kHz linewidth) ECLs, indicating that any improvement in performance after transmission is likely from compensation of nonlinear phase noise. This we intend to show in the following sections

3.2 Optimum phase-transfer bandwidth (B_{OIL})

The phase-transfer bandwidth of the OIL (B_{OIL}) is critical. The phase transfer bandwidth is a separate consideration to the frequency detuning locking bandwidth. The phase transfer bandwidth is the bandwidth of phase modulation that is unaffected by the injection locking process. The frequency detuning locking bandwidth defines the allowed detuning of the incoming carrier from the free-running frequency of the slave laser before locking fails entirely. Within the phase transfer bandwidth amplitude modulation is highly attenuated [22]. If the phase-transfer bandwidth (B_{OIL}) is less than the XPM bandwidth (B_{XPM}), the system performs sub-optimally as the detected signal still contains traces of XPM distortions at frequencies outside the OIL bandwidth (illustrated in Fig. 3a). Reducing the (B_{OIL}) further leads to complete loss of lock and the system fails. At the same time, if the phase-transfer bandwidth of the OIL (B_{OIL}) is higher than the guard band frequency range (B_{guard}), it allows for some portion of the signal's sidebands to influence the local oscillator signal, causing degradation (Fig. 3b). Hence, there is an optimum B_{OIL} at which the proposed system needs to be operated.

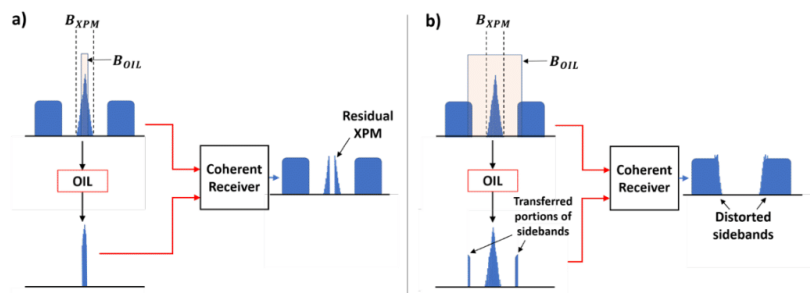


Fig. 3. Spectral effects of OIL's phase-transfer bandwidth on received signals when a) $B_{OIL} < B_{XPM}$ and b) $B_{OIL} > B_{guard}$.

The phase-transfer function of the OIL is important as it reflects the frequency range and the degree of the XPM-dominated nonlinear phase noise that can be cancelled upon coherent reception. To that end, a spectrally flat 20-Gbaud single-carrier QPSK-modulated signal (inset of Fig. 4), generated using zero-padded oversampling, was injected into the OIL at various P_{inj} . An unmodulated portion of the transmit laser was passed to the local oscillator port of the coherent receiver, to allow for homodyne detection experiments, otherwise the output of the OIL laser was used as the LO. The phase transfer function was then simply taken as the phase modulation spectrum measured from the output of the injection locked laser. We then take this as an indication of the injection locking bandwidth of the OIL set-up under injection with a wide-band signal.

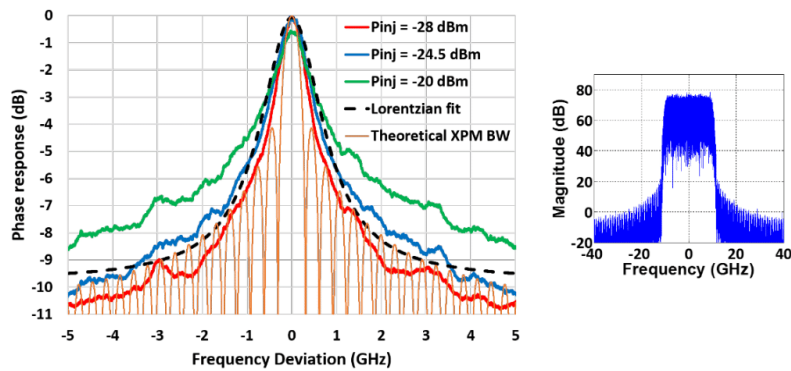


Fig. 4. Phase transfer function of the optical injection locking setup; P_{inj} : Injected power (dBm). Inset: 10-Gbaud modulated signal spectrum. P_{inj} of -28, -24.5 and -20 dBm correspond to injection ratios of -48, -45 and -40 dB, respectively.

Through inspection of Fig. 4, the phase transfer function of the injection locked laser seems to have a Lorentzian distribution, as have free-running lasers, but with a much wider bandwidth. To illustrate this, we fitted a Lorentzian curve to the transfer curves, shown in dashed lines in Fig. 4. Inspecting the separate curves for different injected powers (P_{inj}), we note that the phase transfer bandwidth (B_{OIL}) is broader with increasing injected power, as expected for low injection ratio locking [19,20]. We note that at higher injection ratios ($P_{inj} = -20$ dBm, a -40 dB injection ratio), the phase transfer at low bandwidths is not complete (<0 dB). This may affect the optimal injection ratio in the systems we investigate in later sections

of the paper. The optimum value of B_{OIL} will depend on the performance of the laser used for injection locking [23].

Frequency drifts between the slave laser and incoming signal can be compensated using slow feedback loops [19], to overcome limitations in the injection locking bandwidth (as distinct from the phase transfer bandwidth measured in Fig. 4). In our free-running case, we observed a locking bandwidth of around 2 GHz, although we did not make a rigorous measurement of this parameter in all cases.

Figure 4 also shows the theoretical XPM bandwidth for 40 spans (3200 km link) calculated using Eq. (1) and scaled to the phase transfer measurements. Ideally, these phase transfer characteristics of OIL would be flat within the B_{OIL} bandwidth, to faithfully transfer the XPM phase modulation to the coherent receiver. However, the Lorentzian shape of the phase transfer means that the higher-frequency XPM components are attenuated. Nonetheless, the attenuation is minimal for the main XPM lobe in Fig. 4 and so we should still expect significant cancellation of XPM. The attenuation can be compensated by increasing the P_{inj} at the risk of passing portions of signal sidebands through, as highlighted in Fig. 3. We will investigate this optimum P_{inj} or optimum injection ratio in the next section.

4. Nonlinear system performance

4.1 Experimental setup for transmission experiments

We experimentally identified the optimum phase-transfer bandwidth (B_{OIL}) and the optimum injected power P_{inj} for various link lengths and signal parameters. Figure 5 shows the experimental setup. An ECL array of seven continuous-wave (CW) lasers, each with 150-kHz linewidth and 15-dBm output power, was used. The center frequencies were 50-GHz apart, from 192.95 THz to 193.25 THz. The CW carriers were combined using an 8×1 polarization maintaining coupler, then modulated using a 20-GHz bandwidth IQ modulator (Complex MZM) with a 25-Gbaud OFDM signal with 100 sub-carriers from a 156-point FFT. The modulator drive was generated with a 60-Gsa/s 20-GHz bandwidth arbitrary waveform generator. A central guard-band of 2.5 GHz (10 sub-carriers) was added to prevent the transfer of the phase of the data-carrying subcarriers through the OIL set-up, providing an overall signal bandwidth of 27.5 GHz. The effective symbol rates of both the QPSK and 16-QAM is 25 Gbaud, and we assumed a 7% and 20% FEC overhead for these signals, respectively. This then gives a net rate per polarization of 46.7 Gb/s for QPSK and 83.3 Gb/s for 16-QAM. To de-correlate the neighboring channels, the multichannel signal was dispersed by ~ 14 symbols using an 80-km fiber and a Teraxion *DCML* dispersion compensation module, which flattens the intra-channel differential group delay within each channel, while maintaining inter-channel delay. The de-correlated WDM signal was then passed through a recirculating loop that consists of four 80-km spools of standard single-mode fiber (ITU G.652D). The number of re-circulations was controlled by two acousto-optic modulators (AOMs) to achieve transmission over multiples of 320 km. The noise bandwidth in the system was limited to 400 GHz using a WaveShaper (WSS 1). The power launched into each span was controlled by the output powers of the EDFAs numbered 1 to 5. The output of the recirculating loop was passed through WSS 2, set to select the center channel.

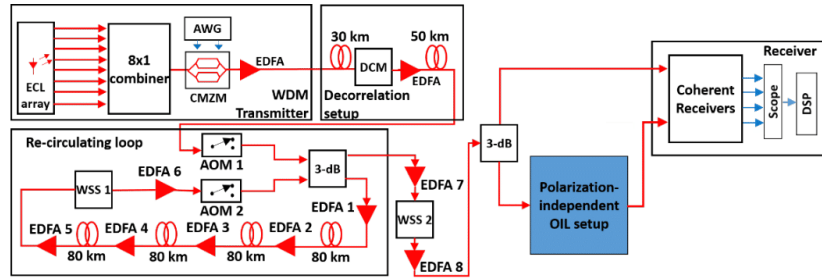


Fig. 5. Experimental setup: AWG- arbitrary waveform generator; DCM- dispersion compensation module; EDFA- erbium doped fiber amplifier; AOM- acousto-optic modulator; WSS- wavelength selective switch (WaveShaper).

The received signal is injected into the polarization-independent OIL described in Section 3.1 and shown in Fig. 2. The output of the OIL is used as the local oscillator (LO) for a coherent receiver, whose outputs were sampled by an 80 GSa/s oscilloscope feeding offline digital signal processing (DSP).

The DSP used to recover the signal (Fig. 6) includes: blind chromatic-dispersion compensation based on a coarse knowledge of the known distance and typical fiber dispersion using the overlap-save method; preamble-enabled frame synchronization using cross-correlation for the known preamble and received signal waveform; training-based channel estimation using the difference between the sent and received training waveforms to determine the channel response for single-tap sub-carrier equalization; M^{th} -power phase estimation for constellation recovery.

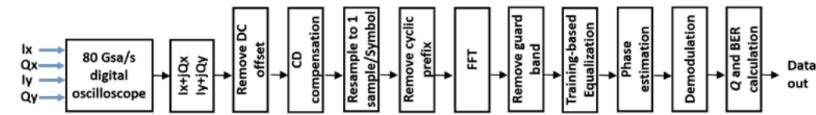


Fig. 6. Receiver side DSP flow implemented for experiments. FFT- fast Fourier transform; I_x , Q_x , I_y , Q_y - electrical waveforms from coherent receiver.

4.2 Optimum injection ratio

To confirm the optimum injection ratio, we measured the dependence of the performance of the recovered signal (using quality factor Q as a metric) on the injected power (P_{inj}) for a fixed transmission distance. P_{inj} represents the total signal power, including the residual carrier. The injection locking extracts a residual carrier from a guard-band in the middle of the signal, with the carrier-to-signal power ratio $\ll 0$ dB, set to be close to the point where injection locking was lost. The residual carrier was produced by biasing the CMZM slightly away from the null point, in order to pass a small amount of unmodulated light through to provide the seed for injection locking.

We use signal quality factor (Q) as a metric to determine optimum injection ratio for the carrier recovery system under test. By measuring Q , we include in our measurement the effects of non-ideal phase transfer through injection locking, as highlighted in Section 3, which help define the efficacy of our carrier recovery system. The Q of the recovered M -QAM signal is calculated from the error-vector magnitude (EVM) as a metric of system performance [24]. For a given EVM, the resulting BER for different M -QAM formats will change depending on the modulation order M . By taking the Q as extracted from measured EVM, the corresponding modulation-level-dependent BER was calculated using Eq. (2). At high EVMs, insufficient bit-errors are present over a reasonable time-frame, given the

processing time of off-line DSP. To ensure that EVM was a reliable measure of performance, we checked that when there were a significant number of errors at low OSNRs, the Q from EVM matches with Q calculated from BER, as

$$Q_{BER}(\text{dB}) = 20 \log_{10} \left(\sqrt{\frac{2(M-1)}{3}} \times \text{erfc}^{-1} \left(\frac{BER \times \log_2 \sqrt{M}}{1 - \frac{1}{\sqrt{M}}} \right) \right). \quad (2)$$

For the measurements shown in Fig. 7, we picked a distance for transmission and used a receiver-side EDFA to ensure that the receiver had sufficient input power. We then adjusted the injection ratio by adjusting the P_{inj} using a VOA (see Fig. 2). Each curve on the plot was then measured for different launch-powers, to probe the noise-limited and the nonlinear regimes.

Figure 7a shows performance against injection ratio plot for 320-km link. We observed an optimum injection ratio, in line with behavior predicted in Section 3.2. At the same time, the launch-power was also varied from -1 dBm to 7 dBm and the Q plotted. The Q increases globally from $P_L = -1$ dBm to 3 dBm and decreases from $P_L = 3$ dBm to 7 dBm, as expected for a nonlinear transmission system. The performance is maximum for $P_L = 3$ dBm (dark blue squares).

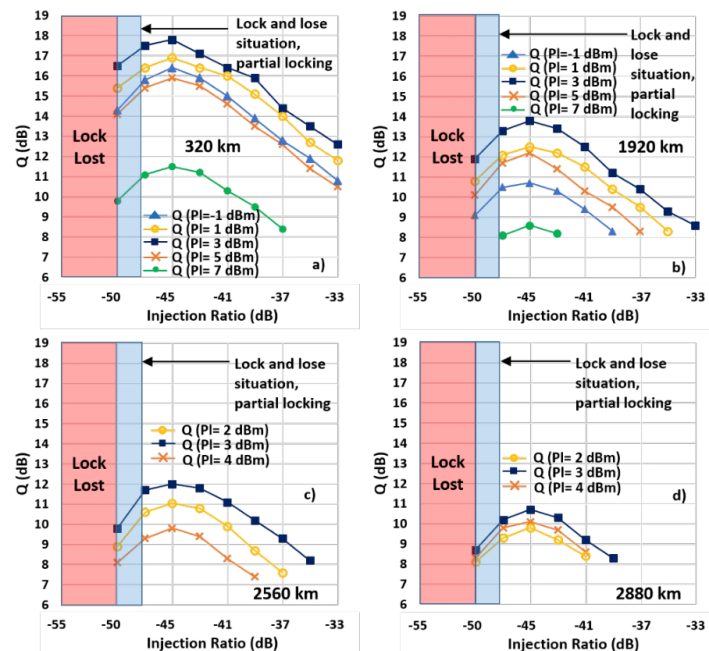


Fig. 7. Q vs. injected power for various launch-powers and link lengths: a) 320 km, b) 1920 km, c) 2560 km, d) 2880 km.

Along the x-axis, the performance for all curves reaches a maximum value at $P_{inj} = -24.5$ dBm, corresponding to an injection ratio of -45 dB, with the slave laser producing $+20$ dBm

of output power in free-running mode. This would then seem to indicate that a -45 dB injection ratio is optimal over a range of transmission distances when the launch power in the link is such that the Q of the received signal is close to its maximum value.

There are several inferences we can make from this result. As the injection ratio where performance is optimized does not seem to change with either launch power or transmission distance, this suggests that the optical signal-to-noise ratio plays only a minor role in determining the optimal injection ratio. Moreover, this also suggests that chromatic and polarization mode dispersion have little impact on the injection ratio that maximizes system Q , which is understandable as the injection locking stage is polarization independent and the bandwidth of injection locking should be nominally independent of dispersion of the injected signal.

In short, as the properties of injection locking are generally dependent on the strength of the injected tone, and even in the case of low OSNR, the power contribution of optical noise over the phase-transfer bandwidth is likely quite low, it may be expected that the injection ratio at the receiver is independent of the propagation distance. This is reflected in the relatively close match in the behaviors of the -1 -dBm launch power curve at 1920 km, the 2-dBm launch power curve at 2560 km, and the 3-dBm curve at 2880 km.

At this optimum injection ratio ($P_{inj} = -24.5$ dBm), Fig. 4 showed that the phase response has full-width half-maximum (FWHM) of 1 GHz with 2.8-dB/GHz roll-off up to 2 GHz. The performance drop on the low-power-side of the optimum in Fig. 7 is due to a reduction in the phase-transfer bandwidth of OIL (B_{OIL}) as shown in Fig. 3a, causing loss of phase information. If the injected power is reduced further, the system oscillates between locked and unlocked states: at lower powers, it experiences a complete loss of lock. The performance drop for injection ratios higher than the optimum is due to the increase in the phase transfer bandwidth of the OIL (B_{OIL}) to have a significant component outside the guard band (B_{guard}), which leads to transfer of the signal sidebands' phase on to the generated LO distorting the detected signal (Fig. 3b).

Similar trends were observed for longer distances (Figs. 7b-d). The Q performance is again maximum for $P_L = 3$ dBm and the optimum injection ratio is again found to be -45 dB. The overall performance decreases with distance, as expected as noise and nonlinear distortions increase with transmission distance. Interestingly, we observe that the optimal injection ratio is independent of the launch-power and the link distance. Comparing this to the expected range of XPM bandwidths for the different distances trialed, this would seem to suggest a broader phase transfer bandwidth would be preferred, for shorter distances, which should imply a change in injection ratio. The conclusion that the injection ratio—and hence phase transfer bandwidth—should be static with changing XPM bandwidth is similar to the set filter bandwidths used in [12]. This is an important and a useful property of the proposed system for optically routed networks where it is very difficult to determine the length of fiber traversed by a particular channel. In addition to this, the launch-powers may also vary in an optical network depending on the link length between subsequent repeaters, so the fact that the same optimum injection ratios are found for a variety of launch powers indicates that our method is robust to these launch power variations. As the operation of the proposed OIL-based system is independent of both transmission reach and launch power, would then seem to be suitable for use in optically routed networks, provided the injection ratio can be set (in this case to -45 dB), e.g. by using a power-controlled receiver-side EDFA.

4.3 Transmission of QPSK and 16-QAM modulated WDM signals

To gain insight on the transmission reach improvements enabled by partially compensating nonlinear distortions, we selected a distance and we swept the launch-powers. Curves were then plotted to understand the performance gain due to the nonlinearity-compensation.

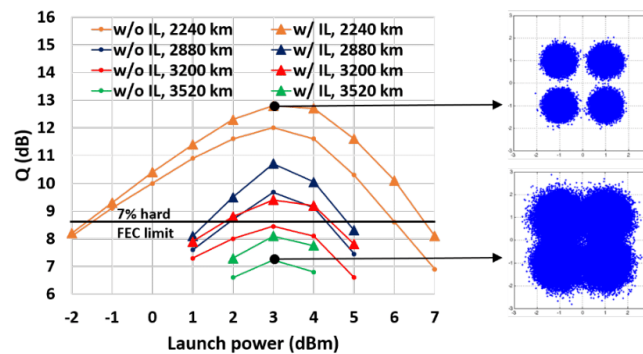


Fig. 8. Q vs. launch power with QPSK modulation. The injection ratio for the OIL was fixed at -45 dB, i.e. the optimum value shown in Fig. 7. The link distance was also varied to observe the maximum reach that can be achieved while the peak Q is greater than 7% hard FEC limit ($Q = 8.5$ dB, $\text{BER} = 3.8 \times 10^{-3}$). Figure 8 shows the performance plots for QPSK modulation. Similar to our observations in Fig. 5, the performance reaches the maximum at $P_L = 3$ dBm and then drops when increased further in to the nonlinear region ($P_L > 3$ dBm).

Figure 8 shows the performance comparison of proposed system with a regular intradyne system without any nonlinearity compensation. The intradyne system uses a spectral peak search method for carrier frequency offset (CFO) compensation. At lower launch-powers, the OIL shows marginal improvement that increases with increase in the nonlinear effects at higher launch powers. We note that the differences in peak Q between the systems with and without OIL means that the low launch power points for longer distances are unable to be measured in the amplifier-noise dominated regime, which results in the observed performance improvement for the OIL system even at low launch powers. The performance gain for higher launch-powers, thus, verifies the compensation of the nonlinear phase noise by the proposed OIL setup. Figure 8 shows that the performance for 3200 km does not reach the HD-FEC limit with the regular intradyne system, whereas, the OIL system with 3200-km link crosses the HD-FEC limit for a good range of launch-powers (2-4 dBm). In this case, we note that the 3200-km system with OIL performs very similarly to the 2880-km system without OIL, indicating that OIL can indeed improve system reach. While the distances we transmit over are fundamentally a product of the laboratory set-up that we measure with, the relative improvement between systems with and without injection locking indicate that OIL is able to compensate for nonlinear phase noise, and that this can translate into improved system reach.

We next measured the performance for 16-QAM modulation, which is being discussed as a potential candidate for high-throughput next-generation optical networks. This is important in the context of nonlinearity compensation, because as nonlinear interference is modulation-dependent [8], the effect of nonlinearity on higher-order QAM is worse than for QPSK.

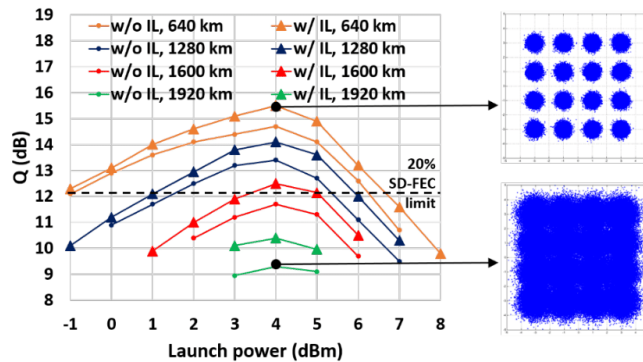


Fig. 9. Q vs. launch-power with 16-QAM modulation.

Figure 9 plots the measured Q for the recovered 16-QAM signal against the launch-power sweep for links of 640 km to 1920 km. The previously used HD-FEC limit was not met when transmitting 16-QAM signals over links longer than 320 km, even for the OIL system. As a result, we consider a 20% soft-decision FEC limit ($BER = 2.7 \times 10^{-2}$, $Q = 12.1$ dB, 20% overhead) for 16-QAM modulated signals [25]. As shown in Fig. 9, the peak Q over 1600-km transmission for an intradyne system without OIL does not meet the pre-FEC requirements for SD-FEC, whereas with OIL system this condition is met. Again, this indicates that reach can be improved through the use of OIL, here with 16-QAM modulated signals.

Table 1. Peak- Q -performance gains for QPSK and 16-QAM modulated signals.

QPSK		16-QAM	
Transmission distance	Peak- Q -improvement	Transmission distance	Peak- Q -improvement
2240 km	0.95	640 km	0.7
2880 km	1	1280 km	0.73
3200 km	1	1600 km	0.8
3520 km	1	1920 km	0.8

Table 1 shows the peak- Q -improvement by the proposed OIL system in the peak- Q . The QPSK signals experienced 0.95-1.1 dB improvements, whereas the 16-QAM system experienced 0.7-0.8 dB improvement. A marginal increase in peak- Q -improvement with transmission distance was observed in both systems. This improvement saturates at 1-dB for QPSK and at 0.8-dB for 16-QAM.

5. Discussion

The OIL system gave a 1-dB improvement over a regular intradyne system in the nonlinear regime for QPSK modulated signal. The best Q was always obtained at 3-dBm (4-dBm) launch-power for QPSK (16-QAM) modulated signal. The performance improvement in the nonlinear regime confirms the nonlinearity compensation by the proposed OIL-based method.

Comparing our results to digital pilot tone-based compensation methods, the proposed method gave a 0.2-dB gain in peak- Q over demonstrations of digital carrier extraction methods, which give 0.5-dB [17, 18] and 0.8-dB [16] improvements over non-compensated links. We believe that the peak- Q improvement in those systems was limited by receiver imperfections, possibly related to the resolution of the ADCs. Moreover, the 0.2-dB improvement we observe over digital pilot recovery systems carrying QPSK was achieved without adding extra steps into the receiver-side digital signal processing (DSP), thus avoids the introduction of extra processing latency, with reasonable increase in hardware complexity.

There are several avenues toward optimising the performance of our system, and to establish rigorous design rules for nonlinear cross-talk suppression using this technique. In this investigation, we used a low signal-to-carrier-power ratio, that was close to what we found experimentally to be the minimum necessary to ensure locking. However, the carrier-to-signal-power ratio could be significantly increased without significant degradation to the required OSNR at the receiver, and we expect that this may help expand the injection locking bandwidth without causing significant penalty from signal leakage. A rigorous study of this trade-off would help establish further design rules for our demonstrated system.

Similarly, there are expected trade-offs between the width of the guard-band employed to host the residual carrier, and performance, especially when holistically including the impact on overall capacity. At higher injection ratios, the leakage of data sidebands into the recovered carrier reduce performance. Clearly, with a wide guard-band, this effect could be reduced, but at the cost of lost capacity. This change in guard-band is also likely to influence the optimal carrier-to-signal power ratio. A full investigation of this trade-off would benefit from using mutual information as a metric. In addition, design of injection locking carrier recovery may change somewhat when using widely tunable lasers. These are some issues that would need to be addressed before commercial translation is a feasible option.

Compensation of inter-channel nonlinearities is proving to be a practically difficult task for multi-channel DBP [4–6], as it requires accurate models of the inter-channel interference along the link. By extracting nonlinear phase distortions optically at the receiver, we attempt to remove the requirement for accurate nonlinear channel models over wide bandwidths. In addition to this, by recovering phase distortions from the signal itself, the proposed system potentially allows for the cancellation of some stochastic nonlinear distortions that are extremely difficult to predict. For example, the proposed method should also cancel the low frequency components (those that fall within the phase transfer bandwidth of the OIL) of both the nonlinear phase noise generated due to amplified spontaneous emission's (ASE) interaction with the nonlinearities (the Gordon-Mollenauer effect).

The motivation to find alternatives to nonlinearity compensation techniques that rely on knowledge of the nonlinear fiber channel has also spurred investigations into in-line nonlinearity compensation techniques [12, 14, 15]. By requiring modification to optical equipment at the receiver-side only, our proposed system does not require modifications to equipment at multiple locations along the link, potentially simplifying implementation.

Commonly, the effectiveness of nonlinearity compensation schemes decrease as the transmission distance increases, for many reasons [4]. Here, we see either no change to efficacy, or a marginal improvement. We note that the characteristic XPM transfer curve in dispersion uncompensated links shrinks in bandwidth as distance increases [10–12]. This would then suggest that as transmission distance increases, more of the XPM distortion lies within the phase transfer bandwidth of the injection locking stage. This would suggest an improving level of nonlinear distortion cancellation. However, as transmission distance increases, so do amplitude distortions from nonlinear effects, which are not likely to be transferred through injection locking. These characteristics may explain why, on balance, our technique seems to provide an unchanged amount of peak- Q improvement in the systems investigated. We believe this warrants further investigation.

The proposed system is capable of mitigating the XPM distortion because of its limited bandwidth, but most of the wide-band SPM remains uncompensated. In contrast to wide-band inter-channel nonlinearity, DBP can significantly mitigate intra-channel nonlinear distortion (such as SPM). As such, the peak- Q and the nonlinearity tolerance can be further increased by adding a digital-backpropagation algorithm in the DSP that takes care of the SPM distortions.

Open questions remain as to whether this technique could be used to improve capacity. If only a small family of FEC options are considered, then the improvement in peak- Q afforded by OIL may be useful in using lower overhead codes (e.g. switching from 20% SD-FEC to 7% HD-FEC). If adaptive modulation or FEC codes are used, then the improvement in peak-

Q may be used to improve capacity for a given transmission distance. The trade-off between peak- Q improvement and the central guard band's bandwidth need to be investigated. The proportional spectral efficiency loss for a given guard band will improve with higher bandwidth signals; here we used a 25-Gbd signal, signals with baud rates over 60-Gbd (e.g [26].) are becoming common, and rates up to 100-Gbd are being reported by some groups (e.g [27].).

6. Conclusions

An all-optical processing approach for nonlinear phase noise compensation, using optical injection locking, has been proposed and experimentally verified on an OFDM signal in a WDM system. The method resulted in 1-dB (QPSK) and 0.7-dB (16-QAM) improvement in Q in the nonlinear power regime, compared with a conventional intradyne receiver. With an injection ratio of -45 dB, the transmission reach of the system was increased by one loop of the recirculating loop (320 km) for a given FEC limit. Thus, the proposed system can extend the transmission distance of optical communication networks, and only requires a sub-system modification at the receiver, rather than additional components in the field.

Funding

Australian Research Council's Laureate Fellowship scheme (FL130100041).

Acknowledgment

We thank VPIphotonics (www.vpi Photonics.com) for their support under the university program.

Bibliography

- [1] H. Mardoyan, R. Rios-Müller, M. A. Mestre, P. Jennevé, L. Schmalen, A. Ghazisaeidi, P. Tran, S. Bigo, and J. Renaudier, "Transmission of single-carrier nyquist-shaped 1-Tb/s line-rate signal over 3,000 km," in *Optical Fiber Communication Conference'15*. Los Angeles, CA, USA, 2015, p. W3G.2.
- [2] Y.-K. Huang, S. Zhang, F. Yaman, T. Inoue, E. Mateo, Y. Inada, T. Wang, and T. Ogata, "Dual-optical-carrier 1-Tbps channel transmission over 4,400-km using RF sub-band multiplexing," in *Conference on Lasers and Electro-Optics*. San Jose, CA, USA, 2016, p. SM4F.1.
- [3] J. M. Senior, *Optical Fiber Communications: Principles and Practice*. Pearson Education, Sydney, 2009.
- [4] T. Okoshi, "Recent progress in heterodyne/coherent optical-fiber communications," *Journal of Lightwave Technology*, vol. 2, no. 4, pp. 341–346, Aug 1984.
- [5] M. G. Taylor, "Coherent detection method using DSP for demodulation of signal and subsequent equalization of propagation impairments," *IEEE Photonics Technology Letters*, vol. 16, no. 2, pp. 674–676, Feb 2004.
- [6] S. J. Savory, G. Gavioli, R. I. Killey, and P. Bayvel, "Electronic compensation of chromatic dispersion using a digital coherent receiver," *Opt. Express*, vol. 15, no. 5, pp. 2120–2126, Mar 2007.
- [7] K. Kikuchi, "Fundamentals of coherent optical fiber communications," *Journal of Lightwave Technology*, vol. 34, no. 1, pp. 157–179, Jan 2016.
- [8] M. G. Taylor, "Phase estimation methods for optical coherent detection using digital signal processing," *Journal of Lightwave Technology*, vol. 27, no. 7, pp. 901–914, April 2009.
- [9] G. P. Agrawal, *Nonlinear Fiber Optics*, ser. Optics and Photonics Series. Academic Press, Cambridge, USA., 2013.

- [10] R. Dar, M. Feder, A. Mecozzi, and M. Shtaif, "Accumulation of nonlinear interference noise in fiber-optic systems," *Opt. Express*, vol. 22, no. 12, pp. 14 199–14 211, Jun 2014.
- [11] M. N. Chughtai, "Thesis: Nonlinear phase noise in fiber optical communication," *Chalmers University of Technology, Goteborg, Sweden*, 2009.
- [12] T. Inoue and S. Namiki, "Carrier recovery for M-QAM signals based on a block estimation process with Kalman filter," *Opt. Express*, vol. 22, no. 13, pp. 15 376–15 387, Jun 2014.
- [13] T. Marshall, B. Szafraniec, and B. Nebendahl, "Kalman filter carrier and polarization-state tracking," *Opt. Lett.*, vol. 35, no. 13, pp. 2203–2205, Jul 2010.
- [14] Z. Liu, J. Y. Kim, D. S. Wu, D. J. Richardson, and R. Slavík, "Homodyne OFDM with optical injection locking for carrier recovery," *Journal of Lightwave Technology*, vol. 33, no. 1, pp. 34–41, Jan 2015.
- [15] O. Lidoyne, P. Gallion, C. Chabran, and G. Debarge, "Locking range, phase noise and power spectrum of an injection-locked semiconductor laser," *IEE Proceedings, J. Optoelectronics*, vol. 137, no. 3, pp. 147–154, Jun 1990.
- [16] R. Appleyard, *Pioneers of Electrical Communication*. Macmillan and Company limited, Basingstoke, United Kingdom., 1930.
- [17] J. J. Fahie, *A history of electric telegraphy to the year 1837*. Princeton press, New Jersey, USA., 1884.
- [18] S. Puleo, *A City So Grand: The Rise of an American Metropolis, Boston 1850-1900*. Beacon Press, Boston, USA., 2010.
- [19] R. Fessenden, "Wireless telegraphy." US Patent 706,735, 1902.
- [20] E. H. Armstrong, "A new system of short wave amplification," *Proceedings of the Institute of Radio Engineers*, vol. 9, no. 1, pp. 3–11, Feb 1921.
- [21] Hittite Microwave Corporation, "Synchronizing system," US Patent 1,990,428, 1932.
- [22] A. Grebene and H. Camenzind, "Phase locking as a new approach for tuned integrated circuits," in *1969 IEEE International Solid-State Circuits Conference*, vol. XII, Feb 1969, pp. 100–101.
- [23] J. P. Costas, "Synchronous communications," *Proceedings of the Institute of Radio Engineers*, vol. 44, no. 12, pp. 1713–1718, Dec 1956.
- [24] D. Taylor and D. Cheung, "A decision-directed carrier recovery loop for duobinary encoded offset QPSK signals," *IEEE Transactions on Communications*, vol. 27, no. 2, pp. 461–468, Feb 1979.

- [25] R. Chang and R. Srinivasagopalan, "Carrier recovery for data communication systems with adaptive equalization," *IEEE Transactions on Communications*, vol. 28, no. 8, pp. 1142–1153, August 1980.
- [26] D. Messerschmitt, "Frequency detectors for PLL acquisition in timing and carrier recovery," *IEEE Transactions on Communications*, vol. 27, no. 9, pp. 1288–1295, Sep 1979.
- [27] A Televideo lecture, *The Wadley Drift Cancelling Loop*. Visit webpage: <http://televideo.ws/wadley.html>.
- [28] Y. Fang, "Carrier phase-jitter extraction method for VSB and SSB data transmission systems," *IEEE Transactions on Communications*, vol. 20, no. 6, pp. 1169–1175, Dec 1972.
- [29] R. Even and N. Voulgaris, "Carrier phase recovery scheme for a low-frequency vestigial sideband video transmission system," *IEEE Transactions on Circuits and Systems*, vol. 21, no. 4, pp. 473–479, Jul 1974.
- [30] J. D. H. Alexander, "Carrier recovery technique for digital phase-modulated signals," *Electronics Letters*, vol. 11, no. 22, pp. 535–536, October 1975.
- [31] C. Hogge, "Carrier and clock recovery for 8 PSK synchronous demodulation," *IEEE Transactions on Communications*, vol. 26, no. 5, pp. 528–533, May 1978.
- [32] T. Pfau, S. Hoffmann, and R. Noe, "Hardware-efficient coherent digital receiver concept with feedforward carrier recovery for M-QAM constellations," *Journal of Lightwave Technology*, vol. 27, no. 8, pp. 989–999, April 2009.
- [33] H. Kobayashi, "Simultaneous adaptive estimation and decision algorithm for carrier modulated data transmission systems," *IEEE Transactions on Communication Technology*, vol. 19, no. 3, pp. 268–280, June 1971.
- [34] G. Ungerboeck, "Adaptive maximum-likelihood receiver for carrier-modulated data-transmission systems," *IEEE Transactions on Communications*, vol. 22, no. 5, pp. 624–636, May 1974.
- [35] A. Luvison and G. Pirani, "Design and performance of an adaptive Kalman receiver for synchronous data transmission," *IEEE Transactions on Aerospace and Electronic Systems*, vol. AES-15, no. 5, pp. 635–648, Sept 1979.
- [36] R. Kalman, "On the general theory of control systems," *IRE Transactions on Automatic Control*, vol. 4, no. 3, pp. 110–110, Dec 1959.

- [37] R. Lawrence and H. Kaufman, "The Kalman filter for the equalization of a digital communications channel," *IEEE Transactions on Communication Technology*, vol. 19, no. 6, pp. 1137–1141, December 1971.
- [38] Y. Yamamoto, "Receiver performance evaluation of various digital optical modulation-demodulation systems in the 0.5-10 μm wavelength region," *IEEE Journal of Quantum Electronics*, vol. 16, no. 11, pp. 1251–1259, November 1980.
- [39] H. Philipp, A. Scholtz, E. Bonek, and W. Leeb, "Costas loop experiments for a 10.6 μm communications receiver," *IEEE Transactions on Communications*, vol. 31, no. 8, pp. 1000–1002, August 1983.
- [40] L. G. Kazovsky, "Decision-driven phase-locked loop for optical homodyne receivers: Performance analysis and laser linewidth requirements," *IEEE Transactions on Electron Devices*, vol. 32, no. 12, pp. 2630–2639, Dec 1985.
- [41] S. Camatel, V. Ferrero, R. Gaudino, and P. Poggiolini, "Optical phase-locked loop for coherent detection optical receiver," *Electronics Letters*, vol. 40, no. 6, pp. 384–385, March 2004.
- [42] L. Kazovsky, "Multichannel coherent optical communications systems," *Journal of Lightwave Technology*, vol. 5, no. 8, pp. 1095–1102, 1987.
- [43] K. Iwashita, "Long-distance coherent communications experiments," in *Optical Fiber Communication*. New Orleans, Louisiana, USA, August 1988, p. WC1.
- [44] K. Tamura, S. B. Alexander, and V. W. S. Chan, "Phase-noise-canceled differential-phase-shift-keying PNC-DPSK modulation for coherent optical communication systems," in *Optical Fiber Communication*. Optical Society of America, 1988, p. WG2.
- [45] M. Nakamura, Y. Kamio, and T. Miyazaki, "Linewidth-tolerant real-time 40-gbit/s 16-QAM self-homodyne detection using a pilot carrier and ISI suppression based on electronic digital processing," *Opt. Lett.*, vol. 35, no. 1, pp. 13–15, Jan 2010.
- [46] Y. H. Cheng, E. A. J. Marcatili, and T. Okoshi, "Phase-noise-canceling heterodyne receivers for coherent optical communication systems," in *Optical Fiber Communication Conference*. Houston, Texas, USA, 1989, p. TUI7.
- [47] D. D. Sampson and D. A. Jackson, "Coherent optical fiber communications system using all-optical correlation processing," *Opt. Lett.*, vol. 15, no. 10, pp. 585–587, May 1990.
- [48] S. Yang, S. B. Alexander, V. W. S. Chan, and J. G. Fujimoto, "Injection locking of a diode laser array for coherent heterodyne optical communication," in *Conference on Lasers and Electro-Optics*. Baltimore, Maryland, USA, 1987, p. THD5.

- [49] K. Croussore, C. Kim, and G. Li, "All-optical regeneration of differential phase-shift keying signals based on phase-sensitive amplification," *Opt. Lett.*, vol. 29, no. 20, pp. 2357–2359, Oct 2004.
- [50] I. Kim, K. Croussore, X. Li, G. Li, T. Hasegawa, and N. Sugimoto, "All-optical carrier phase and polarization recovery using a phase-sensitive oscillator," in *Optical Fiber Communication Conference and Exposition and The National Fiber Optic Engineers Conference*. Anaheim, CA, USA, 2007, p. JWA57.
- [51] R. Slavik, J. Kakande, and D. J. Richardson, "Feed-forward true carrier extraction of high baud rate phase shift keyed signals using photonic modulation stripping and low-bandwidth electronics," *Opt. Express*, vol. 19, no. 27, pp. 26 594–26 599, Dec 2011.
- [52] J. M. D. Mendinueta, B. J. Puttnam, J. Sakaguchi, R. S. Luis, W. Klaus, Y. Awaji, N. Wada, A. Kanno, and T. Kawanishi, "Energy efficient carrier phase recovery for self-homodyne polarization-multiplexed QPSK," in *2013 18th OptoElectronics and Communications Conference held jointly with 2013 International Conference on Photonics in Switching*. Kyoto, Japan, 2013, p. ThR3.5.
- [53] A. Viterbi, "Nonlinear estimation of PSK-modulated carrier phase with application to burst digital transmission," *IEEE Transactions on Information Theory*, vol. 29, no. 4, pp. 543–551, July 1983.
- [54] R. Noé, "Phase noise-tolerant synchronous QPSK/BPSK baseband-type intradyne receiver concept with feedforward carrier recovery," *J. Lightwave Technol.*, vol. 23, no. 2, p. 802, Feb 2005.
- [55] ———, "PLL-free synchronous QPSK polarization multiplex/diversity receiver concept with digital i amp;q baseband processing," *IEEE Photonics Technology Letters*, vol. 17, no. 4, pp. 887–889, April 2005.
- [56] M. Nazarathy, A. Gorshtein, and D. Sadot, "Doubly-differential coherent 100g transmission: Multi-symbol decision-directed carrier phase estimation with intradyne frequency offset cancellation," in *Advanced Photonics & Renewable Energy*. Karlsruhe, Germany, 2010, p. SPWB4.
- [57] J. Qi and F. N. Hauske, "Multiplier-free carrier phase estimation for low complexity carrier frequency and phase recovery," in *Optical Fiber Communication Conference*. Los Angeles, CA, USA, 2012, p. JW2A.66.
- [58] G. Kalogerakis, W.-T. Shaw, and L. G. Kazovsky, "Dsp-based coherent detection techniques," in *Optical Amplifiers and Their Applications/Coherent Optical Technologies and Applications*. Optical Society of America, 2006, p. CWC3.
- [59] M. Qiu, Q. Zhuge, X. Xu, M. Chagnon, M. Morsy-Osman, and D. V. Plant, "Simple and efficient frequency offset tracking and carrier phase recovery algorithms in single carrier transmission systems," *Opt. Express*, vol. 21, no. 7, pp. 8157–8165, Apr 2013.

- [60] Q. Zhuge, M. Morsy-Osman, X. Xu, M. E. Mousa-Pasandi, M. Chagnon, Z. A. El-Sahn, and D. V. Plant, "Pilot-aided carrier phase recovery for M-QAM using superscalar parallelization based pll," *Opt. Express*, vol. 20, no. 17, pp. 19 599–19 609, Aug 2012.
- [61] —, "Pilot-aided carrier phase recovery for M-QAM using superscalar parallelization based pll," *Opt. Express*, vol. 20, no. 17, pp. 19 599–19 609, Aug 2012.
- [62] I. Fatadin, D. Ives, and S. J. Savory, "Laser linewidth tolerance for 16-QAM coherent optical systems using QPSK partitioning," *IEEE Photonics Technology Letters*, vol. 22, no. 9, pp. 631–633, May 2010.
- [63] Y. Wang and E. Serpedin, "A class of blind phase recovery techniques for higher order QAM modulations: estimators and bounds," *IEEE Signal Processing Letters*, vol. 9, no. 10, pp. 301–304, Oct 2002.
- [64] C. Spatharakis, N. Argyris, S. Dris, and H. Avramopoulos, "Frequency offset estimation and carrier phase recovery for high-order QAM constellations using the viterbi-viterbi monomial estimator," in *2014 9th International Symposium on Communication Systems, Networks Digital Sign (CSNDSP)*, July 2014, pp. 781–786.
- [65] N. Argyris, S. Dris, C. Spatharakis, and H. Avramopoulos, "High performance carrier phase recovery for coherent optical QAM," in *Optical Fiber Communication Conference*. Los Angeles, CA, USA, 2015, p. W1E.1.
- [66] X. Zhou, "Hardware efficient carrier recovery algorithms for single-carrier QAM systems," in *Advanced Photonics Congress*. Colorado, USA, 2012, p. SpTu3A.1.
- [67] X. Zhou, J. Yu, M. F. Huang, Y. Shao, T. Wang, L. Nelson, P. Magill, M. Birk, P. I. Borel, D. W. Peckham, R. Lingle, and B. Zhu, "64-Tb/s, 8 b/s/Hz, PDM-36QAM transmission over 320 km using both pre- and post-transmission digital signal processing," *Journal of Lightwave Technology*, vol. 29, no. 4, pp. 571–577, Feb 2011.
- [68] X. Li, Y. Cao, S. Yu, W. Gu, and Y. Ji, "A simplified feedforward carrier recovery algorithm for coherent optical QAM system," *J. Lightwave Technol.*, vol. 29, no. 5, pp. 801–807, Mar 2011.
- [69] M. Morsy-Osman, Q. Zhuge, L. R. Chen, and D. V. Plant, "Feedforward carrier recovery via pilot-aided transmission for single-carrier systems with arbitrary M-QAM constellations," *Opt. Express*, vol. 19, no. 24, pp. 24 331–24 343, Nov 2011.
- [70] —, "Joint mitigation of laser phase noise and fiber nonlinearity for polarization-multiplexed qpsk and 16-QAM coherent transmission systems," *Opt. Express*, vol. 19, no. 26, pp. B329–B336, Dec 2011.

- [71] W.-R. Peng, T. Tsuritani, and I. Morita, "Simple carrier recovery approach for RF-pilot-assisted PDM-CO-OFDM systems," *J. Lightwave Technol.*, vol. 31, no. 15, pp. 2555–2564, Aug 2013.
- [72] X. Zhou, X. Yang, R. Li, and K. Long, "Efficient joint carrier frequency offset and phase noise compensation scheme for high-speed coherent optical OFDM systems," *J. Lightwave Technol.*, vol. 31, no. 11, pp. 1755–1761, Jun 2013.
- [73] A. Meiyappan, P.-Y. Kam, and H. Kim, "A complex-weighted, decision-aided, maximum-likelihood carrier phase and frequency-offset estimation algorithm for coherent optical detection," *Opt. Express*, vol. 20, no. 18, pp. 20 102–20 114, Aug 2012.
- [74] N. Sigron, I. Tselniker, and M. Nazarathy, "Carrier phase estimation for optically coherent QPSK based on wiener-optimal and adaptive multi-symbol delay detection (MSDD)," *Opt. Express*, vol. 20, no. 3, pp. 1981–2003, Jan 2012.
- [75] I. Tselniker, N. Sigron, and M. Nazarathy, "Joint phase noise and frequency offset estimation and mitigation for optically coherent QAM based on adaptive multi-symbol delay detection (MSDD)," *Opt. Express*, vol. 20, no. 10, pp. 10 944–10 962, May 2012.
- [76] M. I. Khalil, M. M. H. Adib, A. M. Chowdhury, M. S. Faruk, and G. Chang, "Low complexity blind level discrimination carrier phase recovery algorithm in optical coherent receiver," in *Asia Communications and Photonics Conference*. Guangzhou, China, 2012, p. AS1C.4.
- [77] L. Barletta, M. Magarini, and A. Spalvieri, "A new lower bound below the information rate of wiener phase noise channel based on Kalman carrier recovery," *Opt. Express*, vol. 20, no. 23, pp. 25 471–25 477, Nov 2012.
- [78] M. Piels, M. I. Olmedo, W. Xue, X. Pang, C. Schäffer, R. Schatz, G. Jacobsen, I. T. Monroy, J. Mørk, S. Popov, and D. Zibar, "Laser rate equation-based filtering for carrier recovery in characterization and communication," *J. Lightwave Technol.*, vol. 33, no. 15, pp. 3271–3279, Aug 2015.
- [79] A. Jain and P. K. Krishnamurthy, "Tracking linear and nonlinear phase noise in 100G QPSK modulated systems using Kalman filter," in *Advanced Photonics 2015*. Vancouver, Canada, 2015, p. JM3A.8.
- [80] T.-H. Nguyen, F. Rottenberg, S.-P. Gorza, J. Louveaux, and F. Horlin, "Extended Kalman filter for carrier phase recovery in optical filter bank multicarrier offset QAM systems," in *Optical Fiber Communication Conference'17*. Los Angeles, CA, USA, 2017, p. Th4C.3.
- [81] L. Linqian, Y. Feng, W. Zhang, N. Cui, H. Xu, X. Tang, L. Xi, and X. Zhang, "Extended Kalman filter for carrier frequency offset and carrier phase noise," in *Conference on Lasers and Electro-Optics*. San Jose, CA, USA, 2017, p. STu3M.7.

- [82] D. Blackwell, "Conditional expectation and unbiased sequential estimation," *Ann. Math. Statist.*, vol. 18, no. 1, pp. 105–110, March 1947.
- [83] S. M. Kay, "Fundamentals of statistical signal processing, volume I: estimation theory," 1993.
- [84] G. Smith, S. Schmidt, and L. McGee, "Application of statistical filter theory to the optimal estimation of position and velocity on board a circumlunar vehicle," <https://books.google.com.au/books?id=x06dcSZYCTIC>, 1962.
- [85] B. A. McElhoe, "An assessment of the navigation and course corrections for a manned flyby of Mars or Venus," *IEEE Transactions on Aerospace and Electronic Systems*, vol. AES-2, no. 4, pp. 613–623, July 1966.
- [86] E. A. Wan and R. Van Der Merwe, "The unscented Kalman filter for nonlinear estimation," in *Adaptive Systems for Signal Processing, Communications, and Control Symposium 2000*. IEEE, 2000, pp. 153–158.
- [87] L. Pakala and B. Schmauss, "Extended Kalman filtering for joint mitigation of phase and amplitude noise in coherent QAM systems," *Opt. Express*, vol. 24, no. 6, pp. 6391–6401, Mar 2016.
- [88] C. Spatharakis, N. Argyris, S. Dris, and H. Avramopoulos, "Frequency offset estimation and carrier phase recovery for high-order QAM constellations using the Viterbi-Viterbi monomial estimator," in *2014 9th International Symposium on Communication Systems, Networks Digital Sign (CSNDSP)*, July 2014, pp. 781–786.
- [89] "Technology options for 400g implementation," <http://www.oiforum.com/documents/technology-options-for-400G-implementation/>, accessed: 2015-07-01.
- [90] D. Chang, F. Yu, Z. Xiao, N. Stojanovic, F. N. Hauske, Y. Cai, C. Xie, L. Li, X. Xu, and Q. Xiong, "LDPC convolutional codes using layered decoding algorithm for high speed coherent optical transmission," in *Optical Fiber Communication Conference'12*. Los Angeles, CA, USA, 2012, p. OW1H.4.
- [91] X. Zhou, L. E. Nelson, P. Magill, R. Isaac, B. Zhu, D. W. Peckham, P. I. Borel, and K. Carlson, "High spectral efficiency 400 Gb/s transmission using PDM time-domain hybrid 32-64 QAM and training-assisted carrier recovery," *Journal of Lightwave Technology*, vol. 31, no. 7, pp. 999–1005, April 2013.
- [92] D. S. Millar and S. J. Savory, "Blind adaptive equalization of polarization-switched QPSK modulation," *Opt. Express*, vol. 19, no. 9, pp. 8533–8538, Apr 2011.

- [93] C. Zhu, A. V. Tran, S. Chen, L. B. Du, T. Anderson, A. J. Lowery, and E. Skafidas, "Frequency-domain blind equalization for long-haul coherent pol-mux 16-QAM system with CD prediction and dual-mode adaptive algorithm," *IEEE Photonics Journal*, vol. 4, no. 5, pp. 1653–1661, Oct 2012.
- [94] S. Zhang, P. Y. Kam, C. Yu, and J. Chen, "Decision-aided carrier phase estimation for coherent optical communications," *Journal of Lightwave Technology*, vol. 28, no. 11, pp. 1597–1607, June 2010.
- [95] Y. Yang, G. Cao, K. Zhong, X. Zhou, Y. Yao, A. P. T. Lau, and C. Lu, "Fast polarization-state tracking scheme based on radius-directed linear Kalman filter," *Opt. Express*, vol. 23, no. 15, pp. 19 673–19 680, Jul 2015.
- [96] T. Xu, G. Jacobson, S. Popov, M. Forzati, J. Martensson, M. Mussolin, K. Wang, Y. Zhang, and A. T. Friberg, "Fast polarization-state tracking scheme based on radius-directed linear Kalman filter," *Opt. Comm.*, vol. 32, no. 2, pp. 19 673–19 680, June 2011.
- [97] M. Selmi, Y. Jaouen, and P. Ciblat, "Accurate digital frequency offset estimator for coherent polmux QAM transmission systems," in *2009 35th European Conference on Optical Communication*, Sept 2009, pp. 1–2.
- [98] T. Fehenberger, M. Mazur, T. A. Eriksson, M. Karlsson, and N. Hanik, "Experimental analysis of correlations in the nonlinear phase noise in optical fiber systems," in *ECOC 2016; 42nd European Conference on Optical Communication*, Sept 2016, pp. 1–3.
- [99] S. Matsuo, K. Takenaga, Y. Sasaki, Y. Amma, S. Saito, K. Saitoh, T. Matsui, K. Nakajima, T. Mizuno, H. Takara, Y. Miyamoto, and T. Morioka, "High-spatial-multiplicity multicore fibers for future dense space-division-multiplexing systems," *J. Lightwave Technol.*, vol. 34, no. 6, pp. 1464–1475, Mar 2016. [Online]. Available: <http://jlt.osa.org/abstract.cfm?URI=jlt-34-6-1464>
- [100] A. Schulzgen, A. Newkirk, J. Anderson, G. Salceda-Delgado, Z. S. Eznavah, J. E. Antonio-Lopez, C. Xia, G. Li, R. G. van Uden, F. M. Huijskens, H. de Waardt, T. A. Koonen, C. Okonkwo, and R. A. Correa, "Multicore fibers," in *Workshop on Specialty Optical Fibers and Their Applications*. Optical Society of America, 2015, p. WF3A.1. [Online]. Available: <http://www.osapublishing.org/abstract.cfm?URI=WSOF-2015-WF3A.1>
- [101] K. Saitoh and S. Matsuo, "High-spatial-multiplicity multicore fibers for future dense space-division-multiplexing systems," *Nanophotonics*, vol. 2, no. 5, pp. 441–454, June 2018. [Online]. Available: <http://jlt.osa.org/abstract.cfm?URI=jlt-34-6-1464>
- [102] J.-P. Elbers, N. Eiselt, A. Dochhan, D. Rafique, and H. Grieser, "PAM4 vs coherent for DCI applications," in *Advanced Photonics 2017 (IPR, NOMA, Sensors, Networks, SPPCom, PS)*. Optical

- Society of America, 2017, p. SpTh2D.1. [Online]. Available: <http://www.osapublishing.org/abstract.cfm?URI=SPPCom-2017-SpTh2D.1>
- [103] W. Shieh, H. Bao, and Y. Tang, "Coherent optical OFDM: theory and design," *Opt. Express*, vol. 16, no. 2, pp. 841–859, Jan 2008.
- [104] Y. Tang and W. Shieh, "Coherent optical OFDM transmission up to 1 tb/s per channel," *Journal of Lightwave Technology*, vol. 27, no. 16, pp. 3511–3517, Aug 2009.
- [105] S. Chen, Q. Yang, Y. Ma, and W. Shieh, "Multi-gigabit real-time coherent optical OFDM receiver," in *Optical Fiber Communication Conference'09*. San Diego, CA, USA, 2009, p. OTuO4.
- [106] S. Chandrasekhar, X. Liu, B. Zhu, and D. W. Peckham, "Transmission of a 1.2-Tb/s 24-carrier no-guard-interval coherent OFDM superchannel over 7200-km of ultra-large-area fiber," in *2009 35th European Conference on Optical Communication*, vol. 2009-Supplement, Sept 2009, pp. 1–2.
- [107] X. Du, J. Zhang, C. Yu, and P.-Y. Kam, "Blind carrier frequency offset estimation for coherent optical OFDM systems," in *Advanced Photonics 2016 (IPR, NOMA, Sensors, Networks, SPPCom, SOF)*. Vancouver, Canada, 2016, p. SpW2G.3.
- [108] M. Li, J. Zhao, and L.-K. Chen, "Blind maximum-likelihood frequency offset estimation for coherent fast OFDM receivers," in *2013 18th OptoElectronics and Communications Conference held jointly with 2013 International Conference on Photonics in Switching*, June 2013, pp. 1–2.
- [109] A. Al-Dweik, A. Hazmi, S. Younis, B. Sharif, and C. Tsimenidis, "Blind iterative frequency offset estimator for orthogonal frequency division multiplexing systems," *IET Communications*, vol. 4, no. 16, pp. 2008–2019, November 2010.
- [110] H. Bolcskei, "Blind estimation of symbol timing and carrier frequency offset in wireless OFDM systems," *IEEE Transactions on Communications*, vol. 49, no. 6, pp. 988–999, Jun 2001.
- [111] T. M. Schmidl and D. C. Cox, "Robust frequency and timing synchronization for OFDM," *IEEE Transactions on Communications*, vol. 45, no. 12, pp. 1613–1621, Dec 1997.
- [112] H. Minn, V. K. Bhargava, and K. B. Letaief, "A robust timing and frequency synchronization for OFDM systems," *IEEE Transactions on Wireless Communications*, vol. 2, no. 4, pp. 822–839, July 2003.
- [113] S. H. Fan, J. Yu, D. Qian, and G. K. Chang, "A fast and efficient frequency offset correction technique for coherent optical orthogonal frequency division multiplexing," *Journal of Lightwave Technology*, vol. 29, no. 13, pp. 1997–2004, July 2011.

- [114] C. Xie and G. Raybon, "Digital PLL based frequency offset compensation and carrier phase estimation for 16-QAM coherent optical communication systems," in *2012 38th European Conference and Exhibition on Optical Communications*, Sept 2012, pp. 1–3.
- [115] M. Lu, H.-C. Park, J. S. Parker, E. Bloch, A. Sivanathan, Z. Griffith, L. A. Johansson, M. J. Rodwell, and L. A. Coldren, "A heterodyne optical phase-locked loop for multiple applications," in *Optical Fiber Communication Conference'13*. Anaheim, CA, USA, 2013, p. OW3D.1.
- [116] L. Naglic, L. Pavlovic, B. Batagelj, and M. Vidmar, "Improved phase detector for electro-optical phase-locked loops," *Electronics Letters*, vol. 44, no. 12, pp. 758–760, June 2008.
- [117] "IEEE standard for information technology–telecommunications and information exchange between systems local and metropolitan area networks–specific requirements - part 11: Wireless LAN medium access control (MAC) and physical layer (PHY) specifications," *IEEE Std 802.11-2016 (Revision of IEEE Std 802.11-2012)*, pp. 1–3534, Dec 2016.
- [118] A. J. Lowery and J. Armstrong, "Orthogonal-frequency-division multiplexing for dispersion compensation of long-haul optical systems," *Opt. Express*, vol. 14, no. 6, pp. 2079–2084, Mar 2006.
- [119] A. J. Lowery, L. Du, and J. Armstrong, "Orthogonal frequency division multiplexing for adaptive dispersion compensation in long haul WDM systems," in *Optical Fiber Communication Conference'06*. Anaheim, CA, USA, 2006, p. PDP39.
- [120] W. Shieh, X. Yi, and Y. Tang, "Transmission experiment of multi-gigabit coherent optical OFDM systems over 1000km SSMF fibre," *Electronics Letters*, vol. 43, no. 3, pp. 183–184, Feb 2007.
- [121] J. Li, R. Schmogrow, D. Hillerkuss, P. C. Schindler, M. Nazarathy, C. Schmidt-Langhorst, S.-B. Ezra, I. Tselniker, C. Koos, W. Freude, and J. Leuthold, "A self-coherent receiver for detection of polmux coherent signals," *Opt. Express*, vol. 20, no. 19, pp. 21 413–21 433, Sep 2012.
- [122] T. Fujita, Y. Toba, Y. Miyoshi, and M. Ohashi, "Optical analog multiplier based on phase sensitive amplification," in *2013 18th OptoElectronics and Communications Conference held jointly with 2013 International Conference on Photonics in Switching*. Madrid, Spain, 2013, p. TuPS.8.
- [123] Corning, "Corning SMF-28e Optics Fiber Product Information." <http://www.tlc.unipr.it/cucinotta/cfa/datasheet.SMF28e.pdf>, 2005, [Online; accessed January-2005].
- [124] M. R. Khanzadi, R. Krishnan, and T. Eriksson, "Estimation of phase noise in oscillators with colored noise sources," *IEEE Communications Letters*, vol. 17, no. 11, pp. 2160–2163, November 2013.

- [125] N. Nambath, M. Anghan, N. B. Thaker, R. Ashok, R. Kamran, A. K. Mishra, and S. Gupta, "First demonstration of an all analog adaptive equalizer for coherent dp-qpsk links," in *Optical Fiber Communication Conference*. Los Angeles, CA, USA, 2017, p. M3D.5.
- [126] A. Umbach, G. Unterborsch, R. P. Braun, and G. Großkopf, "Stable optical source and high-speed photodetector used for remote fiber-optic 64-GHz mm wave generation," in *Optical Fiber Communication Conference'98*. San Jose, CA, USA, 1998, p. ThB3.
- [127] H. K. Sung, T. Jung, D. Tishinin, K. Y. Liou, W. T. Tsang, and M. C. Wu, "Optical injection-locked gain-lever distributed Bragg reflector lasers with enhanced rf performance," in *2004 IEEE International Topical Meeting on Microwave Photonics*, Oct 2004, pp. 225–228.
- [128] H. Lee, R. Ram, O. Kjebon, and R. Schatz, "Bandwidth enhancement and chirp reduction in DBR lasers by strong optical injection," in *Conference on Lasers and Electro-Optics'00*. Nice, France, 2000, p. CMS4.
- [129] S. Uvin, S. Keyvaninia, F. Lelarge, G.-H. Duan, B. Kuyken, and G. Roelkens, "Narrow line width frequency comb source based on an injection-locked III-V on-silicon mode-locked laser," *Opt. Express*, vol. 24, no. 5, pp. 5277–5286, Mar 2016.
- [130] Z. Liu, D. J. Richardson, and R. Slavik, "Optical injection locking based carrier recovery for coherent signal reception," in *Asia Communications and Photonics Conference'15*. Hong Kong, 2015, p. AM3I.3.
- [131] O. Lidoyne, P. Gallion, and D. Erasme, "Analysis of a homodyne receiver using an injection-locked semiconductor laser," *Journal of Lightwave Technology*, vol. 9, no. 5, pp. 659–665, May 1991.
- [132] E. Dale, W. Liang, D. Eliyahu, A. A. Savchenkov, V. S. Ilchenko, A. B. Matsko, D. Seidel, and L. Maleki, "On phase noise of self-injection locked semiconductor lasers," vol. 8960, 2014, pp. 8960–8969.
- [133] S. L. I. Olsson, B. Corcoran, C. Lundstrom, E. Tipsuwannakul, S. Sygletos, A. D. Ellis, Z. Tong, M. Karlsson, and P. A. Andrekson, "Injection locking-based pump recovery for phase-sensitive amplified links," *Opt. Express*, vol. 21, no. 12, pp. 14 512–14 529, Jun 2013.
- [134] R. Adler, "A study of locking phenomena in oscillators," in *Proc. of I.R.E. and waves and electronics*, June 1946, pp. 351–357.
- [135] B. Razavi, "A study of injection locking and pulling in oscillators," *IEEE Journal of solid-state circuits*, vol. 39, no. 9, pp. 1415–1424, Sept 2004.

- [136] J. Ramirez, L. Olvera, H. Nijmeijer, and J. Alvarez, "The sympathy of two pendulum clocks: beyond Huygens' observations," *Scientific Reports*, vol. 6, pp. 23 580–23 590, 2016.
- [137] E. Lau, "Thesis: High-speed modulation of optical injection-locked semiconductor lasers," *University of California at Berkeley, CA, USA*, 2006.
- [138] R. Noe, B. Koch, V. Mirvoda, and D. Sandel, "Endless optical polarization control and PMD compensation," in *Optical Fiber Communication Conference'10*. San Diego, CA, USA, 2010, p. OThJ1.
- [139] A. Fragkos, A. Bogris, D. Syvridis, and R. Phelan, "Amplitude noise limiting amplifier for phase encoded signals using injection locking in semiconductor lasers," *J. Lightwave Technol.*, vol. 30, no. 5, pp. 764–771, Mar 2012.
- [140] P. Robertson and S. Kaiser, "Analysis of the effects of phase-noise in orthogonal frequency division multiplex (OFDM) systems," in *Communications, 1995. ICC '95 Seattle, 'Gateway to Globalization', 1995 IEEE International Conference on*, vol. 3, Jun 1995, pp. 1652–1657 vol.3.
- [141] P. P. Mitra and J. Stark, "Nonlinear limits to the information capacity of optical fiber communications," *Nature*, no. 44, pp. 1027–1030, 2001.
- [142] E. Ip and J. M. Kahn, "Compensation of dispersion and nonlinear impairments using digital backpropagation," *Journal of Lightwave Technology*, vol. 26, no. 20, pp. 3416–3425, Oct 2008.
- [143] E. Ip, "Nonlinear compensation using backpropagation for polarization-multiplexed transmission," *Journal of Lightwave Technology*, vol. 28, no. 6, pp. 939–951, March 2010.
- [144] R. Dar and P. J. Winzer, "On the limits of digital back-propagation in fully loaded WDM systems," *IEEE Photonics Technology Letters*, vol. 28, no. 11, pp. 1253–1256, June 2016.
- [145] E. Temprana, E. Myslivets, V. Ataie, B. P. P. Kuo, N. Alic, V. Vusirikala, V. Dangui, and S. Radic, "Demonstration of coherent transmission reach tripling by frequency-referenced nonlinearity pre-compensation in EDFA-only smf link," in *ECOC 2016; 42nd European Conference on Optical Communication*, Sept 2016, pp. 1–3.
- [146] E. F. Mateo, F. Yaman, and G. Li, "Efficient compensation of inter-channel nonlinear effects via digital backward propagation in WDM optical transmission," *Opt. Express*, vol. 18, no. 14, pp. 15 144–15 154, Jul 2010.
- [147] L. Zhu, F. Yaman, and G. Li, "Experimental demonstration of XPM compensation for WDM fibre transmission," *Electronics Letters*, vol. 46, no. 16, pp. 1140–1141, August 2010.

- [148] X. Chen and W. Shieh, "Closed-form expressions for nonlinear transmission performance of densely spaced coherent optical OFDM systems," *Opt. Express*, vol. 18, no. 18, pp. 19 039–19 054, Aug 2010.
- [149] T. K. Chiang, N. Kagi, M. E. Marhic, and L. G. Kazovsky, "Cross-phase modulation in fiber links with multiple optical amplifiers and dispersion compensators," *Journal of Lightwave Technology*, vol. 14, no. 3, pp. 249–260, Mar 1996.
- [150] R. Dar, M. Feder, A. Mecozzi, and M. Shtaif, "Properties of nonlinear noise in long, dispersion-uncompensated fiber links," *Opt. Express*, vol. 21, no. 22, pp. 25 685–25 699, Nov 2013.
- [151] B. Foo, B. Corcoran, and A. Lowery, "Optoelectronic method for inline compensation of XPM in long-haul optical links," *Opt. Express*, vol. 23, no. 2, pp. 859–872, Jan 2015.
- [152] Z. Tao, W. Yan, S. Oda, T. Hoshida, and J. C. Rasmussen, "A simplified model for nonlinear cross-phase modulation in hybrid optical coherent system," *Opt. Express*, vol. 17, no. 16, pp. 13 860–13 868, Aug 2009.
- [153] M. E. McCarthy, M. A. Z. A. Kahteb, F. M. Ferreira, and A. D. Ellis, "PMD tolerant nonlinear compensation using in-line phase conjugation," *Opt. Express*, vol. 24, no. 4, pp. 3385–3392, Feb 2016.
- [154] L. B. Y. Du and A. J. Lowery, "Pilot-based XPM nonlinearity compensator for CO-OFDM systems," *Opt. Express*, vol. 19, no. 26, pp. B862–B867, Dec 2011.
- [155] B. Inan, S. Randel, S. L. Jansen, A. Lobato, S. Adhikari, and N. Hanik, "Pilot-tone-based nonlinearity compensation for optical OFDM systems," in *36th European Conference and Exhibition on Optical Communication*, Sept 2010, pp. 1–3.
- [156] A. Lobato, B. Inan, S. Adhikari, and S. L. Jansen, "On the efficiency of RF-pilot-based nonlinearity compensation for CO-OFDM," in *Optical Fiber Communication Conference '11*. Los Angeles, CA, USA, 2011, p. OThF2.
- [157] R. Rios-Müller, J. Renaudier, P. Brindel, A. Ghazisaeidi, I. Fernandez, P. Tran, C. Simonneau, L. Schmalen, and G. Charlet, "Spectrally-efficient 400-Gb/s single carrier transport over 7200 km," *J. Lightwave Technol.*, vol. 33, no. 7, pp. 1402–1407, Apr 2015.
- [158] G. Raybon, A. Adamiecki, P. J. Winzer, M. Montoliu, S. Randel, A. Umbach, M. Margraf, J. Stephan, S. Draving, M. Grove, and K. Rush, "All-ETDM 107-Gbaud PDM-16QAM (856-Gb/s) transmitter and coherent receiver," in *39th European Conference and Exhibition on Optical Communication (ECOC 2013)*, Sept 2013, pp. 1–3.

- [159] F. P. Guiomar, S. B. Amado, R. M. Ferreira, J. D. Reis, S. M. Rossi, A. Chiuchiarelli, J. R. F. de Oliveira, A. L. Teixeira, and A. N. Pinto, "Multicarrier digital backpropagation for 400G optical superchannels," *J. Lightwave Technol.*, vol. 34, no. 8, pp. 1896–1907, Apr 2016.
- [160] F. Zhang, Q. Zhuge, M. Qiu, W. Wang, M. Chagnon, and D. V. Plant, "XPM model-based digital backpropagation for subcarrier-multiplexing systems," *J. Lightwave Technol.*, vol. 33, no. 24, pp. 5140–5150, Dec 2015.
- [161] F. Zhang, Q. Zhuge, M. Qiu, and D. V. Plant, "Low complexity digital backpropagation for high baud subcarrier-multiplexing systems," *Opt. Express*, vol. 24, no. 15, pp. 17 027–17 040, Jul 2016.
- [162] F. Guiomar, S. B. Amado, C. Martins, J. D. Reis, A. L. Teixeira, and A. N. Pinto, "Volterra-based digital backpropagation: Performance and complexity assessment," in *Advanced Photonics'15*. Boston, Massachusetts, USA, 2015, p. SpS2C.1.
- [163] R. Dar, M. Feder, A. Mecozzi, M. Shtaif, and P. J. Winzer, "Nonlinear phase and polarization rotation noise in fully loaded WDM systems," in *2015 European Conference on Optical Communication (ECOC)*, Sept 2015, pp. 1–3.
- [164] R. Diggers, *Encyclopedia of Optical Engineering: Volume 2*. Marcel Dekker Inc., New York, USA, 2003.